

Quantum interference and absorption suppression in negative index materials

Dissertation

Jürgen Kästel

Vom Fachbereich Physik der Technischen Universität Kaiserslautern zur Verleihung
des akademischen Grades „Doktor der Naturwissenschaften“ genehmigte Dissertation

Betreuer: Prof. Dr. Michael Fleischhauer

Zweitgutachter: Prof. Dr. Hans Christian Schneider

Datum der wissenschaftlichen Aussprache: 24. September 2008

D 386

Contents

Kurzfassung	vii
Abstract	ix
1 Introduction and outline	3
1.1 Motivation	3
1.2 Metamaterials: State of the art	4
1.3 Electromagnetically induced transparency	9
1.4 Outline of the thesis	13
I Electromagnetically induced magneto-electric cross coupling and negative refraction	17
2 Negative refraction by magneto-electric cross couplings	19
2.1 Magneto-dielectrics without cross coupling	20
2.2 Fundamental concepts	23
2.3 Tensorial effects	27
2.3.1 Biisotropic media	28
2.3.2 Polarization independent media	29
3 Implementation: 5-level scheme	35
3.1 Induced cross-coupling in atomic media	35
3.2 Single particle treatment	40
3.3 Limits of linear response theory	49
3.4 Non-radiative broadenings	53

3.5 Local field effects	56
3.6 Refractive index	60
4 Applicability of the 5-level scheme	65
4.1 Impedance matching	65
4.2 Tunability	68
4.3 Beyond 1D: Tensorial analysis	70
4.3.1 Angular dependence	73
5 Outlook: EIT in metamaterials	79
II Microscopic approach to local field corrections	83
6 Macroscopic approach to local field corrections	85
6.1 Introduction	86
6.2 Magneto-dielectric materials	91
7 Microscopic model of local field corrections in dielectric media	97
7.1 Formal considerations	97
7.2 Multiple scattering in real space	100
7.2.1 General solution	101
7.2.2 Single scatterer	104
7.2.3 Simple cubic lattice of point dipoles	106
7.3 Solution in reciprocal space	113
8 Magnetic media	117
8.1 Multiple scattering in real space	119
8.2 Solution in reciprocal space	121
8.3 The question of H versus B	121
8.3.1 Macroscopic Treatment	122
8.3.2 Microscopic Treatment	122
9 Magneto-dielectric materials	125

III Purcell effect over macroscopic distances using negative-index materials	133
10 Macroscopic field quantization and atomic linewidth	135
10.1 Field quantization	136
10.2 Spontaneous decay rate	138
11 Modified Purcell effect in front of a mirror	143
11.1 Green function for 3-layered media	144
11.2 Purcell effect without $n = -1$ coating	147
11.3 Purcell effect including $n = -1$ coating	148
12 Limitations	151
12.1 Finite absorption	151
12.2 Finite transverse extension	153
12.3 Dispersion effects	155
IV Appendices	159
A The vacuum Green function	161
B The magnetic scattering T-matrix (8.28)	163
C Convergence behavior of (9.7) and (9.8)	167
Bibliography	170
List of Figures	185
Publications	187
Lebenslauf	189

Kurzfassung

Optische Materialien mit negativem Brechungsindex haben sich in den letzten Jahren zu einem der bedeutendsten Forschungsthemen auf dem Gebiet der Photonik entwickelt. Ausgelöst wurde diese Entwicklung durch theoretische und experimentelle Arbeiten zu spektakulären potentiellen Anwendungen dieser Materialien wie der “Superlinse”, die eine optische Abbildung jenseits des Beugungslimits erlauben sollte, sowie optischer “Tarnkappen”, die es ermöglichen sollten, Objekte in bestimmten Frequenzbereichen für elektromagnetische Strahlung wie Vakuum erscheinen zu lassen. Eines der größten Hindernisse für die praktische Realisierung dieser Anwendungen ist die starke Absorption, die die negative Brechung in allen bisher zu diesem Zweck untersuchten bzw. konstruierten Materialien begleitet. Die vorliegende Arbeit “Quantum interference and absorption suppression in negative index materials” untersucht, inwieweit Quanteninterferenzphänomene, wie sie aus der Quantenoptik atomarer Systeme bekannt sind, ausgenutzt werden können, um einerseits die Absorption drastisch zu reduzieren und andererseits bereits bei kleinen Dichten einen negativen Brechungsindex zu erzielen.

Insbesondere werden resonante kohärente Effekte analog zur elektromagnetisch induzierten Transparenz untersucht. Hierbei werden durch Anlegen eines äußeren Kopplungsfeldes die Hauptbeiträge der Absorption unterdrückt und gleichzeitig eine resonant überhöhte Kreuzkopplung zwischen den elektrischen und magnetischen Komponenten des Probe-Feldes induziert. Diese Kreuzkopplung hat den Vorteil, dass man die Bedingung negativer Permeabilität zur gleichzeitigen Erzeugung eines negativen Brechungsindex nicht erfüllen muss, wie es bei Medien ohne Kreuzkopplung der Fall wäre.

In einem einführenden Kapitel werden die Grundlagen der Theorie negativer Brechung erläutert und die experimentellen Techniken zur Herstellung von entsprechenden Materialien dargestellt. Es stellt sich dabei heraus, dass, obwohl die experimentelle Umsetzung negativer Brechung in den letzten Jahren einen rasanten Fortschritt verzeichnen konnte, alle derzeit verfügbaren Medien unter enormer Absorption leiden. Im Hinblick auf die Anwendung elektromagnetisch induzierter Transparenz zur Lösung dieses Problems werden im Anschluss deren grundlegende Resultate einführend zusammengefasst.

In Kapitel 2 werden allgemeine Materialien mit einer Kopplung zwischen elektrischen und magnetischen Freiheitsgraden im Hinblick auf die Realisierung negativer Brechung diskutiert. Solche Kreuzkopplungen manifestieren sich z.B. in einer chiralen Antwort oder im Auftreten eines magnetoelektrischen Effekts. Es wird gezeigt, dass man einen negativen Brechungsindex erzeugen kann ohne gleichzeitig negative Permeabilität vorauszusetzen. Somit kann die größte Schwierigkeit in der

Erzeugung negativer Brechung im optischen Spektralbereich umgangen werden. Das hat zur Folge, dass die Dichte an Streuern im Vergleich zu nichtkreuzgekoppelten Realisierungen mehrere Größenordnungen kleiner und damit realistisch gewählt werden kann.

Kapitel 3 hat eine konkrete Umsetzung der in Kapitel 2 entwickelten Ideen zum Inhalt. Dazu wird ein atomares System untersucht mit einem Niveauschema, in dem ein elektrischer und ein magnetischer Dipolübergang durch Anlegen eines äußeren Feldes gekoppelt werden. In diesem System wird nicht nur die zuvor diskutierte Kreuzkopplung induziert sondern auch elektromagnetisch induzierte Transparenz. Letztere bewirkt eine starke Unterdrückung des Imaginärteils der elektrischen Suszeptibilität. Unter Einbeziehung von Lokalfeldkorrekturen kann damit gezeigt werden, dass negative Brechung induziert werden kann, deren Verhältnis von Brechung zu Absorption einige Größenordnungen größer ist als bei aktuellen experimentellen Umsetzungen. Weiterhin wird gezeigt, dass mit Hilfe des äußeren Feldes auch die Stärke des negativen Index kontrolliert werden kann und sich somit das vorgestellte Schema zur Entwicklung schaltbarer Komponenten eignet.

Während in Teil I der Arbeit die Materialantwort eines Ensembles kohärent getriebener atomarer Dipolstrahler durch makroskopische Suszeptibilitäten beschrieben wurde, wird in Teil II eine mikroskopische Theorie der Materialantwort abgeleitet. Wann immer der Brechungsindex eines Mediums wesentlich von 1 abweicht, ist eine Kontinuumsbeschreibung der optischen Eigenschaften des Materials nicht mehr adäquat. Die wichtigste und von der mikroskopischen Struktur des Materials weitgehend unabhängige Korrektur ist die im dielektrischen Fall als Clausius-Mossotti-Relation bekannte Lokalfeldkorrektur. Teil II der Arbeit beschäftigt sich mit einer mikroskopischen Theorie dieser Korrekturen für Materialien mit magnetischen Freiheitsgraden. Dabei zeigt sich, dass eine Kombination von Lokalfeldkorrekturen für die elektrischen und magnetischen Freiheitsgrade dazu führen kann, dass mit zunehmender Teilchendichte die Absorption des Materials sinkt und der Brechungsindex gleichzeitig dem Wert $n = -2$ zustrebt. Dabei wurde das Medium durch ein Gitter von Punktteilchen modelliert und durch Vielfachstreuung die selbstkonsistente Lösung der elektromagnetischen Antwort ermittelt.

Im letzten Teil wird eine Variante des quantenmechanischen Purcell-Effektes betrachtet. Dabei wird die natürliche Linienbreite eines Atoms vor einem Spiegel betrachtet auf dessen Oberfläche eine Schicht eines Materials mit negativer Brechung aufgebracht wurde. Aufgrund der perfekten fokussierenden Eigenschaften dieser Schicht zeigt ein Atom mit makroskopischem Abstand zum Spiegel je nach Polarisierung totale Unterdrückung oder Überhöhung der spontanen Zerfallsrate.

Abstract

Optical materials with a negative index of refraction have evolved in the last couple of years into one of the most important areas in photonics research. This progress has been stimulated by spectacular proposed applications like the “super-lens” which allows for resolution beyond the diffraction limit and “optical cloaks” which enable objects to appear as vacuum to electromagnetic waves of a certain wavelength. One the major obstacles to the practical implementation of such applications is the strong absorption present in all hitherto constructed media with a negative refractive index. The Thesis “Quantum interference and absorption suppression in negative index materials” deals with the exploitation of quantum interference phenomena known from the quantum optics of atomic systems to yield significant reduction of absorption and simultaneously allow for a negative index of refraction at comparably small densities.

In particular resonant coherent effects similar to electromagnetically induced transparency are studied. An external coupling field is used to suppress the main contributions to the absorption while simultaneously inducing a resonantly enhanced coupling between the electric and magnetic components of the probe field. As an advantage of this coupling compared to media without cross-coupling the constraint of negative permeability does not need to be fulfilled in order to induce negative refraction.

In an introductory chapter the basic theory of negative refraction is sketched and the experimental techniques used to construct materials with a negative index of refraction are explained. Although the experimental realization of negative index materials made breathtaking progress in recent years, it turns out that all actual media suffer from a tremendous absorption. In the following the basic results of the theory of electromagnetically induced transparency are introduced as they will be used in the solution of these problems.

Chapter 2 deals with general materials which display a coupling between electric and magnetic degrees of freedom regarding the realization of negative refraction. Such a cross-coupling is found for example in a chiral response or in materials which show the magneto-electric effect. As a result such media allow for negative refraction without requiring a negative permeability. Thus the major obstacle in the generation of negative index materials in the optical spectrum can be overcome. This allows negative refraction at much lower and therefore realistic densities of scatterers compared to materials without such cross-couplings.

Chapter 3 deals with a particular implementation of the preceding ideas. In particular a level scheme is proposed in which an electric and a magnetic dipole transition are getting coupled by applying a strong external field. By doing so not only the cross-coupling according to chapter 2 is implemented but simultaneously electromagnetically induced transparency is obtained. This leads to a significant reduction of the imaginary part of the electric susceptibility which presents the major contribution to the overall absorption properties. Including local field corrections this results in an induced negative refractive index with a ratio of refraction to absorption which is orders of magnitude larger than in current experiments. Moreover it is shown that the value of the (negative) refractive index can be tuned by means of the external coupling field as well. Hence switchable components for applications seem possible by utilization of the described level scheme.

In part I of this thesis the electromagnetic response of an ensemble of coherently driven atomic dipole emitters has been modeled by macroscopic susceptibilities. In contrast part II utilizes a microscopic theory for the same purpose as a macroscopic description ceases to be adequate as soon as the index of refraction of a medium differs significantly from the vacuum value $n = 1$. The most important correction for dielectric media which does not depend on the particular microscopic structure of the material is the Clausius-Mossotti local field correction factor. Part II of the thesis concerns with a microscopic model of such corrections for media with magnetic degrees of freedom. It turns out that combining appropriate local field corrections for the electric and magnetic degrees of freedom, respectively, yields a decrease of absorption with increasing number density of scatterers. Simultaneously, the refractive index reaches the value $n = -2$ asymptotically. The material is modeled by a lattice of point scatterers and solved for the self-consistent electromagnetic response function using multiple scattering techniques.

The last part deals with a variant of the quantum mechanical Purcell effect. The natural linewidth of an atom placed in front of a mirror with a coating of a negative index material is obtained using a Green function technique. As a result of the perfect focusing properties of the negative refractive coating an atom with a macroscopic distance to the mirror displays either a total suppression or an enhancement of the spontaneous decay rate depending on its polarization state.

for

Katja

CHAPTER 1

Introduction and outline

1.1 Motivation

Photonics research in general and artificial materials with a negative index of refraction in particular experienced an increasing amount of interest in the last couple of years. This progress has been driven by spectacular proposed applications like the “superlens”, which allows for resolution beyond the diffraction limit [1], or even “optical cloaks”, which make objects appear transparent to electromagnetic waves of a certain wavelength [2, 3, 4]. It has led to a tremendous number of metamaterial designs to achieve negative refraction [5, 6, 7, 8, 9, 10, 11]. Simultaneously, the concept of photonic crystals [12, 13] has been applied to concepts of effective negative indices as well [14]. Unlike metamaterials, photonic crystals are characterized by a spatial variation of optical properties due to structured dielectric or metallic bodies on the order of a wavelength rather than subwavelength structures. For certain photonic crystal designs this leads to circular equi-frequency surfaces near the band edge with a negative curvature. As a result beam propagation properties are effectively described by a negative index of refraction [15, 16, 17, 18].

One of the major obstacles to the practical implementation of such applications is the strong absorption present in all media with negative refractive

index investigated so far. This thesis aims at exploiting quantum interference phenomena from quantum optics of atomic systems to yield significant reduction of absorption and simultaneously allow for a negative index of refraction. In particular, resonant coherent effects similar to electromagnetically induced transparency are used to suppress the main contributions to the absorption. In addition an external coupling field is applied to simultaneously induce a resonantly enhanced coupling between the electric and magnetic components of the probe field. As an advantage of this coupling compared to media without cross-coupling the constraint of negative permeability does not need to be fulfilled in order to induce negative refraction.

1.2 Metamaterials: State of the art

The history of negative refraction research separates roughly into two unequal eras. Before the year 2000 there were only few mentionings of the notion of negative refraction [19, 20, 21]. From these the article of V. Veselago [21] is best known as it analyzes negative refraction using the concepts of the material permittivity ε and permeability μ . It also discusses some fundamental phenomena associated with a negative refractive index like the inverse Doppler shift, inverse Cerenkov radiation and most importantly the flat lens [cf. Fig. 1.1(a)]. Although Veselago realized that negative refraction in naturally occurring media does not exist he provided a route to negative refraction: simultaneous negative permittivity and permeability ($\varepsilon, \mu < 0$) yield negative refraction, i.e., $n < 0$. This seems to be peculiar as the definition of the index of refraction $n = \sqrt{\varepsilon\mu}$ at first glance leads to identical results for the two cases $\varepsilon, \mu > 0$ and $\varepsilon, \mu < 0$, respectively. As Veselago noticed ε and μ are fundamentally complex functions with the physical constraint $\text{Im}[\varepsilon], \text{Im}[\mu] \geq 0$ for passive media. As a result the square root of the complex function $n = \sqrt{\varepsilon\mu}$ has to be taken such that $\text{Im}[n] \geq 0$ holds, from which the limit $\text{Re}[n] < 0$ for the case $\text{Re}[\varepsilon], \text{Re}[\mu] < 0$ follows. It is worth noting, that negative index materials always display unavoidable dispersion. The electromagnetic field energy must never attain negative values which can only be fulfilled as long as the conditions $\frac{d}{d\omega}(\omega\text{Re}[\varepsilon(\omega)]) \geq 0$ as well as $\frac{d}{d\omega}(\omega\text{Re}[\mu(\omega)]) \geq 0$ are met.

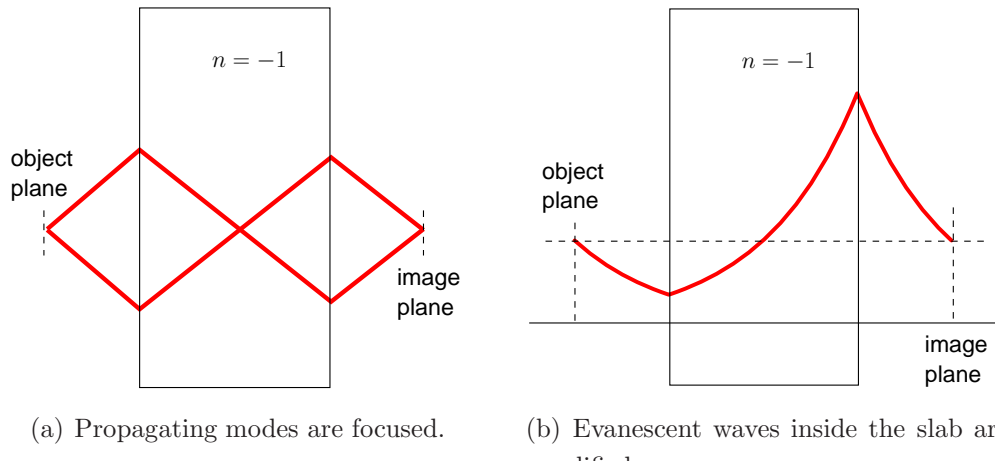


Figure 1.1: The perfect flat lens.

The second era of negative index research started in 2000 in which major experimental and theoretical breakthroughs triggered an exponential grow of interest in this field. In the theoretical article of Sir John Pendry [1] it is shown that Veselago's flat lens is also a perfect lens under the assumptions that the permittivity and the permeability are identically negative and non-absorptive, e.g. $\varepsilon = \mu = -1$, and the impedance of the flat lens is matched to the surroundings. This perfect lens allows for image resolution unlimited by the wavelength λ due to the "amplification" of evanescent waves with transverse wave vectors k_{\perp} larger than $k = 2\pi/\lambda$ inside the slab of the flat lens. As these evanescent modes transport information about object details smaller than λ the resolution of the lens can in principle be infinite. The physical reason of the "amplification" is the off-resonant coupling of the signal field to a surface plasmon mode [22, 23] which results in the amplitude distribution of the evanescent modes depicted in Fig. 1.1(b).

In the year 2000 there was also the first report about the realization of a medium which fulfilled Veselago's requirement of negative permittivity and permeability [5]. This led shortly thereafter to the first experimental verification of negative refraction [6] in the microwave regime using metamaterials. These materials are assembled from artificial functional units whose size is much smaller than the resonance wavelength at which they are supposed to work. Hence with the wavelength of interest these constituents can not be

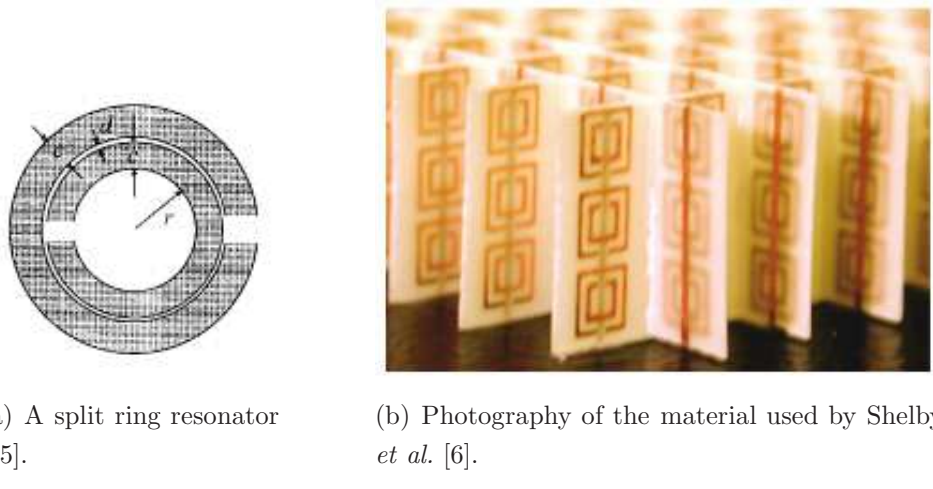
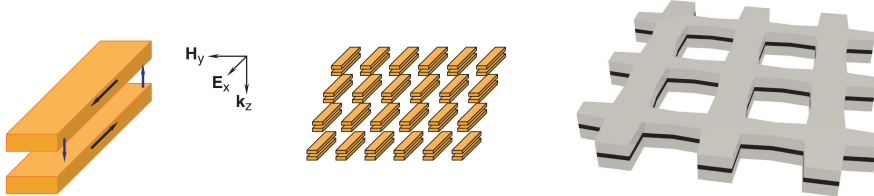


Figure 1.2: The first realization of a negative refracting material [6]. The metallic wires provide $\text{Re}[\varepsilon] < 0$ below the plasma frequency; the split ring resonators yield a strong magnetic resonance with $\text{Re}[\mu] < 0$. The dimension of the unit cell is 5mm whereas the resonant wavelength is 3cm.

resolved. The material is effectively homogeneous and a permittivity and a permeability can be assigned. Again it was Sir John Pendry who made crucial contributions which made overlapping negative electric permittivity [24] and negative magnetic permeability [25], and hence the aforementioned experimental success possible. Here, negative permittivity $\text{Re}[\varepsilon] < 0$ is provided by an array of thin wires which yield a plasma frequency in the GHz-regime [24]. The magnetic response is provided by split ring resonators [25] with a strong magnetic resonance over spectral regions, where $\text{Re}[\mu] < 0$ holds. Fig. 1.2 shows the first experimentally implemented negative index material which made use of ordinary circuit board material.

In the subsequent development the concept of thin wires and split ring resonators was further established [26, 27, 28, 29, 30], and by miniaturization the resonance frequency was increased from THz [7, 31, 32] to the infrared [8, 9] and even to the visible spectrum [9, 33] while simultaneously morphing the complicated split ring resonators into simpler versions (cf. Fig. 1.4). However, this concept did not yield negative refraction but only $\text{Re}[\mu] < 0$ for increasing resonance frequencies.

The metamaterial branch of negative index material research experienced



(a) Short wire pairs [38]: Symmetric and antisymmetric current distributions contribute to the electric and magnetic response, respectively.

(b) Inverted structure according to Babinet's principle: Double fishnet [43].

Figure 1.3: Modern designs of metamaterials.

a major impulse by the invention of rather simple but functional structures. A pair of metallic nanopillars [34] or short wires [10] support an electric as well as a magnetic resonance via symmetric and antisymmetric (Fig. 1.3) current distributions. As miniaturization of wire pairs is fairly easy compared to split ring resonators, $\text{Re}[\mu] < 0$ [34, 35, 36] and $\text{Re}[n] < 0$ materials [10, 37, 38] up to the visible spectrum have been demonstrated. In contrast to the split ring resonator design, these media have the advantage of showing a negative index while being irradiated perpendicularly [see Fig. 1.3(a)] compared to the experimentally problematic parallel propagation axis for split ring metamaterials. Using Babinet's principle of optics [39, 40] the short wire pairs translate to a double fishnet structure with rectangular [11, 41, 42, 43] or circular holes [44] which can support higher currents and hence yield better results in terms of response strength.

Fig. 1.4 shows the time evolution of metamaterial research regarding increasing resonance frequencies. The full and the open symbols denote negative refractive $\text{Re}[n] < 0$ and negative permeability $\text{Re}[\mu] < 0$ media, respectively, while the colors encode the used structure from original (orange) and simplified (green) split ring resonators to short wire pairs (blue) and fishnet (red) designs.

Though there is obviously a tremendous progress in pushing the spectral regions of negative refraction to higher and higher frequencies, there are some fundamental issues that need to be addressed before applications like the super lens [1] or electromagnetic cloaking [2, 3, 4] in the visible spectrum can

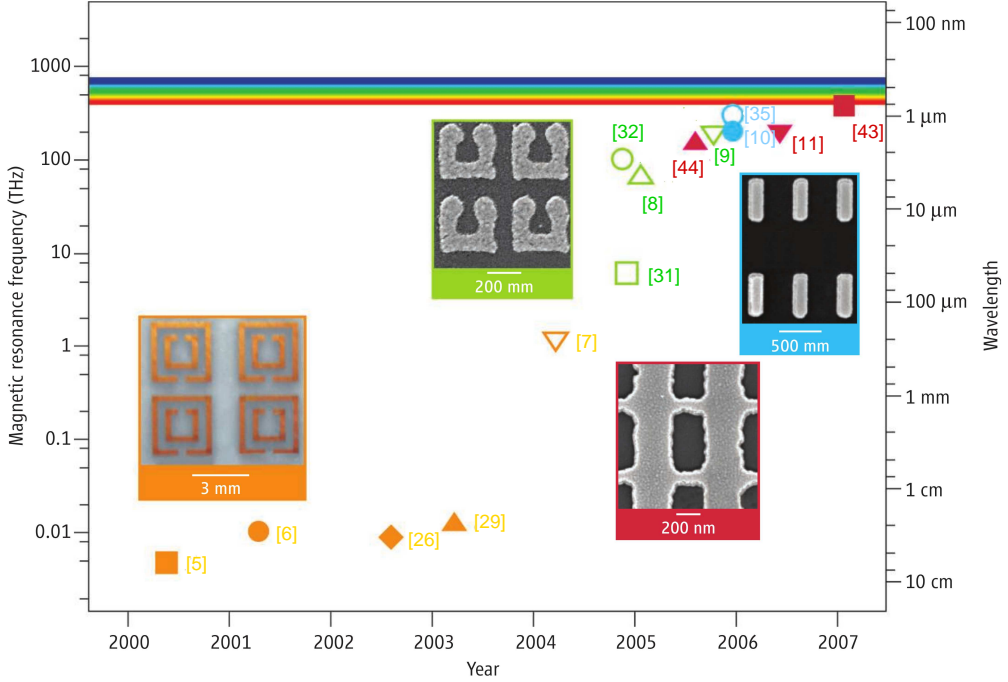


Figure 1.4: The evolution of metamaterial research. The full symbols denote a negative refractive index $\text{Re}[n] < 0$ while the open symbols denote a negative permeability $\text{Re}[\mu] < 0$. The structures evolved from the original split ring resonator design (orange) to a simplified split ring (green) and finally to short wire pairs (blue) and the Babinet inverted fishnet (red). The numbers denote the corresponding references. (graph taken from [45])

be realized. One of these issues is given by the fact that the negative index materials especially for high frequencies are only low-dimensional, i.e., show $\text{Re}[n] < 0$ only for a certain propagation direction. Moreover, the refractive index for this particular propagation direction is polarization dependent. The most severe constraint, though, is given by the large absorption present in the metamaterial approach, commonly measured by the figure of merit

$$FoM = -\frac{\text{Re}[n]}{\text{Im}[n]} \quad (1.1)$$

which is supposed to reach high positive values.

However, the experimental figures of merit for negative index media in the

Reference	year	<i>FoM</i>
[10]	2005	$\ll 1$
[38]	2006	$\ll 1$
[43]	2007	0.5
[44]	2005	$\lesssim 1$
[42]	2006	3

Table 1.1: Exemplary values of *FoM*.

near-infrared or visual spectrum are usually¹ less than 1 ($FoM \ll 1$ [10, 38], $FoM = 0.5$ [43], $FoM \lesssim 1$ [44]) and reach $FoM = 3$ at best [42] (cf. table 1.1). Note that these *FoM*'s are obtained for silver structures, which provide the least metallic losses. As theoretical studies [47, 48] have shown, this is an intrinsic problem as a numerical optimization of design elements of the fishnet materials suggests that $FoM = 3$ is already the theoretical maximum.

1.3 Electromagnetically induced transparency

An effective means of suppressing absorption in ensembles of near resonant quantum oscillators, such as atoms or molecules, is given by electromagnetically induced transparency (EIT), which can alter the absorption spectrum such that a perfect reduction of the losses appears on resonance. It has mostly been observed in atomic vapors [49, 50] as well as in doped crystals [51], but is explicitly not limited to quantum systems² [52]. The most generic system displaying EIT is given by a 3-level atom with a level scheme depicted in Fig. 1.5(a) which due to its similarity to the greek letter Λ is frequently called Λ -scheme. It consists of two (meta-)stable ground states $|1\rangle$ and $|2\rangle$ and a common upper state $|3\rangle$. This upper state is connected by a “coupling” field with Rabi frequency Ω_c to the meta-stable state $|2\rangle$ and similarly by the “probe” field with Rabi frequency Ω_p to the ground state $|1\rangle$. To discuss the key features of EIT we assume the coupling field to be resonant but allow a

¹See also the review [46].

²See also chapter 5.

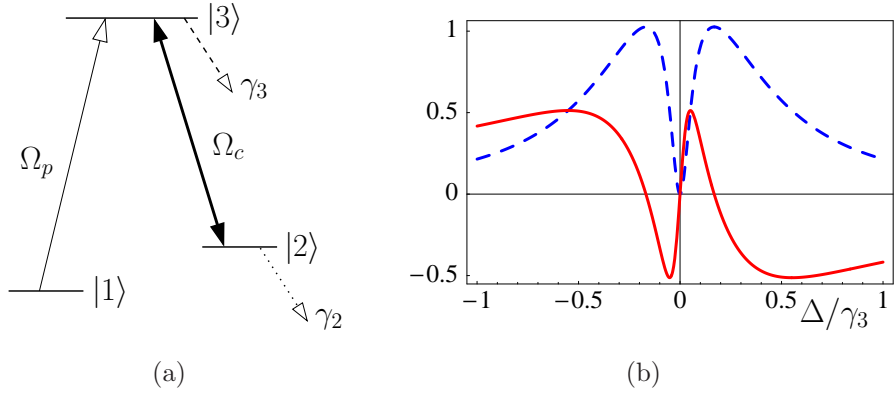


Figure 1.5: (a) The generic Λ -scheme of EIT. (b) Real (solid) and imaginary (dashed) parts of the linear response susceptibility in arbitrary units as a function of the detuning Δ .

detuning $\Delta = \omega_p - \omega_{31}$ for the probe field.

Without coupling field, the linear probe field absorption spectrum has an ordinary Lorentzian structure and a corresponding dispersion of the real part of the susceptibility $\chi(\omega)$. In contrast, the application of the coupling laser can alter the spectrum fundamentally. Fig. 1.5(b) shows a typical spectrum for EIT: The absorption line develops a dip of low absorption while the real part of $\chi(\omega)$ displays strong linear dispersion around resonance. Note that for $\gamma_2 = 0$, i.e., a perfectly stable ground state $|2\rangle$, the susceptibility vanishes exactly on resonance, $\Delta = 0$. The width of the transparency window will then be governed by the coupling strength Ω_c . For large coupling $\Omega_c \gg \gamma_3$ the splitting of the absorption is linear in Ω_c while for small coupling the transparency window becomes significantly smaller than the natural width γ_3 of the resonance line. Note that in all cases ($\gamma_2 = 0$), the susceptibility vanishes for $\Delta = 0$, which can not be explained by simple line splitting. Under the condition

$$\gamma_2 \ll \gamma_3 \quad (1.2)$$

all features of EIT can be obtained if the Rabi frequency satisfies $\Omega_c^2 > \gamma_2 \gamma_3$. The absorption on resonance in that case is governed by $\text{Im}[\chi(0)] \sim \gamma_3 \gamma_2 / \Omega_c^2$. Thus for meta-stable states $|2\rangle$ significant suppression of absorption can be obtained. Note that γ_2 does not have to be the population decay rate out of

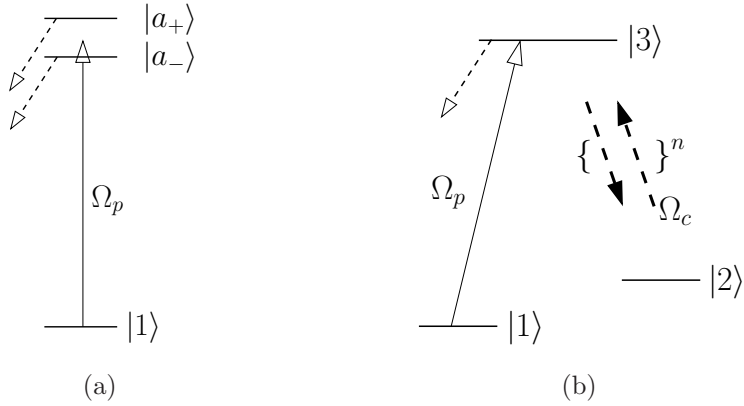


Figure 1.6: Explanations for EIT: (a) dressed state picture (b) quantum interference of different excitation paths.

state $|2\rangle$, but any rate which leads to a dephasing of the coherence between the ground states $|1\rangle$ and $|2\rangle$ must be taken into account³.

Experimentally, EIT can be used to transfer a light beam through otherwise opaque atomic vapors by application of a coupling laser field [54, 55], thus the name electromagnetically induced transparency as proposed by Harris *et al.* [56]. Apart from the spectroscopic properties, EIT has strong influence on the propagation properties of light pulses. Due to the steep linear dispersion within the transparency window the group velocity of light pulses can be reduced by orders of magnitude thus leading to ultraslow light and even stopping of light pulses in coherently driven media [57, 58, 59].

The physical origin of EIT is explained by the effect of coherent population trapping (CPT) [60] which can be described in several ways. The influence of a strong coupling field Ω_c cannot be treated perturbatively in the limit $\gamma_2 \rightarrow 0$. Thus for small Ω_p the subsystem of states $|2\rangle$, $|3\rangle$ including Ω_c forms a new set of eigenstates

$$|a_{\pm}\rangle = \frac{1}{\sqrt{2}} (|2\rangle \pm |3\rangle) \quad (1.3)$$

dressed by the presence of the strong coupling Ω_c . The eigenenergies of these dressed states form a doublet as depicted in Fig. 1.6(a). A probe field tuned to the center between $|a_+\rangle$ and $|a_-\rangle$, which corresponds to $\Delta = 0$, couples

³For quantum dots see, e.g., [53].

to a superposition of $|a_{\pm}\rangle$ with equal weights. As a result the transition probability for leaving the ground state $|1\rangle$ vanishes identically yielding a vanishing susceptibility on resonance. This peculiar result is due to the dressed state decay channels being correlated, i.e., ending up in the same final state. The total transition probability amplitude hence is a superposition of $|1\rangle \rightarrow |a_+\rangle \rightarrow \text{"decay"}$ and $|1\rangle \rightarrow |a_-\rangle \rightarrow \text{"decay"}$ which turn out to interfere destructively.

The aspect of quantum interference can also be discussed in the bare state representation. The transition probability to excite the atom out of the ground state $|1\rangle$ to the upper state $|3\rangle$ and successive decay from that state is a superposition of the probability amplitude of the direct path $|1\rangle \rightarrow |3\rangle \rightarrow \text{"decay"}$ and all amplitudes of higher order paths which reach the final state $|3\rangle$ only after a number of transitions to the state $|2\rangle$ and back to $|3\rangle$, e.g.,

$$|1\rangle \rightarrow |3\rangle \rightarrow |2\rangle \rightarrow |3\rangle \rightarrow \text{"decay"} \quad (1.4)$$

[cf. Fig. 1.6(b)]. In EIT these amplitudes of higher order paths interfere destructively with the direct excitation amplitude such that the total transition amplitude vanishes (see also [57, 61]).

For arbitrary strengths of the probe field Rabi frequency Ω_p the complete 3-state system has to be diagonalized including Ω_c and Ω_p . One finds that one of the new dressed states does not incorporate the strongly decaying upper state $|3\rangle$ but is only comprised of the ground states $|1\rangle$ and $|2\rangle$. As this state does not lead to fluorescence, it is called “dark” state. When fields Ω_c and Ω_p are applied, the system will ultimately be optically pumped into this dark state, in which it does not interact with the electromagnetic fields any more. The population is thus trapped in the dark state thus the name “coherent population trapping”. Besides optical pumping, a major means of reaching the dark state is the use of adiabatic evolution techniques like STIRAP [62].

One essential aspect of EIT, besides the destructive interference of the linear response susceptibility, is the simultaneous constructive interference for the nonlinear response [56, 63]. In particular we assume to drive the transition $|1\rangle - |2\rangle$, which is electric-dipole forbidden, by either a 2-photon or a magnetic transition [cf. Fig. 1.7(a)]. The nonlinear susceptibility χ^{nl} for the

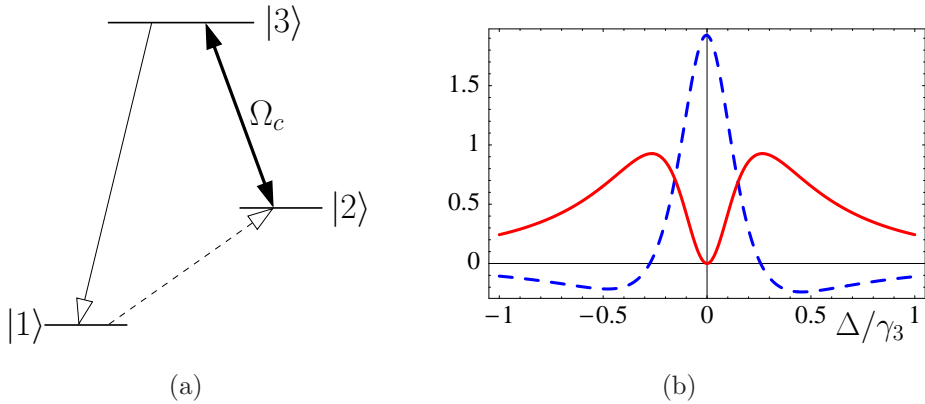


Figure 1.7: (a) Closed loop Λ -scheme with higher order nonlinear susceptibilities. (b) $\text{Im}\chi$ (solid) and $\text{Im}\chi^{nl}$ (dashed) in arbitrary units as a function of the detuning Δ .

parametric generation of radiation from the $|3\rangle - |1\rangle$ transition in the presence of strong coupling Ω_c then has a maximum on resonance [57, 64]. As discussed above, the linear susceptibility for the aforementioned radiation from the $|3\rangle - |1\rangle$ transition simultaneously has a minimum [cf. Fig. 1.7(b)]. Thus EIT allows for efficient nonlinear processes without absorbing the generated radiation.

1.4 Outline of the thesis

One main aspect of this thesis is to connect the ideas of negative refraction using quantum oscillators (atoms, molecules, excitons, ...) with suppression of absorption by means of EIT. In particular, I will show in part I that negative refraction in atomic media is feasible when a magnetoelectric coupling between the electric and magnetic degrees of freedom is introduced. Such a cross-coupling can be induced in atomic systems by strongly coupling electric and magnetic transitions. In chapter 3 it is explicitly analyzed how EIT suppresses the absorption efficiently, while enhancing the nonlinear response, which in this case is given by the cross-coupling. As a result, negative refraction in atomic media takes place at densities which are orders of magnitude smaller than in corresponding proposals that do not employ such induced

cross-couplings. Simultaneously, the absorption coefficient drops due to EIT to values that are orders of magnitude smaller than in current metamaterials [Kästel2007b, Kästel2008]. In chapter 4, I discuss important questions regarding the applicability of those ideas. In particular, I show that a medium that displays such a coupling can be impedance matched to the surroundings, which is a crucial issue for any optical component. I also show that the value of the refractive index can be fine-tuned by external fields which may be important for switchable devices. I conclude this part with an explicit analysis of the tensorial properties of such media.

A crucial input used in part I are Clausius-Mossotti local field correction factors. As the simultaneous application for electric and magnetic degrees of freedom leads to a counterintuitive behavior in the limit of high densities part II is devoted to a microscopic analysis of the local field factors. From a phenomenological derivation based on macroscopic considerations I find in chapter 6 that the simultaneous application of the local field corrections to electric and magnetic oscillators, which employ only purely radiative broadening, results in a vanishing absorption for high densities, while in the same limit the index of refraction approaches the value $n = -2$. In the following section I discuss formal considerations of a microscopic model of the material response, which includes Clausius-Mossotti factors, at the example of dielectric media. By generalizing to pure magnetic and magneto-dielectric materials in chapters 8 and 9, respectively, I confirm the findings of the phenomenological discussion in the framework of this microscopic treatment [Kästel2007c].

Part III is devoted to a quantum optical application of negative refraction. In particular the Purcell effect which an atom experiences in front of a mirror is discussed: The spontaneous population decay rate for dipoles oriented along the surface of the mirror is completely suppressed as the distance of the atom to the mirror vanishes. Likewise, atomic dipoles oriented perpendicularly display an enhanced linewidth. As the distance of the atom to the mirror for this effect must be on the order of the transition wavelength an experimental study represents a hard task. After a review of the quantization procedure of the electromagnetic field including macroscopic dispersive and inhomogeneous bodies in chapter 10 [Kästel2003] I show that this prob-

lem can be alleviated by covering the mirror by a layer of a medium with a negative index of refraction. As a result the effect takes place at potentially macroscopic distances to any surface [Kästel2005a, Kästel2005b]. In chapter 12, I analyze limitations of this effect due to imperfect, i.e., absorbing media, finite apertures and the unavoidable dispersion associated with any negative index material.

Part I

Electromagnetically induced magneto-electric cross coupling and negative refraction

CHAPTER 2

Negative refraction by magneto-electric cross couplings

Linear media are characterized by a linear functional relations between the polarization $\mathbf{P}(\mathbf{r}, \omega)$ and the electric field amplitude $\mathbf{E}(\mathbf{r}, \omega)$ and similar relations for the magnetization $\mathbf{M}(\mathbf{r}, \omega)$ and the magnetic field amplitude $\mathbf{H}(\mathbf{r}, \omega)$

$$\mathbf{P}(\mathbf{r}, \omega) = \bar{\chi}_e(\omega) \mathbf{E}(\mathbf{r}, \omega), \quad \mathbf{M}(\mathbf{r}, \omega) = \bar{\chi}_m(\omega) \mathbf{H}(\mathbf{r}, \omega). \quad (2.1)$$

Here $\bar{\chi}_e(\omega)$ and $\bar{\chi}_m(\omega)$ are the electric and magnetic susceptibility tensors, respectively. It turns out that (2.1) is not capable to describe all effects of linear optical systems such as, e.g., optical activity, which describes the rotation of linear polarization in optically active, chiral media independent of the propagation direction of light. In general the constitutive relations

$$\begin{aligned} \mathbf{P} &= \bar{\chi}_e \mathbf{E} + \frac{\bar{\xi}_{EH}}{4\pi} \mathbf{H} \\ \mathbf{M} &= \frac{\bar{\xi}_{HE}}{4\pi} \mathbf{E} + \bar{\chi}_m \mathbf{H} \end{aligned} \quad (2.2)$$

have to be considered. Here $\bar{\xi}_{EH}$ and $\bar{\xi}_{HE}$ denote tensorial coupling coefficients between the electric and magnetic degrees of freedom. These media with *magneto-electric cross coupling* will become of particular interest in the following. Note that here and in the following the coefficients $\bar{\chi}_e(\omega)$, $\bar{\chi}_m(\omega)$, $\bar{\xi}_{EH}$, and $\bar{\xi}_{HE}$ are unitless as we employ Gaussian units throughout this thesis.

2.1 Magneto-dielectric media without cross coupling

Before introducing concepts related to electromagnetically induced cross coupling we study the possibilities of negative refraction in media with constitutive relations given in (2.1). As negative refraction demands magnetic degrees of freedom we consider a medium composed of two species A, B . Let system A be composed of electric dipole oscillators with a number density ϱ_A and a dipole moment d_A . Likewise species B may consist of magnetic dipole oscillators with corresponding number density ϱ_B and a magnetic dipole moment μ_B . In order to have a sufficiently large medium response we operate near resonance. As the electric and magnetic resonances must overlap spectrally in order to obtain a negative refractive index we choose the respective resonance frequencies to be identical $\omega_A = \omega_B = \omega_0$. We assume a single-resonance response for the linear polarizabilities $\alpha_A(\omega)$ and $\alpha_B(\omega)$ of system A and B , respectively. The permittivity $\varepsilon = 1 + 4\pi\varrho_A\alpha_A(\omega)$ and the permeability $\mu = 1 + 4\pi\varrho_B\alpha_B(\omega)$ then read

$$\varepsilon = 1 + \frac{4\pi}{2\hbar} \frac{\varrho_A d_A^2}{\Delta - i\gamma_A} \quad (2.3)$$

and

$$\mu = 1 + \frac{4\pi}{2\hbar} \frac{\varrho_B \mu_B^2}{\Delta - i\gamma_B}. \quad (2.4)$$

γ_A and γ_B denote the corresponding linewidths and $\Delta = \omega_0 - \omega$ is the detuning of the probe field frequency ω from the (common) resonance frequency ω_0 .

For given oscillators the only experimentally free parameters in (2.3) and (2.4) are the detuning Δ and the densities ϱ_A and ϱ_B . In order to get a negative refractive index $\text{Re}[n] < 0$ we need to have $\text{Re}[\varepsilon] < 0$ and $\text{Re}[\mu] < 0$ simultaneously. Therefore we have to tune close to resonance $\Delta \approx 0$ which will inevitably cause significant absorption of the probe beam. Furthermore we need comparably high densities ϱ_A, ϱ_B to compensate the vacuum contribution in the permittivity and the permeability.

From the Wigner-Weisskopf theory [65] we find that for purely radiatively broadened electric oscillators the natural linewidth γ_A in Gaussian units is

given by

$$\gamma_A = \frac{4\omega_0^3 d_A^2}{3\hbar c^3}, \quad (2.5)$$

i.e., quadratic in the electric transition moment d_A . The same result can be obtained from the vacuum limit of a general quantization scheme¹ which incorporates arbitrary dispersive electric and magnetic media represented by the classical Green function $\mathcal{G}(\mathbf{r}, \mathbf{r}', \omega)$ [66, Kästel2003], from which we find the general expression

$$\gamma_A = \frac{8\pi\omega_0^2 d_A^2}{\hbar c^2} \text{Im}[\mathcal{G}(\mathbf{r}_A, \mathbf{r}_A, \omega_0)]. \quad (2.6)$$

An application of this theory to magnetic oscillators yields the corresponding expression²

$$\gamma_B = \frac{8\pi\mu_B^2}{\hbar} \vec{\nabla} \times \text{Im}[\mathcal{G}(\mathbf{r}_A, \mathbf{r}_A, \omega_0)] \times \vec{\nabla} \quad (2.7)$$

which simplifies for the vacuum case $\mathcal{G} \equiv \mathcal{G}^{(0)}$ to $\gamma_B = 4\omega_0^3 \mu_B^2 / (3\hbar c^3)$. Thus the Wigner-Weisskopf result for electric dipoles in free space applies identically to magnetic ones with the electric dipole moment replaced by the corresponding magnetic one.

In particular the radiative linewidth for each species is proportional to the square of the corresponding transition moment, e.g., $\gamma_A \sim d_A^2$. Provided that the transitions under consideration are radiatively broadened it follows that, sufficiently close to resonance $\Delta \ll \gamma_A, \gamma_B$, electric and magnetic responses have approximately the same strength, entirely determined by the transition frequency ω_0 and the respective density ϱ_i . In other words, as soon as the electric polarizability is strong enough to compensate the vacuum response and therefore result in a negative permittivity $\text{Re}[\varepsilon] < 0$, the permeability reaches negative values as well $\text{Re}[\mu] < 0$.

As an example we assume electric and magnetic atomic transitions in the optical spectral range. We assume a typical value $\gamma_B = 1\text{kHz}$ for the magnetic transition [67] and correspondingly $\gamma_A = 137^2 \gamma_B$ (for the factor 137^2 see the discussion below). The density needed to obtain $\text{Re}[n] < 0$

¹Cf. part III.

²In cartesian coordinates the expression $(\vec{\nabla} \times \text{Im}[\mathcal{G}(\mathbf{r}_A, \mathbf{r}_A, \omega_0)] \times \vec{\nabla})_{in}$ is given by $\lim_{\mathbf{r}_1 \rightarrow \mathbf{r}_A} \lim_{\mathbf{r}_2 \rightarrow \mathbf{r}_A} \varepsilon_{ijk} \partial_j^{\mathbf{r}_1} \partial_m^{\mathbf{r}_2} \text{Im}[\mathcal{G}_{kl}(\mathbf{r}_1, \mathbf{r}_2, \omega)] \varepsilon_{lmn}$.

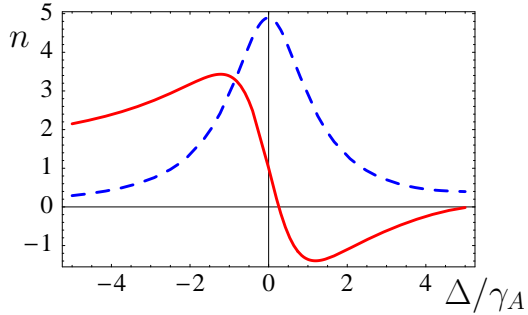


Figure 2.1: Real (solid) and imaginary (dashed) parts of the refractive index $n = \sqrt{\varepsilon\mu}$ of the 2-species model [eqns. (2.3), (2.4)]. Note that $FoM \leq 1$ holds. The parameters are: $\gamma_A = 137^2 \text{kHz}$, $\gamma_B = 1 \text{kHz}$, $\gamma_p = \gamma_A$, $\varrho_A = 2 \cdot 10^{15} \text{/cm}^3$, $\varrho_B = 2 \cdot 10^{19} \text{/cm}^3$. The dipole moments are related to the natural linewidth by Wigner-Weisskopf theory for a wavelength $\lambda = 600 \text{nm}$.

then is about $\varrho_A = \varrho_B = 10^{15} \text{/cm}^3$. In vapors for such densities additional collisional dephasing rates γ_p are in general larger than the radiative width of the magnetic transition γ_B . Due to that additional broadening the strength of the magnetizability $\alpha_B(\omega)$ and hence the magnetic susceptibility is reduced by a factor of up to $\alpha^2 = 137^{-2}$ (α : Fine structure constant) as compared to the electric one. This ratio is due to a general estimate for typical electric and magnetic dipole transition moments in atomic systems [67]

$$\mu_B \approx \alpha d_A. \quad (2.8)$$

As a result the density of magnetic scatterers must be larger than ϱ_A in order to compensate for the reduced magnetizability $\alpha_B(\omega)$. For an additional broadening on the order of the electric radiative linewidth $\gamma_p \approx \gamma_A$ this leads to requiring $\varrho_B \approx 10^{19} \text{/cm}^3$ to obtain $\text{Re}[\mu] < 0$ instead of $\varrho_B \approx 10^{15} \text{/cm}^3$ in the radiative broadening limit. The corresponding refractive index $n = \sqrt{\varepsilon\mu}$ is shown in Fig. 2.1. As the negative refraction is achieved by a resonant scheme we obtain substantial losses and thus the figure of merit at most reaches values on the order of one: $FoM \leq 1$.

Note that high densities with simultaneously small homogeneous broadenings can only be achieved in solid state systems like an ensemble of quantum dots, electron-hole pairs (excitons), doped (laser) crystals or color centers

each of which has its specific advantages, like large transition moments in color centers, but also its drawbacks as the usually tremendous inhomogeneous broadenings in quantum dot ensembles due to the delicate manufacturing process, which can decrease the effective density by many orders of magnitude. The most common materials in the optical regime, which merge the advantages of high density in solid state media with the coherence properties of free space atoms, are doped crystals, in particular at cryogenic temperatures, which allow one to eliminate detrimental effects of crystal properties (phonons) onto the dephasing rates. Compared to laser crystals with doping rates of 1 – 10 mass% [68] in experimental reports about coherence effects in doped crystals [51, 61, 69] the doping rate usually is about 0.05 mass% which corresponds to about $10^{19}/\text{cm}^3$ active particles. As the crystal field contributes a significant inhomogeneous width, the effective density is further reduced. Thus, apart from the absorption problem, a direct implementation of negative refraction in doped crystals seems questionable as the required densities in combination with small homogeneous broadenings can not be provided.

2.2 Magneto-electric cross-coupling and negative refraction: Fundamental concepts

The figure of merit of negative refraction in atomic media can be enhanced significantly while simultaneously relaxing the requirements concerning the necessary density of active scatterers by consideration of more general media as we will show below. In the magneto-dielectric media of section 2.1 the electric and magnetic properties of the material were separated which is reflected in the applied material equations (2.1). We now turn to more general media with a magneto-electric cross-coupling displayed in the material equations

$$\begin{aligned}\mathbf{P} &= \bar{\chi}_e \mathbf{E} + \frac{\bar{\xi}_{EH}}{4\pi} \mathbf{H}, \\ \mathbf{M} &= \frac{\bar{\xi}_{HE}}{4\pi} \mathbf{E} + \bar{\chi}_m \mathbf{H}\end{aligned}\tag{2.9}$$

which can equivalently be expressed as

$$\mathbf{D} = \bar{\varepsilon} \mathbf{E} + \bar{\xi}_{EH} \mathbf{H}, \quad \mathbf{B} = \bar{\xi}_{HE} \mathbf{E} + \bar{\mu} \mathbf{H}. \quad (2.10)$$

The permittivity is given by the electric susceptibility $\bar{\varepsilon} = 1 + 4\pi\bar{\chi}_e$ and similarly the permeability is given by the magnetic susceptibility $\bar{\mu} = 1 + 4\pi\bar{\chi}_m$. Note that all coupling coefficients are in general complex-valued 3×3 -matrices. In such materials the electric Polarization \mathbf{P} is not only induced by the electric field \mathbf{E} as in dielectric or magneto-dielectric materials but also gets a contribution proportional to the magnetic field \mathbf{H} . Likewise the magnetization \mathbf{M} is coupled to the electric field \mathbf{E} . Note that the form of the material equations (2.9) is not unique but presents just one possibility to express the aforementioned cross-coupling of electric and magnetic material properties.

The first usage of material equations which employ cross-coupling coefficients are known from Born [70, 71] and later by Fedorov [72] who used

$$\begin{aligned} \mathbf{D} &= \varepsilon [\mathbf{E} + \beta \nabla \times \mathbf{E}], \\ \mathbf{B} &= \mu [\mathbf{H} + \beta \nabla \times \mathbf{H}] \end{aligned} \quad (2.11)$$

in order to describe optical active media in which the plane of the linear polarization is rotated in the presence of chiral molecules. The strength of the optical activity is given by the factor β which is called chirality parameter. The cross-coupling inherent to equations (2.11) is seen by recasting them with the help of Maxwell's equations for time-harmonic waves into the form

$$\begin{aligned} \mathbf{D} &= \tilde{\varepsilon} \mathbf{E} + \zeta \mathbf{H}, \\ \mathbf{B} &= \tilde{\mu} \mathbf{H} - \zeta \mathbf{E} \end{aligned} \quad (2.12)$$

used by Tellegen [73] to describe an electrical device called gyrator. Note that compared to (2.11) the interpretation of the permittivity has changed. While for time-harmonic fields ε in (2.11) is the permittivity taken at a vanishing magnetic induction $\mathbf{B} = 0$, the corresponding $\tilde{\varepsilon}$ is the permittivity taken at $\mathbf{H} = 0$ with $\tilde{\varepsilon} = \varepsilon / (1 - \omega^2 \varepsilon \mu \beta^2 / c^2)$. Similar considerations apply for the permeabilities μ and $\tilde{\mu}$, respectively. Equations (2.9), (2.10) which will be employed in the following represent a generalization of these early approaches to tensor valued coefficients.

Yet another form of material equations is used in the work of Cheng and Kong [74] who used

$$\begin{aligned} c\mathbf{D} &= \mathcal{P} \cdot \mathbf{E} + c\mathcal{L} \cdot \mathbf{B}, \\ \mathbf{H} &= \mathcal{M} \cdot \mathbf{E} + c\mathcal{Q} \cdot \mathbf{B} \end{aligned} \quad (2.13)$$

which is best suitable for a covariant description of cross-coupled media. Here the coupling coefficients \mathcal{P} , \mathcal{Q} , \mathcal{L} , and \mathcal{M} are again complex-valued 3×3 -matrices. Media of the type (2.13) are called bianisotropic media [75] a term which, in contrast to isotropic, anisotropic or biisotropic, highlights the tensor structure of the parameters. As a realization of cross-coupling they did not consider chirality³, but the magneto-electric effect found in moving dielectrics [76, 77] that get polarized in a magnetic field and magnetized in an electric field, as well as in certain crystals, e.g., antiferromagnets [78]. Note that (2.13) is equivalent to (2.10) with $\bar{\epsilon} = (\mathcal{P} - \mathcal{L} \cdot \mathcal{Q}^{-1} \cdot \mathcal{M})/c$, $\bar{\mu} = \mathcal{Q}^{-1}/c$, $\bar{\xi}_{EH} = \mathcal{L} \cdot \mathcal{Q}^{-1}/c$, and $\bar{\xi}_{HE} = -\mathcal{Q}^{-1} \cdot \mathcal{M}/c$. We thus conclude that, for optical activity, the magneto-electric effect is merely a special case of (2.10) under the assumption of $\bar{\xi}_{EH} = \bar{\xi}_{HE}^t$ as used, e.g., in [79] or in covariant form in [80].

As mentioned above in the following we will use the form (2.10) of the material equations for cross-coupled media to show how negative refraction in such materials emerges. By equating (2.10) with the Maxwell equations in time Fourier space

$$\frac{\omega}{c}\mathbf{D} = -\mathbf{k} \times \mathbf{H}, \quad \frac{\omega}{c}\mathbf{B} = \mathbf{k} \times \mathbf{E} \quad (2.14)$$

we find after elimination of the magnetic field strength \mathbf{H} the Helmholtz equation

$$\left[\bar{\epsilon} + \left(\bar{\xi}_{EH} + \frac{c}{\omega} \mathbf{k} \times \right) \bar{\mu}^{-1} \left(\frac{c}{\omega} \mathbf{k} \times -\bar{\xi}_{HE} \right) \right] \mathbf{E} = 0 \quad (2.15)$$

which governs the propagation $\mathbf{k}(\omega)$ in a medium given by the response tensors $\bar{\epsilon}$, $\bar{\mu}$, $\bar{\xi}_{EH}$, and $\bar{\xi}_{HE}$.

For the sake of simplicity we want to restrict the general form (2.15) to a scalar version in order to discuss the prospects of negative refraction. We hence first arbitrarily choose the wave to propagate into z -direction. Additionally we assume the permittivity $\bar{\epsilon}$ and the permeability $\bar{\mu}$ to be isotropic

³which of course is contained in (2.13) as special case

$\bar{\varepsilon} = \varepsilon \mathbb{1}$, $\bar{\mu} = \mu \mathbb{1}$ as we are interested in the aspects of wave refraction and propagation due to the cross-coupling coefficients. This still leaves the choice of the polarization vector of the transverse beams. As a result, only the upper left 2×2 -submatrices of the tensors $\bar{\xi}_{EH}$ and $\bar{\xi}_{HE}$ are relevant which can be expanded in the four matrices $\mathbf{e}_\pm \otimes \mathbf{e}_\pm^*$, $\mathbf{e}_\pm \otimes \mathbf{e}_\mp^*$ with the circular polarization basis vectors $\mathbf{e}_\pm = (\mathbf{e}_x \pm i\mathbf{e}_y)/\sqrt{2}$. Here \otimes denotes a dyadic product $(\mathbf{a} \otimes \mathbf{b})_{ij} = a_i b_j$ and $*$ means a complex conjugation which for circular polarization basis vectors has to be applied to ensure the orthogonality relations $\mathbf{e}_\pm^* \cdot \mathbf{e}_\pm = 1$, $\mathbf{e}_\pm^* \cdot \mathbf{e}_\mp = 0$. At this point we restrict ourselves to media that allow for conservation of the photonic angular momentum at their interfaces. In particular we assume the response matrices $\bar{\xi}_{EH}$ and $\bar{\xi}_{HE}$ to be diagonal in the basis $\{\mathbf{e}_+, \mathbf{e}_-, \mathbf{e}_z\}$. This results, e.g., for $\bar{\xi}_{EH}$, in

$$\begin{aligned} \bar{\xi}_{EH} &= \xi_{EH}^+ \mathbf{e}_+ \otimes \mathbf{e}_+^* + \xi_{EH}^- \mathbf{e}_- \otimes \mathbf{e}_-^* + \xi_{EH}^z \mathbf{e}_z \otimes \mathbf{e}_z \\ &= \begin{pmatrix} (\xi_{EH}^+ + \xi_{EH}^-)/2 & -i(\xi_{EH}^+ - \xi_{EH}^-)/2 & 0 \\ i(\xi_{EH}^+ - \xi_{EH}^-)/2 & (\xi_{EH}^+ + \xi_{EH}^-)/2 & 0 \\ 0 & 0 & \xi_{EH}^z \end{pmatrix}. \end{aligned} \quad (2.16)$$

By noting that $\mathbf{e}_z \times \mathbf{e}_\pm = \mp i\mathbf{e}_\pm$, the Helmholtz equation (2.15) simplifies for the right⁴ circular polarization vector \mathbf{e}_- to the scalar equation

$$\varepsilon\mu - \left(\xi_{EH}^- + i\frac{c}{\omega}k_z^- \right) \left(\xi_{HE}^- - i\frac{c}{\omega}k_z^- \right) = 0 \quad (2.17)$$

which can be solved for k_z^- . As k_z^- is related to the corresponding refractive index via $n^- = k_z^- c/\omega$ we find

$$n^- = \pm \sqrt{\varepsilon\mu - \frac{(\xi_{EH}^- + \xi_{HE}^-)^2}{4} + \frac{i}{2}(\xi_{EH}^- - \xi_{HE}^-)}. \quad (2.18)$$

The sign of the root has to be chosen such that the resultant imaginary part stays positive for the case of a passive medium. Similarly the refractive index of the right circular polarization is found to read

$$n^+ = \pm \sqrt{\varepsilon\mu - \frac{(\xi_{EH}^+ + \xi_{HE}^+)^2}{4} - \frac{i}{2}(\xi_{EH}^+ - \xi_{HE}^+)}. \quad (2.19)$$

⁴The basis vector \mathbf{e}_- describes a field amplitude which rotates clockwise when viewed against the direction of propagation. Alternatively such a polarization is said to have negative helicity, i.e., transports a spin $-\hbar$ per photon.

From a similar consideration, Pendry [81] noted that for a system under the above mentioned assumptions the refractive index (2.18) can become negative without requiring a negative permeability $\text{Re}[\mu] < 0$ thus circumventing the most prominent obstacle on the road to $\text{Re}[n] < 0$ in atomic media. This important finding can be seen better under the assumption that $\xi_{EH}^- = -\xi_{HE}^-$ in which case the cross-coupling term under the square root vanishes. If we additionally restrict the phase of the complex number ξ_{EH}^- to $\xi_{EH}^- = i\xi$, $\xi > 0$, equation (2.18) simplifies to

$$n^- = \sqrt{\varepsilon\mu} - \xi. \quad (2.20)$$

Thus if we find a system in which the value of ξ gets comparable to $\sqrt{\varepsilon\mu}$ we expect a negative refractive index. Note that here not only the absolute value of ξ matters but that we have to fix the phase of ξ_{EH}^- and ξ_{HE}^- in order to find a *negative* index of refraction $\text{Re}[n^-] < 0$.

In chapter 3 we will show that in atomic media these requirements can be met by artificially inducing a coupling of a magnetic and an electric dipole transition. Considering the amplitude criterion, this is because the cross-coupling coefficients are in general proportional to the combination $d_A\mu_A$ of electric and magnetic transition moments, respectively. From the discussion in section 2.1 it therefore follows (for media with additional broadening mechanisms) that the chiralities scale as $\xi_{EH}^-, \xi_{HE}^- \sim \alpha\chi_e$. This is about a factor of 137 better than the scaling of the magnetic susceptibility, for which we found $\chi_m \sim \alpha^2\chi_e$. We will furthermore show that the introduction of a strong external coupling field leads to quantum interference effects similar to electromagnetically induced transparency (EIT) and thus to low absorption with $FoM \gg 1$.

2.3 Tensorial effects

A comprehensive treatment of the propagation properties of a plane wave in a general linear medium described by (2.10) has to include the tensor properties of $\bar{\varepsilon}$, $\bar{\mu}$, $\bar{\xi}_{EH}$, and $\bar{\xi}_{HE}$, respectively. To find the wave vector \mathbf{k} of a non-trivial field solution one has to solve (2.15) or alternatively exploit the

condition

$$\det \left[\bar{\varepsilon} + (\bar{\xi}_{EH} + \frac{c}{\omega} \mathbf{k} \times) \bar{\mu}^{-1} \left(\frac{c}{\omega} \mathbf{k} \times - \bar{\xi}_{HE} \right) \right] = 0. \quad (2.21)$$

A similar determinantal condition is given by O'Dell [80] who noted that a solution where the tensors $\bar{\varepsilon}$, $\bar{\mu}$, $\bar{\xi}_{EH}$, and $\bar{\xi}_{HE}$ do not fulfill any restrictions is very tedious. For specialized situations such as biisotropic [81, 82] as well as some particular tensor-valued media [83, 84, 85, 86] explicit solutions are known, however.

In order to specialize the general description, the constraints

$$\bar{\varepsilon} = \bar{\varepsilon}^\dagger, \quad \bar{\mu} = \bar{\mu}^\dagger, \quad \bar{\xi}_{HE} = \bar{\xi}_{EH}^\dagger \quad (2.22)$$

are known [75, 85] to be sufficient but not necessary for lossless media. Here † denotes complex conjugation and matrix transposition. For general dissipative media, though, no necessary constraints can be found but the one given by Lakhtakia and Weiglhofer [87]. Without relying on physical concepts like nondissipativity or reciprocity they exploit the mathematical structure of Maxwell's equations. Using the covariant form of electrodynamics they find the scalar condition

$$\text{tr} \left[\bar{\xi}_{EH} \bar{\mu}^{-1} + \bar{\mu}^{-1} \bar{\xi}_{HE} \right] = 0 \quad (2.23)$$

where "tr" denotes the trace of a matrix.

Hence the general response tensors $\bar{\varepsilon}$, $\bar{\mu}$, $\bar{\xi}_{EH}$, and $\bar{\xi}_{HE}$ are only constrained by the single scalar condition (2.23). We will therefore not try to give a general solution but discuss the prospect of negative refraction in cross-coupled materials for two fundamental examples. In particular, we will focus on the possibility of finding an isotropic negative index of refraction, which does not depend on the polarization state of the beam.

2.3.1 Biisotropic media

A special case of (2.16) is represented by biisotropic media which are described by scalar coefficients $\bar{\varepsilon} = \varepsilon \mathbb{1}$, $\bar{\mu} = \mu \mathbb{1}$, $\bar{\xi}_{EH} = \xi_{EH} \mathbb{1}$, and $\bar{\xi}_{HE} = \xi_{HE} \mathbb{1}$, respectively, as already discussed by Pendry [81]. In view of the constraint (2.23) we note that $\xi_{EH} = -\xi_{HE} =: \xi$ must hold. For a beam propagating in the (now arbitrary) z -direction $\mathbf{k} \sim \mathbf{e}_z$ the Helmholtz equation (2.15) decouples into two scalar relations if the polarization vectors are taken to be \mathbf{e}_+

and \mathbf{e}_- , respectively. The corresponding refractive indices $n_{\pm} = k_z^{\pm}c/\omega$ are then found to be given by

$$n^+ = \pm\sqrt{\varepsilon\mu} - i\xi, \quad n^- = \pm\sqrt{\varepsilon\mu} + i\xi. \quad (2.24)$$

Note the sign change of the ξ term. Due to the isotropy of the response tensors the direction of propagation is arbitrary and thus the refractive index is angle independent. But from the aforementioned sign change we conclude that in general

$$n^+ \neq n^-, \quad (2.25)$$

thus the index of refraction depends on the polarization state of the probe beam, i.e., the medium displays isotropic chirality. This isotropy also holds for the energy propagation properties described by the Poynting vector $\mathbf{S} = \text{Re}[\mathbf{E} \times \mathbf{H}^*]/2$, for which we find $\mathbf{S} \sim \mathbf{k}$.

Considering an application of such a material in a flat lens we note that point sources of light do not radiate in a single circular polarization, but beam components for different angles will in general be composed of both \mathbf{e}_+ and \mathbf{e}_- polarizations. As a result, biisotropic materials are useless for a perfect lens as the different polarization components will experience different refraction angles. Furthermore, in view of chapter 3 it is unclear as to how such a material should be implemented in atomic media.

2.3.2 Polarization independent media

As a second example we consider a medium which displays a polarization independent index of refraction for at least one direction of propagation. In particular we assume isotropic permittivity $\bar{\varepsilon} = \varepsilon \mathbb{1}$ and permeability $\bar{\mu} = \mu \mathbb{1}$ but tensors $\bar{\xi}_{EH}$, $\bar{\xi}_{HE}$ which do not couple left and right circular polarizations for at least one propagation direction as discussed in section 2.2. In view of (2.18) and (2.19) we define $\xi_{EH}^- = -\xi_{EH}^+$ and $\xi_{HE}^- = -\xi_{HE}^+$, respectively. This results in tensors of the form

$$\bar{\xi}_{EH} = -\xi_{EH} \mathbf{e}_+ \otimes \mathbf{e}_+^* + \xi_{EH} \mathbf{e}_- \otimes \mathbf{e}_-^* = \begin{pmatrix} 0 & i\xi_{EH} & 0 \\ -i\xi_{EH} & 0 & 0 \\ 0 & 0 & 0 \end{pmatrix} \quad (2.26)$$

where we skipped the \pm indices and similar for $\bar{\xi}_{HE}$. Note that we assumed $\xi_{EH}^z = \xi_{HE}^z = 0$ for the sake of simplicity. In contrast to the biisotropic case we find identical refraction

$$n_+ = n_- = \pm \sqrt{\varepsilon\mu - \frac{(\xi_{EH} + \xi_{HE})^2}{4} + \frac{i}{2}(\xi_{EH} - \xi_{HE})} \quad (2.27)$$

for the two polarizations for the z -direction.

For directions other than that we solve (2.21) for $|\mathbf{k}| = k$ of the angle dependent wave vector $\mathbf{k} = k(\sin \theta \cos \phi, \sin \theta \sin \phi, \cos \theta)$. We find an angle dependent index of refraction $n = kc/\omega$

$$n = \pm \sqrt{\varepsilon\mu - \xi_{EH}\xi_{HE} - \frac{(\xi_{EH} - \xi_{HE})^2 \cos^2 \theta}{4} + \frac{i}{2}(\xi_{EH} - \xi_{HE}) \cos \theta} \quad (2.28)$$

which does not depend on the polarization state. Thus the medium shows a non-chiral but anisotropic response. For $\theta = 0$, i.e., propagation in z -direction, we recover (2.27).

Media, which obey (2.26), allow, in contrast to biisotropic materials, for refractive indices that are polarization independent but display a strong angular dependence. As these angular dependent terms affect only the cross-couplings, a change of direction from z to $-z$ reverses their effect. Thus following the discussion in section 2.2 on negative refraction in materials with cross-couplings we note that reversing the direction of propagation might make a negative index positive⁵.

From equation (2.21) we observe that the cross coupling coefficients are always paired with the operator of the vector product with the \mathbf{k} -vector. This operator reads in $\{x, y, z\}$ -basis

$$\mathbf{k} \times = \begin{pmatrix} 0 & -k_z & k_y \\ k_z & 0 & -k_x \\ -k_y & k_x & 0 \end{pmatrix}. \quad (2.29)$$

For propagation in z -direction, equation (2.29) reduces to a similar structure than (2.26). But in contrast to (2.26) the matrix (2.29) changes for different angles which finally yields the angular dependence of (2.28).

⁵Cf. also section 4.3.

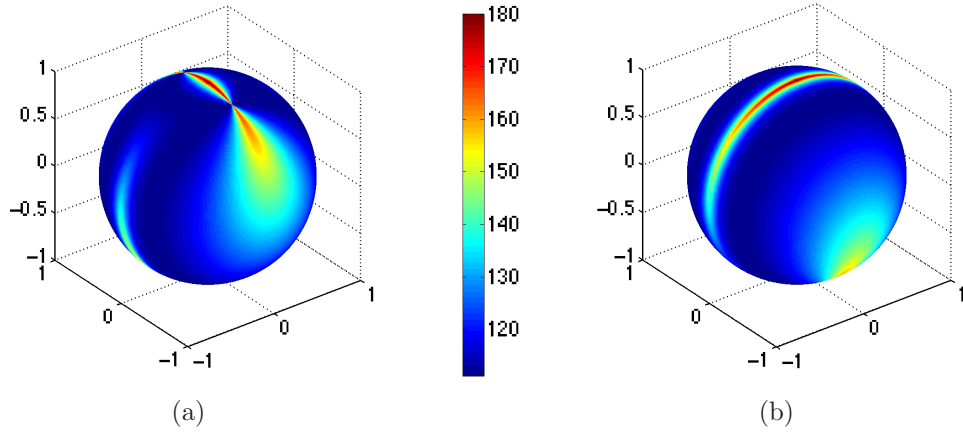


Figure 2.2: (a) The angle α (2.32) between the Poynting vector \mathbf{S} and the wave vector \mathbf{k} as a function of the polar angles θ, ϕ which determine the direction of \mathbf{k} . The z -axis is directed upwards. (b) shows the same inverted along the z -axis.

No weakening of the angular dependence is obtained when additional couplings are introduced to $\bar{\xi}_{EH}$ and $\bar{\xi}_{HE}$, e.g.,

$$\bar{\xi}_{EH} = \frac{1}{\sqrt{3}} \begin{pmatrix} 0 & i\xi_{EH} & -i\xi_{EH} \\ -i\xi_{EH} & 0 & i\xi_{EH} \\ i\xi_{EH} & -i\xi_{EH} & 0 \end{pmatrix}, \quad (2.30)$$

in order to mimic (2.29). The tensor (2.30) just corresponds to a rotation of the preferred axis to the volume diagonal.

The angular dependence of the index of refraction (2.28) vanishes in the case $\xi_{EH} = \xi_{HE} = \xi$ resulting in

$$n = \pm \sqrt{\varepsilon \mu - \xi^2}. \quad (2.31)$$

Thus we find an isotropic index of refraction which does not depend on the polarization state. We emphasize that (2.31) can attain negative values. For example using the values⁶ $\varepsilon = 0.1 + 0.001i$, $\mu = 1.5 + 0.001i$, $\xi = 0.01 + i$ for the permittivity, the permeability and the cross-coupling ξ , respectively, leads to $n = -1.07 + 0.008i$. The propagation properties of light beams are nevertheless highly non-trivial as the Poynting vector⁷ $\mathbf{S} = \text{Re}[\mathbf{E} \times \mathbf{H}^*]/2$

⁶Similar numbers are found in chapter 3.

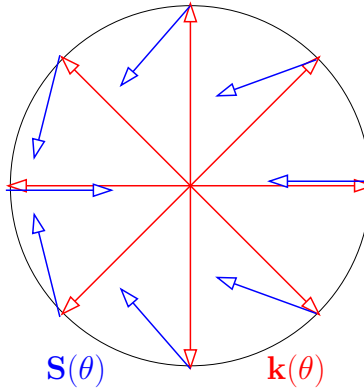


Figure 2.3: Misalignment between the Poynting vector and the wave vector in the x - z -plane.

and the \mathbf{k} -vector in general point in different directions. Figure 2.2 shows the angle

$$\alpha = \arccos \left(\hat{\mathbf{k}} \cdot \mathbf{S} / |\mathbf{S}| \right) \quad (2.32)$$

between the Poynting vector \mathbf{S} and the normalized wave vector $\hat{\mathbf{k}}$ as a function of the polar angles θ, ϕ which describe the direction of \mathbf{k} . Again the values $\varepsilon = 0.1 + 0.001i$, $\mu = 1.5 + 0.001i$, $\xi = 0.01 + i$ have been used to determine the Poynting vector \mathbf{S} . We note that only for $\theta = \{0, \pi\}$, i.e., for forward and backward z -directions, \mathbf{S} and \mathbf{k} are aligned but point in opposite directions. Figure 2.3 shows some more explicit examples for the x - z -plane, in which the Poynting vector and the wave vector always fall into the plane. In general the Poynting vector will also attain components out of the plane. Although the imaging properties of a medium described by (2.26) are not studied in detail it seems questionable that it will allow for applications like a perfect lens. In order to give a final answer to this question the imaging properties of a flat lens need to be analyzed which requires to determine the tensorial Green function for such a medium which is a very involved and difficult task.

In order to find negative refraction in cross-coupled media independent of polarization states and directions of propagation with no beam walk-off, one would need to implement couplings depending on the probe beam direction which contradicts the assumptions of linear response theory.

⁷which is found using (2.10), (2.14) and (2.31)

An explicit example of a medium which is closely related to the case discussed here is given in section 4.3.

CHAPTER 3

Implementation: 5-level scheme

3.1 Concepts of induced cross-coupling in atomic media: 3-level scheme

As mentioned in chapter 2 an implementation of the ideas employing magneto-electric cross-coupling and negative refraction in atomic media involves electric and magnetic dipole transitions linked by an external control field. In the following we will clarify these concepts by application to an appropriate level scheme.

After restriction to a particular propagation direction and a definite polarization state we only have to deal with a scalar theory, for which we rewrite (2.9) effectively as

$$\begin{aligned} D &= \varepsilon E + \xi_{EH} H, \\ B &= \xi_{HE} E + \mu H. \end{aligned} \tag{3.1}$$

Here E , H , B , and D are the (scalar) field amplitudes corresponding to the polarization mode \mathbf{e}_- . Note that (3.1) in general holds only for the particular tensor structures used in (2.16). The scalar coefficients ε and μ are the permittivity and permeability, and ξ_{EH} and ξ_{HE} the scalar cross-coupling tensor elements of the \mathbf{e}_- -mode, respectively. Hence from (3.1) we find (2.18) as the index of refraction. In (3.1) and in the following we will drop the index

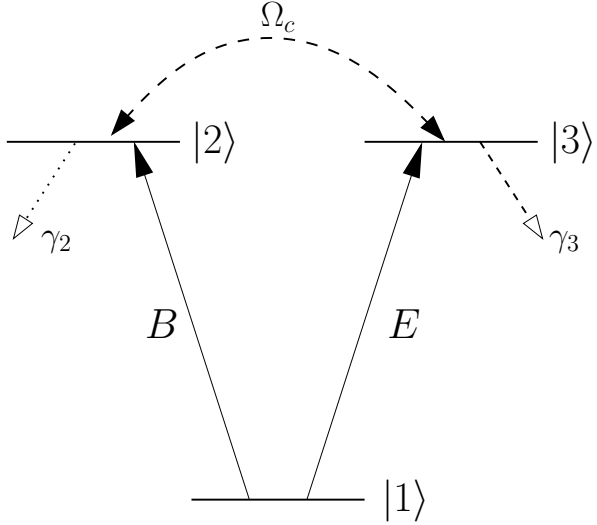


Figure 3.1: 3-level system allowing for the implementation of electro-magnetically-induced cross-coupling. E , B are the electric and magnetic components of the probe field, γ_2 and γ_3 are decay rates out of levels $|2\rangle$ and $|3\rangle$, respectively. Ω_c is an applied field that couples levels $|2\rangle$ and $|3\rangle$.

– for notational simplicity. Note further that for a scalar theory the distinction between chiral and non-chiral magneto-electric effects is irrelevant and we henceforth use the terms “cross-couplings”, “chiralities”, and “chirality parameters” interchangably to denote ξ_{EH} and ξ_{HE} .

Let us consider the 3-level scheme shown in Fig. 3.1. It consists of a common ground state $|1\rangle$ and two upper states $|2\rangle$ and $|3\rangle$. The transition $|1\rangle - |3\rangle$ is supposed to be an electric dipole transition (E1) while $|1\rangle - |2\rangle$ is a magnetic dipole transition (M1). For reasons of parity the transition between levels $|2\rangle$ and $|3\rangle$ is magnetic dipole forbidden and, neglecting higher multipole terms, can thus only support an electric dipole transition. E and B denote the electric and magnetic components of the probe electromagnetic wave which also show up in (3.1). We assume that levels $|2\rangle$ and $|3\rangle$ are energetically degenerate so that the probe field can couple efficiently to both the electric and magnetic dipole transition. So far this scheme is in linear response identical to the one discussed in section 2.1 with $\varrho_A = \varrho_B$, i.e., there is no cross-coupling.

To induce a cross-coupling we add a strong resonant coherent field with a Rabi frequency Ω_c which induces a transition between states $|2\rangle$ and $|3\rangle$. Then the electric dipole transition $|1\rangle - |3\rangle$ and the magnetic transition $|1\rangle - |2\rangle$ are coupled in a way described by (3.1): When an electric field amplitude E is applied, it induces electric dipole transitions and thus a polarization P but due to the coupling Ω_c the magnetic dipole transition will be driven as well which results in a magnetization M proportional to E , i.e., a nonzero chirality ξ_{HE} . Likewise, the coupling leads to a nonzero ξ_{EH} by the application of a magnetic field B . In summary the coupling of an E1 and a M1 transition as in Fig. 3.1 implements the material equations (3.1) and thus potentially leads to $\text{Re}[n] < 0$ without requiring $\text{Re}[\mu] < 0$.

The scheme of Fig. 3.1 has been discussed by Oktel and Müstecaplioglu [88]. However they did not take into account cross-couplings, but relied on the conditions $\text{Re}[\varepsilon], \text{Re}[\mu] < 0$ to induce negative refraction which led to a rather stringent density requirement comparable to that found in section 2.1.

As noted above, the radiative population decay rates γ_i are proportional to the square of the respective transition moment. Thus from $\mu_A \sim \alpha d_A$ we find that $\gamma_2 \ll \gamma_3$, i.e., the magnetic decay rate is much smaller than the one of the electric transition (see also [67]). In other words, state $|2\rangle$, which can be considered meta-stable, is coupled strongly by Ω_c to the E1 probe field transition $|1\rangle - |3\rangle$. On two-photon resonance this fulfills the condition for electromagnetically induced transparency [57]. Therefore we expect the absorption of the direct E -field response, i.e., the permittivity ε , which represents the largest response and thus the main source of absorption, to be suppressed by a factor of about $\gamma_3 \gamma_2 / \Omega_c^2$.

Figure 3.1 represents a closed loop scheme similar to the one from Fig. 1.7. From studies of resonant nonlinear optics [56, 57, 63, 64] it is known that the parametric coupling, which is here given by the chirality, experiences constructive interference as long as the direct coupling interferes destructively, i.e., under conditions of EIT. Hence we expect quantum interference effects to suppress the absorption $\text{Im}[\varepsilon]$ while simultaneously enhancing the cross-coupling coefficients. This should allow low-loss negative refraction for densities significantly lower than in non-chiral proposals.

The simplistic scheme of Fig. 3.1 allows us to discuss qualitatively the

fundamental advantages as compared to non-chiral proposals, and gives a physical understanding of the underlying processes in a comparatively easy way. However, it is not adequate for an experimental implementation, for the following reasons:

- (i) As we noted in section 2.2 the complex phase of the chirality coefficients ξ_{EH} , ξ_{HE} must be adjustable in order to get $\text{Re}[n] < 0$. In the scheme of Fig. 3.1, Ω_c is a *dc*-field which has no phase itself. As a consequence the phases of ξ_{EH} , ξ_{HE} are solely given by the intrinsic phase of the transition moments and therefore can not be controlled.
- (ii) One of the main advantages of the strong coupling Ω_c is high-contrast EIT. As it depends on the coherence between states $|2\rangle$ and $|1\rangle$ given by the density matrix element ρ_{21} the corresponding dephasing rate γ_{21} must stay small. Similar to ordinary EIT- Λ -schemes the transition between the two EIT “ground”-states $|1\rangle$ and $|2\rangle$ is electric dipole forbidden. In vast contrast to ordinary EIT though, the energy splitting of $|1\rangle$ and $|2\rangle$ here is on the order of the probe field frequency, i.e., up to optical frequencies rather than in the microwave regime. As a consequence the coherence ρ_{21} is highly susceptible to additional homogeneous or inhomogeneous broadenings which ultimately destroy electromagnetically induced transparency.
- (iii) Although the level scheme of Fig. 3.1 is not forbidden on fundamental grounds it is a strong restriction to require that electric and magnetic transitions be energetically degenerate while having a common ground state.

Though the items (i)-(iii) indeed display severe limitations, a simple modification of the 3-level scheme of Fig. 3.1 suffices to alleviate these constraints. We replace the ground state $|1\rangle$ of the 3-level scheme by the dark state $|D\rangle = (\Omega_2|1\rangle - \Omega_1|4\rangle)/\sqrt{\Omega_1^2 + \Omega_2^2}$ of the 3-level Λ -type subsystem $\{|1\rangle, |4\rangle, |5\rangle\}$ of the 5-level-scheme shown in Fig. 3.2. The transitions $|5\rangle - |1\rangle$ and $|5\rangle - |4\rangle$ are supposed to be E1 transitions such that the modified 5-level scheme still fulfills parity selection rules. A related scheme has

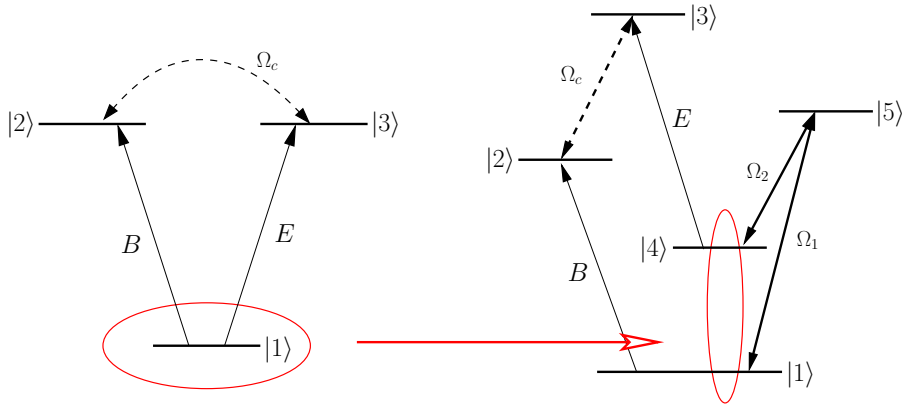


Figure 3.2: Modification of the level scheme of Fig. 3.1. The ground state $|1\rangle$ is substituted by the dark state $|D\rangle = (\Omega_2|1\rangle - \Omega_1|4\rangle)/\sqrt{\Omega_1^2 + \Omega_2^2}$ of the 3-level Λ -type subsystem formed by levels $\{|1\rangle, |4\rangle, |5\rangle\}$, respectively.

been discussed by Thommen and Mandel [89], however without the possibility of EIT and ignoring the chiral nature of the constituent relations¹. Note that level $|4\rangle$ can decay to the ground state only via a 2-photon transition. Hence we assume $|4\rangle$ to be meta-stable $\gamma_4 \ll \gamma_3$. By application of two strong laser fields with Rabi frequencies Ω_1 and Ω_2 , respectively, the subsystem evolves to the dark state $|D\rangle$ by means of optical pumping. Once in the dark state the system will stay there as long as the probe field amplitudes E and B are treated in linear response. One recognizes that problems (i)-(iii) are addressed:

- (i) As the upper states $|2\rangle$ and $|3\rangle$ are not degenerate any more the coupling Rabi frequency Ω_c is now given by an *ac*-field which thus has a phase relative to the beat-note of Ω_1 and Ω_2 . By adjustment of it the phase of the cross-coupling coefficients ξ_{EH} and ξ_{HE} can be controlled and hence the conditions needed to induce negative refraction can be fulfilled.
- (ii) The permittivity of the 5-level system at the probe field frequency is now given by the direct response of the $|3\rangle - |4\rangle$ transition. Thus the critical parameter for EIT is the dephasing rate γ_{24} of the new EIT

¹For a discussion of the Thommen-Mandel scheme and a correction of the results of [89] see [Kästel2007a].

“ground” state coherence ρ_{24} . As levels $|2\rangle$ and $|4\rangle$ can be constrained to be close to degenerate, ρ_{24} is mostly immune against additional broadening mechanisms.

- (iii) Although the electric and magnetic transitions are still degenerate, as in the 3-level system of Fig. 3.1, they do not share a common state. Thus the 5-level scheme leaves much more freedom regarding a realization in atomic systems.

After having discussed the qualitative features of the 3-level scheme we reasoned why we need to consider the slightly more complicated 5-level system for a serious implementation. In the following we will give an analytical solution to the modified scheme and show under which conditions negative refraction with low absorption can be achieved by means of electromagnetically induced chirality.

3.2 Analytical solution: Single particle treatment

For the following quantitative discussion, the 5-level scheme is shown in greater detail in Fig. 3.3. Due to selection rules or non-resonance conditions, only the sketched transitions are relevant. To find an analytical solution of the response of a single system described by the 5-level scheme, we start with the Hamilton operator including electric and magnetic dipole interactions

$$H = H_0 - \mathbf{d} \cdot \mathbf{E}(t) - \boldsymbol{\mu} \cdot \mathbf{B}(t) \quad (3.2)$$

with the free atomic part

$$H_0 = \frac{\mathbf{p}^2}{2m} + V(r) = \sum_{n=1}^5 \hbar\omega_n^A |n\rangle \langle n| \quad (3.3)$$

which is assumed to include the relevant states $|i\rangle$, $i \in \{1, \dots, 5\}$ only. Here the ω_n^A are the atomic eigenfrequencies of states $|n\rangle$, respectively. The electric and magnetic field components can be decomposed into $\mathbf{E}(t) = \mathbf{E} \cos(\omega_p t)$

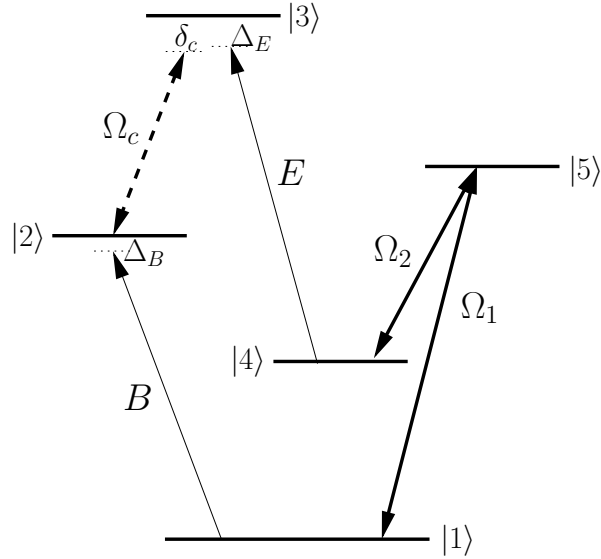


Figure 3.3: 5-level scheme for the implementation of negative refraction via electromagnetically induced chirality. The magnetic dipole transition $|2\rangle - |1\rangle$ and the electric dipole transition $|3\rangle - |4\rangle$ are coupled by Ω_c to induce chirality. The “ground”-state of the system is formed by the dark state $|D\rangle = (\Omega_2|1\rangle - \Omega_1|4\rangle)/\sqrt{\Omega_1^2 + \Omega_2^2}$ of the subsystem $\{|1\rangle, |4\rangle, |5\rangle\}$.

and $\mathbf{B}(t) = \mathbf{B} \cos(\omega_p t)$, respectively, where ω_p denotes the probe field frequency. The electric and magnetic dipole moment operators are given by $\mathbf{d} = e\mathbf{r}$ and $\boldsymbol{\mu} = \mu_B(\mathbf{J} + \mathbf{S})$, respectively [67]. Following the discussion above, we restrict ourselves to a particular mode of the electromagnetic field and will thus use only the scalar amplitudes E and B rather than the full vector fields. Similarly, we will only take into account the corresponding scalar projections of the electric and magnetic dipole moments.

By multiplying from the left and from the right with the identity operator for the 5-level system $\mathbb{1} = \sum_{n=1}^5 |n\rangle \langle n|$ we can rewrite the Hamiltonian in the more convenient form [90]

$$H = \sum_{n=1}^5 \hbar\omega_n^A |n\rangle \langle n| + \left\{ -\frac{1}{2}d_{34}Ee^{-i\omega_p t} |3\rangle \langle 4| - \frac{1}{2}\mu_{21}Be^{-i\omega_p t} |2\rangle \langle 1| - \frac{\hbar}{2}\Omega_1e^{-i\omega_1 t} |5\rangle \langle 1| - \frac{\hbar}{2}\Omega_2e^{-i\omega_2 t} |5\rangle \langle 4| - \frac{\hbar}{2}\Omega_c e^{-i\omega_{ct}} |3\rangle \langle 2| + \text{H.c.} \right\}. \quad (3.4)$$

Here $d_{34} = \langle 3 | e \mathbf{r} \cdot \hat{\mathbf{e}}_{\mathbf{E}} | 4 \rangle$ and $\mu_{21} = \langle 2 | \boldsymbol{\mu} \cdot \hat{\mathbf{e}}_{\mathbf{B}} | 1 \rangle$ are the electric and magnetic dipole moments for the probe field transitions $|3\rangle - |4\rangle$ and $|2\rangle - |1\rangle$, respectively. The strong fields are denoted by their Rabi frequencies $\Omega_1 = \langle 5 | \mathbf{d} | 1 \rangle \cdot \mathbf{E}_1 / \hbar$, $\Omega_2 = \langle 5 | \mathbf{d} | 4 \rangle \cdot \mathbf{E}_2 / \hbar$, and $\Omega_c = \langle 3 | \mathbf{d} | 2 \rangle \cdot \mathbf{E}_c / \hbar$ with corresponding field frequencies ω_1 , ω_2 , and ω_c , respectively. Note that the Hamiltonian (3.4) is given under rotating wave approximation.

In general the dipole transition moments are complex numbers, hence the Rabi frequencies are complex as well, but by adjusting the phases of the atomic states $|n\rangle$ the phases of those complex numbers can be eliminated. In the closed-loop 5-level system we can choose all but one of the transition moments to be real. In particular we choose Ω_1 and Ω_2 as well as d_{34} and μ_{21} real but let Ω_c remain complex.

So far we have only considered unitary time evolution. In order to include losses we use the Liouville equation of the density matrix $\hat{\rho}$

$$\dot{\hat{\rho}} = -\frac{i}{\hbar} [H, \hat{\rho}] - \mathcal{L}(\hat{\rho}) \quad (3.5)$$

where the non-unitary part is given in Lindblad form [90] by

$$\mathcal{L}(\hat{\rho}) = \sum_{ij \in \{21, 32, 34, 54, 51, 41\}} \frac{\gamma_{i \rightarrow j}}{2} (\sigma_+^{ij} \sigma_-^{ij} \hat{\rho} + \hat{\rho} \sigma_+^{ij} \sigma_-^{ij} - 2\sigma_-^{ij} \hat{\rho} \sigma_+^{ij}) . \quad (3.6)$$

Here we restricted the number of decay channels as indicated in the summation where $\gamma_{i \rightarrow j}$ denotes the corresponding decay rate from some upper state $|i\rangle$ to state $|j\rangle$. The projectors are given by $\sigma_+^{ij} = |i\rangle \langle j|$ and $\sigma_-^{ij} = |j\rangle \langle i|$, respectively. Although this treatment is exact for decay processes within the level scheme of Fig. 3.3 we will substitute the density matrix equation for the ground state ρ_{11} by the explicit conservation of probability $\sum_{n=1}^5 \rho_{nn} = 1$. Because in linear response coherence decay rather than population decay processes are of interest, this procedure guarantees the existence of a non-trivial stationary state solution under all circumstances.

Before we solve (3.5), we note that in linear response the excitation of the quantum system is assumed to stay entirely in the ground level. Therefore one usually discards any diagonal density matrix elements ρ_{nn} , $n \neq 1$ which give the probability to find the system in the excited state $|n\rangle$, $n \neq 1$. Then the set of relevant density matrix components simplifies significantly. In

general, this procedure only applies for levels which are connected to the ground state by weak fields. However, for the 5-level scheme the ground state $|1\rangle$ is coupled by strong fields Ω_1 and Ω_2 to the excited states $|4\rangle$ and $|5\rangle$, therefore the subsystem $\{|1\rangle, |4\rangle, |5\rangle\}$ has to be solved exactly. The solution of the full 5-level scheme will be treated in the above mentioned perturbative approach afterwards.

The appropriate differential equations for the density matrix elements of the subsystem $\{|1\rangle, |4\rangle, |5\rangle\}$ are found by projecting the Liouville equation (3.5) for the case $E = B = 0$ onto diagonal components $\rho_{nn} = \langle n|\hat{\rho}|n\rangle$

$$\dot{\rho}_{44} = -\gamma_4 \rho_{44} + \gamma_{5 \rightarrow 4} \rho_{55} + \frac{1}{2} (i\Omega_2 e^{i\omega_2 t} \rho_{54} + \text{c.c.}) ,$$

$$\dot{\rho}_{55} = -\gamma_5 \rho_{55} + \frac{1}{2} (i\Omega_1 e^{-i\omega_1 t} \rho_{15} + i\Omega_2 e^{-i\omega_2 t} \rho_{45} + \text{c.c.})$$

as well as off-diagonal components $\langle n|\hat{\rho}|k\rangle, n > k$

$$\dot{\rho}_{41} = -(i\omega_{41} + \gamma_{41}) \rho_{41} + \frac{i}{2} (\Omega_2 e^{i\omega_2 t} \rho_{51} - \Omega_1 e^{-i\omega_1 t} \rho_{45}) ,$$

$$\dot{\rho}_{51} = -(i\omega_{51} + \gamma_{51}) \rho_{51} + \frac{i}{2} \Omega_2 e^{-i\omega_2 t} \rho_{41} - \frac{i}{2} \Omega_1 e^{-i\omega_1 t} (\rho_{55} - \rho_{11}) ,$$

$$\dot{\rho}_{54} = -(i\omega_{54} + \gamma_{54}) \rho_{54} + \frac{i}{2} \Omega_1 e^{-i\omega_1 t} \rho_{14} - \frac{i}{2} \Omega_2 e^{-i\omega_2 t} (\rho_{55} - \rho_{44}) .$$

Note that we left out the equation for ρ_{11} as it will be replaced by the conservation of probability constraint later. Here $\omega_{ij} = \omega_i^A - \omega_j^A$ denote the atomic level spacings and the γ_i are the total decay rates out of level $|i\rangle$. In particular, we have $\gamma_2 = \gamma_{2 \rightarrow 1}$, $\gamma_3 = \gamma_{3 \rightarrow 2} + \gamma_{3 \rightarrow 4}$, $\gamma_4 = \gamma_{4 \rightarrow 1}$, and $\gamma_5 = \gamma_{5 \rightarrow 1} + \gamma_{5 \rightarrow 4}$. Furthermore $\gamma_{ij} = (\gamma_i + \gamma_j)/2$ denote the natural decoherence rates².

To get rid of the fast oscillatory terms we transform to a rotating frame by setting $\tilde{\rho}_{41} = \rho_{41} e^{i(\omega_1 - \omega_2)t}$, $\tilde{\rho}_{51} = \rho_{51} e^{i\omega_1 t}$, and $\tilde{\rho}_{54} = \rho_{54} e^{i\omega_2 t}$ for the off-diagonal density matrix elements. As we aim at steady state solutions we subsequently ignore the time derivatives $\dot{\tilde{\rho}}_{ij} = 0$ of the slowly varying $\tilde{\rho}_{ij}$. We thus end up with a set of algebraic equations

$$0 = -\gamma_4 \rho_{44} + \gamma_{5 \rightarrow 4} \rho_{55} + \frac{1}{2} (i\Omega_2 \tilde{\rho}_{54} + \text{c.c.}) ,$$

²Additional dephasing will be discussed later.

$$\begin{aligned}
0 &= -\gamma_5 \rho_{55} + \frac{1}{2} (i\Omega_1 \tilde{\rho}_{15} + i\Omega_2 \tilde{\rho}_{45} + \text{c.c.}), \\
0 &= -(i(\delta_1 - \delta_2) + \gamma_{41}) \tilde{\rho}_{41} + \frac{i}{2} (\Omega_2 \tilde{\rho}_{51} - \Omega_1 \tilde{\rho}_{45}), \\
0 &= -(i\delta_1 + \gamma_{51}) \tilde{\rho}_{51} + \frac{i}{2} \Omega_2 \tilde{\rho}_{41} - \frac{i}{2} \Omega_1 (\rho_{55} - \rho_{11}), \\
0 &= -(i\delta_2 + \gamma_{54}) \tilde{\rho}_{54} + \frac{i}{2} \Omega_1 \tilde{\rho}_{14} - \frac{i}{2} \Omega_2 (\rho_{55} - \rho_{44}).
\end{aligned} \tag{3.7}$$

Here the definitions $\delta_1 = \omega_{51} - \omega_1$ and $\delta_2 = \omega_{54} - \omega_2$ for the detunings of the $|5\rangle - |1\rangle$ and $|5\rangle - |4\rangle$ transition apply, respectively. As mentioned above the equation for ρ_{11} has been ignored. It is replaced by the conservation of probability

$$\rho_{11} = 1 - \rho_{44} - \rho_{55} \tag{3.8}$$

which ensures non-zero solutions for the density matrix elements.

Solving (3.7) and (3.8) under the condition of 2-photon resonance $\delta_1 - \delta_2 = 0$ we find for the 3-level Λ -subsystem

$$\begin{aligned}
\rho_{11}^{(0)} &= \frac{|\Omega_2|^2}{|\Omega_1|^2 + |\Omega_2|^2} + O\left(\frac{\gamma_4}{\gamma_5}\right), & \rho_{44}^{(0)} &= \frac{|\Omega_1|^2}{|\Omega_1|^2 + |\Omega_2|^2} + O\left(\frac{\gamma_4}{\gamma_5}\right), \\
\tilde{\rho}_{41}^{(0)} &= -\frac{\Omega_1 \Omega_2}{|\Omega_1|^2 + |\Omega_2|^2} + O\left(\frac{\gamma_4}{\gamma_5}\right), & \rho_{55}^{(0)} &= \tilde{\rho}_{51}^{(0)} = \tilde{\rho}_{54}^{(0)} = 0 + O\left(\frac{\gamma_4}{\gamma_5}\right).
\end{aligned} \tag{3.9}$$

Here $O(\gamma_4/\gamma_5)$ indicates corrections linear in the small ratio γ_4/γ_5 . We added the superscript ⁽⁰⁾ because these solutions are, though correct to all orders of Ω_1 and Ω_2 , of zeroth order in the probe field amplitudes E and B . Note also that (3.9) for a meta-stable state $|4\rangle$, i.e. $\gamma_4 \ll \gamma_5$ indeed corresponds to the pure dark state $|D\rangle = (\Omega_2|1\rangle - \Omega_1|4\rangle)/\sqrt{\Omega_1^2 + \Omega_2^2}$ via $\hat{\rho}^{\text{subsys}} = |D\rangle \langle D|$ as discussed in section 3.1.

Compared to the strong fields Ω_1 and Ω_2 the probe field amplitudes E and B are assumed to be weak. Hence the population distribution given by (3.9) will not change notably and we are allowed to treat the effect of the probe field perturbatively. In the density matrix equations of the 5-level system we therefore set $\rho_{22} = \rho_{33} = 0$ and neglect the coupling Rabi frequencies $\Omega_1 = \Omega_2 = 0$ as they are already taken into account of in the solution (3.9). We specialize to stationary solutions by transforming to a rotating frame

defined by $\tilde{\rho}_{21} = \rho_{21}e^{i\omega_p t}$, $\tilde{\rho}_{31} = \rho_{31}e^{i(\omega_p + \omega_c)t}$, $\tilde{\rho}_{32} = \rho_{32}e^{i\omega_c t}$, $\tilde{\rho}_{42} = \rho_{42}e^{i(\omega_c - \omega_p)t}$, and $\tilde{\rho}_{34} = \rho_{34}e^{i\omega_p t}$ and subsequently neglect time derivatives of the slowly rotating matrix elements. The system of algebraic equations then reads

$$\begin{aligned} 0 &= -(i\Delta_B + \gamma_{21})\tilde{\rho}_{21} + \frac{i}{2} \left(\frac{\mu_{21}B}{\hbar} \rho_{11}^{(0)} + \Omega_c^* \tilde{\rho}_{31} \right), \\ 0 &= -(i(\Delta_B + \delta_c) + \gamma_{31})\tilde{\rho}_{31} + \frac{i}{2} \left(\frac{d_{34}E}{\hbar} \tilde{\rho}_{41}^{(0)} + \Omega_c \tilde{\rho}_{21} - \frac{\mu_{21}B}{\hbar} \tilde{\rho}_{32} \right), \\ 0 &= -(i\delta_c + \gamma_{32})\tilde{\rho}_{32} + \frac{i}{2} \left(\frac{d_{34}E}{\hbar} \tilde{\rho}_{42} - \frac{\mu_{21}B}{\hbar} \tilde{\rho}_{31} \right), \\ 0 &= -(i(\delta_c - \Delta_E) + \gamma_{42})\tilde{\rho}_{42} + \frac{i}{2} \left(\frac{d_{34}E}{\hbar} \tilde{\rho}_{32} - \frac{\mu_{21}B}{\hbar} \tilde{\rho}_{41}^{(0)} - \Omega_c \tilde{\rho}_{43} \right), \\ 0 &= -(i(-\Delta_E) + \gamma_{34})\tilde{\rho}_{43} - \frac{i}{2} \left(\frac{d_{34}E}{\hbar} \rho_{44}^{(0)} + \Omega_c^* \tilde{\rho}_{42} \right). \end{aligned} \quad (3.10)$$

Note that these equations are valid, i.e., stationary solutions exist, only if the condition

$$\omega_c = \omega_1 - \omega_2 \quad (3.11)$$

holds. Otherwise some time dependent exponentials do not vanish. This implies that $\Delta_E = \Delta_B + \delta_c$ must hold to guarantee that the total frequency of a closed loop sums up to zero. Experimentally the constraint (3.11) can be realized by parametric difference frequency generation of the strong fields Ω_1 , Ω_2 , and Ω_c [91].

Before we proceed we note that the induced polarization P is proportional to the coherence $\tilde{\rho}_{34}$ of the electric dipole transition $|3\rangle - |4\rangle$ multiplied by the corresponding transition moment d_{34} . Likewise the induced magnetization M is proportional to the density matrix element $\tilde{\rho}_{21}$ and the magnetic dipole moment μ_{21} . Hence the coefficients of $\tilde{\rho}_{34}$ and $\tilde{\rho}_{21}$ linear in either E or B define the sought polarizabilities

$$\begin{aligned} P &= \varrho d_{34} \tilde{\rho}_{34} := \varrho \alpha^{EE} E + \varrho \alpha^{EB} B, \\ M &= \varrho \mu_{21} \tilde{\rho}_{21} := \varrho \alpha^{BE} E + \varrho \alpha^{BB} B. \end{aligned} \quad (3.12)$$

Here ϱ denotes the number density of atoms (not to be confused with the density operator $\hat{\rho}$). We thus solve for the density matrix elements $\tilde{\rho}_{34} = \tilde{\rho}_{43}^*$

and $\tilde{\rho}_{21}$ linear in E and B and finally obtain the polarizabilities

$$\alpha^{EE} = \frac{i}{2\hbar} \frac{d_{34}^2 \rho_{44}^{(0)} (\gamma_{42} + i(\Delta_E - \delta_c))}{(\gamma_{42} + i(\Delta_E - \delta_c))(\gamma_{34} + i\Delta_E) + |\Omega_c|^2/4}, \quad (3.13)$$

$$\alpha^{BB} = \frac{i}{2\hbar} \frac{\mu_{21}^2 \rho_{11}^{(0)} (\gamma_{31} + i(\Delta_B + \delta_c))}{(\gamma_{31} + i(\Delta_B + \delta_c))(\gamma_{21} + i\Delta_B) + |\Omega_c|^2/4} \quad (3.14)$$

as well as

$$\alpha^{BE} = -\frac{1}{4\hbar} \frac{d_{34} \mu_{21} \rho_{41}^{(0)} \Omega_c^*}{(\gamma_{31} + i(\Delta_B + \delta_c))(\gamma_{21} + i\Delta_B) + |\Omega_c|^2/4}, \quad (3.15)$$

$$\alpha^{EB} = -\frac{1}{4\hbar} \frac{d_{34} \mu_{21} \rho_{41}^{(0)} \Omega_c}{(\gamma_{42} + i(\Delta_E - \delta_c))(\gamma_{34} + i\Delta_E) + |\Omega_c|^2/4}. \quad (3.16)$$

In order to discuss the results (3.13) – (3.16) we plug in some numbers. For the magnetic dipole decay rate we set $\gamma_2 = 1\text{kHz}$, for the electric dipole decay rates $\gamma_3 = \gamma_5 = (137)^2 \gamma_2$ and $\gamma_1 = \gamma_4 = 0$ for the population decay rates of the (meta-)stable states $|1\rangle$ and $|4\rangle$, respectively. From the discussion in section 2.1 we use the Wigner-Weisskopf result to determine the electric and magnetic dipole matrix elements d_{34} and μ_{21} from the respective decay rates $d_{34}(\mu_{21}) = \sqrt{3\gamma_3(\gamma_2)\hbar c^3/(4\omega^3)}$. To comply with the chosen decay rates we use a typical optical frequency corresponding to $\lambda = 600\text{nm}$. We also specialize to $\delta_c = 0$, which corresponds to $\Delta_E = \Delta_B$. In the following all spectra are plotted as functions of $\Delta = -\Delta_E = -\Delta_B$ to ensure increasing photon energies from left to right.

As noted above the Rabi frequencies of the Λ -type subsystem can be chosen to be real. We let $\Omega_1 = \Omega_2 = 10^2 \gamma_2$. In contrast, the coupling Rabi frequency $\Omega_c = |\Omega_c| e^{i\phi}$ is a complex number whose phase (relative to that of Ω_1/Ω_2) can be adjusted by the experimentalist. From (3.15) and (3.16) it is apparent that the phase of the cross-coupling terms α^{EB} and α^{BE} is determined by the phase ϕ of the coupling Rabi frequency Ω_c .

Figure 3.4 shows the resultant polarizabilities (3.13) – (3.16) for the non-coupling case $\Omega_c = 0$. Not surprisingly the chirality coefficients α^{EB} and α^{BE} vanish exactly whereas the electric as well as the magnetic polarizability show a Lorentzian resonance, respectively. Note that α^{EE} and α^{BB} have the same strength. Note further that the frequency axis in the spectrum of

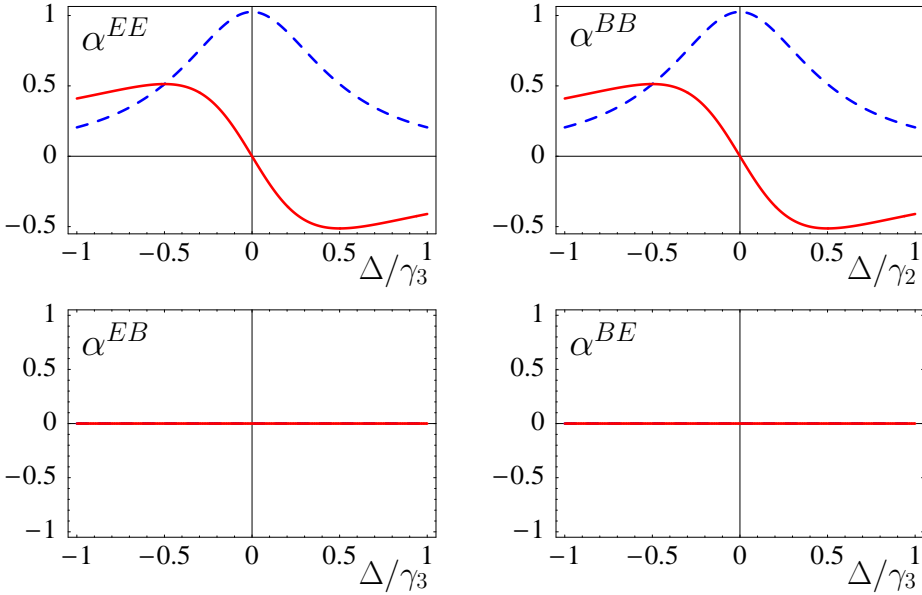


Figure 3.4: Real (solid) and imaginary (dashed) parts of the electric (α^{EE}) and magnetic (α^{BB}) polarizabilities as well as the chirality parameters (α^{EB} , α^{BE}) in arbitrary but the same units for the case $\Omega_c = 0$.

α^{BB} is scaled to the appropriate population decay rate γ_2 of the magnetic transition and is thus approximately a factor $(137)^2$ narrower than the electric resonance.

In Figure 3.5 the resultant spectra for the polarizabilities (3.13) – (3.16) are shown for the case of a strong coupling $\Omega_c \neq 0$. As discussed in section 2.2 a reasonable choice of the phase is such that α^{EB} on resonance is purely positive imaginary while α^{BE} is purely imaginary as well but with a minus sign. This choice can be realized in the 5-level scheme for $\phi = \pi/2$. We therefore set³ $\Omega_c = 10^4 \gamma_2 e^{i\pi/2}$. From Fig. 3.5 we find for this case significantly changed response functions. The electric polarizability α^{EE} displays electromagnetically induced transparency (EIT): As long as the coupling field Ω_c , ($\Omega_c^2 \gg \gamma_2 \gamma_3$) is present we observe from (3.13) that α^{EE} on resonance is linear in the decoherence rate γ_{42} , which in our case is small. Thus the

³An explanation for the value of $|\Omega_c|$ can be given only after the inclusion of additional broadenings (see section 3.4).

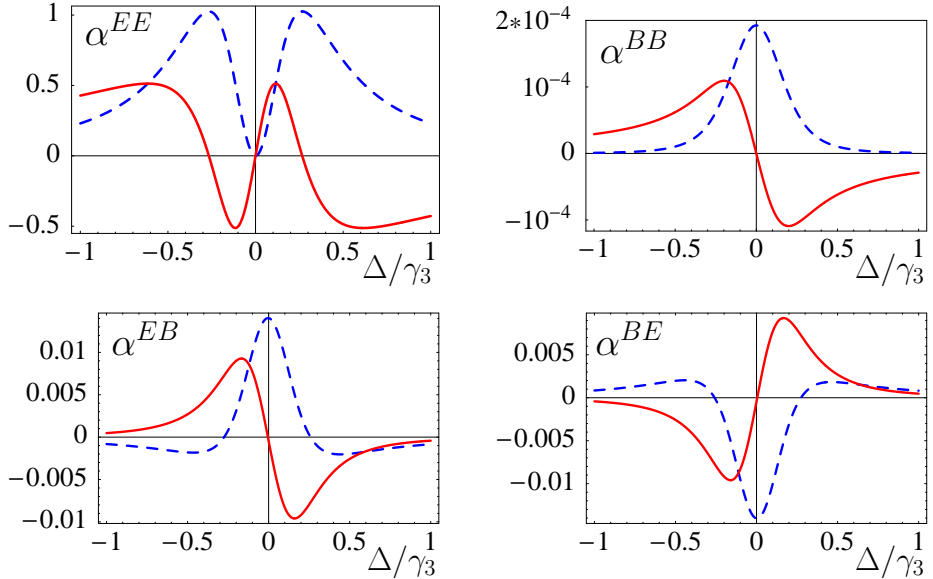


Figure 3.5: Real (solid) and imaginary (dashed) parts of the electric (α^{EE}) and magnetic (α^{BB}) polarizabilities as well as the chirality parameters (α^{EB} , α^{BE}) in arbitrary but the same units for the case $\Omega_c = 10^4 \gamma_2 e^{i\pi/2}$.

most prominent feature of EIT emerges: Suppression of absorption on resonance. At first glance the magnetic polarizability (or magnetizability) α^{BB} are not changed significantly. Note, however, that the spectrum of α^{BB} is now scaled to the width γ_3 of the electric dipole transition. Therefore the magnetic resonance experiences a considerable spectral broadening and reduction in strength. This is due to the presence of the strong coupling Ω_c which opens an additional decay channel of the meta-stable state $|2\rangle$ via the excited state of the electric dipole transition $|3\rangle$. The two cross-couplings α^{EB} and α^{BE} display spectra similar to a Lorentz line. On resonance we indeed find $\alpha^{EB} \sim i$ and $\alpha^{BE} \sim -i$ as intended.

We verified numerically that all polarizabilities and cross-coupling terms (3.13) – (3.16) fulfill the Kramers-Kronig relations [40]

$$\alpha^{IJ}(\Delta) = \frac{1}{\pi i} \mathcal{P} \int_{-\infty}^{\infty} \frac{\alpha^{IJ}(\Delta')}{\Delta' - \Delta} d\Delta' \quad (3.17)$$

and thus represent causal response functions.

3.3 Limits of linear response theory

When dealing with magnetic dipole transitions one has to be careful not to cross the limits of linear response theory. This is because magnetic transitions start to saturate at much lower probe field amplitudes than electric ones. This can be seen from the upper state population of a 2-level electric dipole atom on resonance which in leading order in the transition Rabi frequency $\Omega_E = dE/\hbar$ reads

$$\rho_{22} = \frac{\Omega_E^2}{2\gamma_{21}\gamma_2} + O(\Omega_E^4). \quad (3.18)$$

This result can be found from the Liouville equation (3.5) for a 2-level system with upper state $|2\rangle$ and dipole transition moment d . From the Wigner-Weisskopf result for the population decay rate γ_2 we can rewrite (3.18) explicitly for an electric dipole transition

$$\rho_{22}^{(E)} = \frac{3c^3}{8\hbar\omega^3} \frac{E^2}{\gamma_{21,E}} \quad (3.19)$$

which hence is governed by the applied electric field strength E and the (intrinsic) decoherence rate $\gamma_{21,E}$. The corresponding upper state population of a magnetic transition can be found to be

$$\rho_{22}^{(B)} = \frac{3c^3}{8\hbar\omega^3} \frac{B^2}{\gamma_{21,B}}. \quad (3.20)$$

The assumption that the population stays in the ground state which is employed in linear response theory is violated quadratically with the applied field strength. This corresponds to an additional term in ρ_{21} which adds a $\chi^{(3)}$ nonlinearity and hence marks the limits of linear response.

We compare (3.19) and (3.20) by noting that in Gaussian units the electric and magnetic field amplitudes E and B of a free wave not only have identical units but also the same magnitude, $E = B$. Hence the ratio of upper state populations for an electric and a magnetic 2-level atom can be estimated by

$$\frac{\rho_{22,B}}{\rho_{22,E}} = \frac{\gamma_{21,E}}{\gamma_{21,B}} \quad (3.21)$$

Using $\gamma_{21,B} \approx \alpha^2 \gamma_{21,E}$ which holds in radiatively broadened systems we therefore conclude that magnetic transitions start to saturate at much lower probe field intensities.

In order to find the limits of linear response theory for the 5-level scheme employed here we solve the Liouville equation (3.5) numerically to all orders in the electric and magnetic field amplitudes E and B . Since the estimate (3.21) is worst if additional broadening mechanisms are discarded we here restrict to naturally broadened resonances.

As we focus on steady state solutions, we employ a similar rotating frame as in section 3.2. We cast the resulting set of 25 algebraic equations in a matrix form by arranging the 5 diagonal $\rho_{11} \dots \rho_{55}$ and 20 off-diagonal density matrix elements $\tilde{\rho}_{21} \dots$ in a 25-dimensional vector $\vec{\rho}$. Note again that the equation for ρ_{11} is explicitly given by conservation of probability

$$\rho_{11} + \rho_{22} + \rho_{33} + \rho_{44} + \rho_{55} = 1. \quad (3.22)$$

The set of algebraic equations therefore is given by the inhomogeneous matrix equation

$$\mathcal{M}\vec{\rho} = \vec{a} \quad (3.23)$$

with the inhomogeneity vector $\vec{a} = (1, 0, 0, 0 \dots)$.

From the numerical inversion of the matrix \mathcal{M} , which contains all couplings, detunings, and decay rates, we find the sought density matrix elements $\tilde{\rho}_{34}$ and $\tilde{\rho}_{21}$. As in (3.12) the matrix elements $\tilde{\rho}_{34}$ and $\tilde{\rho}_{21}$ are functions of the electric and magnetic field amplitudes E and B

$$\tilde{\rho}_{34} = f(E, B), \quad \tilde{\rho}_{21} = g(E, B). \quad (3.24)$$

Since we need to compare with the result of linear response theory the functions $f(E, B)$ and $g(E, B)$ have to be separated as in (3.12):

$$d_{34}\tilde{\rho}_{34} = \alpha^{EE}(E, B)E + \alpha^{EB}(E, B)B, \quad (3.25)$$

$$\mu_{21}\tilde{\rho}_{21} = \alpha^{BE}(E, B)E + \alpha^{BB}(E, B)B. \quad (3.26)$$

Note that each of the general polarizabilities $\alpha^{IJ}(E, B)$ is a function of both probe field amplitudes E and B . Therefore at first glance the separation in (3.25) and (3.26) does not seem to be unique. This is not the case, though. From the formal expansion of f and g in a power series in E and B

$$f(E, B) = \sum_{n,m} f_{nm} E^n B^m, \quad g(E, B) = \sum_{n,m} g_{nm} E^n B^m \quad (3.27)$$

we can discard all terms with an even total number of field amplitudes: As each field amplitude in the rotating frame comes with a factor $e^{-i\omega_p t}$, or the complex conjugated $e^{i\omega_p t}$, only with an odd number of probe field amplitudes E and B all but one exponentials cancel such that the (rotating) polarizabilities oscillate with the probe field frequency ω_p . Thus the expansion (3.27) can be separated uniquely into

$$f(E, B) = \sum_{n,m} f_{nm}^E |E|^{2n} |B|^{2m} E + \sum_{n,m} f_{nm}^B |E|^{2n} |B|^{2m} B,$$

$$g(E, B) = \sum_{n,m} g_{nm}^E |E|^{2n} |B|^{2m} E + \sum_{n,m} g_{nm}^B |E|^{2n} |B|^{2m} B.$$

By comparison to (3.25) and (3.26) we find for the sought $\alpha^{IJ}(E, B)$ as functions of the numerically accessible $f(E, B)$ and $g(E, B)$:

$$\alpha^{EE}(E, B) = \frac{d_{34}}{2E} [f(E, B) + f(E, -B)], \quad (3.28)$$

$$\alpha^{EB}(E, B) = \frac{d_{34}}{2B} [f(E, B) + f(-E, B)], \quad (3.29)$$

$$\alpha^{BE}(E, B) = \frac{\mu_{21}}{2E} [g(E, B) + g(E, -B)], \quad (3.30)$$

$$\alpha^{BB}(E, B) = \frac{\mu_{21}}{2B} [g(E, B) + g(-E, B)]. \quad (3.31)$$

The comparison of the exact $\alpha^{IJ}(E, B)$ to the linear response results α^{IJ} from (3.13) – (3.16) is shown in Fig. 3.6. Here we use

$$\log \left| \frac{\alpha^{IJ} - \alpha^{IJ}(E, B)}{\alpha^{IJ}} \right| \quad (3.32)$$

to express the deviation of the approximate linear expressions α^{IJ} from the numerically extracted values $\alpha^{IJ}(E, B)$.

We show the real and imaginary parts of (3.32) for two different probe field Rabi frequencies. The solid lines correspond to $\Omega_E = \gamma_2$ and the dashed lines to $\Omega_E = 10 \times \gamma_2$, respectively. Here $\Omega_E = d_{34}E/\hbar$ and $\Omega_B = \mu_{21}B/\hbar$ apply, thus $\Omega_E = 137\Omega_B$ holds, where E and B are the electric and magnetic probe field amplitudes, respectively.

One recognizes that the relative difference of the exact to the approximate result is always less than 10^{-2} for $\Omega_E = 10\gamma_2$ and less than 10^{-4} for $\Omega_E = \gamma_2$

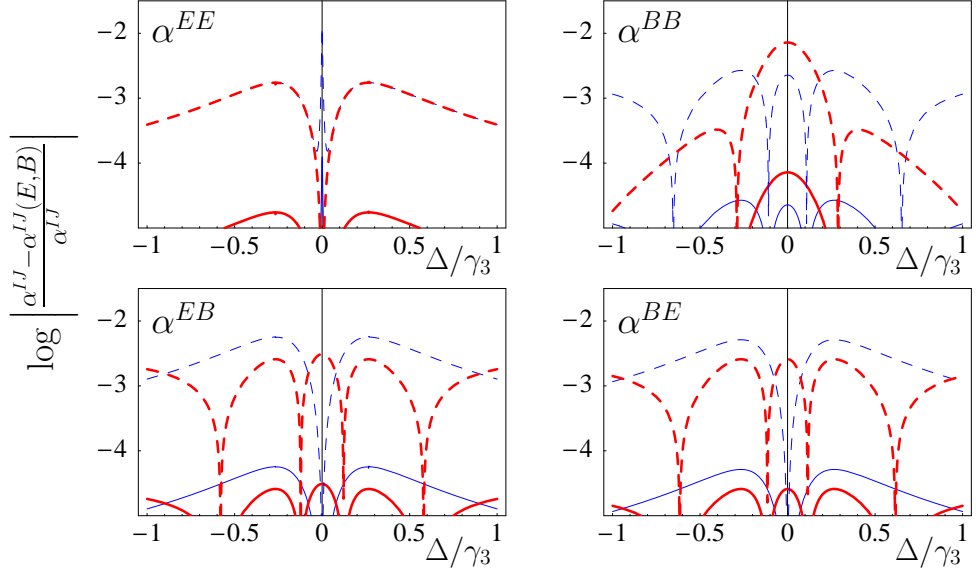


Figure 3.6: Deviation (3.32) of **real** and **imaginary** parts of the exact $\alpha^{IJ}(E, B)$ compared to the linear response results for 2 different probe field Rabi frequencies: $\Omega_E = \gamma_2$ (solid) and $\Omega_E = 10 \times \gamma_2$ (dashed).

and therefore negligible for these probe field Rabi frequencies. Comparing to (3.18) we find that the probe field Rabi frequency $\tilde{\Omega}_E = \gamma_3 \sqrt{\rho_{22}^{(E)}}$ can be estimated for a naturally broadened electric dipole 2-level atom to be $\tilde{\Omega}_E = 13.7\gamma_2$ if we allow for a 1% upper state population $\rho_{22}^{(E)} = 10^{-2}$. As this is the same order of magnitude as the probe field Rabi frequency $\Omega_E = 10\gamma_2$ which led to a 1% error of the linear response result α^{IJ} compared to the exact $\alpha^{IJ}(E, B)$ we conclude that the 5-level scheme is not significantly more sensitive to nonlinearities due to saturation effects than any ordinary electric dipole transition.

This behavior is a consequence of the strong coupling Ω_c by which the magnetic transition is effectively broadened due to additional decay channels as discussed in section 3.2 and hence less susceptible to saturation.

3.4 Non-radiative broadenings

From the discussion in section 2.1 it is apparent that magnetic dipole transitions need to include additional non-radiative broadening mechanisms to yield realistic results. In principle, there are two distinct types of broadening: Homogeneous and inhomogeneous. They will be analyzed separately in the following.

The most common additional homogeneous broadening is due to (elastic) collisions. These collision can occur, for instance, between the same or different kinds of atoms in gaseous media, or between atoms in a doped crystal, and phonons of the crystal lattice. As these collisions happen randomly, the energy levels of the atom are altered randomly during a collision due to the interaction energy. This can be modeled by a random phase with a width γ_p in frequency space. From an averaging treatment in time [90] the distribution is found to be a Lorentzian

$$L(x) = \frac{1}{\pi} \frac{\gamma_p}{\gamma_p^2 + x^2}. \quad (3.33)$$

Its influence on the polarizabilities (3.13) – (3.16) can be determined by adding such random phase terms x_E , x_B , x_c to every static detuning Δ_E , Δ_B , δ_c , respectively, (e.g. $\Delta_E \longrightarrow \Delta_E + x_E$) and convolute with the Lorentzian $L(x)$, e.g.,

$$\tilde{\alpha}^{EE} = \int dx_E dx_B dx_c \alpha^{EE}(x_E, x_B, x_c) L(x_E) L(x_B) L(x_c). \quad (3.34)$$

For the 5-level scheme we assume that levels $|2\rangle$ and $|4\rangle$ are approximately degenerate in such a way that they experience correlated phase fluctuations. As a result we apply the same width γ_p for Δ_E and δ_c but leave γ_{42} unaltered. For reasons of simplicity we also pick γ_p for Δ_B . The convolution (3.34) then has an analytical solution from which we find that the inclusion of a homogeneous broadening into the 5-level scheme Fig. 3.3 is obtained by the substitution rules

$$\begin{aligned} \gamma_{42} &\longrightarrow \gamma_{42}, & \gamma_{21} &\longrightarrow \gamma_{21} + \gamma_p, \\ \gamma_{34} &\longrightarrow \gamma_{34} + \gamma_p, & \gamma_{31} &\longrightarrow \gamma_{31} + 2\gamma_p, \end{aligned} \quad (3.35)$$

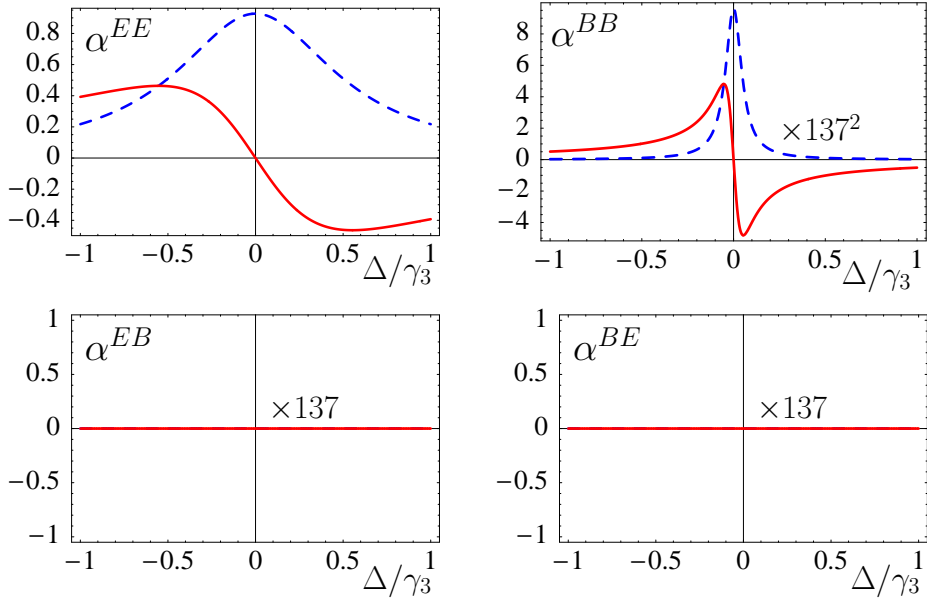


Figure 3.7: Real (solid) and imaginary (dashed) parts of the electric (α^{EE}) and magnetic (α^{BB}) polarizabilities as well as the chirality parameters (α^{EB} , α^{BE}) for arbitrary but the same units for $\Omega_c = 0$. In contrast to Fig. 3.4 additional homogeneous broadenings according to eq. (3.35) with $\gamma_p = 10^3\gamma_2$ apply.

for the polarizabilities (3.13) – (3.16) which affect only the off-diagonal decay rates. Thus γ_{42} , which is relevant for EIT, remains unbroadened. In contrast the coherences between any other pair of states suffer from broadenings γ_p or $2\gamma_p$, respectively.

The additional width of the homogeneous broadening is set to $\gamma_p = 10^3\gamma_2$ which is typical [69] for the most realistic implementation in rare-earth doped crystals at cryogenic temperatures, in which the optically active electrons are protected from the crystal field by outer electrons.

Having chosen the value of γ_p we can now justify the choice of $|\Omega_c|$ in our previous numerical calculations. From (3.15) and (3.16) we note that there exists an optimal value of $|\Omega_c|$ at which α^{BE} and α^{EB} on resonance, and hence the chiral character of the medium, reaches a maximum. These optimal values differ for α^{BE} and α^{EB} due to a non-symmetric influence of

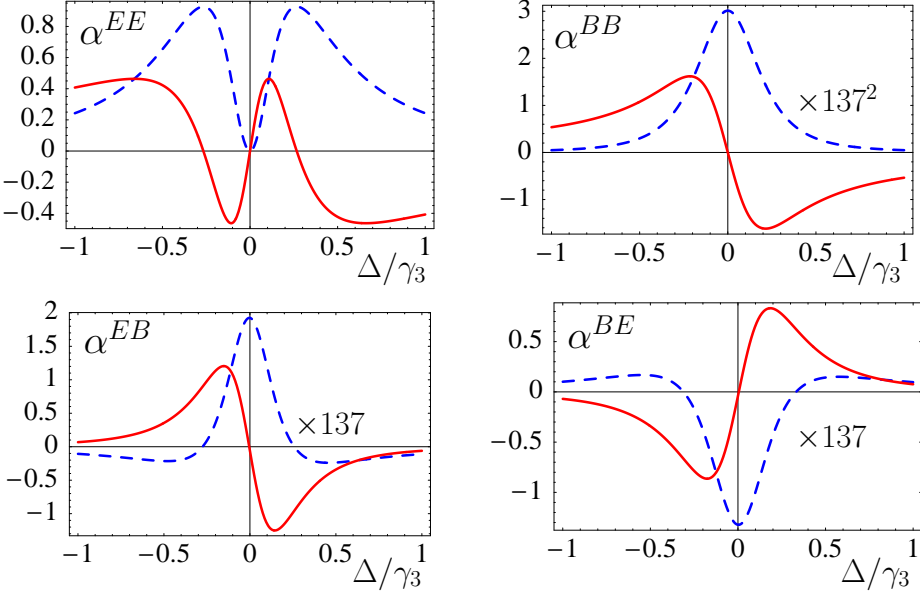


Figure 3.8: Real (solid) and imaginary (dashed) parts of the electric (α^{EE}) and magnetic (α^{BB}) polarizabilities as well as the chirality parameters (α^{EB} , α^{BE}) for arbitrary but the same units for $\Omega_c = 10^4\gamma_2 e^{i\pi/2}$. In contrast to Fig. 3.5 additional homogeneous broadenings according to eq. (3.35) with $\gamma_p = 10^3\gamma_2$ apply.

the additional homogeneous broadening γ_p on the decoherence rates γ_{21} , γ_{31} , γ_{34} , and γ_{42} , respectively. For $\gamma_p = 10^3\gamma_2$ we find $|\Omega_c|_{\text{opt}}$ to be $137\gamma_2$ and $1370\sqrt{20}\gamma_2$ for α^{EB} and α^{BE} , respectively. As a compromise we use the aforementioned value $|\Omega_c| = 10^4\gamma_2$.

The polarizabilities (3.13) – (3.16) including an additional homogeneous broadening are shown in Fig. 3.7 for the case $\Omega_c = 0$ and in Fig. 3.8 for $\Omega_c = 10^4\gamma_2 e^{i\pi/2}$. All other parameters are the same as in section 3.2. The width γ_p is still an order of magnitude smaller than the electric dipole transition. As a result, without coupling (Fig. 3.7) α^{EE} stays almost unchanged compared to the case without homogeneous broadening (Fig. 3.4). For α^{BB} there is a significant change compared to Fig. 3.4, though. The response is now roughly a factor $\alpha^2 = 137^{-2}$ weaker ($\alpha^{EE} \approx 137^2\alpha^{BB}$) and almost as broad as the electric resonance. Note that in contrast to Fig. 3.4 all spectra are scaled

to the width γ_3 of the electric dipole transition. For non-vanishing coupling $\Omega_c = 10^4 \gamma_2 e^{i\pi/2}$ (Fig. 3.8) all polarizabilities α^{IJ} are nearly preserved as the coupling itself provides an effective broadening larger than γ_p : $|\Omega_c| \gg \gamma_p$. Most importantly we note that EIT is preserved.

In contrast to homogeneous broadening, the inclusion of inhomogeneous mechanisms like Doppler broadening cannot be done analytically as it demands the convolution with a Gaussian

$$G(x) = \frac{1}{\sqrt{2\pi}\gamma_G} e^{-x^2/2\gamma_G^2}$$

rather than the Lorentzian $L(x)$. In doped crystals a substantial inhomogeneous width is caused by inhomogeneities of the crystal field. Hence a sufficiently narrow-band probe field will only “see” an effectively reduced density of scatterers which is approximately given by the ratio of the homogeneous to the inhomogeneous width $\varrho_{\text{eff}} \approx \varrho\gamma_p/\gamma_G$. It can be shown that the comparatively long homogeneous coherence times can nevertheless be exploited by the application of certain techniques used recently for the implementation of coherent population transfer methods like RAP [69] or STIRAP [92]: In a first step a spectral hole is burned into the inhomogeneous profile, into which a homogeneously broadened anti-hole is prepared.

3.5 Local field effects: From microscopic to macroscopic responses

So far we have dealt with the local response of an individual atom. These local fields differ, especially for dense media, from the applied external fields. The correspondence between the microscopic polarizabilities α^{IJ} (3.13) – (3.16) and the macroscopic response functions ε , μ , ξ_{EH} , and ξ_{HE} from (3.1) is obtained from local field corrections of the Clausius-Mossotti type (see also part II for a microscopic derivation).

For the implementation of local field corrections we interpret E and B in (3.4) as local fields. As the local fields act in vacuum $B^{\text{loc}} = H^{\text{loc}}$ holds [93]

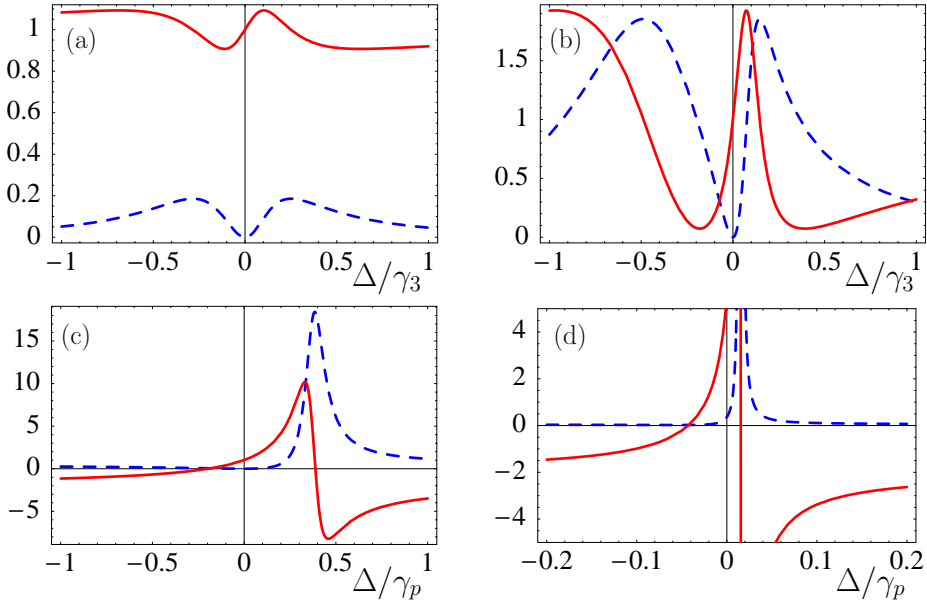


Figure 3.9: Real (solid) and imaginary (dashed) parts of the permittivity ε for the densities (a) $\rho_a = 5 \cdot 10^{13} \text{ cm}^{-3}$, (b) $\rho_b = 5 \cdot 10^{14} \text{ cm}^{-3}$, (c) $\rho_c = 5 \cdot 10^{15} \text{ cm}^{-3}$, and (d) $\rho_d = 5 \cdot 10^{16} \text{ cm}^{-3}$.

and we hence write

$$\begin{aligned} P &= \varrho \alpha^{EE} E^{\text{loc}} + \varrho \alpha^{EB} H^{\text{loc}}, \\ M &= \varrho \alpha^{BE} E^{\text{loc}} + \varrho \alpha^{BB} H^{\text{loc}}. \end{aligned} \quad (3.36)$$

The connection to the macroscopic averaged field amplitudes and to the corresponding macroscopic response functions is given by

$$E^{\text{loc}} = E + \frac{4\pi}{3} P, \quad H^{\text{loc}} = H + \frac{4\pi}{3} M, \quad (3.37)$$

which relates E to its microscopic counterpart E^{loc} , and H to H^{loc} , respectively. These relations can be determined by phenomenological considerations [40, 93] but prove to be consistent with a microscopic theory of local field effects (see part II).

We eliminate the microscopic amplitudes E^{loc} and H^{loc} with the help of (3.37) from (3.36) in favor of the Maxwell fields E and H . By comparison to

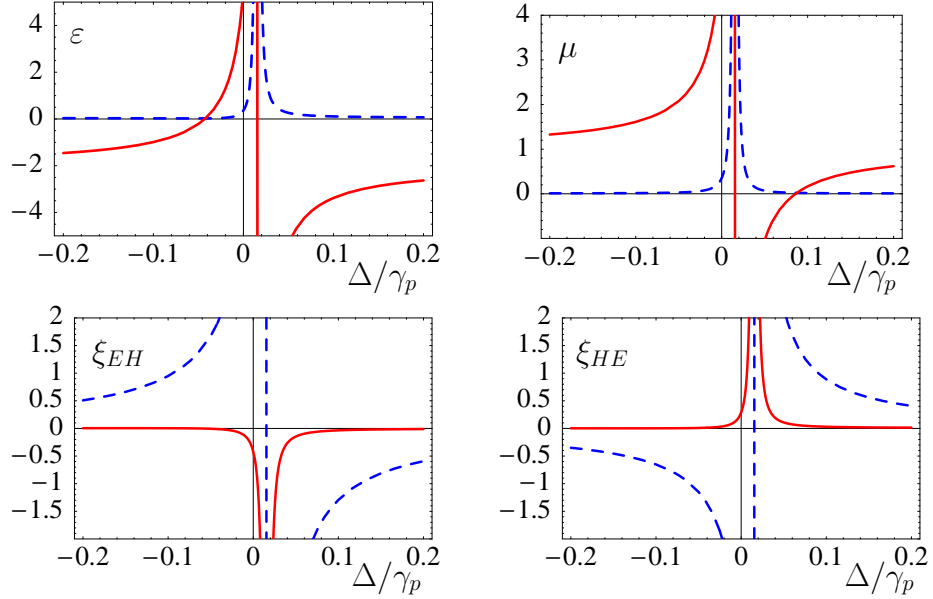


Figure 3.10: Real (solid) and imaginary (dashed) parts of the permittivity ε , the permeability μ , and the cross-coupling coefficients ξ_{EH} and ξ_{HE} including local field corrections for the density $\varrho = 5 \cdot 10^{16} \text{ cm}^{-3}$.

(3.1) we find

$$\begin{aligned} \varepsilon &= 1 + 4\pi \frac{\varrho}{\mathcal{L}^{\text{loc}}} \left\{ \alpha^{EE} + \frac{4\pi}{3} \varrho (\alpha^{EB} \alpha^{BE} - \alpha^{EE} \alpha^{BB}) \right\}, \\ \mu &= 1 + 4\pi \frac{\varrho}{\mathcal{L}^{\text{loc}}} \left\{ \alpha^{BB} + \frac{4\pi}{3} \varrho (\alpha^{EB} \alpha^{BE} - \alpha^{EE} \alpha^{BB}) \right\}, \end{aligned} \quad (3.38)$$

for the permittivity and the permeability and

$$\xi_{EH} = 4\pi \frac{\varrho}{\mathcal{L}^{\text{loc}}} \alpha^{EB}, \quad \xi_{HE} = 4\pi \frac{\varrho}{\mathcal{L}^{\text{loc}}} \alpha^{BE}, \quad (3.39)$$

for the cross-coupling coefficients. The common denominator reads

$$\mathcal{L}^{\text{loc}} = 1 - \frac{4\pi}{3} \varrho \left[\alpha^{EE} + \alpha^{BB} + \frac{4\pi}{3} \varrho (\alpha^{EB} \alpha^{BE} - \alpha^{EE} \alpha^{BB}) \right].$$

Note that (3.38) reduces to the well known Clausius-Mossotti result [40] for the dielectric case $\alpha^{IJ} = 0$, $IJ \in \{EB, BE, BB\}$.

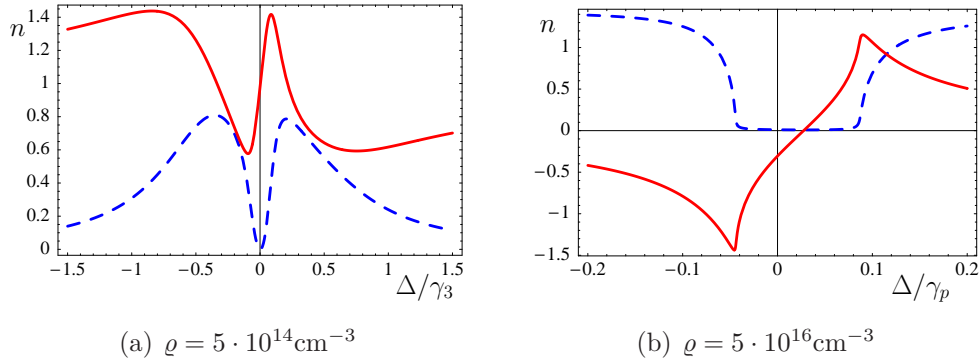


Figure 3.11: Real (solid) and imaginary (dashed) parts of the refractive index, including local field effects for two different densities.

The influence of local field effects on the spectra is shown in Fig. 3.9 for the permittivity ε . Figs. 3.9(a) – 3.9(d) show ε for the densities $\varrho_a = 5 \cdot 10^{13} \text{ cm}^{-3}$, $\varrho_b = 5 \cdot 10^{14} \text{ cm}^{-3}$, $\varrho_c = 5 \cdot 10^{15} \text{ cm}^{-3}$, and $\varrho_d = 5 \cdot 10^{16} \text{ cm}^{-3}$, respectively. For ϱ_a we find a similar spectrum as for the uncorrected α^{EE} of Fig. 3.8. Increasing the density by an order of magnitude mainly increases the strength of the response by a factor of 10 as well [Fig. 3.9(b)]. As a result of the local field corrections an asymmetry emerges. The left part of the spectrum is broadened while the part above resonance moves towards resonance and gets narrower. This behavior is far more pronounced for the increasingly higher densities ϱ_c and ϱ_d . The low frequency part is already out of sight while the blue-detuned part of the spectrum evolves into a sharp resonance. Note that the spectra 3.9(c) and 3.9(d) are scaled to the homogeneous broadening γ_p . This is a common behavior of all four local field corrected response functions (3.38) and (3.39) as shown in Fig. 3.10 for the density $\varrho = 5 \cdot 10^{16} \text{ cm}^{-3}$.

This common effect is mainly governed by the leading term of the denominator \mathcal{L}^{loc} . The position and the width of the resonance of Fig. 3.10 are hence given by the real and imaginary part of the root of the denominator of $1/(1 - \frac{4\pi}{3}\varrho\alpha^{EE})$, respectively.

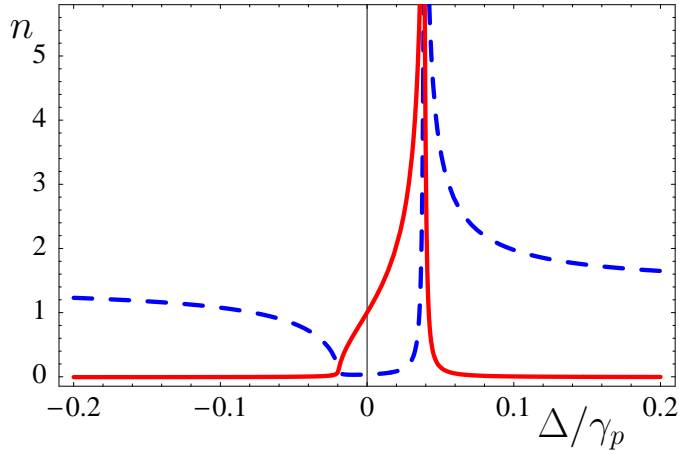


Figure 3.12: Real (solid) and imaginary (dashed) parts of the non-chiral refractive index, including local field effects for a density of $\varrho = 5 \cdot 10^{16} \text{ cm}^{-3}$ as a function of Δ . Compared to Fig. 3.11(b) here $\rho_{41}^{(0)} = 0$ applies.

3.6 Refractive index

With the permittivity ε , the permeability μ as given by eq. (3.38), and the chirality parameters ξ_{EH} and ξ_{HE} (3.39) we have collected all ingredients needed to determine the index of refraction from eq. (2.18). As an example, Fig. 3.11(a) shows the real and imaginary parts of the refractive index as a function of the probe field detuning Δ for a density of $\varrho = 5 \cdot 10^{14} \text{ cm}^{-3}$. As before we use $\gamma_p = 10^3 \gamma_2$ and leave all other parameters as defined in section 3.2. A comparison with Fig. 3.8 reveals that the spectrum of the refractive index is dominated by the permittivity ε including the prominent features of EIT: Suppression of absorption and steep slope of the dispersion on resonance. Obviously there is no negative refraction yet.

In Fig. 3.11(b) the spectrum of n is shown for a higher density of $\varrho = 5 \cdot 10^{16} \text{ cm}^{-3}$. Note that in contrast to Fig. 3.11(a) the frequency axis is scaled in units of the homogeneous broadening γ_p rather than γ_3 . The observed absorption spectrum displays a broad window with $\text{Im}[n] \approx 0$. Simultaneously the refraction becomes negative and shows a strong dispersion around resonance as expected for negative n (see chapter 1). Most importantly we find simultaneously substantial negative refraction and minimal absorption

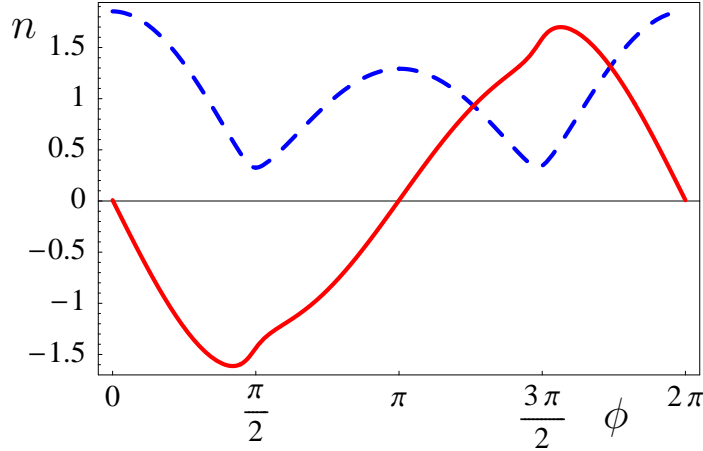


Figure 3.13: Real (solid) and imaginary (dashed) parts of the refractive index as a function of the phase ϕ of the coupling Rabi frequency Ω_c .

[Kästel2007b, Kästel2008] for this density⁴.

Although the Clausius-Mossotti corrections at this density contribute a resonance to the response functions ε , μ , ξ_{EH} , and ξ_{HE} (see Fig. 3.10) this resonance does not show up in the refractive index. Combined Clausius-Mossotti local field corrections for more general media than pure dielectrics tend to yield a negative refractive index for high densities (see part II). To rule out that the negative refraction observed in Fig. 3.11(b) is solely a result of such a behavior, we compare Fig. 3.11(b) to a non-chiral version. Since setting $\Omega_c = 0$ would affect the spectra of ε and μ significantly we artificially set $\rho_{41}^{(0)} = 0$ so that the cross-coupling vanishes without influencing the direct responses ε and μ . The non-chiral version of the index of refraction for a density $\varrho = 5 \cdot 10^{16} \text{ cm}^{-3}$ is shown in Fig. 3.12. Clearly there is no negative refraction for the non-chiral index of refraction at this density. Hence we conclude that the cross-coupling is crucial for $\text{Re}[n] < 0$.

This result can also be seen from Fig. 3.10. In the spectral region where the index of refraction in Fig. 3.11(b) reaches its minimum of about $\text{Re}[n] \approx -1 \dots -1.5$ the magnetic permeability $\text{Re}[\mu]$ is strictly positive. In contrast ξ_{EH} and ξ_{HE} are almost purely imaginary as intended with $\text{Im}[\xi_{EH}] \approx 1 \dots 2$

⁴Note that the required density is about a factor 10^2 smaller than the density needed in a similar scheme in which cross-couplings were not taken into account [88].

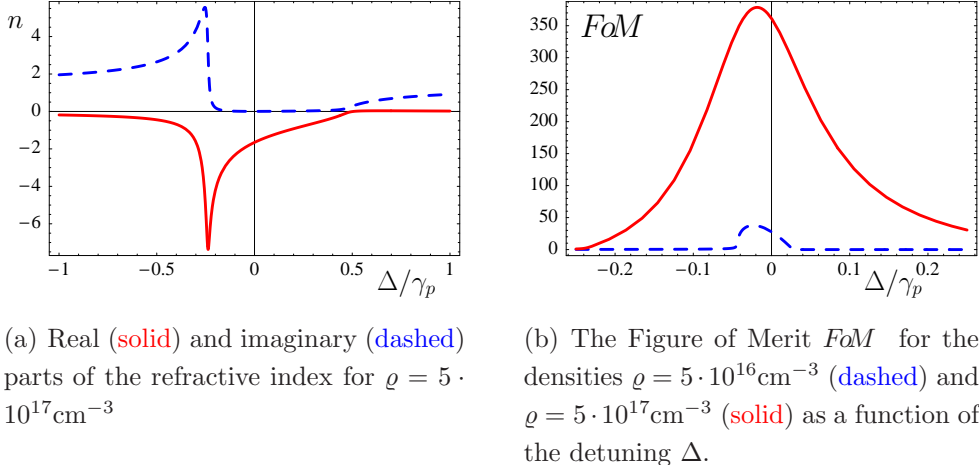
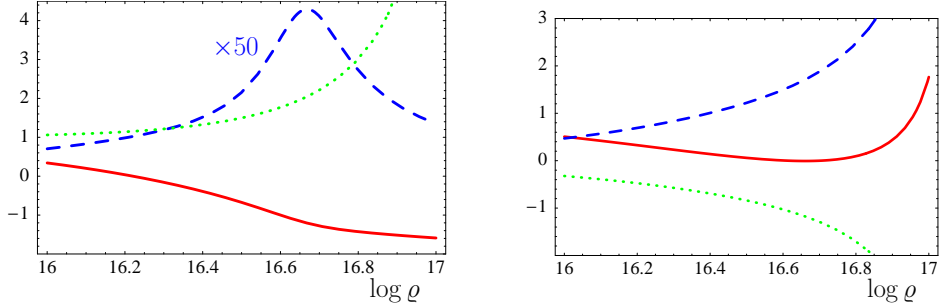


Figure 3.14: The refractive index, including local field effects for a density of $\varrho = 5 \cdot 10^{17} \text{ cm}^{-3}$ as well as the figure of merit FOM for two different densities.

and $\text{Im}[\xi_{HE}] \approx -1 \dots -2$ negative. Therefore we come to the same conclusion: The negative refraction at this density is clearly a consequence of the chiral cross-coupling.

Up to now, the phase ϕ of the coupling Rabi frequency Ω_c has been set to $\phi = \pi/2$ after the qualitative discussion of section 3.2. In Fig. 3.13 we plot the phase dependence of the refractive index taken at the spectral position $\Delta \approx -0.045\gamma_p$ at which n reaches its minimum [cf. Fig. 3.11(b)]. As expected, the value of the refractive index depends strongly on the phase ϕ . For example changing the phase by $\delta\phi = \pi$ reverses the influence of the chirality compared to the non-chiral result which in this case is approximately zero (cf. Fig. 3.12) and thus gives a positive index of refraction $\text{Re}[n] > 0$. Note that the symmetry $\text{Re}[n(\phi)] = -\text{Re}[n(2\pi - \phi)]$ is coincidental since for the chosen parameters $\varepsilon \approx 0$.

By further increasing the density of scatterers ϱ the optical response of the medium increases. As an example Fig. 3.14(a) shows the spectrum of n for $\varrho = 5 \cdot 10^{17} \text{ cm}^{-3}$. Compared to the case of $\varrho = 5 \cdot 10^{16} \text{ cm}^{-3}$ of Fig. 3.11(b) the strength of the response increases while the absorption $\text{Im}[n]$ stays small. As a consequence the figure of merit for negative refraction FOM (1.1) increases with density and reaches rather large values as shown in Fig. 3.14(b). These values which reach $FOM \approx 35$ for $\varrho = 5 \cdot 10^{16} \text{ cm}^{-3}$ and $FOM \gtrsim 350$ for



(a) Real (solid) and imaginary (dashed, $\times 50$) parts of the refractive index, as well as the real part of the permeability (dotted).

(b) Real part of the permittivity ϵ (solid) and the imaginary parts of ξ_{EH} (dashed) and ξ_{HE} (dotted).

Figure 3.15: The response functions as well as the refractive index n as a function of the logarithm of the density $\log \varrho$. The spectral position is taken to be about the minimum of the refractive index shown in Fig. 3.11(b) ($\Delta = -0.043\gamma_p$).

$\varrho = 5 \cdot 10^{17} \text{ cm}^{-3}$ should be contrasted to previous theoretical proposals as well as experimental results on negative refraction in the optical or near infrared regime for which the figure of merit FoM is typically less than unity (see chapter 1).

The density dependence of the response functions ϵ , μ , ξ_{EH} , and ξ_{HE} as well as the index of refraction n taken at the spectral position $\Delta = -0.043\gamma_p$ at which $\text{Re}[n]$ reaches its minimum for $\varrho = 5 \cdot 10^{16} \text{ cm}^{-3}$ is shown in Fig. 3.15. We observe that $\text{Re}[n]$ reaches increasingly negative values with increasing density while $\text{Im}[n]$ forms a maximum but stays comparatively small (note that $\text{Im}[n]$ in Fig. 3.15(a) is amplified by a factor of 50). The permittivity $\text{Re}[\mu]$ increases with increasing densities while $\text{Im}[\xi_{EH}]$ and $\text{Im}[\xi_{HE}]$ [Fig. 3.15(b)] show similar but inverse characteristics. As expected $\text{Re}[\epsilon]$ evolves to negative values for higher densities but as a consequence of the resonance induced by the local field corrections starts to climb again. We once more conclude that the negative refraction $\text{Re}[n] < 0$ observed at this spectral position is a consequence of the cross-coupling.

The maximum of $\text{Im}[n]$ from Fig. 3.15(a) is surprising as an increasing density of scatterers should lead to an increasing absorption. Hence the de-

crease is at first sight a peculiar behavior which demands an explicit explanation. Such an explanation can easily be found: At the densities⁵ employed in Fig. 3.15(a) the spectral band with minimal absorption broadens with increasing density due to local field effects [cf. Figs. 3.11(b) and 3.14(a)]. Hence the chosen spectral position wanders relatively from the tail of the band edge to the middle of the minimal absorption band.

⁵For very high densities local field corrections lead to a decreasing $\text{Im}[n]$ for different reasons. See part II.

CHAPTER 4

Applicability of the 5-level scheme

4.1 Impedance matching

Any optical application has a significant element other than the functional unit: The boundary to its surroundings. For linear optical elements like lenses, prisms, etc., the shape of the boundary even accounts for most of the functionality. Hence as a basis of any application we study the impedance of a flat surface interconnecting a chiral and a non-chiral material. The goal here is to find conditions under which the boundary between non-chiral and chiral, negative refracting media is non or little reflecting.

We suppose a boundary with normal vector $\mathbf{n} = \mathbf{e}_z$ at $z = 0$ between a non-chiral medium 1 ($z < 0$) with ε_1, μ_1 and medium 2 ($z > 0$) which employs a chirality $(\varepsilon_2, \mu_2, \xi_{EH}, \xi_{HE})$. Note that the response tensors are assumed to be of the form used in section 2.2 such that we can restrict to an effectively scalar theory for one polarization state of a wave propagating in z -direction. This is valid as the polarizations \mathbf{e}_+ , \mathbf{e}_- denote eigensolutions for both media.

We decompose the \mathbf{e}_- wave solution for medium 1 into an incoming E^i and a reflected part E^r

$$\mathbf{E}_1(\mathbf{r}) = (E_i e^{ik_1 z} + E_r e^{-ik_1 z}) \mathbf{e}_- \quad (4.1)$$

$(k_1 = |\mathbf{k}_i| = |\mathbf{k}_r|)$. In medium 2 ($z > 0$) only a transmitted wave E_t shall

exist due to the boundary condition at infinity

$$\mathbf{E}_2(\mathbf{r}) = E_t e^{ik_2 z} \mathbf{e}_-. \quad (4.2)$$

A similar decomposition is applied for the magnetic field $\mathbf{H}(\mathbf{r})$. The solutions are connected at the boundary corresponding to the conditions $\mathbf{n} \times (\mathbf{E}_2 - \mathbf{E}_1) = 0$ and $\mathbf{n} \times (\mathbf{H}_2 - \mathbf{H}_1) = 0$ for the electric and magnetic field strengths, respectively, from which we find at $z = 0$

$$E_i + E_r = E_t, \quad H_i + H_r = H_t. \quad (4.3)$$

A second set which connects the electric and magnetic fields within materials 1 and 2 respectively is obtained from Maxwell's equations in Fourier space (2.14) together with the material equations (2.10). For medium 1 we get

$$\mathbf{k}_i \times \mathbf{e}_- E_i e^{ik_1 z} + \mathbf{k}_r \times \mathbf{e}_- E_r e^{-ik_1 z} = \frac{\omega}{c} \mu_1 (H_i e^{ik_1 z} + H_r e^{-ik_1 z}) \mathbf{e}_-. \quad (4.4)$$

We note that $\mathbf{e}_z \times \mathbf{e}_\pm = \mp i \mathbf{e}_\pm$ holds. Hence (4.4) simplifies for $z = 0$ to the scalar equation

$$ik_1 (E_i - E_r) = \frac{\omega}{c} \mu_1 (H_i + H_r). \quad (4.5)$$

Here $\mathbf{k}_i = -\mathbf{k}_r = k_1 \mathbf{e}_z$ has been applied. Similarly we obtain for medium 2

$$ik_2 E_t = \frac{\omega}{c} (\xi_{HE} E_t + \mu_2 H_t). \quad (4.6)$$

From (4.3), (4.5), and (4.6) we eliminate the magnetic field amplitudes and solve the resulting equations for the ratio of reflected and incoming electric field wave amplitudes which reads

$$\frac{E_r}{E_i} = \frac{1 - \sqrt{\frac{\mu_1}{\varepsilon_1}} \frac{n_2 + i\xi_{HE}}{\mu_2}}{1 + \sqrt{\frac{\mu_1}{\varepsilon_1}} \frac{n_2 + i\xi_{HE}}{\mu_2}}. \quad (4.7)$$

The wave numbers k_1 and k_2 in (4.5) and (4.6) have been replaced by $k_1 = n_1 \omega / c = \sqrt{\varepsilon_1 \mu_1} \omega / c$ and $k_2 = n_2 \omega / c$, respectively. Equation (4.7) is a generalization of the well-known Fresnel formulas for normal incidence to a chiral medium. Impedance matching is defined as the vanishing of the

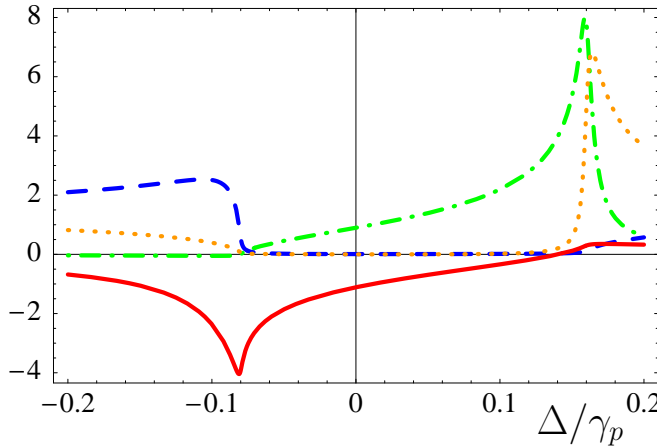


Figure 4.1: Real (solid) and imaginary (dashed) parts of the refractive index as well as the real (dash-dotted) and imaginary (dotted) parts of the inverse impedance Z_2^{-1} from (4.9) as a function of the detuning Δ for $\varrho = 1.56 \cdot 10^{17} \text{ cm}^{-3}$.

reflected wave $E_r = 0$, i.e., a complete transfer of the incoming field into medium 2:

$$\sqrt{\frac{\mu_1}{\varepsilon_1}} \frac{n_2 + i\xi_{HE}}{\mu_2} = 1. \quad (4.8)$$

Using the explicit form of n_2 for the particular polarization mode (2.18) we find the more convenient expression

$$\sqrt{\frac{\varepsilon_1}{\mu_1}} = \sqrt{\frac{\varepsilon_2}{\mu_2}} \left[\pm \sqrt{1 - \left(\frac{\xi_{EH} + \xi_{HE}}{2\sqrt{\varepsilon_2\mu_2}} \right)^2} + \frac{i}{2} \frac{\xi_{EH} + \xi_{HE}}{\sqrt{\varepsilon_2\mu_2}} \right] \quad (4.9)$$

which obviously simplifies for the non-chiral case $\xi_{EH} = \xi_{HE} = 0$ to the well known [40] result

$$\sqrt{\frac{\varepsilon_1}{\mu_1}} = \sqrt{\frac{\varepsilon_2}{\mu_2}}.$$

The right hand side of (4.9) hence is the inverse impedance Z_2^{-1} of the chiral medium 2. Note that as a result of causality the sign of the square root in Z_2 has to be taken for passive media such that $\text{Re}[Z_2] \geq 0$ is obtained [30]. We plot the real and imaginary parts of Z_2^{-1} as well as the spectrum of the index of refraction in Fig. 4.1. Under the assumption of medium 1 being

vacuum $\epsilon_1 = \mu_1 = 1$ impedance matching exists if the right hand side of (4.9) equates to $1+i0$. The density $\varrho = 1.56 \cdot 10^{17} \text{ cm}^{-3}$ has been optimized roughly such that we find at the spectral position $\Delta = 1.17 \cdot 10^{-2} \gamma_p$ for the index of refraction $n = -1,0003 + i0,009$ while the impedance simultaneously reads $1.003 + i0.0006$. The corresponding figure of merit then is about $FoM \approx 110$.

4.2 Tunability

The most astounding application of a negative refractive index is the so called perfect lens¹ [1] which allows sub-diffraction limit resolution [94] due to an amplification of evanescent waves inside a slab of a material with $\text{Re}[n] < 0$ [23]. One major requirement for the material of the flat superlens is an all-angle negative refractive index. Hence most current metamaterials are not suited for sub-diffraction limit imaging applications as they in general show $\text{Re}[n] < 0$ behavior only for a particular direction of propagation. Consequently there are only few reports of experimental sub wavelength resolution based on negative refraction. It has been demonstrated using 2D photonic crystals [95, 96], a 3D photonic crystal [17] in the microwave regime as well as for a left-handed 2D transmission line material[97, 98] which operated in the microwave spectrum as well.

From an analysis of the dispersion relation of surface plasmons [99] which influence the transmission properties of a negatively refracting slab significantly Smith *et al.* [100] and Merlin [101] independently realized that an isotropic index $\text{Re}[n] < 0$ is not sufficient for sub-diffraction limit imaging, though. In fact for a slab of thickness d surrounded by vacuum and an intended resolution Δx the refractive index must match $n = -1$ with an error Δn not exceeding

$$\Delta n = \exp \left\{ -\frac{2\pi d}{\Delta x} \right\}. \quad (4.10)$$

For high frequencies sub-diffraction limit resolution has been reported only within the near field domain [102, 103]. There an ultraviolet (365nm) image has been shown to display a significant improvement of the resolution when a thin metallic slab is placed between the source and the image. This is a

¹Cf. chapter 1.

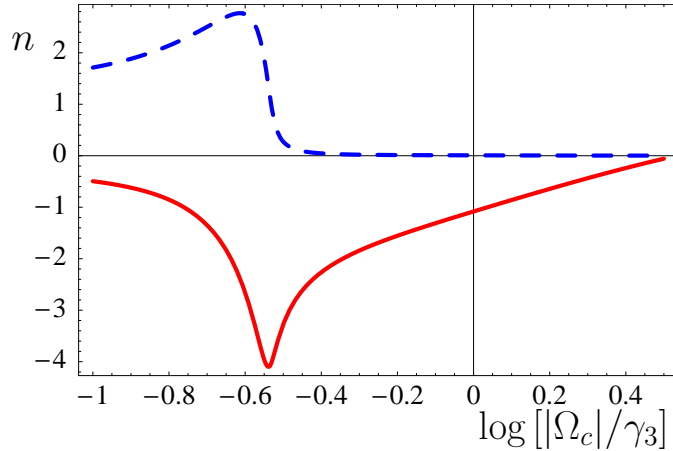


Figure 4.2: Real (solid) and imaginary (dashed) parts of the refractive index as a function of the coupling field Rabi-frequency $|\Omega_c|$ relative to the radiative decay rate γ_3 , for $\varrho = 1.56 \cdot 10^{17} \text{ cm}^{-3}$.

direct consequence of the operation in the near or static field regime in which electric and magnetic field amplitudes can be regarded as being independent. Hence a metal (usually silver to minimize losses) slightly below the plasma frequency fulfills $\text{Re}[\varepsilon] < 0$ and thus suffices to focus the electric field and produce an image.

For a metamaterial with $\text{Re}[n] < 0$ eq. (4.10) presents a considerable obstacle for the operation of a superlens approaching far field distances as it demands an extreme fine-tuning of the refractive index in order to achieve a resolution beyond the diffraction limit. Such a fine-tuning can be provided by the tunability of the strength of the coupling field. In Fig. 4.2 we show the real and imaginary parts of n as a function of $\log[|\Omega_c|/\gamma_3]$ for the density $\varrho = 1.56 \cdot 10^{17} \text{ cm}^{-3}$ employed in section 4.1. We find that for values of the coupling Rabi frequency Ω_c around the electric dipole decay rate γ_3 negative refraction around $n = -1$ with a slope $\gamma_3 \frac{\partial \text{Re}[n]}{\partial |\Omega_c|} \lesssim 1$. Hence by a stabilization of the coupling laser power the quantum interference scheme allows for small Δn and therefore for accordingly small values of Δx , i.e., potentially sub-diffraction limit imaging even in the far field regime.

Apart from potential imaging applications the 5-level quantum interfer-

ence scheme allows for switchable devices operating in a wide range of positive and negative refractive indices with simultaneously small losses.

4.3 Beyond 1D: Tensorial analysis

In section 2.2 we specialized our discussion to an effectively scalar 1D theory by restricting to a particular direction of propagation and left circular polarization (\mathbf{e}_+). Fig. 4.3 shows a level structure and geometry in which the requirements of section 2.2 are fulfilled and hence the scalar theory is valid. We assume propagation along the \mathbf{e}_z -direction and similarly the field vector of the coupling field \mathbf{E}_c should point in \mathbf{e}_z -direction as well [Fig. 4.3(a)]. Compared to Fig. 3.2 the states $|2\rangle$ and $|3\rangle$ are replaced by the magnetic Zeeman-levels corresponding to an angular momentum with $J = 1$. The Clebsch-Gordon coefficients for the $J = 1$ to $J = 1$ transition $|2\rangle - |3\rangle$ allow for the \mathbf{e}_z -polarized coupling field \mathbf{E}_c only the couplings $|2, +\rangle - |3, +\rangle$ and $|2, -\rangle - |3, -\rangle$. Hence the cross-coupling tensors $\bar{\xi}_{EH}$, $\bar{\xi}_{HE}$ indeed have the form (2.16) with $\xi_{EH}^z = 0 = \xi_{HE}^z$. As a result for the tensor elements ξ_{EH}^- , ξ_{HE}^- , as well as ε^- and μ^- for right circularly polarized waves the scalar theory of chapter 3, i.e., the solutions (3.38) and (3.39), applies (see Figs. 3.8 and 3.11).

In order to find the corresponding response for the \mathbf{e}_+ -polarization we have to replace the transition moments for the “-”-branch (Fig. 4.3) by the corresponding “+”-branch moments. In general transition moments between states $|\gamma, J, M\rangle$ and $|\gamma', J', M'\rangle$ where J and M denote angular and magnetic quantum numbers while all other quantum numbers are summarized in γ are given by the Wigner-Eckart theorem [67]

$$\langle \gamma, J, M | \mathcal{O}_q | \gamma', J', M' \rangle = (-1)^{J-M} \begin{pmatrix} J & 1 & J' \\ -M & q & M' \end{pmatrix} \langle \gamma, J | \mathcal{O} | \gamma', J' \rangle. \quad (4.11)$$

Here \mathcal{O}_q denotes the q th component ($q \in \{+1, 0, -1\}$) of the irreducible vector operator \mathcal{O} which for electric dipole transitions is given by (cf. section 3.2) $\mathcal{O} = e\mathbf{r}$ while for magnetic transitions we have to use $\mathcal{O} = \mu_B(\mathbf{J} + \mathbf{S})$. As the reduced matrix element $\langle \gamma, J | \mathcal{O} | \gamma', J' \rangle$ is independent of M and M'

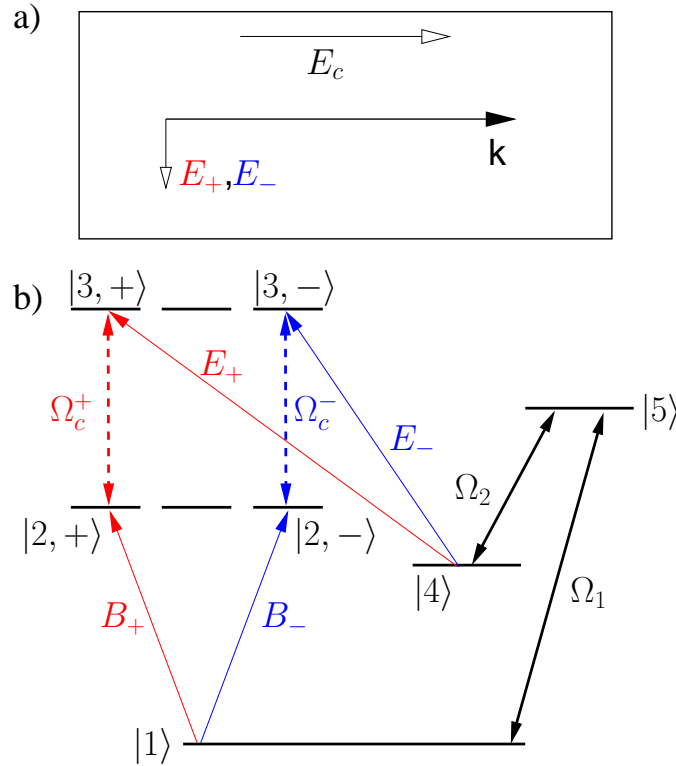


Figure 4.3: (a) Geometry of the 1D implementation: The probe light travels in z -direction with corresponding transversal field vectors while the field vector of the coupling field points along \mathbf{e}_z . (b) Level scheme for 1D implementation. No cross coupling between right and left circular polarization components occurs.

any differences of the matrix elements due to magnetic quantum numbers M , M' are solely given by the product of $(-1)^{J-M}$ and the Wigner 3-j symbol. Hence once a particular matrix element for specific values of M and M' is known, all matrix elements of the same J, J' configuration can be found from (4.11) by comparison.

We note that we assigned in section 2.2 an index $-$ to material tensor components corresponding to right circular waves with \mathbf{e}_- -polarization. Similarly we decompose the electromagnetic field vectors as

$$\mathbf{E} = E_x \mathbf{e}_x + E_y \mathbf{e}_y + E_z \mathbf{e}_z = -E_+ \mathbf{e}_+ + E_- \mathbf{e}_- + E_z \mathbf{e}_z \quad (4.12)$$

with $E_{\pm} = \mp(E_x \mp iE_y)/\sqrt{2}$. In particular E_+ and E_- denote the amplitudes of the left and right circular polarizations, respectively. The magnetic induction B is decomposed similarly. With the orthogonality properties of \mathbf{e}_{\pm} taken into account the interaction Hamiltonian $-\boldsymbol{\mu} \cdot \mathbf{B}$ for magnetic dipole transitions translates to

$$-\boldsymbol{\mu} \cdot \mathbf{B} = -\mu_B(J_+ + S_+)B_+ - \mu_B(J_- + S_-)B_- - \mu_B(J_0 + S_0)B_z. \quad (4.13)$$

Here $J_{\pm} = \mp(J_x \pm iJ_y)/\sqrt{2}$ and $J_0 = J_z$ [104] as well as corresponding relations for \mathbf{S} denote the components $q \in \{+1, 0, -1\}$ of the irreducible vector operator $\boldsymbol{\mu} = \mu_B(\mathbf{J} + \mathbf{S})$. As a result of the properties of the 3-j symbol in (4.11) the transition moment between states $|2, -\rangle$ and $|1\rangle$ has a contribution solely from the $q = -1$ vector component as already depicted in Fig. 4.3(b), i.e., a transition with \mathbf{e}_- -polarization. Similar to the field amplitude we thus indicate with a $-$:

$$\mu_{21}^- = \langle 2, - | \mu_B(J_- + S_-) | 1 \rangle = \frac{1}{\sqrt{3}} \langle 2 | |\boldsymbol{\mu}| | 1 \rangle. \quad (4.14)$$

To find μ_{21}^+ we now can exploit the Wigner-Eckart theorem from which we easily obtain

$$\mu_{21}^+ = \langle 2, + | \mu_B(J_+ + S_+) | 1 \rangle = \frac{1}{\sqrt{3}} \langle 2 | |\boldsymbol{\mu}| | 1 \rangle. \quad (4.15)$$

Thus the matrix elements of the magnetic dipole transitions are independent of the polarization state

$$\mu_{21}^- = \mu_{21}^+. \quad (4.16)$$

Similarly we find for the electric dipole probe field transition $|3\rangle - |4\rangle$, which is a $J = 1$ to $J = 0$ transition as well, that $d_{34}^- = d_{34}^+$ holds. For the matrix elements which appear in the coupling Rabi frequencies Ω_c^{\pm} we find however

$$d_{32}^+ = \langle 3, + | ez | 2, + \rangle = \frac{1}{\sqrt{6}} \langle 3 | |\mathbf{d}| | 2 \rangle \quad (4.17)$$

and

$$d_{32}^- = \langle 3, - | ez | 2, - \rangle = -\frac{1}{\sqrt{6}} \langle 3 | |\mathbf{d}| | 2 \rangle, \quad (4.18)$$

respectively. Hence the coupling Rabi frequencies of the left and right circular branches $\Omega_c^\pm = d_{32}^\pm E_{c,z}/\hbar$ display a relative sign

$$\Omega_c^+ = -\Omega_c^-.$$
 (4.19)

Inspecting equations (3.13) – (3.16) we note that this results in $\alpha_-^{EB} = -\alpha_+^{EB}$ and similarly $\alpha_-^{BE} = -\alpha_+^{BE}$ for the cross coupling coefficients while the electric and magnetic polarizabilities are identical for both polarizations $\alpha_+^{EE} = \alpha_-^{EE}$ and $\alpha_+^{BB} = \alpha_-^{BB}$. From the treatment of the local field corrections in section 3.5 we find similar relations for the coefficients relevant for the refractive index:

$$\begin{aligned} \varepsilon^+ &= \varepsilon^-, & \mu^+ &= \mu^-, \\ \xi_{EH}^+ &= -\xi_{EH}^-, & \xi_{HE}^+ &= -\xi_{HE}^-. \end{aligned}$$
 (4.20)

In the following we will hence suppress the index \pm for the permittivity and the permeability.

One recognizes that these sign relations correspond identically to the example discussed in section 2.3.2. Most importantly we conclude that the refractive index is independent of the polarization state of the incoming wave

$$n_+ = n_-.$$
 (4.21)

Therefore the electromagnetically induced cross coupling in the scheme of Fig. 4.3 does not correspond to a chirality for which the circular components should have different refractive indices.

4.3.1 Angular dependence

To extent the discussion to waves for which propagation is not restricted to the \mathbf{e}_z -direction we allow for angles θ, ϕ for the direction of incidence \mathbf{k} with respect to the coupling field \mathbf{E}_c . We assume a local basis where $\mathbf{e}_z \sim \mathbf{k}$ serves as quantization axis of the atoms. Therefore a wave propagating in θ, ϕ direction will encounter an unchanged atomic level structure but an angle dependent coupling field with components

$$E_{c,x} = |\mathbf{E}_c| \sin \theta \cos \phi, \quad E_{c,y} = |\mathbf{E}_c| \sin \theta \sin \phi, \quad E_{c,z} = |\mathbf{E}_c| \cos \theta.$$
 (4.22)

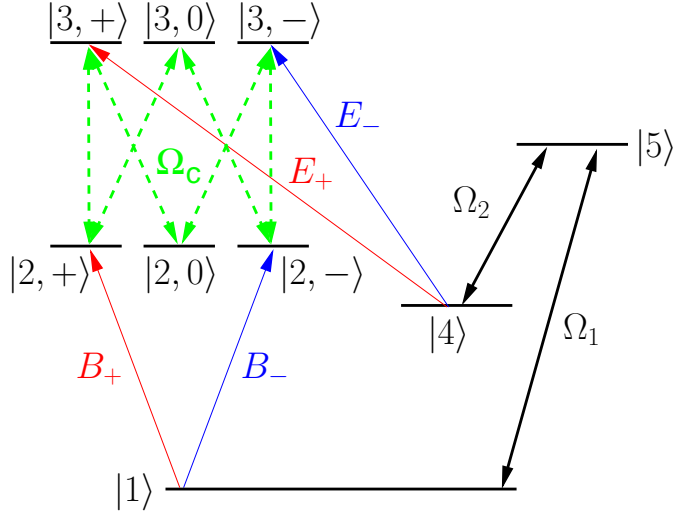


Figure 4.4: For a direction of incidence other than the direction of the coupling field vector \mathbf{E} numerous additional angle dependent couplings occur.

Thus a change of the propagation direction in the local basis affects only the coupling Ω_c . The $|1\rangle - |4\rangle$ transition is assumed to be a $J = 0, M = 0$ to $J = 0, M = 0$ transition and thus the dark state is spherically symmetric and does not depend on polar angles ϕ and θ . For $\theta = 0$ the description therefore reduces to the scheme of Fig. 4.3 as discussed before. Figure 4.4 shows the corresponding level scheme with all angle dependent strong couplings. We note that the angle dependent coupling field amplitudes for the circular components are given by $E_{c,\pm} = |\mathbf{E}_c| \sin \theta e^{\mp i\phi} / \sqrt{2}$. Hence the amplitudes of the various Rabi frequencies between states $\{|3\rangle\}$ and $\{|2\rangle\}$ are given by

$$\begin{aligned}
 \Omega_c^{++} &= \frac{\langle 3, + | d_0 | 2, + \rangle E_{c,z}}{\hbar} = +\Omega_{c,0} \cos \theta, \\
 \Omega_c^{--} &= \frac{\langle 3, - | d_0 | 2, - \rangle E_{c,z}}{\hbar} = -\Omega_{c,0} \cos \theta, \\
 \Omega_c^{+0} &= \frac{\langle 3, + | d_+ | 2, 0 \rangle E_{c,+}}{\hbar} = +\frac{\Omega_{c,0}}{\sqrt{2}} \sin \theta, e^{-i\phi} \\
 \Omega_c^{0-} &= \frac{\langle 3, 0 | d_+ | 2, - \rangle E_{c,+}}{\hbar} = +\frac{\Omega_{c,0}}{\sqrt{2}} \sin \theta, e^{-i\phi} \\
 \Omega_c^{-0} &= \frac{\langle 3, - | d_- | 2, 0 \rangle E_{c,-}}{\hbar} = +\frac{\Omega_{c,0}}{\sqrt{2}} \sin \theta, e^{i\phi}
 \end{aligned} \tag{4.23}$$

$$\Omega_c^{0+} = \frac{\langle 3, 0 | d_- | 2, + \rangle E_{c,-}}{\hbar} = + \frac{\Omega_{c,0}}{\sqrt{2}} \sin \theta \cdot e^{i\phi}$$

Here $\Omega_{c,0} = \langle 3 || \mathbf{d} || 2 \rangle \cdot |\mathbf{E}_c| / (\sqrt{6}\hbar)$ applies. As a result of the angle dependent coupling Rabi frequencies the polarizabilities become angle dependent as well. The cross coupling coefficients for electrically induced magnetization are found from a similar treatment as in section 3.2. They read

$$\bar{\alpha}^{BE} = \alpha^{BE} \begin{pmatrix} \cos \theta & 0 & \sin \theta \frac{e^{-i\phi}}{\sqrt{2}} \\ 0 & -\cos \theta & \sin \theta \frac{e^{+i\phi}}{\sqrt{2}} \\ \sin \theta \frac{e^{+i\phi}}{\sqrt{2}} & \sin \theta \frac{e^{-i\phi}}{\sqrt{2}} & 0 \end{pmatrix} \quad (4.24)$$

with

$$\alpha^{BE} = -\frac{1}{4\hbar} \frac{d_{34}\mu_{21}\rho_{41}^{(0)}\Omega_{c,0}^*}{(\gamma_{31} + i(\Delta_B + \delta_c))(\gamma_{21} + i\Delta_B) + |\Omega_c|^2/4}. \quad (4.25)$$

Here we used $d_{34}^+ = d_{34}^0 = d_{34}^-$ as well as $\mu_{21}^+ = \mu_{21}^0 = \mu_{21}^-$ according to the Wigner-Eckart theorem. Note that the matrix (4.24) is given in the $\{+, -, z\}$ -basis², the coefficient α_{+z}^{EB} for example which describes the \mathbf{e}_+ -polarized electric field induced by a \mathbf{e}_z -polarized magnetic field is given by the upper right entry. A similar result for $\bar{\alpha}^{EB}$ applies with α^{BE} replaced by

$$\alpha^{EB} = -\frac{1}{4\hbar} \frac{d_{34}\mu_{21}\rho_{41}^{(0)}\Omega_{c,0}}{(\gamma_{42} + i(\Delta_E - \delta_c))(\gamma_{34} + i\Delta_E) + |\Omega_c|^2/4}. \quad (4.26)$$

Similarly the electric polarizability reads

$$\bar{\alpha}^{EE} = \alpha^{EE} \mathbb{1} + \frac{\alpha^{EE} |\Omega_c|^2}{D_{42} D_{34}} \begin{pmatrix} \frac{\sin^2 \theta}{8} & -\frac{\sin^2 \theta e^{2i\phi}}{8} & -\frac{\sin \theta \cos \theta e^{i\phi}}{4\sqrt{2}} \\ -\frac{\sin^2 \theta e^{-2i\phi}}{8} & \frac{\sin^2 \theta}{8} & \frac{\sin 2\theta e^{-i\phi}}{8\sqrt{2}} \\ -\frac{\sin \theta \cos \theta e^{-i\phi}}{4\sqrt{2}} & \frac{\sin 2\theta e^{i\phi}}{8\sqrt{2}} & \frac{\cos^2 \theta}{4} \end{pmatrix} \quad (4.27)$$

²This applies to the matrix (4.27) as well.

with

$$\alpha^{EE} = \frac{i}{2\hbar} \frac{d_{34}^2 \rho_{44}^{(0)} (\gamma_{42} + i(\Delta_E - \delta_c))}{(\gamma_{42} + i(\Delta_E - \delta_c))(\gamma_{34} + i\Delta_E) + |\Omega_c|^2/4} \quad (4.28)$$

and $D_{42} = (\gamma_{42} + i(\Delta_E - \delta_c))$, $D_{34} = (\gamma_{34} + i\Delta_E)$. The magnetic polarizability $\bar{\alpha}^{BB}$ is given by (4.27) with α^{EE} replaced by

$$\alpha^{BB} = \frac{i}{2\hbar} \frac{\mu_{21}^2 \rho_{11}^{(0)} (\gamma_{31} + i(\Delta_B + \delta_c))}{(\gamma_{31} + i(\Delta_B + \delta_c))(\gamma_{21} + i\Delta_B) + |\Omega_c|^2/4} \quad (4.29)$$

and $D_{42}D_{34}$ substituted by $D_{31}D_{21} = (\gamma_{31} + i(\Delta_B + \delta_c))(\gamma_{21} + i\Delta_B)$.

Note that all scalar coefficients α^{IJ} are identical to the ones (3.13) – (3.16) obtained from the scalar treatment. For incidence in z -direction the tensors simplify significantly. The cross-couplings reduce to the diagonal elements of the upper left 2×2 -submatrix denoting the magneto-electric couplings of the left and right circular components, respectively. The polarizabilities $\bar{\alpha}^{EE}$, $\bar{\alpha}^{BB}$ simplify in the limit $\theta = 0$ to diagonal tensors with entries (3.13) and (3.14), respectively, for the left and right circular components, i.e., including EIT for the electric polarizability, and a simple resonance structure for the α_{zz} components. Note furthermore that the constraint (2.23) is fulfilled identically by the scheme from Fig. 4.4 for any angles θ , ϕ .

The angular dependence results in a refractive index which is angle dependent as well. Under the assumption of isotropic permittivity and permeability we find angle dependent terms identical to (2.28):

$$n = \pm \sqrt{\epsilon\mu - \xi_{EH}\xi_{HE} - \frac{(\xi_{EH} - \xi_{HE})^2 \cos^2 \theta}{4}} + \frac{i}{2}(\xi_{EH} - \xi_{HE}) \cos \theta. \quad (4.30)$$

The true index of refraction which takes the full form of (4.27) into account, i.e., the angle dependent correction to ϵ and μ gets however much more complicated. We therefore just note that even for the idealized case of (4.30) with isotropic ϵ and μ the value of $\text{Re}[n]$ will in general vary over a broad spectrum of positive and negative values for different angles. This can be seen from (4.30) by consideration of the two limiting cases for which the beam propagates either in “ $+\mathbf{e}_z$ ”- or “ $-\mathbf{e}_z$ ”-direction, i.e., for $\theta = \{0, \pi\}$. Compared to $+\mathbf{e}_z$ -incidence for $\theta = \pi$ only the cross-coupling coefficients change sign due to the term $\cos \theta$. Fig. 4.5 shows the resulting idealized index of refraction (4.30) as a function of the polar angle θ for a density $\varrho = 5 \cdot 10^{16} \text{ cm}^{-3}$ and

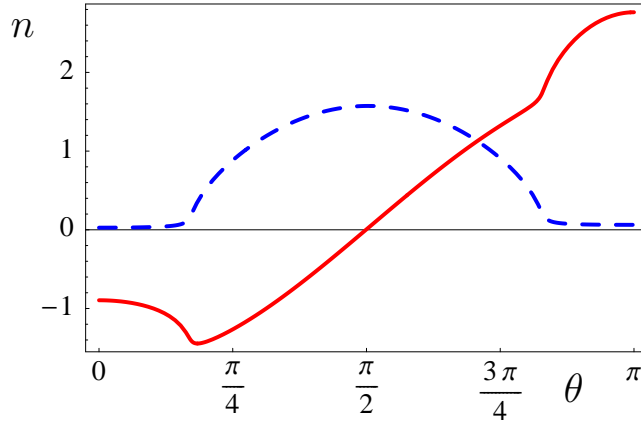


Figure 4.5: Real (solid) and imaginary (dashed) parts of the refractive index as a function of θ .

spectral position slightly below resonance³, $\Delta/\gamma_p = -0.035$. A similar effect can be induced alternatively by changing the phase of the Rabi frequency Ω_c by a factor of π which as well leads to drastic changes of the value of the refractive index as can be seen from Fig. 3.13. Thus the application of a \mathbf{e}_z -polarized coupling field induces a preferred axis with a unique direction and hence beam propagation properties which are strongly angular dependent.

³Cf. Fig. 3.11(b).

CHAPTER 5

Outlook: EIT in metamaterials

As noted in chapter 1 the concept of EIT is not limited to quantum systems like atoms but is applicable to classical oscillators as well [52]. Whenever

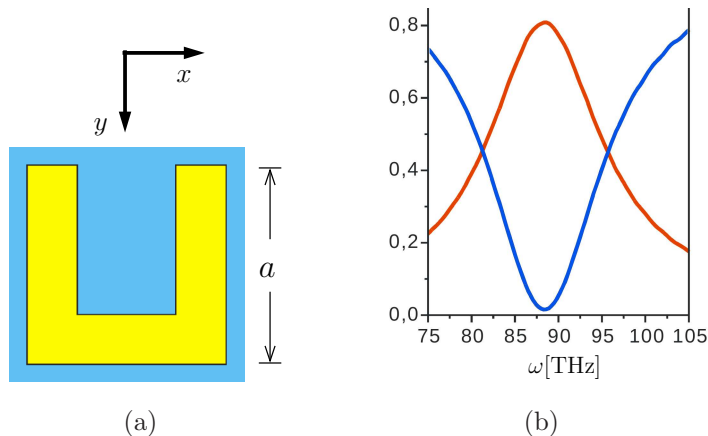


Figure 5.1: (a) Simple SRR structure used in current metamaterial experiments. (b) Measured **reflection** and **transmission** spectra due to an electric field polarized along the x -direction. (figures taken from [105])

an oscillator with a broad resonance, i.e. with large damping is coupled to an oscillator with a narrow resonance, i.e. small damping an “EIT dip” in the loss power spectrum appears. This statement holds in particular also for split ring resonators (SRR) used in metamaterial research as shown in

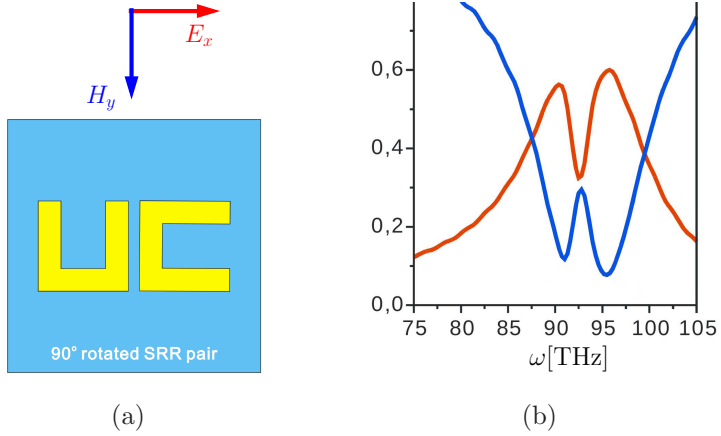


Figure 5.2: (a) SRR molecule used for the implementation of EIT in meta-material structures. One SRR is rotated by 90° with respect to the other. (b) Measured **reflection** and **transmission** spectra. (figures taken from [105])

Fig. 5.1(a).

A single SRR with the open side pointing in y -direction as the one in Fig. 5.1(a) displays several electric and magnetic resonances dependent on propagation direction and polarization state. For an electric field polarization in x -direction an oscillating current density connecting the two open ends of the SRR can be excited leading to an electric resonance at some frequency ω_0 . This frequency is governed by the effective length $3a$ of the antenna like structure where a denotes the arm length of the SRR. If for example $a = 400\text{nm}$ holds, the resonance frequency is around 90THz at which a single Lorentzian line appears as shown in Fig. 5.1(b). The linewidth γ in Fig. 5.1(b) taken from [105] is mostly due to radiative broadening. Similarly an electric field polarized in y -direction “sees” roughly an effective length of only $1a$ corresponding to a resonance frequency of about $3\omega_0$. In addition to the electric resonances the SRR displays a magnetic resonance at about ω_0 for magnetic fields pointing in z -direction.

Consider for example the structure shown in Fig. 5.2(a) as proposed by H. Giessen *et al.* [105]. It consists of two simplified split ring resonators one of which is rotated by 90° with respect to the other. The incident light shall have the polarization indicated in Fig. 5.2(a), i.e. it is assumed to travel in z -direction. As a single SRR is frequently termed “artificial atom”

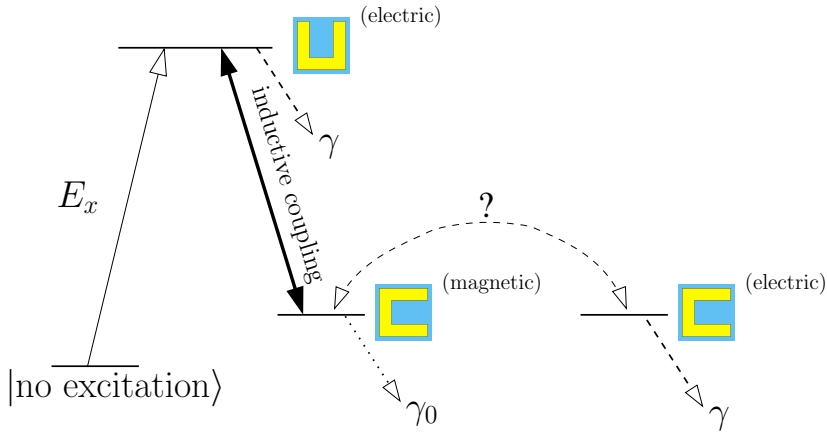


Figure 5.3: Effective Λ -type 3-level scheme for EIT in metamaterials.

the combination of two SRRs shall be called “artificial molecule”. From the discussion above we note that the incident light couples only to the electric resonance with frequency ω_0 of the left SRR as the electric resonance of the right SRR for this polarization is far off resonance. The right SRR nevertheless gets excited due to inductive or different coupling as the distance between the two SRRs becomes smaller.

The right SRR does of course possess also an electric resonance at frequency ω_0 , however with polarization in y -direction. Thus at the frequency ω_0 there are in principle two possibilities to excite the right split ring resonator: either via the electric or the magnetic resonance. The experimental data indicate that the electric resonance of the right SRR associated with the magnetic resonance of the right SRR as indicated in Fig. 5.3 must be weak. As the linewidth γ_0 of the magnetic resonance is much smaller than the electric one γ we find EIT conditions fulfilled. We hence sketch the results of the discussion in an effective Λ -scheme as shown in Fig. 5.3. The relevant “bare” states of the artificial molecule are given by the ground state in which no electric current is excited at all and an “upper” state corresponding to the current distribution of the electric resonance in the left SRR. These two states are coupled by the applied x -polarized electric field E_x . The third state of the Λ -scheme is represented by the magnetic resonance current distribution in the right SRR which is connected to the upper state

via the inductive coupling. In addition the coupling of electric and magnetic resonances at ω_0 of the right SRR is indicated.

Fig. 5.2(b) shows a measured spectrum of the absorption profile. Compared to the uncoupled case [Fig. 5.1(b)] we find a prominent dip in the absorption line which is typical for EIT. The separation of the two newly established absorption lines in combination with the depth of the absorption dip is too small to warrant an explanation on the lines of simple line splitting.

This results represent the first demonstration of EIT in metamaterials, a field which experiences a rapidly growing amount of interest. Of course these measurements display only a first step to low loss negative refraction metamaterials incorporating EIT. Future directions must contain a better understanding of the loss mechanisms of the various states depicted in Fig. 5.3. In particular it is not clear as to how strong the coupling between the magnetic and the still existing electric resonance in the right SRR is as well as how such a coupling influences the EIT performance. A good deal of work should be devoted to the development of new designs which incorporate ideas related to EIT [106] in order to connect with a negative index of refraction. In particular the fact that combined split ring resonators allow for magneto-electric cross-coupling tensors as, e.g.

$$\bar{\xi}_{EH} = \begin{pmatrix} 0 & 0 & \xi_{EH}^{xz} \\ 0 & 0 & \xi_{EH}^{yz} \\ 0 & 0 & 0 \end{pmatrix} \quad (5.1)$$

should be considered in detail regarding the possibility of inducing $\text{Re}[n] < 0$ without having the constraint $\text{Re}[\mu] < 0$ to be fulfilled.

Part II

Microscopic approach to local field corrections

CHAPTER 6

Macroscopic approach to local field corrections

Negative refraction requires a magnetic response of some sort. Either a magnetization has to be induced by magnetic fields, corresponding to a permeability μ as, e.g., in classic metamaterial experiments [5, 6] or due to a magneto-electric coupling effect [81, 82] (see part I). Another key point to media with a negative reactive index lies in the general need for the response to be rather large in order to overcome the vacuum contribution to the refractive index and obtain $\text{Re}[n] < 0$. It is known that a description in terms of macroscopic material response functions ceases to be adequate under such conditions. The most important correction due to microscopic theories for dielectric media which does not depend on the particular microscopic model of the material is the Clausius-Mossotti local field correction factor. In this chapter a quasi-macroscopic theory of virtual cavity local field correction factors is generalized to magneto-dielectric media which display a non-trivial magnetic permeability and the resultant effects of the combined local field corrections are discussed. It will be shown that local field contributions on a combined system of electric and magnetic resonances with an overlapping spectrum have, under certain conditions, a rather peculiar effect.

6.1 Introduction

The linear response of a medium composed of particles with a vacuum (electric) polarizability α is governed by the “local”, i.e., microscopic, field $\mathbf{E}_{\text{local}}$ which acts on the constituents rather than the averaged Maxwell field \mathbf{E}_M . Derivations of the local field acting on a particle in a solid located at \mathbf{r}_i usu-

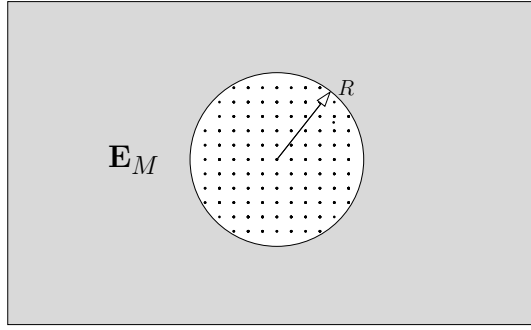


Figure 6.1: Virtual sphere separating the near zone from the far zone.

ally separate the surrounding material in a part far from \mathbf{r}_i which is treated macroscopically and the near vicinity treated in a microscopic fashion. This separation into near and far zones is most often done by introduction of a virtual sphere (cf. Fig. 6.1) with radius R which is supposed to be small compared to the characteristic length scale over which the averaged field \mathbf{E}_M changes. This length scale will in general be at least on the order of a wavelength but can also be given by, e.g., the absorption length. Thus $\mathbf{E}_{\text{local}}$ is composed of the averaged Maxwell field and a contribution due to scattering from surrounding particles

$$\mathbf{E}_{\text{local}}(\mathbf{r}_i) = \mathbf{E}_M(\mathbf{r}_i) + \sum_{j \neq i} \mathbf{E}^{ij}. \quad (6.1)$$

Here \mathbf{E}^{ij} denotes the field at \mathbf{r}_i scattered from particle “ j ” located inside the virtual cavity. This shows that the determination of the self-consistent scattering solution and therefore the local field presents a genuine many-body problem.

For dilute materials the contribution \mathbf{E}^{ij} is negligible due to large averaged separations between the constituents in the sphere with radius R . Thus

the induced atomic dipole moment in linear response is solely given by the averaged field $\mathbf{p} = \alpha \mathbf{E}_M$. Therefore for spectral regions far off resonance where the polarizability is small enough or a sufficiently small density of polarizable particles the permittivity ε is simply given by

$$\varepsilon(\omega) = 1 + 4\pi\varrho\alpha(\omega). \quad (6.2)$$

The polarizability $\alpha(\omega)$ is in general frequency dependent and ϱ denotes the number density of particles. Note further that the factor 4π stems from the usage of Gaussian units. For a vanishing $\alpha(\omega)$ (6.2) simplifies to $\varepsilon(\omega) = 1$ and thus to the case of propagation in vacuum.

In contrast the scattered field amplitude in dense media can differ significantly from the Maxwell field \mathbf{E}_M and is usually strongly space dependent on length scales of the average nearest neighbor distance. As (6.2) establishes a relation between the microscopic atomic or molecular polarizability $\alpha(\omega)$ and the macroscopic response function $\varepsilon(\omega)$ this issue naturally is not captured by the theory of macroscopic electrodynamics which deals with fields averaged over volumes which can contain a huge number of particles.

Surprisingly enough there are phenomenological treatments from a time at which not even the particle nature of matter has been established. Mossotti [107] and Clausius [108] independently calculated the dielectric constant of metallic particles embedded in dielectrics and Lorenz [109] and Lorentz [110] studied the corresponding refractive index¹. The result is hence named Clausius-Mossotti or Lorentz-Lorenz relation depending whether it is written in terms of the permittivity ε or the refractive index n of the medium in question.

Following a classical derivation of the local field effects for dielectric media [40, 111] we turn to a quantitative treatment. As noted above the local field (at any point) is decomposed as

$$\mathbf{E}_{\text{local}} = \mathbf{E}_M + \mathbf{E}_i \quad (6.3)$$

where the scattering contribution is summarized as an additional microscopic *internal* field \mathbf{E}_i . The surrounding medium is assumed to be divided by a

¹See [40, 111, 112].

virtual sphere into an inner and an outer part as discussed above. This cavity is assumed to be macroscopically small but still large enough to contain very many identically polarized atoms. Following the discussion above the term “macroscopically small” means that the macroscopic (averaged) polarization \mathbf{P} can be taken to be constant over the volume of the virtual cavity. To obtain the local field quantitatively we evaluate the field strength due to the polarized atoms inside the cavity for both a microscopic and a macroscopic model:

- (a) The atoms inside the cavity are considered to be arranged in a simple cubic lattice. As the cavity is microscopically large we can approximately assume an infinite lattice with a discrete translational invariance. Due to the macroscopically small radius of the cavity we furthermore assume the particles to be polarized equally both in magnitude and orientation.
- (b) The medium in the virtual cavity is treated macroscopically. Only the total dipole moment of the medium inside the cavity is known.

The internal field \mathbf{E}_i thus is given by the difference of the microscopic and the averaged macroscopic results:

$$\mathbf{E}_i = \mathbf{E}_{(a)} - \mathbf{E}_{(b)}. \quad (6.4)$$

The microscopic contribution $\mathbf{E}_{(a)}$ is determined by a summation of the field amplitudes due to the dipole radiation patterns of all individual dipoles of the infinite lattice which yields [40]

$$\mathbf{E}_{(a)} = 0 \quad (6.5)$$

due to the symmetry of the lattice. Note that the dipoles of the lattice are not supposed to interact with each other directly. In contrast $\mathbf{E}_{(b)}$ is given by the field strength inside a homogeneously polarized sphere with polarization \mathbf{P} [40]

$$\mathbf{E}_{(b)} = -\frac{4\pi}{3}\mathbf{P}. \quad (6.6)$$

The local field $\mathbf{E}_{\text{local}}$ is therefore given by

$$\mathbf{E}_{\text{local}} = \mathbf{E}_M + \frac{4\pi}{3}\mathbf{P}. \quad (6.7)$$

From that one can find the connection between the microscopic polarizability α and the susceptibility χ using the corresponding definitions of the polarization \mathbf{P} . Microscopically it is defined as the average induced atomic dipole moment which is proportional to the microscopic field strength $\mathbf{E}_{\text{local}}$

$$\mathbf{P} = \varrho \mathbf{p} = \varrho \alpha(\omega) \mathbf{E}_{\text{local}} = \varrho \alpha(\omega) \left(\mathbf{E}_M + \frac{4\pi}{3} \mathbf{P} \right) \quad (6.8)$$

while the macroscopic susceptibility is defined as the ratio of \mathbf{P} and the average field \mathbf{E}_M

$$\mathbf{P} = \chi(\omega) \mathbf{E}_M. \quad (6.9)$$

Here ϱ is the number density of atoms and \mathbf{p} is the induced atomic dipole moment. From (6.8) and (6.9) we readily find the sought local field correction to the susceptibility [40, 93]

$$\chi(\omega) = \frac{\varrho \alpha(\omega)}{1 - \frac{4\pi}{3} \varrho \alpha(\omega)}. \quad (6.10)$$

Equivalently the ratio $\mathbf{E}_{\text{local}}/\mathbf{E}_M$ of local and average field amplitudes can be expressed using $\varepsilon = 1 + 4\pi\chi$ as the Clausius-Mossotti local field factor

$$\mathcal{L}_{\text{CM}} = \frac{\varepsilon + 2}{3} \quad (6.11)$$

which is also named Lorentz-Lorenz or virtual cavity local field factor for the case $\varepsilon = n^2$.

It is instructive to discuss the emergence of local field effects in gaseous media. From chapter 7 it will become apparent that the Clausius-Mossotti relations are implicitly contained in the Green function given by

$$\mathcal{G}(\mathbf{r}, \mathbf{r}') = \mathcal{G}^{(0)}(\mathbf{r}, \mathbf{r}') + \sum_i \int d^3 \mathbf{r}_1 \mathcal{G}^{(0)}(\mathbf{r}, \mathbf{r}_1) V_i(\mathbf{r}_1) \mathcal{G}(\mathbf{r}_1, \mathbf{r}') \quad (6.12)$$

where V_i denotes the optical potential of the i th particle and $\mathcal{G}^{(0)}$ and \mathcal{G} denote the vacuum and full Green functions, respectively. As the positions of the scatterers in a gas are not fixed one usually transforms (6.12) into a non-discrete version using an averaged particle position distribution $p(\mathbf{r})$.

$$\begin{aligned} \mathcal{G}(\mathbf{r}, \mathbf{r}') &= \mathcal{G}^{(0)}(\mathbf{r}, \mathbf{r}') + V \int d^3 \mathbf{r}_1 p(\mathbf{r}_1) \mathcal{G}^{(0)}(\mathbf{r}, \mathbf{r}_1) \mathcal{G}^{(0)}(\mathbf{r}_1, \mathbf{r}') \\ &+ V^2 \int d^3 \mathbf{r}_1 d^3 \mathbf{r}_2 p(\mathbf{r}_1, \mathbf{r}_2) \mathcal{G}^{(0)}(\mathbf{r}, \mathbf{r}_1) \mathcal{G}^{(0)}(\mathbf{r}_1, \mathbf{r}_2) \mathcal{G}^{(0)}(\mathbf{r}_2, \mathbf{r}') + \dots \end{aligned} \quad (6.13)$$

The higher order terms are given by joint particle position probabilities, e.g., $p(\mathbf{r}_1, \mathbf{r}_2)$ to find particle 2 at position \mathbf{r}_2 under the condition that particle 1 is located at \mathbf{r}_1 . These joint probabilities separate into single particle probabilities

$$p(\mathbf{r}_1, \mathbf{r}_2) \approx p(\mathbf{r}_1)p(\mathbf{r}_2) \quad (6.14)$$

in good approximation which allows to simplify (6.13) for homogeneous single particle distributions to

$$\mathcal{G}(\mathbf{r}, \mathbf{r}') = \mathcal{G}^{(0)}(\mathbf{r}, \mathbf{r}') + \varrho V \int d^3 \mathbf{r}_1 \mathcal{G}^{(0)}(\mathbf{r}, \mathbf{r}_1) \mathcal{G}(\mathbf{r}_1, \mathbf{r}') \quad (6.15)$$

which can be solved for \mathcal{G} in Fourier space. This then yields expression (6.2) for the permittivity. The mistake made assuming (6.14) in a continuum description of the medium is for the case $\mathbf{r}_1 = \mathbf{r}_2$, i.e., for the spatial nullset for which 2 particles are physically on the same position. As this is not allowed the joint probability has to vanish on this nullset. One might naively argue that this should have no consequence as it affects only a nullset in coordinate space. The importance of this nullset stems from the δ -function in the vacuum Green function $\mathcal{G}^{(0)}$ (cf. Appendix A) which leads to a finite contribution. Removing the δ -contribution in $\mathcal{G}^{(0)}$ which effectively accounts for $p(\mathbf{r}, \mathbf{r}) = 0$ results in the local field factor (6.10) [113]. Thus local field effects are due to 2 particles being forbidden to take a single position which is automatically fulfilled for the lattice model used above.

Experimental tests of the validity of the local field factor (6.11) make use of the Purcell effect [114] named after E. M. Purcell who first claimed that the natural linewidth of atomic resonances depends on the radiative density of states. Most prominently this happens for emitters inside a resonant cavity [115] for which the Purcell effect has been first confirmed experimentally [116, 117, 118, 119, 120]. Similar to a resonator the mode spectrum of the electrodynamic vacuum is shaped as well by the presence of only one metallic or dielectric surface [121, 122, 123, 124, 125]².

In order to alter the radiative density of states fundamentally a simple dielectric medium suffices, however. For the case of decaying atoms embedded in a dielectric material with a permittivity ε and a refractive index $n = \sqrt{\varepsilon}$

²Cf. also part III.

the Purcell effect amounts to the correction of the spontaneous emission rate according to [126]

$$\Gamma = n\Gamma_0. \quad (6.16)$$

Here Γ denotes the radiative decay rate which is compared to the corresponding linewidth in vacuum Γ_0 . Additionally local field factors apply to (6.16) which have to be taken quadratically as the spontaneous decay rate is proportional the square of the electric field

$$\Gamma = n\mathcal{L}_{\text{CM}}^2\Gamma_0. \quad (6.17)$$

In addition to the virtual cavity local field correction factor \mathcal{L}_{CM} there is a second well known model which assumes a macroscopic dielectric medium with a real cavity of radius R in the center of which the particular atom is placed. One finds [127, Kästel2003]

$$\mathcal{L}_{\text{RC}} = \frac{3\varepsilon}{2\varepsilon + 1}. \quad (6.18)$$

Interestingly enough both local field factors are applicable depending on the system under examination. There are experimental reports which favor the virtual cavity model [128, 129, 130] but also experiments which use the real cavity correction factor [131, 132, 133]. As a bottomline, for pure media the virtual cavity model seems to be valid [134, 135] while the spontaneous decay of an atom of a different species embedded in a dielectric host material can be governed by either \mathcal{L}_{CM} or \mathcal{L}_{RC} depending on whether the impurity substitutes a host atom or is placed on an interstitial position [136, 137], respectively. Hence for pure media with a negative refractive index we have to consider Clausius-Mossotti virtual cavity local field correction factors as well (cf. section 3.5).

6.2 Magneto-dielectric materials

As opposed to pure dielectrics, there is only little literature [93] about pure magnetic media. As electric and magnetic effects in linear response are connected by means of a duality transformation, pure magnetic materials with

a permeability μ are governed by a similar Clausius-Mossotti relation with the electric polarizability α_e replaced by the magnetizability α_m .

Even more general materials which involve electric and magnetic subsystems simultaneously and thus are crucial to the understanding of negative refraction have, to our knowledge, not been treated. Since in classical macroscopic electrodynamics the problems for the electric and the magnetic degrees of freedom separate, Clausius-Mossotti relations have to be applied independently. In order to understand the differences to pure media arising from this treatment let us first consider a purely dielectric medium with a polarizability

$$\alpha_e(\omega) = \alpha'_e(\omega) + i \alpha''_e(\omega) \quad (6.19)$$

which does not depend on the density. In particular let us assume that the linewidth of $\alpha_e(\omega)$ is density independent and the medium is radiatively broadened. Using (6.19) the high density limit of the permittivity $\varepsilon = 1 + 4\pi\chi(\omega)$ including Clausius-Mossotti local field corrections (6.10) is found to be

$$\varepsilon(\omega) \xrightarrow{\varrho \rightarrow \infty} -2 + i \frac{9\alpha''_e(\omega)}{4\pi|\alpha_e(\omega)|^2} \varrho^{-1}. \quad (6.20)$$

We note that for sufficiently high densities the response saturates at a value of -2 while the imaginary part vanishes as $1/\varrho$. Thus the corresponding refractive index will attain a purely imaginary value $n = i\sqrt{2}$, i.e., the local field corrections ensure that high densities lead to increasing absorption and ultimately to the emergence of a stop band for which the medium becomes totally opaque.

In order to analyze this general result in more detail we assume a single resonance polarizability

$$\alpha_e(\omega) = \frac{1}{2\hbar} \frac{d^2}{\Delta - i\gamma} \quad (6.21)$$

as in (2.3). The effect of virtual cavity local field factors to the macroscopic response then amounts to

$$\varepsilon(\omega) = 1 + 4\pi \frac{d^2 \varrho}{2\hbar(\Delta - \Delta_L - i\gamma)} \quad (6.22)$$

with the density dependent Lorentz frequency shift $\Delta_L = \frac{4\pi}{3} \frac{d^2}{2\hbar} \varrho$ [138]. The detuning is given by $\Delta = \omega_0 - \omega$ where ω_0 denotes the atomic resonance

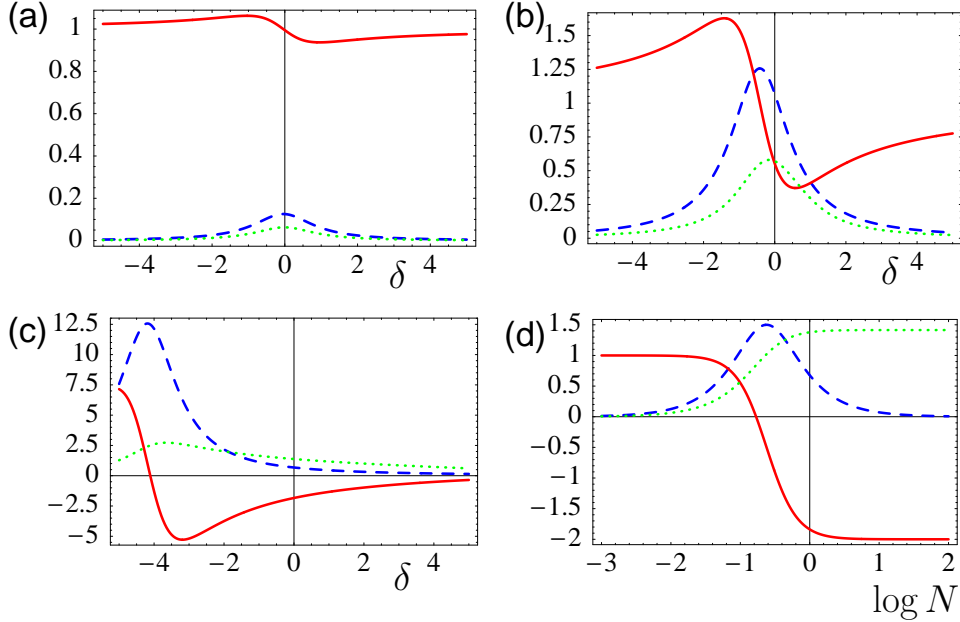


Figure 6.2: Real (solid) and imaginary (dashed) parts of the permittivity $\varepsilon(\omega)$ as well as the imaginary (dotted) part of $n(\omega) = \sqrt{\varepsilon(\omega)}$. Figures (a), (b), and (c) show spectra as a function of the detuning δ for (a) $N = 0.01$, (b) $N = 0.1$, and (c) $N = 1$ while (d) shows the dependence of $\varepsilon(0)$ and $n(0)$ on the rescaled density parameter N .

frequency. Figure 6.2(a) shows a spectrum of (6.22) as well as $\text{Im}[n(\omega)] = \text{Im}[\sqrt{\varepsilon(\omega)}]$ as a function of the dimensionless detuning $\delta = -\Delta/\gamma$ for the rescaled (dimensionless) density parameter $N = d^2\varrho/(2\hbar\gamma) = 0.01$, i.e., in the linear limit for which local field corrections do not contribute significantly. In Figures 6.2(b) and 6.2(c) similar spectra are shown for $N = d^2\varrho/(2\hbar\gamma) = 0.1$ and $N = d^2\varrho/(2\hbar\gamma) = 1$, respectively. We observe that, as soon as the response differs significantly from 1, the resonance shifts to lower energies due to the Lorentz shift while the strength of the response increases due to the fundamental dependence of $\varepsilon(\omega)$ on the density ϱ . As a result the values of the permittivity and the index of refraction attain the values $\varepsilon(0) = -2$ and $n(0) = i\sqrt{2}$ with increasing density as shown in 6.2(d). We note that the absorption $\text{Im}[n(\omega)]$ increases monotonically with increasing density. We

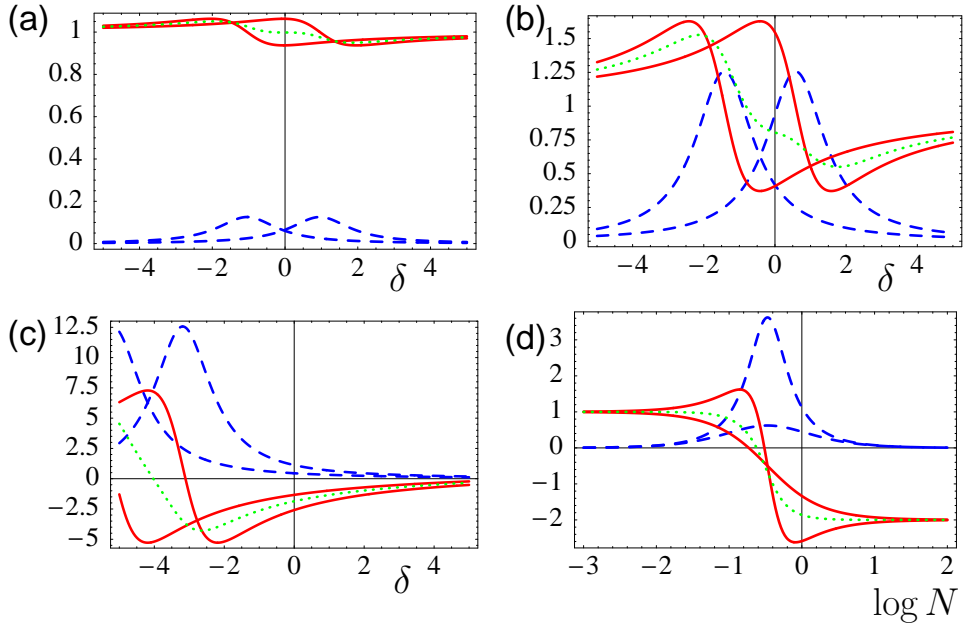


Figure 6.3: Real (solid) and imaginary (dashed) parts of the permittivity $\epsilon(\omega)$ and the permeability $\mu(\omega)$ as well as the imaginary (dotted) part of $n(\omega) = \sqrt{\epsilon(\omega)\mu(\omega)}$. Figures (a), (b), and (c) show spectra³ as a function of the detuning δ for (a) $N = 0.01$, (b) $N = 0.1$, and (c) $N = 1$ while (d) shows the dependence of the response functions $\epsilon(0)$ and $\mu(0)$ as well as $n(0)$ on the rescaled density parameter N .

stress again that this analysis does not depend on the nature of the resonance and thus is valid for magnetic resonances as well.

If the Clausius-Mossotti relations are assumed to apply independently to the electric and magnetic subsystems a dramatic change occurs for media with overlapping electric and magnetic resonances. Denoting the magnetizability by $\alpha_m(\omega) = \alpha'_m(\omega) + i\alpha''_m(\omega)$ yields an identical limiting behavior of the permeability for high densities compared to (6.20). Hence both the permittivity and the permeability asymptotically attain values of $\epsilon = -2$ and $\mu = -2$ independently. In contrast to pure media this does not lead to strong absorption, though, but rather to a negative refractive index with

vanishing absorption for increasing densities

$$n(\omega) = -2 + i \left(\frac{9\alpha_e''(\omega)}{8\pi|\alpha_e(\omega)|^2} + \frac{9\alpha_m''(\omega)}{8\pi|\alpha_m(\omega)|^2} \right) \varrho^{-1}. \quad (6.23)$$

This quite peculiar behavior is illustrated in Figs. 6.3(a)–(c) which show the spectra of a permittivity and permeability with a spectral overlap³. The Lorentz shift applies independently to both degrees of freedom. Hence when both material functions develop negative real values the index of refraction becomes negative as well. Figure 6.3(d) shows the density dependence of the material functions taken at zero detuning. It is apparent that due to the Lorentz shift with simultaneous increase of the response strength the refractive index attains $n = -2 + i0$ in the limit of high densities.

In conclusion, an increase of the number density of scatterers leads to a decrease of absorption. This most unexpected behavior seems unphysical and demands a more profound investigation on the basis of a purely microscopic model.

³ It is not relevant which resonance line is assumed to be the magnetic one.

CHAPTER 7

Microscopic model of local field corrections in dielectric media

As mentioned above the derivation of local field corrections is a genuine many-body problem, which is an aspect not considered in the macroscopic treatment of chapter 6, and hence is not capable of a satisfactory support of the result of section 6.2. In addition it does not give any information about the kind of polarizability $\alpha(\omega)$ that has to enter the macroscopic permittivity (6.10) for the case of dense media. One might expect to find a polarizability dressed by the surrounding medium.

In order to address these questions we will present in the following two different microscopic derivations of local field effects in dielectrics which include many-body physics: The solution of the electromagnetic multiple scattering problem of a lattice model and the solution of the Heisenberg equations of motion for the electric and magnetic field operators in reciprocal space. Both models will be needed for a subsequent generalization to magnetic and magneto-dielectric media.

7.1 Formal considerations

In order to describe dielectric materials microscopically and thus include many-body effects we consider a simple cubic lattice of atoms with an electric

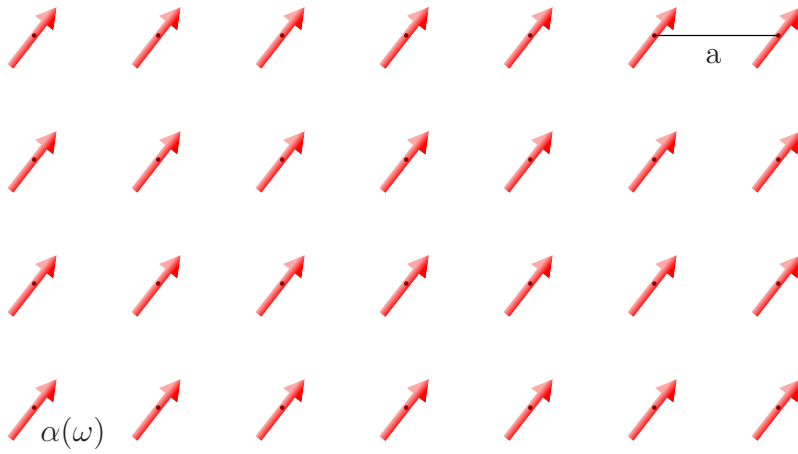


Figure 7.1: Microscopic model of a pure dielectric material. Polarizable particles with a polarizability $\alpha(\omega)$ form a simple cubic lattice with lattice constant a .

dipole moment $\alpha(\omega)$ (Fig. 7.1). Note that we assume any effects of permanent dipole moments to vanish exactly. The connection between the electric field $\mathbf{E}(\mathbf{r}, \omega)$ and the Polarization $\mathbf{P}(\mathbf{r}, \omega)$ in linear response approximation can be written

$$\mathbf{P}(\mathbf{r}, \omega) = \alpha(\mathbf{r}, \omega)\mathbf{E}(\mathbf{r}, \omega) \quad (7.1)$$

with a dimensionless function $\alpha(\mathbf{r}, \omega)$. Note that $\alpha(\mathbf{r}, \omega)$ fulfills the relation $\alpha(\mathbf{r}, \omega) = \alpha(\mathbf{r} + \mathbf{R}, \omega)$ for any lattice vector $\mathbf{R} = a(n\mathbf{e}_x + m\mathbf{e}_y + l\mathbf{e}_z)$ of the simple cubic lattice. Here a is the lattice constant of the simple cubic lattice and $\{n, m, l\}$ are integer numbers. Note further that the \mathbf{r} -dependent function $\alpha(\mathbf{r}, \omega)$ is not the polarizability of the atoms but generalizes the factor $\varrho\alpha(\omega)$ in (6.8).

In order to find the dispersion relation $\mathbf{k}(\omega)$ and thus the refractive index including local field effects we continue by formulating the basic equation governing the electromagnetic many-body problem in terms of a Helmholtz equation. To do so we start with the Heisenberg equations for the electric and magnetic field operators in dielectric media which are given by Maxwell's

equations

$$\begin{aligned}\nabla \cdot \hat{\mathbf{B}}(\mathbf{r}, t) &= 0, \\ \nabla \cdot \hat{\mathbf{D}}(\mathbf{r}, t) &= 4\pi\hat{\varrho}(\mathbf{r}, t)\end{aligned}\tag{7.2}$$

as well as

$$\begin{aligned}\nabla \times \hat{\mathbf{E}}(\mathbf{r}, t) + \frac{1}{c} \frac{\partial}{\partial t} \hat{\mathbf{B}}(\mathbf{r}, t) &= 0, \\ \nabla \times \hat{\mathbf{H}}(\mathbf{r}, t) - \frac{1}{c} \frac{\partial}{\partial t} \hat{\mathbf{D}}(\mathbf{r}, t) &= \frac{4\pi}{c} \hat{\mathbf{j}}(\mathbf{r}, t).\end{aligned}\tag{7.3}$$

Here $\hat{\varrho}(\mathbf{r}, t)$ and $\hat{\mathbf{j}}(\mathbf{r}, t)$ are the charge density and current density operators of the free sources, respectively. We Fourier transform (7.2) and (7.3) with respect to time which, along with $\hat{\mathbf{H}}(\mathbf{r}, \omega) = \hat{\mathbf{B}}(\mathbf{r}, \omega)$ for dielectric media, which yields

$$\begin{aligned}\nabla \cdot \hat{\mathbf{B}}(\mathbf{r}, \omega) &= 0, \\ \nabla \cdot \hat{\mathbf{D}}(\mathbf{r}, \omega) &= 4\pi\hat{\varrho}(\mathbf{r}, \omega),\end{aligned}\tag{7.4}$$

$$\begin{aligned}\nabla \times \hat{\mathbf{E}}(\mathbf{r}, \omega) - i\frac{\omega}{c} \hat{\mathbf{B}}(\mathbf{r}, \omega) &= 0, \\ \nabla \times \hat{\mathbf{B}}(\mathbf{r}, \omega) + i\frac{\omega}{c} \hat{\mathbf{D}}(\mathbf{r}, \omega) &= \frac{4\pi}{c} \hat{\mathbf{j}}(\mathbf{r}, \omega).\end{aligned}\tag{7.5}$$

Utilizing the continuity equation in Fourier space $i\omega\hat{\varrho}(\mathbf{r}, \omega) = \nabla \cdot \hat{\mathbf{j}}(\mathbf{r}, \omega)$, equations (7.4) follow immediately from (7.5). Eliminating the magnetic field $\hat{\mathbf{B}}(\mathbf{r}, \omega)$ from (7.5) and letting $\hat{\mathbf{D}}(\mathbf{r}, \omega) = \hat{\mathbf{E}}(\mathbf{r}, \omega) + 4\pi\hat{\mathbf{P}}(\mathbf{r}, \omega)$ thus leads to the vectorial Helmholtz equation

$$\nabla \times \nabla \times \hat{\mathbf{E}}(\mathbf{r}, \omega) - \frac{\omega^2}{c^2} \hat{\mathbf{E}}(\mathbf{r}, \omega) = 4\pi i \frac{\omega}{c^2} \hat{\mathbf{j}}(\mathbf{r}, \omega) + 4\pi \frac{\omega^2}{c^2} \hat{\mathbf{P}}(\mathbf{r}, \omega)\tag{7.6}$$

which in the following serves as a starting point for the determination of the dispersion relation $\mathbf{k}(\omega)$ and thus the local field corrections to the linear response. As $\alpha(\mathbf{r}, \omega)$ is assumed to model the microscopic spatial positions of electrically polarizable particles as well as corresponding atomic charge densities, $\hat{\mathbf{E}}(\mathbf{r}, \omega)$ represents the microscopic electric field including many-body scattering contributions.

7.2 Multiple scattering in real space

As we will see, one way to solve (7.6) in general is the use of Green function techniques within a multiple scattering formalism. We thus introduce the complex valued classical Green tensor $\mathcal{G}(\mathbf{r}, \mathbf{r}', \omega)$ which relates the electric field operator $\hat{\mathbf{E}}(\mathbf{r}, \omega)$ at \mathbf{r} with the source current density at position \mathbf{r}'

$$\hat{\mathbf{E}}(\mathbf{r}, \omega) = -4\pi i \frac{\omega}{c^2} \int d^3 \mathbf{r}' \mathcal{G}(\mathbf{r}, \mathbf{r}', \omega) \hat{\mathbf{j}}(\mathbf{r}', \omega). \quad (7.7)$$

We emphasize that unless we restrict to some particular polarization $\mathcal{G} \equiv \mathcal{G}_{ij}$ is in general a tensorial function. As discussed earlier for linear media the polarization operator $\hat{\mathbf{P}}(\mathbf{r}, \omega)$ is related to the electric field operator via

$$\hat{\mathbf{P}}(\mathbf{r}, \omega) = \alpha(\mathbf{r}, \omega) \hat{\mathbf{E}}(\mathbf{r}, \omega). \quad (7.8)$$

Here only the electromagnetic field is treated quantum mechanically. The dynamics of each atom of the lattice is assumed to be already solved independently and its effect is summarized in the *c*-number polarizability $\alpha(\omega)$. As this restricts the approach to the perturbative linear response limit and assumes fixed positions of the scatterers, cooperative effects such as super- and subradiance [139, 140] as well as effects due to center of mass properties of the atoms like atomic scattering and phonons which represent effective broadening mechanisms in solid state physics are not contained in the theory. The many-body aspects are reduced to electromagnetic back-action due to scattering of photons which suffices to describe local field corrections. Note that $\alpha(\mathbf{r}, \omega)$ is in general a tensorial, complex-valued function of space and frequency.

We insert (7.7) together with (7.8) into (7.6) which results in the classical Helmholtz equation for the tensor Green function $\mathcal{G}(\mathbf{r}, \mathbf{r}', \omega)$

$$\left[\frac{\omega^2}{c^2} \mathbb{1} - \nabla^{\mathbf{r}} \times \nabla^{\mathbf{r}} \times \right] \mathcal{G}(\mathbf{r}, \mathbf{r}', \omega) = \delta(\mathbf{r} - \mathbf{r}') \mathbb{1} - 4\pi \frac{\omega^2}{c^2} \alpha(\mathbf{r}, \omega) \mathcal{G}(\mathbf{r}, \mathbf{r}', \omega). \quad (7.9)$$

Note that the coefficient in (7.7) has been chosen such that only a $\delta(\mathbf{r} - \mathbf{r}')$ contribution remains from the source current density $\hat{\mathbf{j}}(\mathbf{r}, \omega)$ and that the sign on the left hand side complies with the convention of [134]. Note again that (7.9) contains no quantum mechanical operators. Thus the Green function

formalism combined with the approximations mentioned above allows one to map the quantum mechanical to a purely classical problem.

7.2.1 General solution

In the following we show that the general solution of (7.9) naturally leads to an interpretation in terms of multiple scattering, even for the simple case of a single scatterer in vacuum. We first note that the full Green function $\mathcal{G}(\mathbf{r}, \mathbf{r}', \omega)$ fulfills a Dyson equation

$$\mathcal{G}(\mathbf{r}, \mathbf{r}', \omega) = \mathcal{G}^{(0)}(\mathbf{r} - \mathbf{r}', \omega) - 4\pi \frac{\omega^2}{c^2} \int d^3\mathbf{r}_1 \mathcal{G}^{(0)}(\mathbf{r} - \mathbf{r}_1, \omega) \alpha(\mathbf{r}_1, \omega) \mathcal{G}(\mathbf{r}_1, \mathbf{r}', \omega) \quad (7.10)$$

which can be seen immediately from the Helmholtz equation (7.9). Unfortunately $\mathcal{G}(\mathbf{r}, \mathbf{r}', \omega)$ is determined by (7.10) only through an integral relation in terms of $\alpha(\mathbf{r}, \omega)$ and the vacuum Green function¹ $\mathcal{G}^{(0)}(\mathbf{r} - \mathbf{r}', \omega)$. Hence, (7.10) in general demands a self-consistent treatment. For the sake of generality we define the optical potential $V(\mathbf{r}, \mathbf{r}', \omega) = -4\pi \frac{\omega^2}{c^2} \alpha(\mathbf{r}, \omega) \delta(\mathbf{r} - \mathbf{r}')$ such that (7.10) reads

$$\mathcal{G}(\mathbf{r}, \mathbf{r}', \omega) = \mathcal{G}^{(0)}(\mathbf{r} - \mathbf{r}', \omega) + \iint d^3\mathbf{r}_1 d^3\mathbf{r}_2 \mathcal{G}^{(0)}(\mathbf{r} - \mathbf{r}_1, \omega) V(\mathbf{r}_1, \mathbf{r}_2, \omega) \mathcal{G}(\mathbf{r}_2, \mathbf{r}', \omega). \quad (7.11)$$

To interpret the aspects of multiple scattering equation (7.11) is frequently represented graphically in terms of diagrams

$$\begin{array}{c} \mathbf{r} \quad \mathbf{r}' \\ \hline \hline \end{array} = \begin{array}{c} \mathbf{r} \quad \mathbf{r}' \\ \hline \end{array} + \begin{array}{c} \mathbf{r} \quad \mathbf{r}' \\ \hline \mathbf{r}_1 \quad \mathbf{r}_2 \quad \hline \end{array} \quad (7.12)$$

where $\begin{array}{c} \mathbf{r} \quad \mathbf{r}' \\ \hline \hline \end{array}$ and $\begin{array}{c} \mathbf{r} \quad \mathbf{r}' \\ \hline \end{array}$ denote the full and vacuum Green tensors $\mathcal{G}(\mathbf{r}, \mathbf{r}', \omega)$ and $\mathcal{G}^{(0)}(\mathbf{r}, \mathbf{r}', \omega)$, respectively, while the optical potential $V(\mathbf{r}, \mathbf{r}', \omega)$ is denoted by $\begin{array}{c} \mathbf{r} \quad \mathbf{r}' \\ \bullet \quad \bullet \end{array}$.

In order to investigate (7.11) systematically we introduce a notation similar to Dirac's brackets of quantum mechanics. This allows us to formulate the theory in a coordinate independent manner which simplifies the amount of algebra significantly. To this end we interpret all constituents of (7.11) as

¹Cf. Appendix A.

operators of an abstract Hilbert space, e.g., $\hat{\mathcal{G}}(\omega)$, $\hat{V}(\omega)$ etc. The corresponding representations in real space are then given by a scalar product with real space state vectors $|\mathbf{r}\rangle$. In particular

$$V(\mathbf{r}, \mathbf{r}', \omega) = \langle \mathbf{r} | \hat{V}(\omega) | \mathbf{r}' \rangle \quad (7.13)$$

leads to the aforementioned definition of the optical potential since $\hat{V}(\omega) = -4\pi \frac{\omega^2}{c^2} \hat{\alpha}(\omega)$ is diagonal in real space

$$\hat{V}(\omega) |\mathbf{r}\rangle = -4\pi \frac{\omega^2}{c^2} \alpha(\mathbf{r}, \omega) |\mathbf{r}\rangle \quad (7.14)$$

and the state vectors $|\mathbf{r}\rangle$ fulfill

$$\langle \mathbf{r} | \mathbf{r}' \rangle = \delta(\mathbf{r} - \mathbf{r}'). \quad (7.15)$$

The operator $\hat{\mathcal{G}}(\omega)$ of the Green function² relates the state of the current density to the state of the electric field

$$\left| \hat{\mathbf{E}}(\omega) \right\rangle = -4\pi i \frac{\omega}{c^2} \hat{\mathcal{G}}(\omega) \left| \hat{\mathbf{j}}(\omega) \right\rangle \quad (7.16)$$

which evaluates to (7.7) under a projection onto real space. This follows from

$$\hat{\mathbf{E}}(\mathbf{r}, \omega) = \left\langle \mathbf{r} \left| \hat{\mathbf{E}}(\omega) \right\rangle \right\rangle \quad (7.17)$$

and the completeness relation

$$\int d^3\mathbf{r} |\mathbf{r}\rangle \langle \mathbf{r}| = \mathbb{1}. \quad (7.18)$$

Following these guidelines the coordinate free version of the integral equation (7.11) reads

$$\hat{\mathcal{G}}(\omega) = \hat{\mathcal{G}}^{(0)}(\omega) + \hat{\mathcal{G}}^{(0)}(\omega) \hat{V}(\omega) \hat{\mathcal{G}}(\omega) \quad (7.19)$$

which is sketched in a similar way as above.

$$\text{Diagram: Two horizontal lines with arrows pointing right.} = \text{Diagram: One horizontal line with arrow pointing right.} + \text{Diagram: Two horizontal lines with arrows pointing right, and a vertical line connecting them.} \quad (7.20)$$

²We observe that all such representation independent operators are elements of just one abstract Hilbert space. This concept thus serves only as a means to simplify the algebra.

Note that in contrast to (7.12) no coordinates appear. On the same lines (7.19) can be used to find the Fourier representation by evaluating the corresponding matrix elements.

Unlike the real space version (7.11), the abstract form (7.19) gives a closed formula for the full Green function $\hat{\mathcal{G}}(\omega)$. Instead of straightforwardly solving (7.19) for $\hat{\mathcal{G}}(\omega)$ it is instructive to obtain the result by iteration which yields

$$\hat{\mathcal{G}}(\omega) = \hat{\mathcal{G}}^{(0)}(\omega) + \hat{\mathcal{G}}^{(0)}(\omega)\hat{V}(\omega)\hat{\mathcal{G}}^{(0)}(\omega) + \hat{\mathcal{G}}^{(0)}(\omega)\hat{V}(\omega)\hat{\mathcal{G}}^{(0)}(\omega)\hat{V}(\omega)\hat{\mathcal{G}}^{(0)}(\omega) + \dots \quad (7.21)$$

This can be cast in the form

$$\hat{\mathcal{G}}(\omega) = \hat{\mathcal{G}}^{(0)}(\omega) + \hat{\mathcal{G}}^{(0)}(\omega)\hat{T}(\omega)\hat{\mathcal{G}}^{(0)}(\omega) \quad (7.22)$$

which serves as the definition of the scattering T -matrix

$$\hat{T}(\omega) = \hat{V}(\omega) + \hat{V}(\omega)\hat{\mathcal{G}}^{(0)}(\omega)\hat{V}(\omega) + \dots \quad (7.23)$$

of the system which is entirely given by the known optical potential $\hat{V}(\omega)$ and the vacuum Green function $\hat{\mathcal{G}}^{(0)}(\omega)$. In the diagram representation equation (7.22) reads

$$\text{---} \bullet \text{---} = \text{---} \bullet \text{---} + \text{---} \bullet \text{---} \square \text{---} \bullet \text{---}$$

where the rectangular box represents the T -matrix. This equation is straightforwardly interpreted. The propagation of an electromagnetic wave in a polarizable medium [$\hat{\mathcal{G}}(\omega)$] is given by a vacuum contribution [$\hat{\mathcal{G}}^{(0)}(\omega)$] and a scattering part which consists of a vacuum propagation scattered at the lattice followed by yet another propagation in vacuum. The direction and amplitude of the scattering are contained in the T -matrix which we denote as an empty square and which is given entirely by the optical potential $\hat{V}(\omega)$ and the vacuum propagator

$$\square = \bullet + \bullet \text{---} \bullet + \bullet \text{---} \bullet \text{---} \bullet + \dots \quad (7.24)$$

Thus from (7.24) we see that the effective scattering T -matrix can be interpreted as an infinite superposition of fundamental scattering events to all orders in the optical potential $\hat{V}(\omega)$, hence the term multiple scattering. This is a characteristic feature which is already found in classical problems, e.g.,

the transmission properties of a Fabry-Perot interferometer can be explained by an infinite superposition of multiple reflections (scattering events) at the mirrors [141].

We conclude the general treatment by noting that the geometric sum appearing in (7.23) can be summed formally to a closed formula for the scattering T -matrix

$$\hat{T}(\omega) = \hat{V}(\omega) \sum_{n=0}^{\infty} \left[\hat{\mathcal{G}}^{(0)}(\omega) \hat{V}(\omega) \right]^n = \hat{V}(\omega) \left[\mathbb{1} - \hat{\mathcal{G}}^{(0)}(\omega) \hat{V}(\omega) \right]^{-1}. \quad (7.25)$$

Similarly the full Green function $\hat{\mathcal{G}}(\omega)$ is given by³

$$\hat{\mathcal{G}}(\omega) = \left[\mathbb{1} - \hat{\mathcal{G}}^{(0)}(\omega) \hat{V}(\omega) \right]^{-1} \hat{\mathcal{G}}^{(0)}(\omega). \quad (7.26)$$

Hence the solution of the full scattering problem and therefore the Helmholtz equation (7.6) can be expressed in terms of $\hat{\mathcal{G}}(\omega)$ or $\hat{T}(\omega)$, respectively. Unfortunately a particular representation of the operator $\left[\mathbb{1} - \hat{\mathcal{G}}^{(0)}(\omega) \hat{V}(\omega) \right]^{-1}$ can be obtained analytically only for systems with a high intrinsic symmetry.

7.2.2 Single scatterer

The most fundamental example of a system for which the inverse operator $\left[\mathbb{1} - \hat{\mathcal{G}}^{(0)}(\omega) \hat{V}(\omega) \right]^{-1}$ can be obtained analytically is a single point-like scatterer located at \mathbf{r}_A in free space (vacuum). To find the full Green function as well as the scattering T -matrix we separate $\alpha(\mathbf{r}, \omega)$ in the frequency dependent polarizability $\alpha(\omega)$ and a space dependent term which for a point-like particle is given by a single Dirac delta-function

$$\alpha(\mathbf{r}, \omega) = \alpha(\omega) \delta(\mathbf{r} - \mathbf{r}_A). \quad (7.27)$$

With (7.14) and (7.18) we find for the single particle scattering T -matrix⁴ $t(\mathbf{r}, \mathbf{r}', \omega) = \langle \mathbf{r} | \hat{T}(\omega) | \mathbf{r}' \rangle$ from equation (7.25)

$$t(\mathbf{r}, \mathbf{r}', \omega) = \int d^3 \mathbf{r}_1 \langle \mathbf{r} | \hat{V}(\omega) | \mathbf{r}_1 \rangle \langle \mathbf{r}_1 | \sum_{n=0}^{\infty} \left[\hat{\mathcal{G}}^{(0)}(\omega) \hat{V}(\omega) \right]^n | \mathbf{r}' \rangle. \quad (7.28)$$

³Cf. equation (7.19).

⁴which we denote by a small t

The recursive application of

$$\langle \mathbf{r}_1 | \hat{\mathcal{G}}^{(0)}(\omega) \hat{V}(\omega) | \mathbf{r}_2 \rangle = \mathcal{G}^{(0)}(\mathbf{r}_1 - \mathbf{r}_A, \omega) V(\omega) \delta(\mathbf{r}_2 - \mathbf{r}_A) \quad (7.29)$$

then yields for the T -matrix

$$t(\mathbf{r}, \mathbf{r}', \omega) = V(\omega) [\mathbb{1} - V(\omega) \mathcal{G}^{(0)}(0, \omega)]^{-1} \delta(\mathbf{r} - \mathbf{r}_A) \delta(\mathbf{r}' - \mathbf{r}_A). \quad (7.30)$$

Here $V(\omega) = -4\pi \frac{\omega^2}{c^2} \alpha(\omega)$ [note the difference to the operator $\hat{V}(\omega)$] is the frequency dependent optical potential of the point scatterer. Like $\alpha(\mathbf{r}, \omega)$ the T -matrix can thus be separated into a space dependent and a dispersive part:

$$t(\mathbf{r}, \mathbf{r}', \omega) = t(\omega) \delta(\mathbf{r} - \mathbf{r}_A) \delta(\mathbf{r}' - \mathbf{r}_A) \quad (7.31)$$

with

$$t(\omega) = \frac{1}{V(\omega)^{-1} \mathbb{1} - \mathcal{G}^{(0)}(0, \omega)}. \quad (7.32)$$

The corresponding full Green function $\mathcal{G}(\mathbf{r}, \mathbf{r}', \omega)$ is found immediately from (7.22) and reads

$$\mathcal{G}(\mathbf{r}, \mathbf{r}', \omega) = \mathcal{G}^{(0)}(\mathbf{r} - \mathbf{r}', \omega) + t(\omega) \mathcal{G}^{(0)}(\mathbf{r} - \mathbf{r}_A, \omega) \mathcal{G}^{(0)}(\mathbf{r}_A - \mathbf{r}', \omega). \quad (7.33)$$

Thus a field generated at point \mathbf{r}' and observed at \mathbf{r} consists of the unperturbed (vacuum) propagation interfering with a term which stems from a free propagation to the point-like atom located at \mathbf{r}_A from where it is scattered with an amplitude $t(\omega)$ to the detector which is placed at \mathbf{r} .

Note that only the use of a point-like scatterer allows to sum the T -matrix exactly. As a drawback the T -matrix incorporates the vacuum Green function taken at the origin $\mathcal{G}^{(0)}(0, \omega)$ which is divergent [134] and thus leads to an unphysically vanishing T -matrix. One way to obtain finite physical quantities is to regularize $\mathcal{G}^{(0)}(\mathbf{r}, \omega)$ by introducing cut-off parameters Λ_T and Λ_L in reciprocal space for the transverse and longitudinal parts of the Green function, respectively. In order to find the physical T -matrix the additionally emerging terms due to the cut-off parameters need to be interpreted along the lines of some atomic model with a finite support [134] instead of pointlike particles. Unfortunately the regularization procedure is not unique and as a result the T -matrix is not unique as well. This leaves unwanted ambiguities which do not allow for a comparison to experimental data.

This discrepancy is solved by the assumption that the potential $V(\omega)$ and likewise the polarizability $\alpha(\omega)$ of a mathematical point particle do not belong to physical reality but are just unphysical notions which are commonly denoted by the term “bare” potential and “bare” polarizability, respectively. Only the sum of the unphysical inverse potential and the unphysical divergent Green function $\mathcal{G}^{(0)}(0, \omega)$ gives the real, observable potential

$$\tilde{V}(\omega)^{-1} = V(\omega)^{-1} \mathbb{1} - \mathcal{G}^{(0)}(0, \omega) \quad (7.34)$$

which we denote by a tilde. Correspondingly the physical polarizability $\tilde{\alpha}(\omega)$ reads

$$\tilde{\alpha}(\omega)^{-1} = -4\pi \frac{\omega^2}{c^2} \tilde{V}(\omega)^{-1}. \quad (7.35)$$

The T -matrix hence is now identical to the physical potential

$$t(\omega) = \tilde{V}(\omega). \quad (7.36)$$

Thus the interpretation of the T -matrix in terms of multiple scattering events is only valid for the bare potential. The renormalized scattering amplitude of a single physical scattering event emerges as multiple scattering series of bare events.

7.2.3 Simple cubic lattice of point dipoles

Having solved the scattering problem for a single particle we will next consider a whole lattice of point-like scatterers following [134]. The dispersion relation, which contains information about local field corrections for dense media, will then be given by the T -matrix.

We assume a simple cubic lattice of point dipoles like the ones from section 7.2.2. Again $\alpha(\mathbf{r}, \omega)$ separates in the polarizability $\alpha(\omega)$ which is assumed to be identical for all lattice sites and a lattice function

$$\alpha(\mathbf{r}, \omega) = \alpha(\omega) \sum_{\mathbf{R}} \delta(\mathbf{r} - \mathbf{R}). \quad (7.37)$$

The lattice vectors \mathbf{R} of the simple cubic lattice are given by $\mathbf{R} \equiv \mathbf{R}_{nml} = a(n\mathbf{e}_x + m\mathbf{e}_y + l\mathbf{e}_z)$ for integer $\{n, m, l\}$. In contrast to the case of just one scatterer here the system has a discrete translational symmetry

$$\alpha(\mathbf{r} + \mathbf{R}, \omega) = \alpha(\mathbf{r}, \omega) \quad (7.38)$$

for any lattice vector \mathbf{R} . We therefore introduce a reciprocal wave vector $\tilde{\mathbf{k}} = \mathbf{k} - \mathbf{K}$ which separates into a contribution \mathbf{k} from the first Brillouin zone (1.BZ) and a reciprocal lattice vector \mathbf{K} . The reciprocal lattice vectors are defined by $\mathbf{R} \cdot \mathbf{K} = 2\pi m$ with an integer number m and form a simple cubic lattice themselves with lattice constant $2\pi/a$. Note that the sign of \mathbf{K} has been chosen such that our definition corresponds to [134]. The completeness relation in reciprocal space can hence be written

$$\begin{aligned} \mathbb{1} &= \int_{\mathbb{R}^3} d^3 \tilde{\mathbf{k}} |\tilde{\mathbf{k}}\rangle \langle \tilde{\mathbf{k}}| = \sum_{\mathbf{K}} \int_{V_{\mathbf{k}-\mathbf{K}}} d^3 \tilde{\mathbf{k}} |\tilde{\mathbf{k}}\rangle \langle \tilde{\mathbf{k}}| \\ &= \sum_{\mathbf{K}} \int_{V_{\mathbf{k}}} d^3 \mathbf{k} |\mathbf{k} - \mathbf{K}\rangle \langle \mathbf{k} - \mathbf{K}|. \end{aligned} \quad (7.39)$$

Here $V_{\mathbf{k}}$ denotes the volume of the first Brillouin zone and $V_{\mathbf{k}-\mathbf{K}}$ the same volume but centered around $-\mathbf{K}$. We thus express the electric field by its Fourier components

$$\begin{aligned} \hat{\mathbf{E}}(\mathbf{r}, \omega) &= \sum_{\mathbf{K}} \int_{V_{\mathbf{k}}} d^3 \mathbf{k} \langle \mathbf{r} | \mathbf{k} - \mathbf{K} \rangle \langle \mathbf{k} - \mathbf{K} | \hat{\mathbf{E}}(\omega) \rangle \\ &= (2\pi)^{-3/2} \sum_{\mathbf{K}} \int_{V_{\mathbf{k}}} d^3 \mathbf{k} e^{i(\mathbf{k}-\mathbf{K}) \cdot \mathbf{r}} \hat{\mathbf{E}}(\mathbf{k} - \mathbf{K}, \omega) \end{aligned} \quad (7.40)$$

where we used

$$\langle \mathbf{r} | \mathbf{k} \rangle = (2\pi)^{-3/2} e^{i\mathbf{k} \cdot \mathbf{r}}. \quad (7.41)$$

Due to the quasi-homogeneity of the material composed of the lattice of point particles the eigensolutions are plain waves with a dispersion relation $\mathbf{k}(\omega)$. This dispersion relation implicitly contains the sought connection between the microscopic polarizability $\alpha(\omega)$ and the (macroscopic) susceptibility $\chi(\omega)$, i.e., the Clausius-Mossotti local field corrections. It can be shown [142] that the dispersion relation $\mathbf{k}(\omega)$ is determined by

$$\det [T(\mathbf{k}, \omega)^{-1}] = 0, \quad (7.42)$$

the determinant of the inverse scattering T -matrix. In order to find $\mathbf{k}(\omega)$ we thus, as for a single scatterer, explicitly sum the diagram series (7.25) to find the T -matrix of the simple cubic lattice represented by (7.37). In contrast

to the case of a single dipole we now seek the T -matrix in \mathbf{k} -space

$$\begin{aligned} T(\mathbf{k}, \mathbf{k}', \omega) &= \langle \mathbf{k} | \hat{T}(\omega) | \mathbf{k}' \rangle \\ &= \iint d^3 \mathbf{r}_1 d^3 \mathbf{r}_2 \langle \mathbf{k} | \mathbf{r}_1 \rangle \langle \mathbf{r}_1 | \hat{V}(\omega) \sum_n \left[\hat{\mathcal{G}}^{(0)}(\omega) \hat{V}(\omega) \right]^n | \mathbf{r}_2 \rangle \langle \mathbf{r}_2 | \mathbf{k}' \rangle. \end{aligned} \quad (7.43)$$

For the first summand ($n = 0$) of (7.43) we employ the representation of $\hat{V}(\omega)$ in \mathbf{k} -space

$$\frac{V(\omega)}{(2\pi)^3} \sum_{\mathbf{R}} e^{-i(\mathbf{k}-\mathbf{k}')\mathbf{R}}. \quad (7.44)$$

For higher terms we need to evaluate summands like

$$\mathcal{S}_n = \frac{V(\omega)}{(2\pi)^3} \sum_{\mathbf{R}} \int d^3 \mathbf{r}_2 e^{-i\mathbf{k}\mathbf{R}} e^{i\mathbf{k}'\mathbf{r}_2} \langle \mathbf{R} | \left[\hat{\mathcal{G}}^{(0)}(\omega) \hat{V}(\omega) \right]^n | \mathbf{r}_2 \rangle \quad (7.45)$$

for any positive integer $n > 0$. For $n = 1$ we find

$$\mathcal{S}_1 = \frac{V(\omega)}{(2\pi)^3} \sum_{\mathbf{R}} e^{-i(\mathbf{k}-\mathbf{k}')\mathbf{R}} V(\omega) \sum_{\mathcal{R}} e^{-i\mathbf{k}'\mathcal{R}} \mathcal{G}^{(0)}(\mathcal{R}, \omega) \quad (7.46)$$

where the summation index \mathbf{R}' from the real space representation of the second optical potential term $\hat{V}(\omega)$ has been replaced by the lattice vector $\mathcal{R} = \mathbf{R} - \mathbf{R}'$ which for any \mathbf{R} corresponds to a finite shift of the infinite sum. Note that this procedure is only valid for an infinitely extended medium. With the same technique we find for \mathcal{S}_2

$$\mathcal{S}_2 = \frac{V(\omega)}{(2\pi)^3} \sum_{\mathbf{R}} e^{-i(\mathbf{k}-\mathbf{k}')\mathbf{R}} \left[V(\omega) \sum_{\mathcal{R}} e^{-i\mathbf{k}'\mathcal{R}} \mathcal{G}^{(0)}(\mathcal{R}, \omega) \right]^2. \quad (7.47)$$

By iteration one easily finds that in general for \mathcal{S}_n we get

$$\mathcal{S}_n = \frac{V(\omega)}{(2\pi)^3} \sum_{\mathbf{R}} e^{-i(\mathbf{k}-\mathbf{k}')\mathbf{R}} \left[V(\omega) \sum_{\mathcal{R}} e^{-i\mathbf{k}'\mathcal{R}} \mathcal{G}^{(0)}(\mathcal{R}, \omega) \right]^n. \quad (7.48)$$

Similar to the formal solution of the diagram series here the summands of (7.43) form a geometric series. Hence the scattering T -matrix of an infinitely extended simple cubic lattice of point dipoles reads [136]

$$T(\mathbf{k}, \mathbf{k}', \omega) = (2\pi)^{-3} \sum_{\mathbf{R}} e^{-i(\mathbf{k}-\mathbf{k}')\mathbf{R}} \left\{ V(\omega)^{-1} - \sum_{\mathcal{R}} e^{-i\mathbf{k}'\mathcal{R}} \mathcal{G}^{(0)}(\mathcal{R}, \omega) \right\}^{-1} \quad (7.49)$$

where, as above, the “bare” optical potential $V(\omega)$ is given by the polarizability via $V(\omega) = -4\pi\frac{\omega^2}{c^2}\alpha(\omega)$.

As for a single scatterer we encounter a term proportional to the divergent $\mathcal{G}^{(0)}(0, \omega)$ which we combine as in (7.34) with the “bare” potential $V(\omega)$ to the physical potential of a single scatterer in free space, $\tilde{V}(\omega)$. The such renormalized physical T -matrix for a lattice of point particles reads

$$T(\mathbf{k}, \mathbf{k}', \omega) = (2\pi)^{-3} \sum_{\mathbf{R}} e^{-i(\mathbf{k}-\mathbf{k}')\cdot\mathbf{R}} \left\{ \tilde{V}(\omega)^{-1} - \sum_{\mathbf{R} \neq 0} e^{-i\mathbf{k}'\cdot\mathbf{R}} \mathcal{G}^{(0)}(\mathbf{R}, \omega) \right\}^{-1} \quad (7.50)$$

which now only involves the physical polarizability of a single particle $\tilde{V}(\omega)$ and the contribution due to the multiple scattering to all orders at the lattice. It is this scattering part which leads to the Clausius-Mossotti local field corrections.

In order to prove this statement we need to sum the scattering contribution, which unfortunately cannot be done exactly. We therefore establish an approximate result for the limit of high densities of scatterers ϱ in which $ka \ll 1$ for the wave vector $k = |\mathbf{k}|$ and the lattice constant a holds. We start by artificially including the $\mathbf{R} = 0$ term in the summation

$$\sum_{\mathbf{R} \neq 0} e^{-i\mathbf{k}\cdot\mathbf{R}} \mathcal{G}^{(0)}(\mathbf{R}, \omega) = \sum_{\mathbf{R}} \Xi(|\mathbf{R}|) e^{-i\mathbf{k}\cdot\mathbf{R}} \mathcal{G}^{(0)}(\mathbf{R}, \omega). \quad (7.51)$$

In order to exclude the singular point $\mathbf{R} = 0$ the smooth function $\Xi(|\mathbf{R}|)$ is introduced which vanishes at the origin exactly, $\Xi(0) = 0$, and approaches unity on a length scale which is small compared to the lattice constant a . By application of Poisson’s summation formula [143]

$$\sum_{n=-\infty}^{\infty} f(n) = \sum_{k=-\infty}^{\infty} \int_{-\infty}^{\infty} dx f(x) e^{-2\pi i k x} \quad (7.52)$$

the sum over lattice vectors is transformed into a real space integral plus a sum over reciprocal lattice vectors

$$\sum_{\mathbf{R} \neq 0} e^{-i\mathbf{k}\cdot\mathbf{R}} \mathcal{G}^{(0)}(\mathbf{R}, \omega) = \sum_{\mathbf{K}} \int d^3 \mathbf{r} \frac{\Xi(|\mathbf{r}|)}{a^3} e^{-i(\mathbf{k}+\mathbf{K})\cdot\mathbf{r}} \mathcal{G}^{(0)}(\mathbf{r}, \omega). \quad (7.53)$$

The appearance of the reciprocal lattice vectors \mathbf{K} in (7.53) reflects the discrete nature of the medium. In the continuous medium limit $ka \ll 1$, i.e.,

when the wavelength of the radiation in question is large compared to the lattice spacing, the medium is essentially homogeneous and we are allowed to keep only the $\mathbf{K} = 0$ term in the sum. Thus for high densities the sum in (7.51) is being replaced by an integral which, importantly, excludes the origin by means of the function Ξ . Note that the restriction to low wave numbers $\mathbf{K} = 0$ corresponds to a spatial averaging over volumes with a diameter of at least the lattice constant a [40] by which we formally transform the microscopically treated medium to an averaged material as it appears in macroscopic electrodynamics.

In the following we evaluate (7.53) by explicitly setting

$$\Xi(r) = 1 - e^{-r^2/\Delta^2} \quad (7.54)$$

which fulfills the condition $\Xi(0) = 0$. As we only deal with high densities we only want to solve the integration in the limit $\Delta \rightarrow 0$. We introduce the Fourier transform of the retarded vacuum Green function (see Appendix A)

$$\begin{aligned} \widetilde{\mathcal{G}^{(0)}}(\mathbf{p}, \omega) &= \frac{1}{(\omega^2/c^2 + i\epsilon)\mathbb{1} - p^2\Delta_{\mathbf{p}}} \\ &= \frac{1}{\omega^2/c^2 - p^2 + i\epsilon}\Delta_{\mathbf{p}} + \frac{1}{\omega^2/c^2}\hat{\mathbf{p}} \otimes \hat{\mathbf{p}} \end{aligned} \quad (7.55)$$

into (7.53). For the special case of (7.54) we hence find

$$\begin{aligned} \sum_{\mathbf{R} \neq 0} e^{-i\mathbf{k}\mathbf{R}} \mathcal{G}^{(0)}(\mathbf{R}, \omega) &\approx \frac{1}{a^3} \widetilde{\mathcal{G}^{(0)}}(\mathbf{k}, \omega) \\ &\quad - \frac{1}{a^3} \frac{1}{(2\pi)^3} \int d^3\mathbf{p} \widetilde{\mathcal{G}^{(0)}}(\mathbf{p}, \omega) \int d^3\mathbf{r} e^{-r^2/\Delta^2} e^{i(\mathbf{p}-\mathbf{k}) \cdot \mathbf{r}} \end{aligned} \quad (7.56)$$

As the \mathbf{r} -integration represents just a Fourier transform of the Gaussian, this can be simplified to

$$\begin{aligned} \sum_{\mathbf{R} \neq 0} e^{-i\mathbf{k}\mathbf{R}} \mathcal{G}^{(0)}(\mathbf{R}, \omega) &\approx \frac{1}{a^3} \widetilde{\mathcal{G}^{(0)}}(\mathbf{k}, \omega) \\ &\quad - \frac{1}{a^3} \frac{\pi^{3/2} \Delta^3}{(2\pi)^3} \int d^3\mathbf{p} \widetilde{\mathcal{G}^{(0)}}(\mathbf{p}, \omega) e^{-\Delta^2|\mathbf{p}-\mathbf{k}|^2/4}. \end{aligned} \quad (7.57)$$

The remaining \mathbf{p} -integration is performed in spherical coordinates. To do so we expand the angle dependent terms of the Gaussian for small Δ

$$e^{-\Delta^2|\mathbf{p}-\mathbf{k}|^2/4} \approx e^{-\Delta^2(p^2+k^2)/4} [1 + \Delta^2/2(k_z p \cos \theta + k_y p \cos \phi \sin \theta + k_x p \sin \theta \sin \phi)] \quad (7.58)$$

but keep the exponential for the $p = |\mathbf{p}|$ dependent contribution that provides a cut-off in reciprocal space. Having performed the integration over the angles θ and ϕ we are left with just one integration over p

$$\begin{aligned} \sum_{\mathbf{R} \neq 0} e^{i\mathbf{k}\mathbf{R}} \mathcal{G}^{(0)}(\mathbf{R}, \omega) &\approx \frac{1}{a^3} \widetilde{\mathcal{G}^{(0)}}(\mathbf{k}, \omega) - \frac{1}{a^3} \frac{\pi^{3/2} \Delta^3}{(2\pi)^3} \\ &\cdot \int dp p^2 e^{-\Delta^2(p^2+k^2)/4} \frac{4\pi(3\frac{\omega^2}{c^2} - p^2 + i\epsilon)}{3\frac{\omega^2}{c^2}(\frac{\omega^2}{c^2} - p^2 + i\epsilon)} \mathbb{1} \end{aligned} \quad (7.59)$$

which can be carried out analytically. As mentioned above, for the continuous media limit we restrict to the zeroth order in Δ for which we finally obtain

$$\sum_{\mathbf{R} \neq 0} e^{i\mathbf{k}\mathbf{R}} \mathcal{G}^{(0)}(\mathbf{R}, \omega) \approx \frac{1}{a^3} \widetilde{\mathcal{G}^{(0)}}(\mathbf{k}, \omega) - \frac{1}{a^3} \frac{1}{3\omega^2/c^2} \mathbb{1}. \quad (7.60)$$

Thus the approximative renormalized T -matrix (7.50) for high densities for the case of a simple cubic lattice of point electric dipoles reads

$$T(\mathbf{k}, \mathbf{k}', \omega) = (2\pi)^{-3} \sum_{\mathbf{R}} e^{-i(\mathbf{k}-\mathbf{k}')\mathbf{R}} \left\{ \tilde{V}(\omega)^{-1} - \frac{1}{a^3} \widetilde{\mathcal{G}^{(0)}}(\mathbf{k}, \omega) + \frac{1}{a^3} \frac{1}{3\omega^2/c^2} \mathbb{1} \right\}^{-1}. \quad (7.61)$$

The only unknown parameter left, the dispersion relation $\mathbf{k}(\omega)$, is fixed by the condition (7.42). We hence have to determine the root of the determinant of the inverse T -matrix which explicitly reads

$$\det \left[-\frac{1}{\omega^2} \tilde{\alpha}(\omega)^{-1} - \frac{1}{a^3} \widetilde{\mathcal{G}^{(0)}}(\mathbf{k}, \omega) + \frac{1}{a^3} \frac{1}{3\omega^2/c^2} \mathbb{1} \right] = 0. \quad (7.62)$$

To comply with the notation of chapter 6, we replace $1/a^3$ by the number density of scatterers ϱ . For an isotropic polarizability $\tilde{\alpha}(\omega) \equiv \tilde{\alpha}(\omega) \mathbb{1}$ we

expect the permittivity to be isotropic as well and the dispersion relation to be quasi-scalar $\mathbf{k}(\omega) = k(\omega)\hat{\mathbf{k}}$. We solve (7.62) for the permittivity $\varepsilon(\omega)$ given by $k(\omega)^2 = \varepsilon(\omega)\omega^2/c^2$ from which we find the Clausius-Mossotti relation

$$\varepsilon(\omega) = 1 + 4\pi \frac{\varrho\tilde{\alpha}(\omega)}{1 - \frac{4\pi}{3}\varrho\tilde{\alpha}(\omega)} \quad (7.63)$$

which is identical to the expression found from macroscopic considerations.

In contrast to (6.10), here the free space single-particle polarizability $\tilde{\alpha}(\omega)$ appears explicitly, which was not clear from the macroscopic treatment. This results from the fact that only radiative interactions between atoms are covered by this treatment. Scattering processes between atoms and phonons will contribute significantly to the effective polarizability.

We note that the derivation of (7.62) is not restricted to scalar polarizabilities. The procedure developed above is therefore also applicable to more complicated situations, such as birefringent crystals. As a general example we consider the anisotropic but diagonal polarizability

$$\alpha(\omega) = \begin{pmatrix} \alpha_x(\omega) & 0 & 0 \\ 0 & \alpha_y(\omega) & 0 \\ 0 & 0 & \alpha_z(\omega) \end{pmatrix}. \quad (7.64)$$

Note that we can always find a coordinate system in which the tensor $\alpha(\omega)$ has the structure of (7.64) due the general symmetry properties of pure dielectric response tensors [75, 85]. We then find for a wave propagating in x -direction $\mathbf{k} = k(\omega)\mathbf{e}_x$ two distinct solutions

$$\varepsilon_y(\omega) = 1 + 4\pi \frac{\varrho\tilde{\alpha}_y(\omega)}{1 - \frac{4\pi}{3}\varrho\tilde{\alpha}_y(\omega)} \quad (7.65)$$

and

$$\varepsilon_z(\omega) = 1 + 4\pi \frac{\varrho\tilde{\alpha}_z(\omega)}{1 - \frac{4\pi}{3}\varrho\tilde{\alpha}_z(\omega)} \quad (7.66)$$

for linear y - and z -polarization, respectively. For waves traveling in other

directions similar results apply. Hence the permittivity reads

$$\varepsilon(\omega) = \mathbb{1} + 4\pi \begin{pmatrix} \frac{\varrho\tilde{\alpha}_x(\omega)}{1 - \frac{4\pi}{3}\varrho\tilde{\alpha}_x(\omega)} & 0 & 0 \\ 0 & \frac{\varrho\tilde{\alpha}_y(\omega)}{1 - \frac{4\pi}{3}\varrho\tilde{\alpha}_y(\omega)} & 0 \\ 0 & 0 & \frac{\varrho\tilde{\alpha}_z(\omega)}{1 - \frac{4\pi}{3}\varrho\tilde{\alpha}_z(\omega)} \end{pmatrix}. \quad (7.67)$$

7.3 Solution in reciprocal space

In the following we will pursue a different approach to find solutions of the Helmholtz equation (7.6) that will become important for non-pure, i.e., magneto-dielectric materials. Conceptually we have dealt up to now with scattering effects of a wave traveling from a spatial point \mathbf{r}' , at which it has been excited, to a point \mathbf{r} . In contrast, we will now look for electromagnetic field eigensolutions in the lattice system following [134], i.e., we consider the Helmholtz equation (7.6) without free sources:

$$\nabla \times \nabla \times \hat{\mathbf{E}}(\mathbf{r}, \omega) - \frac{\omega^2}{c^2} \hat{\mathbf{E}}(\mathbf{r}, \omega) = 4\pi \frac{\omega^2}{c^2} \hat{\mathbf{P}}(\mathbf{r}, \omega). \quad (7.68)$$

As before, the polarization is connected to the electric field strength via $\hat{\mathbf{P}}(\mathbf{r}, \omega) = \alpha(\mathbf{r}, \omega) \hat{\mathbf{E}}(\mathbf{r}, \omega)$, and $\alpha(\mathbf{r}, \omega)$ separates into the polarizability $\alpha(\omega)$ and the spatial distribution function for the simple cubic lattice of point electric dipoles

$$\alpha(\mathbf{r}, \omega) = \alpha(\omega) \sum_{\mathbf{R}} \delta(\mathbf{r} - \mathbf{R}) = \frac{\alpha(\omega)}{a^3} \sum_{\mathbf{K}} e^{i\mathbf{K}\mathbf{r}}. \quad (7.69)$$

Note that we also give the representation in terms of reciprocal lattice vectors \mathbf{K} , which can be obtained by means of Poisson's summation formula (7.52). With the representation of the electric field vector in reciprocal space (7.40) the Helmholtz equation thus reads

$$\begin{aligned} \int_{V_k} d\mathbf{k} \sum_{\mathbf{K}} \left[\frac{\omega^2}{c^2} + (\mathbf{k} - \mathbf{K}) \times (\mathbf{k} - \mathbf{K}) \times \right] \hat{\mathbf{E}}(\mathbf{k} - \mathbf{K}, \omega) e^{i(\mathbf{k}-\mathbf{K})\mathbf{r}} &= \\ = - \int_{V_k} d\mathbf{k} \sum_{\mathbf{K}} \sum_{\mathbf{K}'} 4\pi \frac{\omega^2}{c^2} \frac{\alpha(\omega)}{a^3} e^{i\mathbf{K}'\mathbf{r}} \hat{\mathbf{E}}(\mathbf{k} - \mathbf{K}, \omega) e^{i(\mathbf{k}-\mathbf{K})\mathbf{r}}. \end{aligned} \quad (7.70)$$

Note that with $\mathbf{p} \times \mathbf{p} \times = -|\mathbf{p}|^2 \Delta_{\mathbf{p}}$ the term in the brackets on the left hand side represents the inverse vacuum Green function in reciprocal space (7.55). On the right hand side we replace the summation over \mathbf{K}' by $\mathbf{K}'' = \mathbf{K} - \mathbf{K}'$ and afterwards interchange the notations for \mathbf{K} and \mathbf{K}'' . Since $\int_{V_k} d\mathbf{k} \sum_{\mathbf{K}} \dots e^{i(\mathbf{k}-\mathbf{K})\mathbf{r}}$ is an ordinary Fourier transformation we obtain the Fourier transformation of the Helmholtz equation by restriction to the kernel

$$\left[\widetilde{\mathcal{G}^{(0)}}(\mathbf{k} - \mathbf{K}, \omega) \right]^{-1} \hat{\mathbf{E}}(\mathbf{k} - \mathbf{K}, \omega) = - \sum_{\mathbf{K}''} 4\pi \frac{\omega^2}{c^2} \frac{\alpha(\omega)}{a^3} \hat{\mathbf{E}}(\mathbf{k} - \mathbf{K}'', \omega). \quad (7.71)$$

Note that the effect of the lattice now manifests itself in a coupling of elementary waves with different reciprocal lattice vectors \mathbf{K} . We proceed by multiplying with $\widetilde{\mathcal{G}^{(0)}}(\mathbf{k} - \mathbf{K}, \omega)$ from the left and summing everything over \mathbf{K} . This results for a plane wave solution $\hat{\mathbf{E}}_{\mathbf{k}}(\mathbf{r} = 0, \omega) = \sum_{\mathbf{K}} \hat{\mathbf{E}}(\mathbf{k} - \mathbf{K}, \omega)$ to a given wave vector \mathbf{k} in the fundamental algebraic (in polarization space) set of equations

$$\left[\sum_{\mathbf{K}} \widetilde{\mathcal{G}^{(0)}}(\mathbf{k} - \mathbf{K}, \omega) + \frac{1}{4\pi \frac{\omega^2}{c^2} \frac{\alpha(\omega)}{a^3}} \right] \hat{\mathbf{E}}_{\mathbf{k}}(0, \omega) = 0. \quad (7.72)$$

Nontrivial solutions to the Helmholtz equation therefore exist if and only if the determinant of the system matrix

$$\det \left[\sum_{\mathbf{K}} \widetilde{\mathcal{G}^{(0)}}(\mathbf{k} - \mathbf{K}, \omega) + \frac{1}{4\pi \frac{\omega^2}{c^2} \frac{\alpha(\omega)}{a^3}} \right] = 0 \quad (7.73)$$

vanishes. Again the only free parameter left in (7.73) is the wave vector $\mathbf{k}(\omega)$. Note that this condition corresponds exactly to (7.42) for dielectric media. This follows immediately from comparing (7.72) and (7.49) together with the corresponding relation between the bare polarizability $\alpha(\omega)$ and the bare optical potential $V(\omega)$ using (see Appendix A)

$$\frac{1}{a^3} \sum_{\mathbf{K}} \widetilde{\mathcal{G}^{(0)}}(\mathbf{k} - \mathbf{K}, \omega) = \sum_{\mathbf{R}} e^{-i\mathbf{k}\mathbf{R}} \mathcal{G}^{(0)}(\mathbf{R}, \omega). \quad (7.74)$$

Correspondingly the infinite sum over \mathbf{K} in (7.73) contains the divergent $\mathcal{G}^{(0)}(0, \omega)$. As in section 7.2 the physical polarizability $\tilde{\alpha}(\omega)$ is introduced as

the combination (7.34) of the bare optical potential $V(\omega)$ and $\mathcal{G}^{(0)}(0, \omega)$. As expected, the treatment in reciprocal space thus gives the same dispersion relation as the Green function formalism. But only the multiple scattering Green function technique allowed us to find the single scatterer result which appears in the renormalization treatment of the lattice.

CHAPTER 8

Magnetic media

Local field effects are of course not restricted to dielectric materials. Although atomic magnetic dipole transition moments are usually orders of magnitude smaller than corresponding electric dipole transition moments, local-field corrections can become important in pure magnetic systems or artificial media, such as metamaterials, for which magnetic dipole moments can have the same order of magnitude than corresponding electric dipole moments. Thus along the lines of chapter 7 we will now analyze local field corrections for diamagnetic¹ media. Similarly as for dielectric materials we will make use of a simple cubic lattice of point magnetic dipoles (see Fig. 8.1) which will allow us to sum the diagram series of the T -matrix analytically and determine the dispersion relation which includes the Clausius-Mossotti corrections.

We start with a classical treatment similar to the dielectric case. Along the same lines as for dielectrics (cf. chapter 7) one can show [93] that the local magnetic field, i.e., the field which excites the individual magnetic dipoles on a microscopic level, is given by the macroscopic magnetic field \mathbf{H} and the magnetization \mathbf{M} as

$$\mathbf{H}_{\text{local}} = \mathbf{H} + \frac{4\pi}{3}\mathbf{M}. \quad (8.1)$$

The magnetization \mathbf{M} itself is defined by $\varrho \mathbf{m}$ where ϱ denotes the number density of the magnetizable particles and \mathbf{m} the induced magnetic moment.

¹As for dielectric media no permanent dipole moments is assumed to exist.

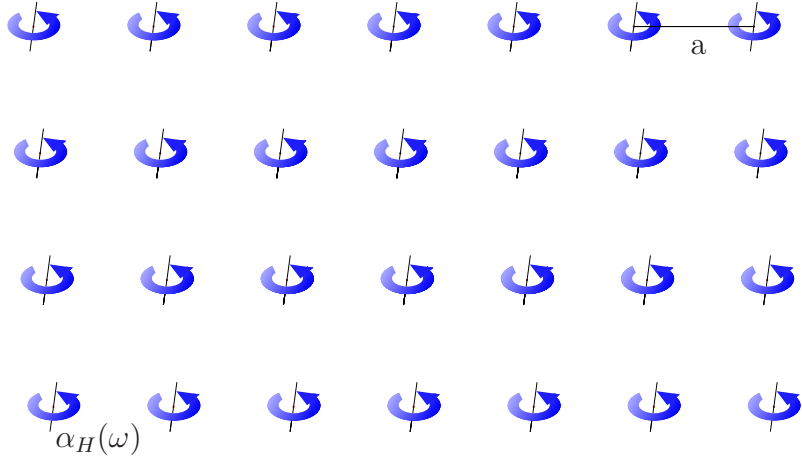


Figure 8.1: Microscopic model of a pure diamagnetic material. Point magnetic dipoles with a magnetizability $\alpha_H(\omega)$ form a simple cubic lattice with lattice constant a .

For linear media, \mathbf{m} is proportional to the local magnetic field

$$\mathbf{m} = \alpha_H(\omega) \mathbf{H}_{\text{local}} \quad (8.2)$$

where $\alpha_H(\omega)$ denotes the corresponding magnetizability constant. We eliminate $\mathbf{H}_{\text{local}}$ and obtain a connection between the macroscopic fields \mathbf{H} and \mathbf{M} in terms of the microscopic factor $\alpha_H(\omega)$. As in chapter 7 we find

$$\mathbf{M} = \varrho \alpha_H(\omega) \left(\mathbf{H} + \frac{4\pi}{3} \mathbf{M} \right) \quad (8.3)$$

which can be compared to $\mathbf{M} = \chi_m(\omega) \mathbf{H}$. The magnetic susceptibility $\chi_m(\omega)$ thus reads

$$\chi_m(\omega) = \frac{\varrho \alpha_H(\omega)}{1 - \frac{4\pi}{3} \varrho \alpha_H(\omega)} \quad (8.4)$$

which is in exact analogy to the dielectric result (6.10). As in the dielectric case we treat this case in the following in a fully microscopic treatment based on a simple cubic lattice of point scatterers.

8.1 Multiple scattering in real space

Similar to the macroscopic treatment above we construct a microscopic theory in one-to-one correspondence to the dielectric case. We derive from Maxwell's equations (7.2) and (7.3) a Helmholtz equation for the magnetic field. In contrast to the dielectric case, the electric displacement operator is now given by $\hat{\mathbf{D}}(\mathbf{r}, \omega) = \hat{\mathbf{E}}(\mathbf{r}, \omega)$ whereas the magnetic field is related to the induced magnetization via $\hat{\mathbf{B}}(\mathbf{r}, \omega) = \hat{\mathbf{H}}(\mathbf{r}, \omega) + 4\pi\hat{\mathbf{M}}(\mathbf{r}, \omega)$. This results in the vectorial Helmholtz equation

$$\nabla \times \nabla \times \hat{\mathbf{H}}(\mathbf{r}, \omega) - \frac{\omega^2}{c^2} \hat{\mathbf{H}}(\mathbf{r}, \omega) = \frac{4\pi}{c} \nabla \times \hat{\mathbf{j}}(\mathbf{r}, \omega) + 4\pi \frac{\omega^2}{c^2} \hat{\mathbf{M}}(\mathbf{r}, \omega). \quad (8.5)$$

Under the assumption of linear media the magnetization is proportional to the magnetic field

$$\hat{\mathbf{M}}(\mathbf{r}, \omega) = \alpha_H(\mathbf{r}, \omega) \hat{\mathbf{H}}(\mathbf{r}, \omega) \quad (8.6)$$

with $\alpha_H(\mathbf{r}, \omega)$ being the independently obtained single particle magnetizability modulated with a spatial distribution function. We introduce the Green function $\mathcal{G}_H(\mathbf{r}, \mathbf{r}', \omega)$ indicated with $_H$ in order to make a distinction to the electric case by

$$\hat{\mathbf{H}}(\mathbf{r}, \omega) = -\frac{4\pi}{c} \int d^3 \mathbf{r}' \mathcal{G}_H(\mathbf{r}, \mathbf{r}', \omega) \nabla^{\mathbf{r}'} \times \hat{\mathbf{j}}(\mathbf{r}', \omega). \quad (8.7)$$

The magnetic Helmholtz equation (8.5) hence translates to the defining equation for the Green function

$$\left[\frac{\omega^2}{c^2} \mathbb{1} - \nabla^{\mathbf{r}} \times \nabla^{\mathbf{r}} \times \right] \mathcal{G}_H(\mathbf{r}, \mathbf{r}', \omega) = \delta(\mathbf{r} - \mathbf{r}') \mathbb{1} - 4\pi \frac{\omega^2}{c^2} \alpha_H(\mathbf{r}, \omega) \mathcal{G}_H(\mathbf{r}, \mathbf{r}', \omega). \quad (8.8)$$

Note that the form of (8.8) is equivalent to the corresponding dielectric equation (7.9). Without any further calculations we therefore summarize the results for the scattering at a single magnetic point dipole in vacuum and a simple cubic lattice of magnetic point particles, respectively.

- (a) For a single point magnetic dipole $\alpha_H(\mathbf{r}, \omega)$ consists of the magnetizability $\alpha_H(\omega)$ which acts at a single position \mathbf{r}_A

$$\alpha_H(\mathbf{r}, \omega) = \alpha_H(\omega) \delta(\mathbf{r} - \mathbf{r}_A) \quad (8.9)$$

The corresponding single particle T -matrix then reads

$$t_H(\mathbf{r}, \mathbf{r}', \omega) = t_H(\omega) \delta(\mathbf{r} - \mathbf{r}_A) \delta(\mathbf{r}' - \mathbf{r}_A). \quad (8.10)$$

where the spectral scattering amplitude $t_H(\omega)$ contains the divergent term $\mathcal{G}_H^{(0)}(0, \omega)$ which we together with the bare magnetizability interpret on the lines of (7.34) as the physical magnetizability $\tilde{\alpha}_H(\omega)$. As a result the renormalized T -matrix reduces to

$$t_H(\omega) = \tilde{V}_H(\omega) \quad (8.11)$$

with $\tilde{V}_H(\omega) = -4\pi(\omega^2/c^2)\tilde{\alpha}_H(\omega)$ being the physical optical potential. Note that the vacuum Green function for the magnetic case $\mathcal{G}_H^{(0)}(\mathbf{r} - \mathbf{r}', \omega)$ is of course identical to the vacuum Green function $\mathcal{G}^{(0)}(\mathbf{r} - \mathbf{r}', \omega)$ for the dielectric case. To simplify the notation in the following we will therefore only use $\mathcal{G}^{(0)}(\mathbf{r} - \mathbf{r}', \omega)$ rather than $\mathcal{G}_H^{(0)}(\mathbf{r} - \mathbf{r}', \omega)$.

(b) For a simple cubic lattice of magnetic point particles with a magnetizability $\alpha_H(\omega)$ we set

$$\alpha_H(\mathbf{r}, \omega) = \alpha_H(\omega) \sum_{\mathbf{R}} \delta(\mathbf{r} - \mathbf{R}). \quad (8.12)$$

By comparison with (7.50), this leads to the expression

$$T_H(\mathbf{k}, \mathbf{k}', \omega) = \frac{1}{(2\pi)^3} \sum_{\mathbf{R}} e^{-i(\mathbf{k}-\mathbf{k}')\mathbf{R}} \left\{ \tilde{V}_H(\omega)^{-1} - \sum_{\mathcal{R} \neq 0} e^{-i\mathbf{k}'\mathcal{R}} \mathcal{G}^{(0)}(\mathcal{R}, \omega) \right\}^{-1} \quad (8.13)$$

for the renormalized scattering T -matrix of the lattice. By exploiting the determinantal condition (7.42), we determine the dispersion relation $\mathbf{k}(\omega)$ for the high density limit ($ka \ll 1$). In contrast to section 7.2 the wave vector for a scalar magnetizability $\alpha_H(\omega)$ is now related via $k(\omega)^2 = \mu(\omega)\omega^2/c^2$ to the permeability $\mu(\omega) = 1 + 4\pi\chi_m(\omega)$ of the medium rather than the permittivity. It reads

$$\mu(\omega) = 1 + 4\pi \frac{\varrho\tilde{\alpha}_H(\omega)}{1 - \frac{4\pi}{3}\varrho\tilde{\alpha}_H(\omega)}. \quad (8.14)$$

All conclusions and generalizations to tensorial media apply identically compared to the case of dielectric materials.

8.2 Solution in reciprocal space

The treatment in reciprocal space has the same similarity to the dielectric case as the summation of the T -matrix. In particular, the Helmholtz equation without free sources for the magnetic case reads

$$\nabla \times \nabla \times \hat{\mathbf{H}}(\mathbf{r}, \omega) - \frac{\omega^2}{c^2} \hat{\mathbf{H}}(\mathbf{r}, \omega) = 4\pi \frac{\omega^2}{c^2} \hat{\mathbf{M}}(\mathbf{r}, \omega). \quad (8.15)$$

Note that this is formally identical to (7.68) under the duality transformation $\hat{\mathbf{E}}(\mathbf{r}, \omega) \rightarrow \hat{\mathbf{H}}(\mathbf{r}, \omega)$ and $\hat{\mathbf{P}}(\mathbf{r}, \omega) \rightarrow \hat{\mathbf{M}}(\mathbf{r}, \omega)$. For linear media we thus get the reciprocal version of the Helmholtz equation

$$\left[\sum_{\mathbf{K}} \widetilde{\mathcal{G}^{(0)}}(\mathbf{k} - \mathbf{K}, \omega) + \frac{\mathbb{1}}{4\pi \frac{\omega^2}{c^2} \frac{\alpha_H(\omega)}{a^3}} \right] \hat{\mathbf{H}}_{\mathbf{k}}(0, \omega) = 0. \quad (8.16)$$

The roots of the determinant of the system matrix of the algebraic set of equations (8.16) then determine the dispersion relation which for a scalar medium response is characterized by the permeability (8.14).

8.3 The question of \mathbf{H} versus \mathbf{B}

In the treatment of the magnetic materials we implicitly accepted that the magnetization is induced by the magnetic field \mathbf{H} . By contrast, in a Hamiltonian description of the interaction of light and (magnetic) matter the interaction term in dipole approximation reads

$$\hat{H}_{\text{int}} = -\mathbf{m} \cdot \mathbf{B} \quad (8.17)$$

with the magnetic induction field \mathbf{B} rather than \mathbf{H} . This suggests to use the definition

$$\mathbf{m} = \alpha_B(\omega) \mathbf{B}_{\text{local}} \quad (8.18)$$

rather than (8.2) on the microscopic level in order to derive local field corrections. Note that $\alpha_B(\omega)$ and $\alpha_H(\omega)$ from (8.2) have to be distinguished.

8.3.1 Macroscopic Treatment

From a phenomenological treatment [93] the local magnetic induction field $\mathbf{B}_{\text{local}}$ is given by the macroscopic induction field \mathbf{B} and the magnetization \mathbf{M} via

$$\mathbf{B}_{\text{local}} = \mathbf{B} - 2\frac{4\pi}{3}\mathbf{M}. \quad (8.19)$$

This can be understood in a simple manner. The fields $\mathbf{H}_{\text{local}}$ and $\mathbf{B}_{\text{local}}$ are microscopic fields by nature. Thus there are only point-like free sources whose locations form a null set in space. Apart from this null set the fields thus exist in vacuum and are hence identical $\mathbf{H}_{\text{local}} = \mathbf{B}_{\text{local}}$. Note that the contribution of the magnetization of the probe dipole is explicitly excluded in the evaluation of the local field at the position of the probe dipole. Equating (8.19) and (8.1) then simply results in the definition $\mathbf{H} = \mathbf{B} - 4\pi\mathbf{M}$ for the macroscopic fields.

Equations (8.18) and (8.19) together with $\mathbf{M} = \varrho \mathbf{m}$ yield the relation of the magnetization \mathbf{M} and the field induction \mathbf{B} in terms of the microscopic magnetizability $\alpha_B(\omega)$. Comparing to the macroscopic version

$$\mathbf{M} = \chi_m(\omega) \mathbf{H} = \frac{\chi_m(\omega)}{\mu(\omega)} \mathbf{B} = \frac{\chi_m(\omega)}{1 + 4\pi\chi_m(\omega)} \mathbf{B} \quad (8.20)$$

gives the sought relation between the microscopic and macroscopic parameters

$$\chi_m(\omega) = \frac{\varrho\alpha_B(\omega)}{1 - \frac{4\pi}{3}\varrho\alpha_B(\omega)}. \quad (8.21)$$

Note that this result is exactly identical to the corresponding result (8.4) with $\alpha_H(\omega)$ replaced by $\alpha_B(\omega)$. From the macroscopic derivation we thus cannot distinguish between $\alpha_B(\omega)$ and $\alpha_H(\omega)$.

8.3.2 Microscopic Treatment

For a microscopic derivation of (8.21) we replace $\hat{\mathbf{H}}(\mathbf{r}, \omega)$ by the magnetic induction $\hat{\mathbf{B}}(\mathbf{r}, \omega)$ in the Maxwell equations (7.2) and (7.3), from which we then obtain the Helmholtz equation

$$\nabla \times \nabla \times \hat{\mathbf{B}}(\mathbf{r}, \omega) - \frac{\omega^2}{c^2} \hat{\mathbf{B}}(\mathbf{r}, \omega) = \frac{4\pi}{c} \nabla \times \hat{\mathbf{j}}(\mathbf{r}, \omega) + 4\pi \nabla \times \nabla \times \hat{\mathbf{M}}(\mathbf{r}, \omega). \quad (8.22)$$

for $\hat{\mathbf{B}}(\mathbf{r}, \omega)$ rather than (8.5). Similar to (8.7) we introduce the Green function $\mathcal{G}_B(\mathbf{r}, \mathbf{r}', \omega)$, which relates the magnetic induction field strength to the source current

$$\hat{\mathbf{B}}(\mathbf{r}, \omega) = -\frac{4\pi}{c} \int d^3 \mathbf{r}' \mathcal{G}_B(\mathbf{r}, \mathbf{r}', \omega) \nabla^{\mathbf{r}'} \times \hat{\mathbf{j}}(\mathbf{r}', \omega). \quad (8.23)$$

As mentioned above, we use $\hat{\mathbf{M}}(\mathbf{r}, \omega) = \alpha_B(\mathbf{r}, \omega) \hat{\mathbf{B}}(\mathbf{r}, \omega)$, which yields the defining equation for the Green function $\mathcal{G}_B(\mathbf{r}, \mathbf{r}', \omega)$

$$\left[\frac{\omega^2}{c^2} \mathbb{1} - \nabla^{\mathbf{r}} \times \nabla^{\mathbf{r}} \times \right] \mathcal{G}_B(\mathbf{r}, \mathbf{r}', \omega) = \delta(\mathbf{r} - \mathbf{r}') \mathbb{1} - 4\pi \nabla \times \nabla \times \alpha_B(\mathbf{r}, \omega) \mathcal{G}_B(\mathbf{r}, \mathbf{r}', \omega). \quad (8.24)$$

Note the characteristic double curl expression in the material term. As a result $\mathcal{G}_B(\mathbf{r}, \mathbf{r}', \omega)$ and $\mathcal{G}_H(\mathbf{r}, \mathbf{r}', \omega)$ differ in general. Nevertheless the diagram series for the T -matrices can be summed analytically for the single particle as well as the lattice case (see Appendix B).

- The single particle T -matrix reads

$$t_B(\mathbf{r}, \mathbf{r}', \omega) = t_B(\omega) \delta(\mathbf{r} - \mathbf{r}_A) \delta(\mathbf{r}' - \mathbf{r}_A). \quad (8.25)$$

with the spectral amplitude $t_B(\omega)$ given by the bare magnetizability $\alpha_B(\omega)$ and a divergent term which involves the double curl of the free space Green function $\mathcal{G}^{(0)}(0, \omega)$

$$t_B(\omega)^{-1} = - \left(4\pi \frac{\omega^2}{c^2} \alpha_B(\omega) \right)^{-1} - \frac{1}{\omega^2/c^2} \nabla \times \nabla \times \mathcal{G}^{(0)}(0, \omega). \quad (8.26)$$

Hence we introduce the physical magnetizability $\tilde{\alpha}_B(\omega)$ which replaces the sum of the bare one and the divergent Green function term such that (8.26) simplifies to

$$t_B(\omega)^{-1} = - \left(4\pi \frac{\omega^2}{c^2} \tilde{\alpha}_B(\omega) \right)^{-1}. \quad (8.27)$$

- For the case of a simple cubic lattice the T -matrix reads

$$T_B(\mathbf{k}, \mathbf{k}', \omega) = \frac{1}{(2\pi)^3} \sum_{\mathbf{R}} e^{-i(\mathbf{k}-\mathbf{k}')\mathbf{R}} \left\{ V_B(\omega)^{-1} - \sum_{\mathcal{R}} \frac{e^{-i\mathbf{k}'\mathcal{R}}}{\omega^2/c^2} \nabla \times \nabla \times \mathcal{G}^{(0)}(\mathcal{R}, \omega) \right\}^{-1} \quad (8.28)$$

with the characteristic double curl showing up again. We combine the $\mathcal{R} = 0$ contribution of the infinite series and the bare $\alpha_B(\omega)$ response to the renormalized single particle magnetizability $\tilde{\alpha}_B(\omega)$. Noting that $\nabla \times \nabla \times \mathcal{G}^{(0)}(\mathcal{R}, \omega) = (\omega^2/c^2)\mathcal{G}^{(0)}(\mathcal{R}, \omega)$ for $\mathcal{R} \neq 0$ holds, (8.28) simplifies to

$$T_B(\mathbf{k}, \mathbf{k}', \omega) = \frac{1}{(2\pi)^3} \sum_{\mathbf{R}} e^{-i(\mathbf{k}-\mathbf{k}')\mathbf{R}} \left\{ \tilde{V}_B(\omega)^{-1} - \sum_{\mathcal{R} \neq 0} e^{-i\mathbf{k}'\mathcal{R}} \mathcal{G}^{(0)}(\mathcal{R}, \omega) \right\}^{-1}, \quad (8.29)$$

i.e., has the same form as (8.13). As a consequence we obtain the permeability² (8.14) including Clausius-Mossotti local field corrections with $\tilde{\alpha}_H(\omega)$ replaced by $\tilde{\alpha}_B(\omega)$.

Because the permeability must be unique we conclude that for the physical magnetizabilities $\tilde{\alpha}_H(\omega) = \tilde{\alpha}_B(\omega)$ holds. This is reasonable as **B** and **H** for a single particle in free space are indistinguishable. In contrast the relation between the bare term $\alpha_B(\omega)$ and the physical $\tilde{\alpha}_B(\omega)$ differs from the corresponding treatment of $\alpha_H(\omega)$ since

$$\tilde{V}_B(\omega)^{-1} \mathbb{1} = V_B(\omega)^{-1} \mathbb{1} - (c^2/\omega^2) \nabla \times \nabla \times \mathcal{G}^{(0)}(0, \omega) \quad (8.30)$$

holds for $V_B(\omega) = -4\pi(\omega^2/c^2)\alpha_B(\omega)$ rather than

$$\tilde{V}_H(\omega)^{-1} \mathbb{1} = V_H(\omega)^{-1} \mathbb{1} - \mathcal{G}^{(0)}(0, \omega) \quad (8.31)$$

for the corresponding $V_H(\omega) = -4\pi(\omega^2/c^2)\alpha_H(\omega)$. Here

$$\nabla \times \nabla \times \mathcal{G}^{(0)}(0, \omega) = (\omega^2/c^2)\mathcal{G}^{(0)}(0, \omega) - \delta(0) \quad (8.32)$$

contains a factor $\delta(0)$. This factor stems from the aforementioned difference between the microscopic fields **B**_{local} and **H**_{local} on the null set of real space which contains the point particles. For a single particle this solely amounts to the single point $\mathbf{r} = 0$.

As the bare factors are not observable we conclude that for the determination of local field effects it does not matter whether we work with $\alpha_H(\omega)$ or $\alpha_B(\omega)$. Since the usage of **H** prevents the clumsy double curl factors we will therefore use that case in the treatment of more general materials.

²Note that this result can also be derived using a treatment in reciprocal space.

CHAPTER 9

Magneto-dielectric materials

After having discussed the Clausius-Mossotti type local field corrections for pure electric and magnetic media we turn to the case of materials with simultaneous nontrivial permittivity ε and permeability μ . Microscopically such materials incorporate polarizable as well as magnetizable particles. From the macroscopic treatment of section 6.2 we predicted a rather peculiar behavior of the refractive index in the limit of high densities: The real part saturates at $n = -2$ while simultaneously the absorption vanishes as $1/\varrho$. Though the microscopic results obtained for pure electric and magnetic media comply with the respective macroscopic ones it is not clear whether this is true for the case of magneto-dielectric media as well.

The simplest microscopic model of a magneto-dielectric medium employs an electric and a magnetic simple cubic lattice displaced by $\Delta\mathbf{r}$ (see Fig. 9.1). The corresponding electric and magnetic response functions read

$$\alpha_E(\mathbf{r}, \omega) = \alpha_E(\omega) \sum_{\mathbf{R}} \delta(\mathbf{r} - \mathbf{R}) = \frac{\alpha_E(\omega)}{a^3} \sum_{\mathbf{K}} e^{i\mathbf{K}\mathbf{r}} \quad (9.1)$$

and

$$\alpha_H(\mathbf{r}, \omega) = \alpha_H(\omega) \sum_{\mathbf{R}} \delta(\mathbf{r} - \mathbf{R} - \Delta\mathbf{r}) = \frac{\alpha_H(\omega)}{a^3} \sum_{\mathbf{K}} e^{i\mathbf{K}(\mathbf{r}-\Delta\mathbf{r})}, \quad (9.2)$$

where the two sublattices are assumed to have the same lattice constant a and thus identical lattice vectors \mathbf{R} and inverse lattice vectors \mathbf{K} .

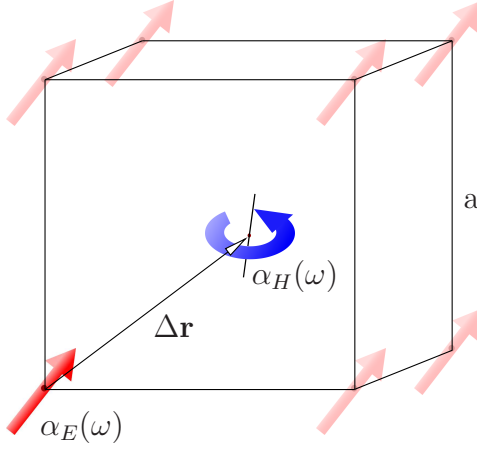


Figure 9.1: Unit cell of the simple cubic lattice with lattice constant a containing an electric and a magnetic dipole with polarizability $\alpha_E(\omega)$ and magnetizability $\alpha_H(\omega)$, respectively. The magnetic dipole is displaced from the electric one by a vector $\Delta\mathbf{r}$.

Since for magneto-dielectric materials both the magnetization $\hat{\mathbf{M}}$ and the polarization $\hat{\mathbf{P}}$ have to be taken into account we derive two coupled Helmholtz equations

$$\left[\nabla \times \nabla \times -\frac{\omega^2}{c^2} \right] \hat{\mathbf{E}}(\mathbf{r}, \omega) = \frac{4\pi}{c} i \frac{\omega}{c} \hat{\mathbf{j}}(\mathbf{r}, \omega) + 4\pi \frac{\omega^2}{c^2} \hat{\mathbf{P}}(\mathbf{r}, \omega) + 4\pi i \frac{\omega}{c} \nabla \times \hat{\mathbf{M}}(\mathbf{r}, \omega) \quad (9.3)$$

and

$$\left[\nabla \times \nabla \times -\frac{\omega^2}{c^2} \right] \hat{\mathbf{H}}(\mathbf{r}, \omega) = \frac{4\pi}{c} \nabla \times \hat{\mathbf{j}}(\mathbf{r}, \omega) + 4\pi \frac{\omega^2}{c^2} \hat{\mathbf{M}}(\mathbf{r}, \omega) - 4\pi i \frac{\omega}{c} \nabla \times \hat{\mathbf{P}}(\mathbf{r}, \omega) \quad (9.4)$$

for the electric and magnetic field operators, respectively. Note that equation (9.4) is determined by the curl of equation (9.3). Thus in principle it suffices to use one of the two equations to describe the electromagnetic fields in a magneto-dielectric medium.

Before we tackle the problem of finding a solution to equations (9.3) and (9.4) we note that the pure electric and magnetic systems of chapters 7 and 8 were conceptually identical. In a first step the scattering problem for a single point-like particle was solved by a direct summation of the respective T -matrix. Afterwards for the generalization to quasi-homogeneous bulk media

a lattice model of point scatterers was employed. Since the lattice is built by stacking unit cells in all directions, the T -matrix of the lattice contains a contribution due to the scattering at different lattice sites as well as the scattering at an individual unit cell, i.e., a single particle, which has been obtained previously. The problem presented by magneto-dielectric media is different since the unit cell contains two point particles: A polarizable and a magnetizable one. As a result the solution of the scattering problem of a single unit cell already becomes involved. Fortunately, it turns out that it suffices to consider the \mathbf{k} -space solution for the lattice case since, as we show below, the same renormalization procedures as in the pure media cases are going to be applied independently. Hence no additional information about the scattering of electromagnetic waves at a single magneto-dielectric unit cell is needed.

We substitute the magnetization $\hat{\mathbf{M}}(\mathbf{r}, \omega)$ and similarly the polarization $\hat{\mathbf{P}}(\mathbf{r}, \omega)$ in the two Helmholtz equations (9.3) and (9.4) using (9.2) and (9.1), respectively. As indicated above it suffices in principle to use one of the two equations (9.3) and (9.4). To do so, we would have to eliminate one of the two fields $\hat{\mathbf{E}}(\mathbf{r}, \omega)$ and $\hat{\mathbf{H}}(\mathbf{r}, \omega)$ with the help of Maxwell's equations in the material terms. This would lead to clumsy curl terms which make the solution tedious. We will pursue a different approach: The usage of both Helmholtz equations simultaneously. Hence we deal with $[\mathbf{j}(\mathbf{r}, \omega) = 0]$

$$\left[\nabla \times \nabla \times -\frac{\omega^2}{c^2} \right] \hat{\mathbf{E}}(\mathbf{r}, \omega) = 4\pi \frac{\omega^2}{c^2} \alpha_E(\mathbf{r}, \omega) \hat{\mathbf{E}}(\mathbf{r}, \omega) + 4\pi i \frac{\omega}{c} \nabla \times \alpha_H(\mathbf{r}, \omega) \hat{\mathbf{H}}(\mathbf{r}, \omega) \quad (9.5)$$

and

$$\left[\nabla \times \nabla \times -\frac{\omega^2}{c^2} \right] \hat{\mathbf{H}}(\mathbf{r}, \omega) = 4\pi \frac{\omega^2}{c^2} \alpha_H(\mathbf{r}, \omega) \hat{\mathbf{H}}(\mathbf{r}, \omega) - 4\pi i \frac{\omega}{c} \nabla \times \alpha_E(\mathbf{r}, \omega) \hat{\mathbf{E}}(\mathbf{r}, \omega). \quad (9.6)$$

As a result of the cross coupling of the two equations it is not clear whether the local field corrections decouple in an electric and a magnetic part as they do in the macroscopic treatment.

In a similar manner as in section 7.3 we derive the Fourier representations

of (9.5) and (9.6) which read

$$\left[\sum_{\mathbf{K}} \widetilde{\mathcal{G}^{(0)}}(\mathbf{k} - \mathbf{K}, \omega) + \frac{1}{4\pi \frac{\omega^2}{c^2} \frac{\alpha_E(\omega)}{a^3}} \right] \hat{\mathbf{E}}_{\mathbf{k}}(0, \omega) = \frac{\alpha_H(\omega)}{c \alpha_E(\omega)} \sum_{\mathbf{K}} \frac{e^{i\mathbf{K}\Delta\mathbf{r}}(\mathbf{k} - \mathbf{K}) \times}{\frac{\omega^2}{c^2} \mathbb{1} - |\mathbf{k} - \mathbf{K}|^2 \Delta_{\mathbf{k}-\mathbf{K}}} \hat{\mathbf{H}}_{\mathbf{k}}(\Delta\mathbf{r}, \omega) \quad (9.7)$$

and

$$\left[\sum_{\mathbf{K}} \widetilde{\mathcal{G}^{(0)}}(\mathbf{k} - \mathbf{K}, \omega) + \frac{1}{4\pi \frac{\omega^2}{c^2} \frac{\alpha_H(\omega)}{a^3}} \right] \hat{\mathbf{H}}_{\mathbf{k}}(\Delta\mathbf{r}, \omega) = -\frac{\alpha_E(\omega)}{c \alpha_H(\omega)} \sum_{\mathbf{K}} \frac{e^{-i\mathbf{K}\Delta\mathbf{r}}(\mathbf{k} - \mathbf{K}) \times}{\frac{\omega^2}{c^2} \mathbb{1} - |\mathbf{k} - \mathbf{K}|^2 \Delta_{\mathbf{k}-\mathbf{K}}} \hat{\mathbf{E}}_{\mathbf{k}}(0, \omega). \quad (9.8)$$

Here we used the abbreviations $\hat{\mathbf{E}}_{\mathbf{k}}(0, \omega) = \sum_{\mathbf{K}} \hat{\mathbf{E}}(\mathbf{k} - \mathbf{K}, \omega)$ and $\hat{\mathbf{H}}_{\mathbf{k}}(\Delta\mathbf{r}, \omega) = \sum_{\mathbf{K}} e^{-i\mathbf{K}\cdot\Delta\mathbf{r}} \hat{\mathbf{H}}(\mathbf{k} - \mathbf{K}, \omega)$ for the amplitudes of the plane wave solutions with respect to the wave vector \mathbf{k} evaluated at $\mathbf{r} = 0$ and $\mathbf{r} = \Delta\mathbf{r}$, respectively.

As discussed in sections 7.2 and 7.3 the term $\sum_{\mathbf{K}} \widetilde{\mathcal{G}^{(0)}}(\mathbf{k} - \mathbf{K}, \omega)$ contains the divergent contribution $\mathcal{G}^{(0)}(0, \omega)$. Together with the bare polarizabilities $\alpha_E(\omega)$ and $\alpha_H(\omega)$ it forms the physical polarizabilities $\tilde{\alpha}_E(\omega)$ and $\tilde{\alpha}_H(\omega)$, respectively, in complete agreement with the treatment for pure electric and magnetic materials.

In contrast the terms $\sum_{\mathbf{K}} e^{\pm i\mathbf{K}\cdot\Delta\mathbf{r}} \{ \omega^2/c^2 \mathbb{1} - |\mathbf{k} - \mathbf{K}|^2 \Delta_{\mathbf{k}-\mathbf{K}} \}^{-1} (\mathbf{k} - \mathbf{K}) \times$ are finite as we show in Appendix C. Thus after absorbing the divergent term $\mathcal{G}^{(0)}(0, \omega)$ in the physical polarizabilities we restrict the analysis to $\mathbf{K} = 0$ so that (9.7) and (9.8) simplify to

$$\begin{aligned} \left[\widetilde{\mathcal{G}^{(0)}}(\mathbf{k}, \omega) - \frac{1}{3\omega^2/c^2} + \frac{1}{4\pi \frac{\omega^2}{c^2} \frac{\tilde{\alpha}_E(\omega)}{a^3}} \right] \hat{\mathbf{E}}_{\mathbf{k}}(0, \omega) &= \\ &= \frac{\alpha_H(\omega)}{c \alpha_E(\omega)} \frac{\mathbf{k} \times}{\frac{\omega^2}{c^2} \mathbb{1} - k^2 \Delta_{\mathbf{k}}} \hat{\mathbf{H}}_{\mathbf{k}}(\Delta\mathbf{r}, \omega) \end{aligned} \quad (9.9)$$

and

$$\begin{aligned} \left[\widetilde{\mathcal{G}^{(0)}}(\mathbf{k}, \omega) - \frac{1}{3\omega^2/c^2} + \frac{1}{4\pi \frac{\omega^2}{c^2} \frac{\tilde{\alpha}_H(\omega)}{a^3}} \right] \hat{\mathbf{H}}_{\mathbf{k}}(\Delta \mathbf{r}, \omega) = \\ = -\frac{\alpha_E(\omega)}{\frac{\omega}{c} \alpha_H(\omega)} \frac{\mathbf{k} \times}{\frac{\omega^2}{c^2} \mathbb{1} - k^2 \Delta_{\mathbf{k}}} \hat{\mathbf{E}}_{\mathbf{k}}(0, \omega). \end{aligned} \quad (9.10)$$

Note that, apart from $\hat{\mathbf{H}}_{\mathbf{k}}(\Delta \mathbf{r}, \omega)$ which is irrelevant for the determination of the dispersion relation $\mathbf{k}(\omega)$, for $\mathbf{K} = 0$ the dependence of the final expressions on $\Delta \mathbf{r}$ vanishes identically.

The dispersion $\mathbf{k}(\omega)$ can be obtained from (9.9) and (9.10) as before by noting that non-trivial field solutions exist if and only if the determinant of the system matrix vanishes (cf. section 7.3). Thus we have to eliminate one of the field amplitudes and condition $\mathbf{k}(\omega)$ on the vanishing of the system determinant.

Although this procedure yields the correct dispersion relation and thus the local field corrections, the resultant equation can be simplified significantly by projecting onto transverse solutions. This can be done by using the projector $\Delta_{\mathbf{k}}$, with which we multiply equations (9.9) and (9.10) from the left. Noting that $\Delta_{\mathbf{k}} \cdot \hat{\mathbf{k}} \otimes \hat{\mathbf{k}} = 0$ and $\Delta_{\mathbf{k}} \mathbf{k} \times = \mathbf{k} \times \Delta_{\mathbf{k}}$ holds, we find

$$\begin{aligned} \left[\frac{1}{\frac{\omega^2}{c^2} - k^2} - \frac{1}{3\omega^2/c^2} + \frac{1}{4\pi \frac{\omega^2}{c^2} \frac{\tilde{\alpha}_E(\omega)}{a^3}} \right] \Delta_{\mathbf{k}} \hat{\mathbf{E}}_{\mathbf{k}}(0, \omega) = \\ = \frac{\alpha_H(\omega)}{\frac{\omega}{c} \alpha_E(\omega)} \frac{1}{\frac{\omega^2}{c^2} - k^2} \mathbf{k} \times \Delta_{\mathbf{k}} \hat{\mathbf{H}}_{\mathbf{k}}(\Delta \mathbf{r}, \omega) \end{aligned} \quad (9.11)$$

and

$$\begin{aligned} \left[\frac{1}{\frac{\omega^2}{c^2} - k^2} - \frac{1}{3\omega^2/c^2} + \frac{1}{4\pi \frac{\omega^2}{c^2} \frac{\tilde{\alpha}_H(\omega)}{a^3}} \right] \mathbf{k} \times \Delta_{\mathbf{k}} \hat{\mathbf{H}}_{\mathbf{k}}(\Delta \mathbf{r}, \omega) = \\ = \frac{\alpha_E(\omega)}{\frac{\omega}{c} \alpha_H(\omega)} \frac{k^2}{\frac{\omega^2}{c^2} - k^2} \Delta_{\mathbf{k}} \hat{\mathbf{E}}_{\mathbf{k}}(0, \omega), \end{aligned} \quad (9.12)$$

respectively. Note that by this the system matrix becomes diagonal, i.e., a scalar. After elimination of one of the two field variables the condition for the existence of non-trivial solutions reads

$$\begin{aligned} & \left[\frac{1}{\frac{\omega^2}{c^2} - k^2} - \frac{1}{3\omega^2/c^2} + \frac{1}{4\pi \frac{\omega^2}{c^2} \frac{\tilde{\alpha}_E(\omega)}{a^3}} \right] \left[\frac{1}{\frac{\omega^2}{c^2} - k^2} - \frac{1}{3\omega^2/c^2} + \frac{1}{4\pi \frac{\omega^2}{c^2} \frac{\tilde{\alpha}_H(\omega)}{a^3}} \right] \\ &= \frac{k^2}{\frac{\omega^2}{c^2} \left(\frac{\omega^2}{c^2} - k^2 \right)^2}. \end{aligned} \quad (9.13)$$

Note that the bare polarizabilities $\alpha_E(\omega)$ and $\alpha_H(\omega)$ drop out as they should. Thus the resulting index of refraction $n(\omega)$ introduced via $k = n(\omega)\omega/c$ solely depends on the renormalized physical polarizabilities $\tilde{\alpha}_E(\omega)$ and $\tilde{\alpha}_H(\omega)$. In complete agreement with the classical treatment we find [Kästel2007c] for $n(\omega)$

$$n(\omega) = \sqrt{1 + 4\pi \frac{\varrho \tilde{\alpha}_E(\omega)}{1 - \frac{4\pi}{3} \varrho \tilde{\alpha}_E(\omega)}} \sqrt{1 + 4\pi \frac{\varrho \tilde{\alpha}_H(\omega)}{1 - \frac{4\pi}{3} \varrho \tilde{\alpha}_H(\omega)}} \quad (9.14)$$

which therefore separates nicely into the permittivity (7.63) and the permeability (8.14).

We conclude that the microscopic treatment of chapters 7 – 9 supports the reasoning of section 6.2. In particular, (9.14) leads to the high density limit $n = -2 + i0$, i.e., predicts vanishing absorption with increasing density of scatterers. As already noted in section 6.2 this result seems unphysical. It indeed is a consequence of the assumptions made, the main one for the densities considered here being:

Only pure electromagnetic interactions are considered. Interatomic collisions, or collisions of atoms with phonons are not taken into account as the simple cubic lattice is assumed to be rigid.

Collisions would most importantly add dephasing rates to the free space linewidth, which would therefore become density dependent. Thus the high

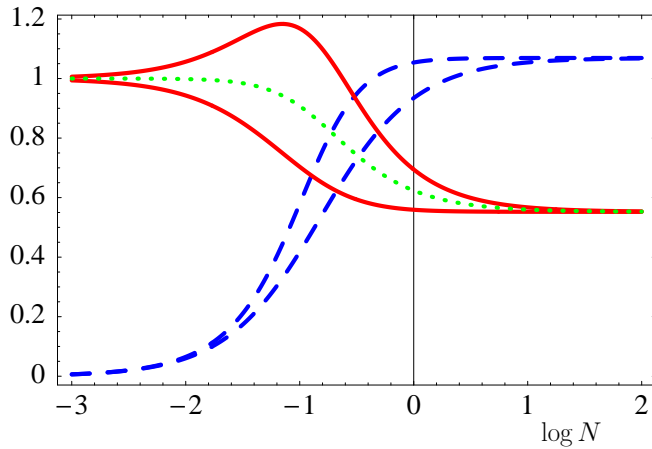


Figure 9.2: Real (solid) and imaginary (dashed) parts of the permittivity $\varepsilon(0)$ and the permeability $\mu(0)$ as well as the imaginary (dotted) part of $n(0) = \sqrt{\varepsilon(0)\mu(0)}$ as a function of the rescaled density parameter N . The linewidth is assumed to be density dependent $\gamma = \gamma_0(1 + \beta N)$ with $\beta = 10$.

density limit will depend crucially on the specific type of density dependence of the additional collisional broadening.

For illustration purposes we consider a linear density dependence of the linewidth assuming

$$\gamma = \gamma_0(1 + \beta N) \quad (9.15)$$

with $\beta > 0$. We apply the notation from section 6.2 using a single resonance model for the permittivity as well as the permeability. In particular $N = d^2\varrho/(2\hbar\gamma_0)$ holds¹. Fig. 9.2 shows the resulting density dependence of the response functions on resonance using (9.15) with $\beta = 10$ rather than $\beta = 0$ as in Fig. 6.3(d). Note that the index of refraction takes on positive values including strong absorption with increasing number density of scatterers. Note further that this general conclusion is not specific to the choice of linear density dependence but for intermediate densities is valid for higher exponents as well.

¹Cf. section (6.2).

Part III

Purcell effect over macroscopic
distances using negative-index
materials

CHAPTER 10

Macroscopic field quantization and atomic linewidth

This part is devoted to the Purcell effect [114]¹ displayed by emitters put in front of a (perfect) mirror. The presence of the mirror leads to a deformation of the local density of states of the electromagnetic field. As the available electromagnetic modes represent final states of a spontaneous decay process it is apparent from Fermi's golden rule that the natural linewidth will depend on the surrounding geometry.

After the quantization procedure for electromagnetic fields including arbitrary geometries presented by linear response functions ε and μ has shortly been reviewed in the present chapter we will focus on a geometry given by a perfect mirror coated with a negatively refracting medium in chapter 11. We show in particular that for the case of this layer having $\varepsilon = \mu = -1$ the Purcell effect known from an atom put onto the surface of a perfect mirror now takes place for potentially macroscopic distances between the atom and the mirror. In chapter 12 limitations of this findings due to absorption, finite transversal extension of the geometry and frequency dispersion will be analyzed.

¹See also section 6.1.

10.1 Quantization of the electromagnetic field in the presence of macroscopic bodies

The usual scheme used to quantize the electromagnetic field in vacuum can not be applied to situations in which boundary conditions due to dispersing and absorbing macroscopic bodies have to be fulfilled. This is due to the fact that the electromagnetic field in the presence of absorption can no longer be decomposed into modes. Instead we here use a quantization scheme which is based on classical Green functions in the macroscopic linear passive medium [66, Kästel2003]. This Green function implicitly contains information about all spatial and spectral properties and can be viewed as a generalization of the mode decomposition technique.

We start from the Heisenberg equation of the electric field operator in time Fourier space, i.e., the Helmholtz equation (9.3) without free sources

$$\left[\nabla \times \nabla \times -\frac{\omega^2}{c^2} \right] \hat{\mathbf{E}}(\mathbf{r}, \omega) = 4\pi \frac{\omega^2}{c^2} \hat{\mathbf{P}}(\mathbf{r}, \omega) + 4\pi i \frac{\omega}{c} \nabla \times \hat{\mathbf{M}}(\mathbf{r}, \omega). \quad (10.1)$$

In contrast to part II we do not focus on finding the Green function or equivalently the T -matrix for a microscopic arrangement of scatterers, though. Instead the polarization $\hat{\mathbf{P}}$ and magnetization $\hat{\mathbf{M}}$ are related to the electric and magnetic field strengths by macroscopic susceptibilities, respectively. For absorbing media we additionally have to introduce Langevin noise operators [65] in order to preserve the quantum mechanical commutation relations

$$\hat{\mathbf{P}}(\mathbf{r}, \omega) = \chi_e(\mathbf{r}, \omega) \hat{\mathbf{E}}(\mathbf{r}, \omega) + \hat{\mathbf{P}}_N(\mathbf{r}, \omega), \quad (10.2)$$

$$\hat{\mathbf{M}}(\mathbf{r}, \omega) = \chi_m(\mathbf{r}, \omega) \hat{\mathbf{B}}(\mathbf{r}, \omega) + \hat{\mathbf{M}}_N(\mathbf{r}, \omega). \quad (10.3)$$

In a microscopic description the noise operators can ultimately be related to matter operators. Since magnetization \mathbf{M} and polarization \mathbf{P} result in general from different constituents of the material we have to distinguish noise operators for \mathbf{P} and \mathbf{M} . Since $\langle \hat{\mathbf{P}}_N(\mathbf{r}, \omega) \rangle = 0$ and $\langle \hat{\mathbf{M}}_N(\mathbf{r}, \omega) \rangle = 0$ hold for the noise sources the expectation values of equations (10.2) and (10.3) simplify to the classical relations.

We introduce the classical Green function as in chapter 7 via

$$\hat{\mathbf{E}}(\mathbf{r}, \omega) = 4\pi i \frac{\omega}{c^2} \int d^3 \mathbf{r}' \mathcal{G}(\mathbf{r}, \mathbf{r}', \omega) \hat{\mathbf{j}}_N(\mathbf{r}', \omega) \quad (10.4)$$

with the tensor valued Green function now being a solution of

$$\left[\nabla^{\mathbf{r}} \times \frac{1}{\mu(\mathbf{r}, \omega)} \nabla^{\mathbf{r}} \times -\frac{\omega^2}{c^2} \varepsilon(\mathbf{r}, \omega) \right] \mathcal{G}(\mathbf{r}, \mathbf{r}', \omega) = \delta(\mathbf{r} - \mathbf{r}'). \quad (10.5)$$

Here $\mu(\mathbf{r}, \omega) = [1 - 4\pi\chi_m(\mathbf{r}, \omega)]^{-1}$ and $\varepsilon(\mathbf{r}, \omega) = 1 + 4\pi\chi_e(\mathbf{r}, \omega)$ are the in general inhomogeneous and frequency dependent complex permeability and permittivity, respectively. In contrast to part II the electric field (10.4) here is not given by free sources but is entirely determined by the quantum noise source

$$\hat{\mathbf{j}}_N(\mathbf{r}', \omega) = -i\omega \hat{\mathbf{P}}_N(\mathbf{r}, \omega) + c \nabla \times \hat{\mathbf{M}}_N(\mathbf{r}, \omega), \quad (10.6)$$

i.e., (10.4) gives the quantum mechanical vacuum electric field operator.

We rewrite the noise polarization $\hat{\mathbf{P}}_N(\mathbf{r}, \omega)$ and the noise magnetization $\hat{\mathbf{M}}_N(\mathbf{r}, \omega)$ using

$$\hat{\mathbf{P}}_N(\mathbf{r}, \omega) = -\sqrt{\frac{\hbar}{4\pi^2} \text{Im}[\varepsilon(\mathbf{r}, \omega)]} \hat{\mathbf{f}}^{(e)}(\mathbf{r}, \omega) \quad (10.7)$$

and

$$\hat{\mathbf{M}}_N(\mathbf{r}, \omega) = i\sqrt{\frac{\hbar}{4\pi^2} |\text{Im}[\kappa(\mathbf{r}, \omega)]|} \hat{\mathbf{f}}^{(m)}(\mathbf{r}, \omega) \quad (10.8)$$

with $\kappa(\mathbf{r}, \omega) = 1/\mu(\mathbf{r}, \omega)$ being the inverse permeability. It can be shown [66, Kästel2003] that the assumption of independent bosonic commutation relations

$$\begin{aligned} \left[f_k^{(a)}(\mathbf{r}, \omega), f_{k'}^{(b)\dagger}(\mathbf{r}', \omega') \right] &= \delta_{ab} \delta_{kk'} \delta(\mathbf{r} - \mathbf{r}') \delta(\omega - \omega') \\ \left[f_k^{(a)}(\mathbf{r}, \omega), f_{k'}^{(b)}(\mathbf{r}', \omega') \right] &= 0 \end{aligned} \quad (10.9)$$

for the noise polarization and magnetization leads to the correct equal time² commutation relations of the electromagnetic field operators

$$\begin{aligned} \left[\hat{E}_k(\mathbf{r}, t), \hat{E}_{k'}(\mathbf{r}', t) \right] &= 0 = \left[\hat{B}_k(\mathbf{r}, t), \hat{B}_{k'}(\mathbf{r}', t) \right], \\ \left[\hat{E}_k(\mathbf{r}, t), \hat{B}_{k'}(\mathbf{r}', t) \right] &= -i\hbar 4\pi c \varepsilon_{kk'l} \partial_l^{\mathbf{r}} \delta(\mathbf{r} - \mathbf{r}'). \end{aligned} \quad (10.10)$$

²Time dependent operators are given by Fourier transforming according to $\hat{O}(t) = \int_0^\infty d\omega e^{-i\omega t} \hat{O}(\omega) + \text{h.c.} = \hat{O}^{(+)}(t) + \hat{O}^{(-)}(t)$.

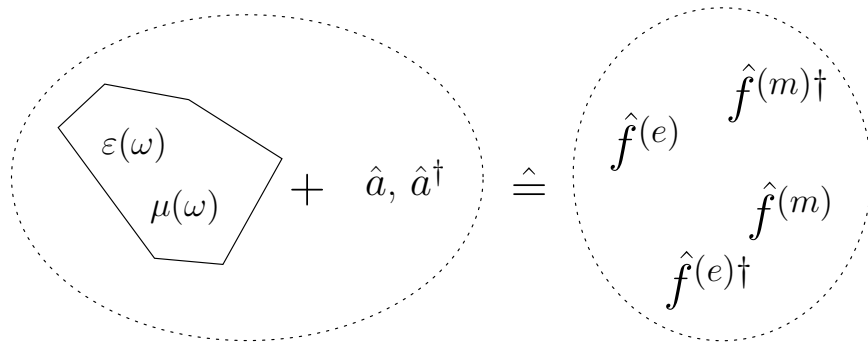


Figure 10.1: Sketch of the quantization scheme of the electromagnetic field in the presence of macroscopic magneto-dielectric bodies.

Note that in the course of proving (10.10) the relation

$$\begin{aligned} \text{Im} [\mathcal{G}_{ij}(\mathbf{r}, \mathbf{r}', \omega)] &= \int d^3\mathbf{s} \frac{\omega^2}{c^2} \text{Im}[\varepsilon(\mathbf{s}, \omega)] \mathcal{G}_{im}(\mathbf{r}, \mathbf{s}, \omega) \mathcal{G}_{jm}^*(\mathbf{r}', \mathbf{s}, \omega) \\ &+ \int d^3\mathbf{s} |\text{Im}[\kappa(\mathbf{s}, \omega)]| \partial_n^{\mathbf{s}} \mathcal{G}_{im}(\mathbf{r}, \mathbf{s}, \omega) [\partial_n^{\mathbf{s}} \mathcal{G}_{jm}^*(\mathbf{r}', \mathbf{s}, \omega) - \partial_m^{\mathbf{s}} \mathcal{G}_{jn}^*(\mathbf{r}', \mathbf{s}, \omega)] \end{aligned} \quad (10.11)$$

has to be applied which will get important in the following as well.

It is worth noticing that in the vacuum limit $\varepsilon(\mathbf{r}, \omega) \rightarrow 1 + i0$, $\mu(\mathbf{r}, \omega) \rightarrow 1 + i0$ the quantization scheme presented here attains [66, 144] the well known plane wave mode decomposition quantization scheme [65].

Hence (10.4) defines a valid quantization of the electromagnetic quantum vacuum in the presence of general linear and passive magneto-dielectric bodies. As a summary the electromagnetic fields and the macroscopic material distributions are getting combined to a medium-assisted electromagnetic field and subsequently quantized as sketched in Fig. 10.1.

10.2 Spontaneous decay rate

In order to find an expression for the natural linewidth of an atom coupled to the quantized electromagnetic field we need to consider time evolution

problems. We thus first note that the Hamilton operator of the field reads

$$\hat{H}_F = \int d^3\mathbf{r} \int_0^\infty d\omega \sum_{a=e,m} \hbar\omega \hat{\mathbf{f}}^{(a)\dagger}(\mathbf{r}, \omega) \cdot \hat{\mathbf{f}}^{(a)}(\mathbf{r}, \omega). \quad (10.12)$$

We next introduce a 2-level atom with transition frequency ω_A which is governed by the atomic Hamilton operator

$$\hat{H}_A = \hbar\omega_A |u\rangle\langle u| \quad (10.13)$$

where $|u\rangle\langle u|$ is the projector onto the upper state $|u\rangle$. Note that this extra atom does not belong to the macroscopic bodies included in the quantization process obtained in section 10.1. The interaction between atom and medium-assisted electromagnetic field in dipole and rotating wave approximations is given by [66, 145]

$$\hat{H}_I = -\hat{\sigma}^\dagger \hat{\mathbf{E}}^{(+)}(\mathbf{r}_A) \cdot \mathbf{d} - \text{h.c.} \quad (10.14)$$

where $\sigma = |l\rangle\langle l|$ with $|l\rangle$ being the atomic ground state.

The sought time evolution of the system is given by the Schrödinger equation

$$i\hbar \frac{d}{dt} |\Psi\rangle = \hat{H} |\Psi\rangle \quad (10.15)$$

where $\hat{H} = \hat{H}_F + \hat{H}_A + \hat{H}_I$ is the full Hamilton operator. We expand the state vector according to

$$|\Psi\rangle = C_u(t) e^{-i\omega_A t} |u\rangle \otimes |0\rangle + \int d^3\mathbf{r} \int_0^\infty d\omega \sum_{a=e,m} C_i^{(a)}(\mathbf{r}, \omega, t) e^{-i\omega t} |l\rangle \otimes |1_i^{(a)}, \mathbf{r}, \omega\rangle. \quad (10.16)$$

Here $|1_i^{(a)}, \mathbf{r}, \omega\rangle = f_i^{(a)}(\mathbf{r}, \omega) |0\rangle$ are one-photon Fock states of the electromagnetic field including macroscopic bodies which are characterized by the permittivity ε and the permeability μ and $|0\rangle$ denotes the electromagnetic vacuum state. From the Schrödinger equation we derive differential equations for the probability amplitudes $C_u(t)$ of the atomic upper state

$$\begin{aligned} \dot{C}_u(t) = & -\frac{i}{\hbar} \int_0^\infty d\omega \frac{4\pi\omega d_k}{c} \sqrt{\frac{\hbar}{4\pi^2}} \int d^3\mathbf{r} \\ & \cdot \left[\frac{\omega}{c} \sqrt{\text{Im}[\varepsilon(\mathbf{r}, \omega)]} \mathcal{G}_{kj}(\mathbf{r}_A, \mathbf{r}, \omega) C_j^{(e)}(\mathbf{r}, \omega, t) \right. \\ & \left. - \sqrt{|\text{Im}[\kappa(\mathbf{r}, \omega)]|} \varepsilon_{jmn} \partial_m^{\mathbf{r}} \mathcal{G}_{kj}(\mathbf{r}_A, \mathbf{r}, \omega) C_n^{(m)}(\mathbf{r}, \omega, t) \right] e^{-i(\omega - \omega_A)t} \end{aligned} \quad (10.17)$$

as well as the electromagnetic field probabilities

$$\begin{aligned} \dot{C}_i^{(e)}(\mathbf{r}, \omega, t) = & -\frac{i}{\hbar} \frac{4\pi\omega d_k}{c} \sqrt{\frac{\hbar}{4\pi^2}} \frac{\omega}{c} \\ & \cdot \sqrt{\text{Im}[\varepsilon(\mathbf{r}, \omega)]} \mathcal{G}_{ki}^*(\mathbf{r}_A, \mathbf{r}, \omega) C_u(t) e^{i(\omega - \omega_A)t} \end{aligned} \quad (10.18)$$

and

$$\begin{aligned} \dot{C}_i^{(m)}(\mathbf{r}, \omega, t) = & \frac{i}{\hbar} \frac{4\pi\omega d_k}{c} \sqrt{\frac{\hbar}{4\pi^2}} \\ & \cdot \sqrt{|\text{Im}[\kappa(\mathbf{r}, \omega)]|} \varepsilon_{jmi} \partial_m^{\mathbf{r}} \mathcal{G}_{kj}^*(\mathbf{r}_A, \mathbf{r}, \omega) C_u(t) e^{i(\omega - \omega_A)t}. \end{aligned} \quad (10.19)$$

Including the boundary condition $C_i^{(a)}(\mathbf{r}, \omega, 0) = 0$ we integrate the differential equations (10.18) and (10.19) of the photonic probability amplitudes formally, and plug the solutions into (10.17). As a result of (10.11) the upper state population of the atom is thus governed by the integro-differential equation

$$\dot{C}_u(t) = - \int_0^\infty d\omega \frac{4\omega^2 d_k d_l}{\hbar c^2} \text{Im}[\mathcal{G}_{kl}(\mathbf{r}_A, \mathbf{r}_A, \omega)] \int_0^t d\tau e^{-i(\omega - \omega_A)(t - \tau)} C_u(\tau). \quad (10.20)$$

In order to find an approximate analytical solution we assume that the frequency spectrum of the Green function is sufficiently flat such that the ω -integration would yield a sharply peaked function in time. Hence we are allowed to extend the lower limit of the τ -integration to $-\infty$. Furthermore the time scale on which the upper state population changes shall be small compared to the aforementioned sharply peaked function in time. Thus we take the quantity $C_u(\tau)$ at time t with little error. After having applied this so called Markov approximation the time integral can be evaluated analytically with the result

$$\dot{C}_u(t) = - \int_0^\infty d\omega \frac{4\omega^2 d_k d_l}{\hbar c^2} \text{Im}[\mathcal{G}_{kl}(\mathbf{r}_A, \mathbf{r}_A, \omega)] C_u(t) \left(\pi\delta(\omega - \omega_A) - i\mathcal{P} \frac{1}{\omega - \omega_A} \right) \quad (10.21)$$

or equivalently

$$\dot{C}_u(t) = \left(-\frac{\gamma_A}{2} + i\delta\omega_A \right) C_u(t). \quad (10.22)$$

The coefficients are given by

$$\gamma_A = \frac{8\pi\omega_A^2 d_k d_l}{\hbar c^2} \text{Im}[\mathcal{G}_{kl}(\mathbf{r}_A, \mathbf{r}_A, \omega_A)] \quad (10.23)$$

and

$$\delta\omega_A = \frac{4d_k d_l}{\hbar} \mathcal{P} \int_0^\infty d\omega \frac{\omega^2}{c^2} \frac{\text{Im}[\mathcal{G}_{kl}(\mathbf{r}_A, \mathbf{r}_A, \omega)]}{\omega - \omega_A} \quad (10.24)$$

and denote the spontaneous upper state population decay rate and the Lamb shift, respectively. Note that $\delta\omega_A$ though does not give correct results as the Lamb shift is a relativistic effect.

In contrast γ_A represents a valid result. The atomic decay rate in vacuum for example can be found from the corresponding Green function given in Appendix A. We note that $\text{Im}[\mathcal{G}^{(0)}(\mathbf{r}_A, \mathbf{r}_A, \omega_A)] = 1\omega_A/(6\pi c)$ holds, therefore (10.23) reduces to the well known Wigner-Weisskopf solution (2.5)

$$\gamma_A^{(0)} = \frac{4\omega_0^3 d_A^2}{3\hbar c^3}. \quad (10.25)$$

In general we conclude from (10.23) that the natural linewidth depends on the photonic density of modes given by the Green function which is commonly known as Purcell effect.

CHAPTER 11

Modified Purcell effect in front of a mirror

In this chapter we discuss a modification of the Purcell effect in front of a mirror which alleviates the necessity to bring the radiating dipole within a distance smaller than λ to the surface. We consider the Purcell effect of a 2-level atom in front of a mirror covered by a layer of a material with an index of refraction $n = -1$ [cf. Fig. 11.1(a)]. As discussed in chapter 1 such a layer forms a perfect lens [cf. Fig. 1.1] when placed in vacuum.

Without the layer the upper state population decay rate displays strong deviations from the free space rate if the distance of the atom to the surface of the mirror is decreased below the transition wavelength [122]. In a classical explanation [see Fig. 11.1(b)] the field amplitudes of the emitting dipole and the induced mirror dipole interfere. For dipole polarizations parallel to the surface these two fields are of the same strength but differ by a phase π as soon as the distance of the atom and the mirror tend to zero. Hence the respective decay rate should vanish exactly. Contrary for a perpendicular polarization the decay rate is expected to be enhanced due to constructive interference.

A major drawback of this effect is that it takes place only in the close vicinity of a solid interface which represents a major experimental obstacle. Consequently only few experimental publications exist [121, 123, 124, 125] and there are no technological applications. As we show below coating the

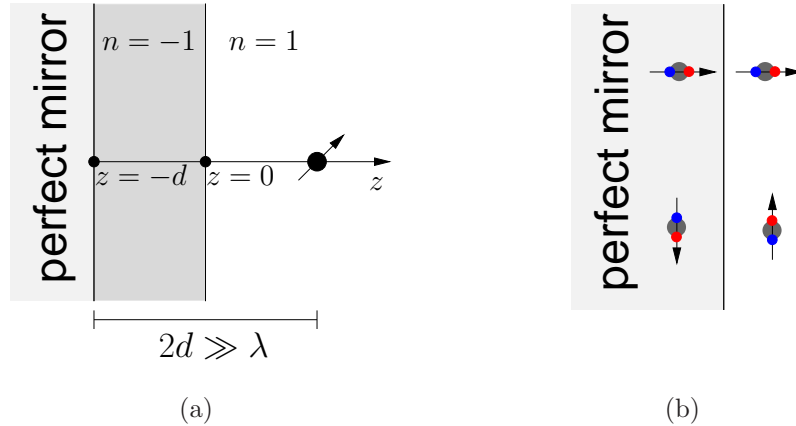


Figure 11.1: (a) Atom in front of a perfect lens attached to a mirror. The atom is placed in its own focus. (b) Mirror dipoles for parallel and perpendicular polarization

mirror with a slab of a $\varepsilon = \mu = -1$ material avoids this obstacle. The negative index slab acts as a perfect lens which virtually transfers the presence of the mirror regarding electromagnetic fields to a potentially macroscopic distance into free space.

11.1 Green function for 3-layered media

To tackle these problems of an atom in front of a mirror with and without a layer of a negative index material with $n = -1$ we note from (10.23) that we need to find the corresponding Green functions. We will hence give the retarded Green function corresponding to a 3-layer geometry as it includes both cases.

The Green function of a homogeneous magneto-dielectric material with permittivity $\varepsilon(\omega)$ and permeability $\mu(\omega)$ expanded into plane waves can be written as [146]

$$\begin{aligned} \mathcal{G}^{(0)}(\mathbf{r}, \mathbf{r}', \omega) &= -\mathbf{e}_z \otimes \mathbf{e}_z \frac{\delta(\mathbf{r} - \mathbf{r}')}{k^2} \mu(\omega) \\ &+ \frac{i\mu(\omega)}{8\pi^2} \int d^2 k_{\perp} \frac{1}{k_z} \begin{cases} [\hat{\mathbf{e}} \otimes \hat{\mathbf{e}} + \hat{\mathbf{h}}_f \otimes \hat{\mathbf{h}}_f] e^{i\mathbf{k}(\mathbf{r}-\mathbf{r}')} & z > z' \\ [\hat{\mathbf{e}} \otimes \hat{\mathbf{e}} + \hat{\mathbf{h}}_b \otimes \hat{\mathbf{h}}_b] e^{i\mathbf{K}(\mathbf{r}-\mathbf{r}')} & z < z' \end{cases} \end{aligned} \quad (11.1)$$

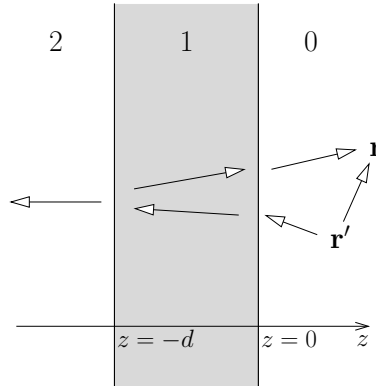


Figure 11.2: 3-layer geometry with the spatial regions 0 ($z > 0$), 1 ($-d \leq z \leq 0$), and 2 ($z < -d$). The Green function for the case of \mathbf{r} and \mathbf{r}' being placed in region 0 simultaneously is given by a superposition of the direct path and a reflected path.

which is well suited for the planar geometry depicted in Fig. 11.1. It is given by a superposition of either forward [$\mathbf{k} = (k_x, k_y, k_z)$] or backward [$\mathbf{K} = (k_x, k_y, -k_z)$] traveling plane waves with a polarization given by projections onto the respective transverse basis vectors $\hat{\mathbf{e}} = \mathbf{k} \times \mathbf{e}_z / |\mathbf{k} \times \mathbf{e}_z|$ and $\hat{\mathbf{h}}_f = \hat{\mathbf{e}} \times \mathbf{k} / |k|$ or $\hat{\mathbf{h}}_b = \hat{\mathbf{e}} \times \mathbf{K} / |k|$ denoting TE and TM modes, respectively. In equation (11.1) \otimes denotes a dyadic product, $k_{\perp} = \sqrt{k_x^2 + k_y^2} > 0$ the perpendicular wave vector component ($d^2 k_{\perp} = dk_x dk_y$) and $k_z = \sqrt{k^2 - k_{\perp}^2}$ with $k^2 = |\mathbf{k}|^2 = \varepsilon(\omega) \mu(\omega) \omega^2 / c^2$.

The Green function for the full 3-layer geometry as defined in Fig. 11.2 can be constructed from (11.1) by appropriate superposition of forward and backward waves. In particular, the Green function $\mathcal{G}^{(00)}$ for which \mathbf{r} and \mathbf{r}' are assumed to be in the vacuum region 0 [$\varepsilon_0(\omega) = \mu_0(\omega) = 1$] is given by ($z < z'$)

$$\begin{aligned} \mathcal{G}^{(00)}(\mathbf{r}, \mathbf{r}', \omega) &= \frac{i}{8\pi^2} \int d^2 k_{\perp} \frac{1}{k_z} e^{-i\mathbf{K}\mathbf{r}'} \cdot \\ &\left[(R^{\text{TE}} e^{i\mathbf{k}\cdot\mathbf{r}} \hat{\mathbf{e}} + e^{i\mathbf{K}\cdot\mathbf{r}} \hat{\mathbf{e}}) \otimes \hat{\mathbf{e}} + (R^{\text{TM}} e^{i\mathbf{k}\cdot\mathbf{r}} \hat{\mathbf{h}}_f + e^{i\mathbf{K}\cdot\mathbf{r}} \hat{\mathbf{h}}_b) \otimes \hat{\mathbf{h}}_b \right]. \end{aligned} \quad (11.2)$$

Here R^{TE} , R^{TM} are reflection coefficients for TE and TM waves, respectively.

Likewise $\mathcal{G}^{(10)}$, i.e., for \mathbf{r} in region 1, reads

$$\begin{aligned}\mathcal{G}^{(10)}(\mathbf{r}, \mathbf{r}', \omega) = & \frac{i}{8\pi^2} \int d^2 k_{\perp} \frac{1}{k_z} \left[(C_f^{\text{TE}} e^{i\mathbf{k}_1 \cdot \mathbf{r}} \hat{\mathbf{e}}_1 + C_b^{\text{TE}} e^{i\mathbf{K}_1 \cdot \mathbf{r}} \hat{\mathbf{e}}_1) \otimes \hat{\mathbf{e}} \right. \\ & \left. + (C_f^{\text{TM}} e^{i\mathbf{k}_1 \cdot \mathbf{r}} \hat{\mathbf{h}}_{f,1} + C_b^{\text{TM}} e^{i\mathbf{K}_1 \cdot \mathbf{r}} \hat{\mathbf{h}}_{b,1}) \otimes \hat{\mathbf{h}}_b \right] e^{-i\mathbf{K}\mathbf{r}'}\end{aligned}\quad (11.3)$$

where the index 1 denotes the z component of the wave vector to be explicitly given by the permittivity $\varepsilon_1(\omega)$ and permeability $\mu_1(\omega)$ of medium 1, $k_{z,1} = \sqrt{\varepsilon_1(\omega)\mu_1(\omega)\omega^2/c^2 - k_{\perp}^2}$, and finally $\mathcal{G}^{(20)}$ is given by

$$\mathcal{G}^{(20)}(\mathbf{r}, \mathbf{r}', \omega) = \frac{i}{8\pi^2} \int d^2 k_{\perp} \frac{1}{k_z} [T^{\text{TE}} \hat{\mathbf{e}}_2 \otimes \hat{\mathbf{e}} + T^{\text{TM}} \hat{\mathbf{h}}_{b,2} \otimes \hat{\mathbf{h}}_b] e^{i\mathbf{K}_2 \cdot \mathbf{r}} e^{-i\mathbf{K}\cdot \mathbf{r}'} \quad (11.4)$$

with corresponding TE and TM transmission coefficients.

Applying the boundary condition for electric and magnetic fields at the interface between regions 0 and 1 [$\mathbf{r} = (x, y, 0)$]

$$\mathbf{e}_z \times \mathcal{G}^{00}(\mathbf{r}, \mathbf{r}', \omega) = \mathbf{e}_z \times \mathcal{G}^{10}(\mathbf{r}, \mathbf{r}', \omega), \quad (11.5)$$

$$\frac{1}{\mu_0(\omega)} \mathbf{e}_z \times [\nabla^{\mathbf{r}} \times \mathcal{G}^{00}(\mathbf{r}, \mathbf{r}', \omega)] = \frac{1}{\mu_1(\omega)} \mathbf{e}_z \times [\nabla^{\mathbf{r}} \times \mathcal{G}^{10}(\mathbf{r}, \mathbf{r}', \omega)] \quad (11.6)$$

as well as at the interface between regions 1 and 2 [$\mathbf{r} = (x, y, -d)$]

$$\mathbf{e}_z \times \mathcal{G}^{10}(\mathbf{r}, \mathbf{r}', \omega) = \mathbf{e}_z \times \mathcal{G}^{20}(\mathbf{r}, \mathbf{r}', \omega), \quad (11.7)$$

$$\frac{1}{\mu_1(\omega)} \mathbf{e}_z \times [\nabla^{\mathbf{r}} \times \mathcal{G}^{10}(\mathbf{r}, \mathbf{r}', \omega)] = \frac{1}{\mu_2(\omega)} \mathbf{e}_z \times [\nabla^{\mathbf{r}} \times \mathcal{G}^{20}(\mathbf{r}, \mathbf{r}', \omega)] \quad (11.8)$$

we find the reflection coefficients of TE and TM waves

$$R^{\text{TE}} = \frac{R_{01} + R_{12} e^{i2k_{z,1}d}}{1 + R_{01} R_{12} e^{i2k_{z,1}d}} \quad (11.9)$$

and

$$R^{\text{TM}} = \frac{S_{01} + S_{12} e^{i2k_{z,1}d}}{1 + S_{01} S_{12} e^{i2k_{z,1}d}}. \quad (11.10)$$

Here, R_{ij} and S_{ij} are the basic reflection coefficients at the boundaries between the regions i and j for TE and TM modes

$$R_{ij} = \frac{\mu_j(\omega)k_{z,i} - \mu_i(\omega)k_{z,j}}{\mu_j(\omega)k_{z,i} + \mu_i k_{z,j}}, \quad S_{ij} = \frac{\varepsilon_j(\omega)k_{z,i} - \varepsilon_i(\omega)k_{z,j}}{\varepsilon_j(\omega)k_{z,i} + \varepsilon_i(\omega)k_{z,j}}. \quad (11.11)$$

11.2 Purcell effect without $n = -1$ coating

According to (10.23) the Green function $\mathcal{G}^{(00)}(\mathbf{r}_A, \mathbf{r}_A, \omega_A)$ (11.2) together with the reflection coefficients R^{TE} and R^{TM} is sufficient to quantitatively describe the Purcell effect of atoms in such a 3-layer geometry. Setting $\varepsilon_1(\omega) = -\infty$, $\mu_1(\omega) = 1$ corresponds to the 0 – 1 interface being a perfect mirror, i.e., the scenario without mirror coating. As a result we find $R_{01} = -1$ and $S_{01} = 1$ from which we conclude

$$R^{\text{TE}} = -1, \quad R^{\text{TM}} = 1. \quad (11.12)$$

The decay rates for dipoles with parallel and perpendicular orientation read

$$\gamma_A^{\parallel} = \frac{8\pi\omega_A^2 d_x^2}{\hbar c^2} \text{Im} [\mathcal{G}_{xx}^{(00)}(\mathbf{r}_A, \mathbf{r}_A, \omega_A)] \quad (11.13)$$

and

$$\gamma_A^{\perp} = \frac{8\pi\omega_A^2 d_z^2}{\hbar c^2} \text{Im} [\mathcal{G}_{zz}^{(00)}(\mathbf{r}_A, \mathbf{r}_A, \omega_A)], \quad (11.14)$$

respectively. With $[\hat{\mathbf{e}} \otimes \hat{\mathbf{e}}]_{xx} = k_x^2/k_{\perp}^2$ and $[\hat{\mathbf{h}}_b \otimes \hat{\mathbf{h}}_b]_{xx} = -[\hat{\mathbf{h}}_f \otimes \hat{\mathbf{h}}_b]_{xx} = k_x^2 k_z^2/(k^2 k_{\perp}^2)$ the expression for γ_A^{\parallel} simplifies significantly to

$$\gamma_A^{\parallel} = \frac{\omega_A^2 d_x^2}{\hbar \pi c^2} \text{Re} \left[\int d^2 k_{\perp} \frac{k_x^2}{k_z k_{\perp}^2} (1 - e^{2ik_z z_A}) \left(1 + \frac{k_z^2}{k^2} \right) \right] \quad (11.15)$$

which can be integrated analytically to the expression ($k = \omega_A/c$)

$$\gamma_A^{\parallel} = \gamma_A^{(0)} \left[1 - \frac{3 \sin(2kz_A)}{4kz_A} - \frac{3 \cos(2kz_A)}{8k^2 z_A^2} + \frac{3 \sin(2kz_A)}{16k^3 z_A^3} \right]. \quad (11.16)$$

Similarly we find an expression corresponding to (11.15) for perpendicular dipole orientation using $[\hat{\mathbf{e}} \otimes \hat{\mathbf{e}}]_{zz} = 0$ and $[\hat{\mathbf{h}}_b \otimes \hat{\mathbf{h}}_b]_{zz} = [\hat{\mathbf{h}}_f \otimes \hat{\mathbf{h}}_b]_{zz} = k_{\perp}^2/k^2$

$$\gamma_A^{\perp} = \frac{2\omega_A^2 d_z^2}{\hbar \pi c^2} \text{Re} \left[\int d^2 k_{\perp} \frac{k_{\perp}^2}{k_z k^2} (1 + e^{2ik_z z_A}) \right]. \quad (11.17)$$

After performing the integrations this results in

$$\gamma_A^{\perp} = \gamma_A^{(0)} \left[1 - \frac{3 \cos(2kz_A)}{4k^2 z_A^2} + \frac{3 \sin(2kz_A)}{8k^3 z_A^3} \right]. \quad (11.18)$$

Note that (11.16) and (11.18) correspond identically to the classical result for the Purcell effect of an atom in front of a mirror [122]. In particular for emitters put directly onto the mirror ($z_A = 0$) we find indeed the two cases

$$\gamma_A^{\parallel} = 0, \quad \gamma_A^{\perp} = 2\gamma_A^{(0)}, \quad (11.19)$$

i.e., perfect suppression or enhancement by a factor of 2 for parallel and perpendicular orientations, respectively, as expected from the classical reasoning above.

11.3 Purcell effect including $n = -1$ coating

The second case of a perfect mirror plus a coating layer with $n = -1$ is found from analogous considerations. We set $\varepsilon_1(\omega) = \mu_1(\omega) = -1$ for the negative index material layer and $\varepsilon_2(\omega) = -\infty$, $\mu_2(\omega) = 1$ for region 2 as to get the properties of a perfect mirror at the interface 1 – 2. Noting that under these circumstances $k_{z,1} = -k_z$ due to the left-handedness of medium 1 with a negative index of refraction we find

$$R^{\text{TE}} = -e^{-2ik_z d}, \quad R^{\text{TM}} = e^{-2ik_z d} \quad (11.20)$$

for the TE and TM reflection coefficients, respectively, which lead to a spatial shift on the order of twice the lens thickness d . A comparison to (11.15) and (11.17) reveals that the space dependent spontaneous decay rates for the modified Purcell effect [Fig. 11.1(a)] are indeed given by (11.16) for parallel and (11.18) for perpendicular orientations with z_A replaced by $z_A - d$. In particular the values

$$\gamma_A^{\parallel} = 0, \quad \gamma_A^{\perp} = 2\gamma_A^{(0)} \quad (11.21)$$

are now found not at $z_A = 0$ but at $z_A = d$, i.e., depending on the thickness of the perfect lens layer, a distance d from the nearest surface in free space. Fig. 11.3 shows the corresponding distance dependent linewidths for parallel and perpendicular dipole orientations, respectively. Note that in the scaling used here the surface 0 – 1 is placed at $z = -d$. In particular the atom is a potentially macroscopic distance $2d$ from the perfect mirror when placed

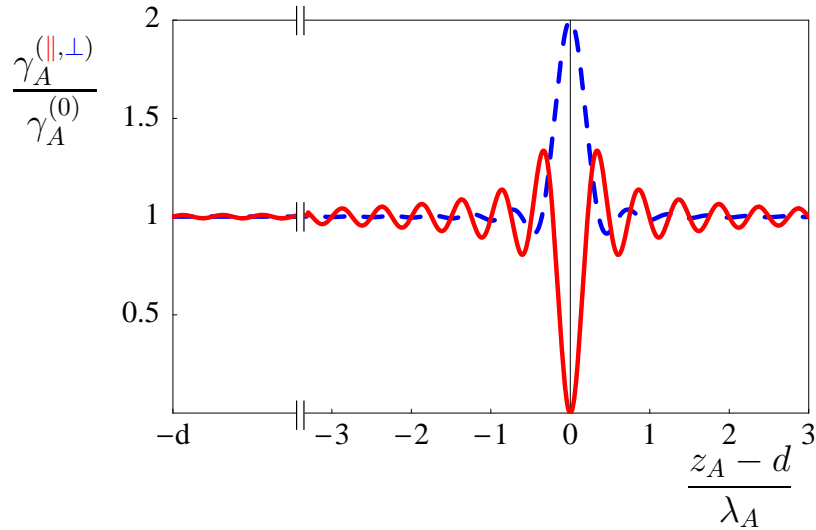


Figure 11.3: Spatial dependence of the normalized rate of spontaneous emission $\gamma_A^{\parallel}(z_A)/\gamma_A^{(0)}$ (solid) and $\gamma_A^{\perp}(z_A)/\gamma_A^{(0)}$ (dashed) to the mirror surface.

into its own focus in which the strongest deviations from the free space decay rate are obtained [Kästel2005a, Kästel2005b].

We conclude that a perfect lens of thickness d between a perfect mirror and an atom put at a distance $2d$ from the mirror allows for perfect suppression of the spontaneous decay rate. We emphasize that this setup removes the necessity of placing the atom within a distance smaller than λ to any surface. Thus experimental techniques based on atomic traps are potentially applicable which would enable single atom studies of the spatial dependence of the Purcell effect.

CHAPTER 12

Limitations

The investigation of the modified Purcell effect of an atom in front of a mirror covered by a negative index material layer in chapter 11 assumed idealized conditions and thus needs to be checked for realistic conditions in experiments. Furthermore, the effect of perfect suppression of spontaneous emission as the atom is put into its own focus seem to be valid independently of the distance to the layered medium which would contradict causality. We will hence study how the visibility of the suppression of γ_A^{\parallel} for $z_A = d$ is modified in the presence of absorption in the negative index layer and by a finite radius of the mirror/layer geometry. Finally, in section 12.3 we show that dispersion of the $n < 0$ material sets a maximum distance for the effect to be seen, in accordance with causality arguments.

12.1 Finite absorption of the negative-index material

From chapter 1 it is apparent that one of the most severe limitations of negative index media is given by strong absorption. Even combining $n < 0$ with electromagnetically induced transparency as in part I leaves small imaginary parts which can affect the performance of a flat lens significantly as soon as its thickness exceeds the transition wavelength λ_A substantially

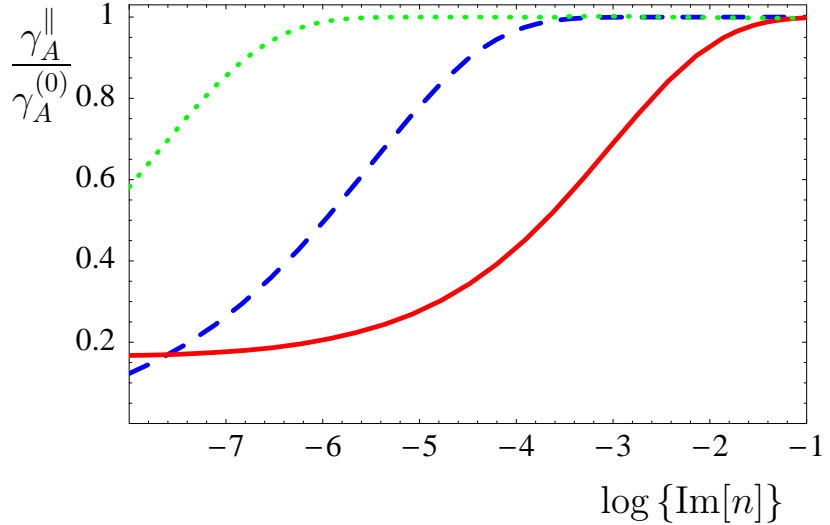


Figure 12.1: The spontaneous decay rate $\gamma_A^{\parallel}/\gamma_A^{(0)}$ as function of the imaginary part $\text{Im}[n]$ of the refractive index for different values of the layer thickness d : $d = 1\lambda_A$ (solid), $d = 10\lambda_A$ (dashed), and $d = 100\lambda_A$ (dotted).

[cf. (4.10)].

We study the influence of absorption losses by introducing a similar imaginary part to the permittivity $\varepsilon_1(\omega)$ and permeability $\mu_1(\omega)$ of the coating layer. This effectively introduces an imaginary part to the index of refraction as well $n = -1 + i\text{Im}[n]$ while the real part is assumed to still have the perfect value -1 . As a result, the reflection coefficients R^{TE} and R^{TM} and hence the Green function can not be simplified as in sections 11.2 and 11.3 but requires numerical integration. Fig. 12.1 shows the spontaneous decay rate $\gamma_A^{\parallel}/\gamma_A^{(0)}$ as a function of $\log\{\text{Im}[n]\}$ for different layer thicknesses d . The spatial position has been chosen $z_A = d$ where we have found perfect suppression for the idealized case. This suppression is still present for small absorption coefficients but is degraded as $\text{Im}[n]$ increases. We note that the results for $d = 10\lambda_A$ and $d = 100\lambda_A$ are entirely given by propagating modes, although for very small thickness and hence small distance of the emitter to the surface ($d = 1\lambda_A$) non-radiative decay channels start to play a role. This fact allows for a simple interpretation of the features found in Fig. 12.1 in terms of traveling beams. Increasing $\text{Im}[n]$ leads to absorption of propagating modes inside the

layer medium. For increasing thickness the emitter cannot “see” the mirror any more as soon as the absorption reaches a sufficient strength. For large enough absorption coefficients/thickness the decay rate therefore attains its free-space value. We note, however, that for sufficiently small thicknesses a visible effect should occur at absorption coefficients which seem realistic for media which employ electromagnetically induced transparency (cf. part I).

12.2 Finite transverse extension

The geometry discussed in chapter 11 suffers from an idealization, which can never be implemented in experiments: The transverse extension of the mirror including negative index coating is supposed to stretch to infinity. For a rigorous analytical treatment, this assumption is necessary, though, as the Green function can be expressed in closed form only in geometries with high symmetry.

Due to a finite radius this symmetry is no longer present. An approxi-

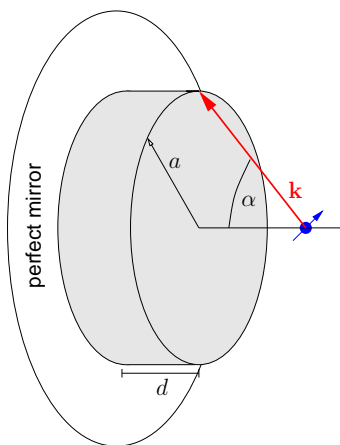


Figure 12.2: Finite extension of the geometry in transverse direction.

mative solution can be given, though, as the imaginary part of the Green function $\text{Im}[\mathcal{G}^{(00)}(\mathbf{r}_A, \mathbf{r}_A, \omega_A)]$ for non-absorbing layer media is only composed of propagating modes, i.e., modes with $k_{\perp} \leq k$. We assign an angle $\sin(\alpha) = k_{\perp}/k$ measured against the surface of the layered medium under

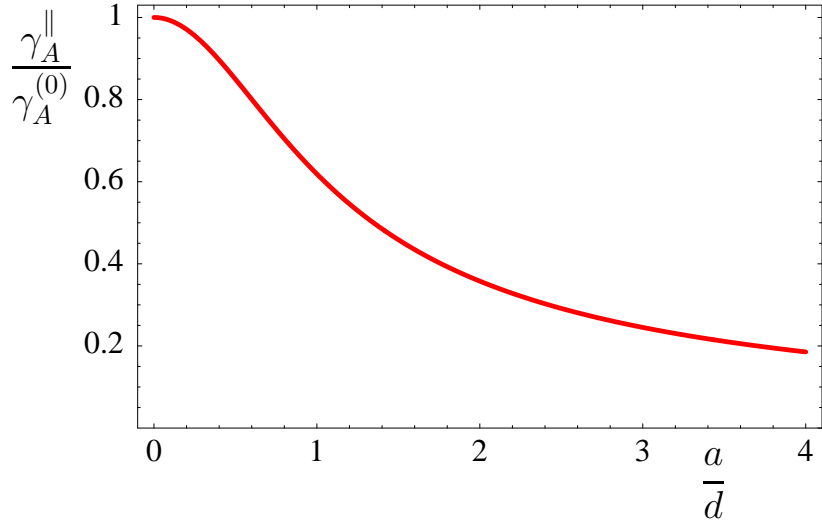


Figure 12.3: The spontaneous decay rate $\gamma_A^{\parallel}/\gamma_A^{(0)}$ as a function of transverse radius a of the negative index material with thickness $d = 1\lambda_A$. The mirror itself was assumed to be of the same dimension as the coating.

which such modes propagate. The maximum angle α_{\max} under which the coating is still present is given by $\sin(\alpha_{\max}) = a/\sqrt{a^2 + d^2}$, where the parameter a denotes the transverse extension of the negative index layer as depicted in Fig. 12.2. In order to simulate finite transverse radii we restrict the integration over transverse wave vectors k_{\perp} in the definition of the Green function (11.2) to values

$$k_{\perp} \leq k \frac{\frac{a}{d}}{\sqrt{1 + \left(\frac{a}{d}\right)^2}}. \quad (12.1)$$

As the mirror itself is assumed to have the same radius for angles greater than α_{\max} , we have to use the free space Green function. For $z_A = d$ the resulting integrations can be done analytically with the result

$$\frac{\gamma_A^{\parallel}}{\gamma_A^{(0)}} = \left(1 + \frac{3}{4}(a/d)^2\right) \left(\frac{1}{1 + (a/d)^2}\right)^{3/2}, \quad (12.2)$$

which is shown in Fig. 12.3. Note that for $z_A = d$ only angles α larger than α_{\max} contribute to (12.2). Note furthermore that the visibility of the

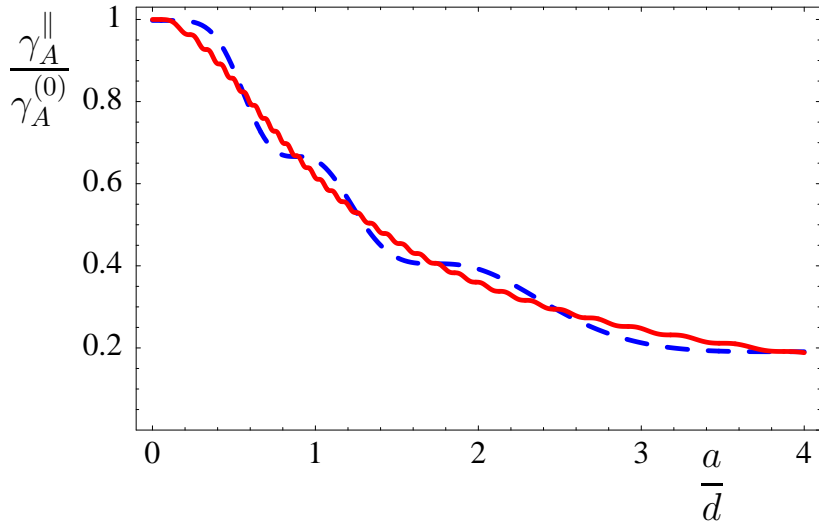


Figure 12.4: The spontaneous decay rate $\gamma_A^{\parallel}/\gamma_A^{(0)}$ as a function of the transverse radius a of the negative index material for $d = 10\lambda_A$ (solid) and $d = 1\lambda_A$ (dashed), respectively. The mirror itself was assumed to still extend to infinity.

suppression of $\gamma_A^{\parallel}/\gamma_A^{(0)}$ depends only on the ratio of the transverse radius a to the thickness d . As this ratio in experimental situations will usually be large, the limitation due to the transverse extension of the perfect lens does not degrade the effect significantly.

If we assume that only the coating layer has a finite radius but the mirror itself still extends to infinity for $\alpha > \alpha_{\max}$ we need to use $\text{Im}[\mathcal{G}^{(00)}(\mathbf{r}_A, \mathbf{r}_A, \omega_A)]$ with $n = +1$ rather than $n = -1$. Again only angles α larger than α_{\max} contribute so that the geometry thus corresponds to a mirror with a circular hole of radius a . As a result, diffraction effects are added to (12.2) such that a dependency on d remains as shown in Fig. 12.4. For increasing thickness (and thus distance d) they vanish, though, as the limit of ray optics is approached.

12.3 Dispersion effects

From the discussion above it seems as if the suppression of $\gamma_A^{\parallel}/\gamma_A^{(0)}$ would prevail for any distance d as long as the transverse extension of the mir-

ror/coating construction is large enough while the absorption coefficient $\text{Im}[n]$ stays negligible. For reasons of causality this must not be, though, as for distances d larger than $c/\gamma_A^{(0)}$ an atom would decay before any (virtual) photon reached the mirror in order to “find out” that the atom should not to be decaying at all.

We note from (10.23) that the spontaneous emission rate is determined by the imaginary part of the Green function $\text{Im}[\mathcal{G}(\mathbf{r}_A, \mathbf{r}_A, \omega_A)]$ taken at the transition frequency ω_A . Thus, due to the linewidth of the resonance the results from chapter 11 regarding the case of the index of refraction of the coating layer $n = -1$ are valid only as long as the spectral width in which $n \approx -1$ is larger than $\gamma_A^{(0)}$. From the constraint that the electromagnetic field energy be positive we conclude that media with a negative index of refraction are unavoidably dispersive¹, which requires that

$$\frac{d}{d\omega}(\omega \text{Re}[\varepsilon(\omega)]) \geq 0, \quad \frac{d}{d\omega}(\omega \text{Re}[\mu(\omega)]) \geq 0 \quad (12.3)$$

hold. In the following we show that it is this dispersion which sets a limit to the maximum distance for which $\gamma_A^{\parallel}/\gamma_A^{(0)} = 0$ for $z_A = d$ can be found.

On resonance, at which $n(\omega_A) = -1$ [$\varepsilon(\omega_A) = \mu(\omega_A) = -1$] holds, (12.3) implies a minimal dispersion

$$\frac{d}{d\omega}n(\omega_A) \geq \frac{1}{\omega_A}. \quad (12.4)$$

To see how dispersion affects the Green function $\mathcal{G}^{(00)}(\omega)$ we assume a linear dispersion $n(\omega) = -1 + \alpha(\omega - \omega_A)$, $\alpha \in \mathbb{R}$, around the resonance frequency ω_A . We estimate the exponential term $e^{2i(k_{z,1}+k_z)d}$ in (11.2) to be most sensitive to a variation of the index of refraction. Hence we keep terms linear in α in the exponential, and set $n = -1$ in all other terms. As a result we obtain approximately

$$\text{Im}[\mathcal{G}^{(00)}(\omega)] \sim \text{Re} \left[\int_0^1 d\xi \sqrt{1 - \xi^2} (1 + \xi^2) \left(1 - e^{i \frac{2\omega_A d}{c} \frac{1}{\xi} \alpha(\omega - \omega_A)} \right) \right]. \quad (12.5)$$

In order to prove this estimate, we numerically integrate the exact $\mathcal{G}^{(00)}(\omega)$ using a particular causal model for the permittivity and the permeability

$$\varepsilon(\omega) = \mu(\omega) = 1 + \frac{\omega_p^2}{\omega_0^2 - \omega^2 - i\gamma\omega_0} \quad (12.6)$$

¹Cf. chapter 1.

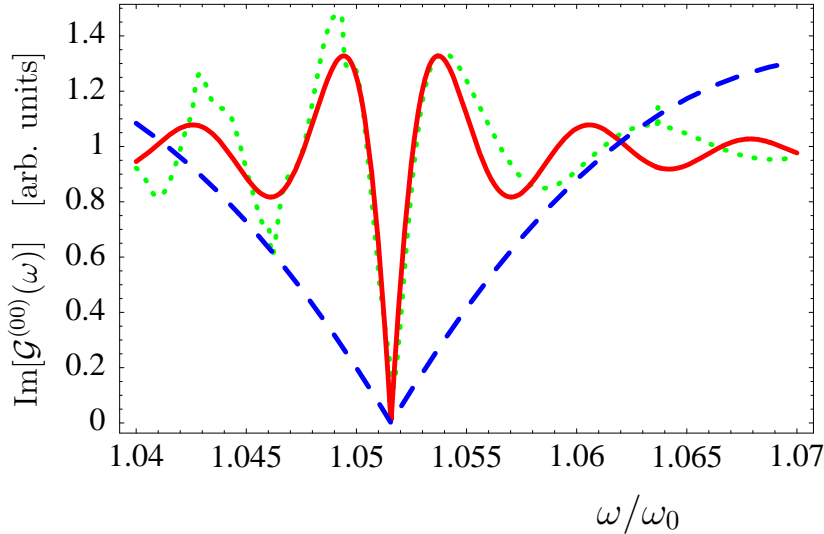


Figure 12.5: The approximate Green function $\text{Im}[\mathcal{G}^{(00)}(\omega)]$ from (12.5) using a linear dispersion model for $d = 10\lambda_A/(2\pi)$ (solid) and $d = 1\lambda_A/(2\pi)$ (dashed) as well as an exact integration of $\text{Im}[\mathcal{G}^{(00)}(\omega)]$ (dotted) using a causal model for $n(\omega)$ for $d = 10\lambda_A/(2\pi)$.

with $\omega_p = 0.46\omega_0$, $\gamma = 10^{-4}\omega_0$. This model yields $n(\omega_A) = -1 + i10^{-3}$ at a frequency $\omega_A \approx 1.05157\omega_0$. Correspondingly, the imaginary part of the Green function displays a strong dip near $\omega = \omega_A$ for $d = 10\lambda_A/(2\pi)$ as shown in Fig. 12.5. We compare this to the approximate solution (12.5) using the same parameters (including $\alpha = 39/\omega_0$) from (12.6). From Fig. 12.5 we note that the dip around $\omega = \omega_A$ is well described by (12.5), which suffices for our purpose.

In Fig. 12.5 we also show (12.5) using $d = 1\lambda_A/(2\pi)$, for which the spectral width $\Delta\omega$ of the dip in the Green function increases. In general we find from (12.5) that

$$\Delta\omega \approx \frac{c}{\omega_A d \alpha} \quad (12.7)$$

holds approximately. Remembering the lower bound on the dispersion $\alpha = \frac{d}{d\omega}n(\omega_A)$ in (12.4), we conclude that the frequency window of the Green function narrows with increasing distance d as

$$\Delta\omega \leq c/d. \quad (12.8)$$

As a consequence the assumption that the spectrum of the Green function is sufficiently flat, which is used in the Markov approximation, is violated if d is too large (cf. section 10.2). In particular, $\Delta\omega \gg \gamma_A^{(0)}$ must be fulfilled. Therefore the results of chapter 11 which implicitly made use of the Markov approximation only hold for

$$d \ll \frac{c}{\gamma_A^{(0)}}. \quad (12.9)$$

The condition (12.9) supports the simple picture used in the beginning of this section: The Purcell effect works only as long as the free space decay time is long compared to the time a photon travels to the mirror geometry.

Part IV

Appendices

APPENDIX A

The vacuum Green function

The Helmholtz equation (7.9) simplifies for $\alpha(\mathbf{r}, \omega) = 0$, i.e., for vacuum, to

$$\left[\frac{\omega^2}{c^2} \mathbb{1} - \nabla^{\mathbf{r}} \times \nabla^{\mathbf{r}} \times \right] \mathcal{G}^{(0)}(\mathbf{r} - \mathbf{r}', \omega) = \delta(\mathbf{r} - \mathbf{r}') \mathbb{1} \quad (\text{A.1})$$

with $\mathcal{G}^{(0)}(\mathbf{r} - \mathbf{r}', \omega)$ being the corresponding vacuum Green function. Note that due to the translational invariance, we already used

$$\mathcal{G}^{(0)}(\mathbf{r}, \mathbf{r}', \omega) = \mathcal{G}^{(0)}(\mathbf{r} - \mathbf{r}', \omega). \quad (\text{A.2})$$

Fourier transforming (A.1) with respect to the spatial coordinate yields

$$\left[\frac{\omega^2}{c^2} \mathbb{1} + \mathbf{k} \times \mathbf{k} \times \right] \widetilde{\mathcal{G}^{(0)}}(\mathbf{k}, \omega) = \mathbb{1} \quad (\text{A.3})$$

which can be inverted to find the \mathbf{k} -space representation of the vacuum Green function

$$\widetilde{\mathcal{G}^{(0)}}(\mathbf{k}, \omega) = \frac{1}{\frac{\omega^2}{c^2} \mathbb{1} - |\mathbf{k}|^2 \Delta_{\mathbf{k}}}. \quad (\text{A.4})$$

Here the projector $\Delta_{\mathbf{k}} = \mathbb{1} - \hat{\mathbf{k}} \otimes \hat{\mathbf{k}}$ onto a space transverse to $\hat{\mathbf{k}} = \mathbf{k}/k$ ($k = |\mathbf{k}|$) has been introduced. The matrix elements of the dyadic product $\hat{\mathbf{k}} \otimes \hat{\mathbf{k}}$ are given by

$$(\hat{\mathbf{k}} \otimes \hat{\mathbf{k}})_{ij} = \frac{1}{k^2} k_i k_j. \quad (\text{A.5})$$

The explicit solution to (A.1) is found by Fourier transforming (A.4) back into real space [134]. The retarded version reads

$$\mathcal{G}^{(0)}(\mathbf{r}) = -\frac{e^{i\omega r/c}}{4\pi r} [P(i\omega r/c)\mathbb{1} + Q(i\omega r/c)\hat{\mathbf{r}} \otimes \hat{\mathbf{r}}] + \frac{\delta(\mathbf{r})}{3\omega^2/c^2}\mathbb{1} \quad (\text{A.6})$$

where $r = |\mathbf{r}|$, $\hat{\mathbf{r}} = \mathbf{r}/r$ and the functions P and Q are given by

$$P(x) = 1 - \frac{1}{x} + \frac{1}{x^2}, \quad Q(x) = -1 + \frac{3}{x} - \frac{3}{x^2}, \quad (\text{A.7})$$

respectively. Note the contact contribution proportional to $\delta(\mathbf{r})$ in (A.6).

As an important relation between the real space and the reciprocal space representations we prove that

$$\frac{1}{a^3} \sum_{\mathbf{K}} \widetilde{\mathcal{G}^{(0)}}(\mathbf{k} - \mathbf{K}, \omega) = \sum_{\mathbf{R}} e^{-i\mathbf{k}\mathbf{R}} \mathcal{G}^{(0)}(\mathbf{R}, \omega) \quad (\text{A.8})$$

holds. Here \mathbf{R} and \mathbf{K} are lattice vectors and reciprocal lattice vectors of a simple cubic lattice, respectively. We first replace $\widetilde{\mathcal{G}^{(0)}}(\mathbf{k} - \mathbf{K}, \omega)$ on the left hand side by its definition as the Fourier transform of $\mathcal{G}^{(0)}(\mathbf{r}, \omega)$

$$\frac{1}{a^3} \sum_{\mathbf{K}} \widetilde{\mathcal{G}^{(0)}}(\mathbf{k} - \mathbf{K}, \omega) = \frac{1}{a^3} \sum_{\mathbf{K}} \int d^3\mathbf{r} \mathcal{G}^{(0)}(\mathbf{r}, \omega) e^{-i(\mathbf{k}-\mathbf{K})\mathbf{r}} \quad (\text{A.9})$$

and use $\sum_{\mathbf{K}} e^{i\mathbf{K}\mathbf{r}} = a^3 \sum_{\mathbf{R}} \delta(\mathbf{r} - \mathbf{R})$, which can be proven by means of Poisson's summation formula. Thus the right hand side of (A.9) can be integrated to yield (A.8).

APPENDIX B

The magnetic scattering T -matrix (8.28)

The Helmholtz equation (8.24) for the Green function $\mathcal{G}_B(\mathbf{r}, \mathbf{r}', \omega)$, in which we substitute

$$\alpha_B(\mathbf{r}, \omega) = \alpha_B(\omega) \sum_{\mathbf{R}} \delta(\mathbf{r} - \mathbf{R}), \quad (\text{B.1})$$

for a single cubic lattice of point magnetic scatterers with magnetizability $\alpha_B(\omega)$ is solved by

$$\begin{aligned} \mathcal{G}_B(\mathbf{r}, \mathbf{r}', \omega) = & \mathcal{G}^{(0)}(\mathbf{r} - \mathbf{r}', \omega) + \\ & + \int d^3 \mathbf{r}_1 \sum_{\mathbf{R}} \mathcal{G}^{(0)}(\mathbf{r} - \mathbf{r}_1, \omega) \nabla^{\mathbf{r}_1} \times \nabla^{\mathbf{r}_1} \times [-4\pi \alpha_B(\omega) \delta(\mathbf{r}_1 - \mathbf{R})] \mathcal{G}_B(\mathbf{r}_1, \mathbf{r}', \omega) \end{aligned} \quad (\text{B.2})$$

which follows immediately from (8.24) and the properties of the free space Green function $\mathcal{G}^{(0)}(\mathbf{r}, \mathbf{r}', \omega)$. In order to get rid of the derivatives of delta functions we integrate (B.2) partially, which yields terms involving $\mathcal{G}^{(0)}(\mathbf{r} - \mathbf{r}_1, \omega) \times \overleftarrow{\nabla}^{\mathbf{r}_1} \times \overleftarrow{\nabla}^{\mathbf{r}_1}$. In cartesian coordinates the result reads

$$\left[\mathcal{G}^{(0)}(\mathbf{r} - \mathbf{r}_1, \omega) \times \overleftarrow{\nabla}^{\mathbf{r}_1} \times \overleftarrow{\nabla}^{\mathbf{r}_1} \right]_{in} = \partial_k^{\mathbf{r}_1} \partial_m^{\mathbf{r}_1} \mathcal{G}_{ij}^{(0)}(\mathbf{r} - \mathbf{r}_1, \omega) \varepsilon_{jkl} \varepsilon_{lmn}. \quad (\text{B.3})$$

Since the free space Green function is invariant under matrix transpositions $\mathcal{G}_{ij}^{(0)}(\mathbf{r}) = \mathcal{G}_{ji}^{(0)}(\mathbf{r})$ the same feature holds for its defining equation (A.1). We thus observe that the vacuum Green function fulfills

$$\mathcal{G}^{(0)}(\mathbf{r}, \omega) \times \overleftarrow{\nabla} \times \overleftarrow{\nabla} = \nabla \times \nabla \times \mathcal{G}^{(0)}(\mathbf{r}, \omega). \quad (\text{B.4})$$

The first term $\mathcal{G}^{(0)}(\mathbf{r} - \mathbf{r}_1, \omega) \times \overleftarrow{\nabla}^{\mathbf{r}_1} \times \overleftarrow{\nabla}^{\mathbf{r}_1}$ of (B.2) can therefore be simplified to $(\omega^2/c^2)\mathcal{G}^{(0)}(\mathbf{r} - \mathbf{r}_1, \omega)$ if we restrict ourselves to $\mathbf{r} \neq \mathbf{r}_1$, i.e., if the source and the observation point arguments of the Green function differ. Under this assumption an iteration yields

$$\begin{aligned}
\mathcal{G}_B(\mathbf{r}, \mathbf{r}', \omega) = & \mathcal{G}^{(0)}(\mathbf{r} - \mathbf{r}', \omega) + \\
& + \int d^3\mathbf{r}_1 \sum_{\mathbf{R}} \frac{\omega^2}{c^2} \mathcal{G}^{(0)}(\mathbf{r} - \mathbf{r}_1, \omega) [-4\pi\alpha_B(\omega)\delta(\mathbf{r}_1 - \mathbf{R})] \mathcal{G}^{(0)}(\mathbf{r}_1 - \mathbf{r}', \omega) \\
& + \int d^3\mathbf{r}_1 d^3\mathbf{r}_2 \sum_{\mathbf{R}, \mathbf{R}'} \frac{\omega^2}{c^2} \mathcal{G}^{(0)}(\mathbf{r} - \mathbf{r}_1, \omega) [-4\pi\alpha_B(\omega)\delta(\mathbf{r}_1 - \mathbf{R})] \\
& \mathcal{G}^{(0)}(\mathbf{r}_1 - \mathbf{r}_2, \omega) \times \overleftarrow{\nabla}^{\mathbf{r}_2} \times \overleftarrow{\nabla}^{\mathbf{r}_2} [-4\pi\alpha_B(\omega)\delta(\mathbf{r}_2 - \mathbf{R})] \mathcal{G}^{(0)}(\mathbf{r}_2 - \mathbf{r}', \omega) \\
& + \dots
\end{aligned} \tag{B.5}$$

Note that we are allowed to simplify the double curl terms only for outer vertices of the diagram series, i.e., for terms involving the coordinates \mathbf{r} or \mathbf{r}' . The other terms which involve only dummy indices $\mathbf{r}_1, \mathbf{r}_2, \dots$ correspond to multiple scattering events at lattice sites. Therefore expressions like $\mathbf{r}_1 - \mathbf{r}_2$ can become zero and thus do not fulfill the restriction of above. Since the T -matrix in real space representation is defined by

$$\begin{aligned}
\mathcal{G}_B(\mathbf{r}, \mathbf{r}', \omega) = & \mathcal{G}^{(0)}(\mathbf{r} - \mathbf{r}', \omega) \\
& + \int d^3\mathbf{r}_1 d^3\mathbf{r}_2 \mathcal{G}^{(0)}(\mathbf{r} - \mathbf{r}_1, \omega) T_B(\mathbf{r}_1, \mathbf{r}_2, \omega) \mathcal{G}^{(0)}(\mathbf{r}_2 - \mathbf{r}', \omega)
\end{aligned}$$

we find

$$\begin{aligned}
T_B(\mathbf{r}_1, \mathbf{r}_2, \omega) = & \sum_{\mathbf{R}} \frac{\omega^2}{c^2} [-4\pi\alpha_B(\omega)] \delta(\mathbf{r}_1 - \mathbf{R}) \delta(\mathbf{r}_1 - \mathbf{r}_2) \\
& + \sum_{\mathbf{R}, \mathbf{R}'} \frac{\omega^2}{c^2} [-4\pi\alpha_B(\omega)]^2 \delta(\mathbf{r}_1 - \mathbf{R}) \\
& \cdot [\nabla^{\mathbf{r}_2} \times \nabla^{\mathbf{r}_2} \times \mathcal{G}^{(0)}(\mathbf{r}_1 - \mathbf{r}_2, \omega)] \delta(\mathbf{r}_2 - \mathbf{R}') \\
& + \dots
\end{aligned} \tag{B.6}$$

This general result can be specialized to the case of a single scatterer in free space by keeping only one term $\mathbf{R} = \mathbf{r}_A$ of the sum over lattice vectors.

Summing the resulting geometric series we find

$$t_B(\mathbf{r}_1, \mathbf{r}_2, \omega) = \frac{-4\pi \frac{\omega^2}{c^2} \alpha_B(\omega)}{1 + 4\pi \alpha_B(\omega) \nabla \times \nabla \times \mathcal{G}^{(0)}(0)} \delta(\mathbf{r}_1 - \mathbf{r}_A) \delta(\mathbf{r}_2 - \mathbf{r}_A) \quad (\text{B.7})$$

for the T -matrix of a single magnetic scatterer located at \mathbf{r}_A . Note that this T -matrix is only valid to construct Green functions between spatial points \mathbf{r}, \mathbf{r}' other than \mathbf{r}_A .

For the case of a simple cubic lattice we cast (B.6) in reciprocal space

$$T_B(\mathbf{k}, \mathbf{k}', \omega) = \int d^3 \mathbf{r} d^3 \mathbf{r}' \langle \mathbf{k} | \mathbf{r} \rangle T_B(\mathbf{r}, \mathbf{r}', \omega) \langle \mathbf{r}' | \mathbf{k}' \rangle. \quad (\text{B.8})$$

Renaming the summation indices similar to (7.49) by, e.g., $\mathcal{R} = \mathbf{R} - \mathbf{R}'$ then gives

$$T_B(\mathbf{k}, \mathbf{k}', \omega) = \frac{1}{(2\pi)^3} \sum_{\mathbf{R}} e^{-i(\mathbf{k}-\mathbf{k}')\mathbf{R}} \left\{ V_B(\omega)^{-1} - \sum_{\mathcal{R}} e^{-i\mathbf{k}'\mathcal{R}} \frac{1}{\omega^2/c^2} \nabla \times \nabla \times \mathcal{G}^{(0)}(\mathcal{R}) \right\}^{-1} \quad (\text{B.9})$$

with the optical potential $V_B(\omega) = -4\pi \frac{\omega^2}{c^2} \alpha(\omega)$.

APPENDIX C

Convergence behavior of (9.7) and (9.8)

We analyze the convergence behavior of the series

$$\sum_{\mathbf{K}} \frac{e^{\pm i\mathbf{K}\Delta\mathbf{r}}(\mathbf{k} - \mathbf{K}) \times}{\frac{\omega^2}{c^2} \mathbb{1} - |\mathbf{k} - \mathbf{K}|^2 \Delta_{\mathbf{k}-\mathbf{K}}} \quad (\text{C.1})$$

which emerge in the Fourier representation of the Helmholtz equations (9.7) and (9.8) for the case of magneto-dielectric materials. In order to clarify the notation we note that the cross product $(\mathbf{k} - \mathbf{K}) \times$ can be represented as a matrix which in the canonical basis reads

$$(\mathbf{k} - \mathbf{K}) \times = \begin{pmatrix} 0 & -(k_z - K_z) & (k_y - K_y) \\ (k_z - K_z) & 0 & -(k_x - K_x) \\ -(k_y - K_y) & (k_x - K_x) & 0 \end{pmatrix}. \quad (\text{C.2})$$

Since it commutes with $[\omega^2/c^2 \mathbb{1} - |\mathbf{k} - \mathbf{K}|^2 \Delta_{\mathbf{k}-\mathbf{K}}]^{-1} = \widetilde{\mathcal{G}^{(0)}}(\mathbf{k} - \mathbf{K}, \omega)$ equation (C.1) is well defined.

We start by replacing the vacuum Green function $\widetilde{\mathcal{G}^{(0)}}(\mathbf{k} - \mathbf{K}, \omega)$ by its Fourier transform. The cross product $(\mathbf{k} - \mathbf{K}) \times$ can then be interpreted as a curl of the exponential $\exp[-i(\mathbf{k} - \mathbf{K})\mathbf{r}]$. After a partial integration, equation (C.1) thus transforms into

$$-i \sum_{\mathbf{K}} \int d^3\mathbf{r} e^{\pm i\mathbf{K}\Delta\mathbf{r}} e^{-i(\mathbf{k}-\mathbf{K})\mathbf{r}} \nabla \times \mathcal{G}^{(0)}(\mathbf{r}, \omega). \quad (\text{C.3})$$

Following equation (9.2), we replace the sum over reciprocal lattice vectors by a sum over real space lattice vectors

$$-ia^3 \sum_{\mathbf{R}} \int d^3\mathbf{r} \delta(\mathbf{r} - \mathbf{R} \pm \Delta\mathbf{r}) e^{-i\mathbf{kr}} \nabla \times \mathcal{G}^{(0)}(\mathbf{r}, \omega), \quad (\text{C.4})$$

from which we get after an integration

$$-ia^3 \sum_{\mathbf{R}} e^{-i\mathbf{k}(\mathbf{R} \mp \Delta\mathbf{r})} \nabla \times \mathcal{G}^{(0)}(\mathbf{R} \mp \Delta\mathbf{r}, \omega). \quad (\text{C.5})$$

Hence for $\Delta\mathbf{r} \neq 0$, (C.1) contains no contribution proportional to the divergent term $\mathcal{G}^{(0)}(0, \omega)$. Note that the small \mathbf{r} behavior of (C.5) corresponds to the large \mathbf{K} behavior of (C.1).

The behavior for large \mathbf{R} on the other hand can be studied best in \mathbf{k} -space as the limit of small wave vectors. We rewrite the Green function $\widetilde{\mathcal{G}^{(0)}}(\mathbf{k} - \mathbf{K}, \omega)$, which shows up in (C.1), in terms of projectors onto transverse $\Delta_{\mathbf{k}-\mathbf{K}}$ and longitudinal $(\widehat{\mathbf{k} - \mathbf{K}}) \otimes (\widehat{\mathbf{k} - \mathbf{K}})$ parts with respect to $\mathbf{k} - \mathbf{K}$

$$\frac{1}{\frac{\omega^2}{c^2} \mathbb{1} - |\mathbf{k} - \mathbf{K}|^2 \Delta_{\mathbf{k}-\mathbf{K}}} = \frac{1}{\frac{\omega^2}{c^2} \mathbb{1} - |\mathbf{k} - \mathbf{K}|^2} \Delta_{\mathbf{k}-\mathbf{K}} + \frac{1}{\omega^2/c^2} (\widehat{\mathbf{k} - \mathbf{K}}) \otimes (\widehat{\mathbf{k} - \mathbf{K}}). \quad (\text{C.6})$$

Using the identities $\mathbf{k} \times (\hat{\mathbf{k}} \otimes \hat{\mathbf{k}}) = 0$ and $\mathbf{k} \times \Delta_{\mathbf{k}} = \mathbf{k} \times$ equation (C.1) thus simplifies to

$$\sum_{\mathbf{K}} \frac{e^{\pm i\mathbf{K}\Delta\mathbf{r}}}{\frac{\omega^2}{c^2} \mathbb{1} - |\mathbf{k} - \mathbf{K}|^2} (\mathbf{k} - \mathbf{K}) \times. \quad (\text{C.7})$$

We note that the vector \mathbf{k} is an element of the 1. Brillouin zone of the simple cubic lattice with reciprocal lattice vectors \mathbf{K} . Thus $|\mathbf{k}| \leq |\mathbf{K}|$ holds. In addition, the dispersion $|\mathbf{k}(\omega)|$ has in general the same order of magnitude as the free photon dispersion ω/c . A divergency of the series for small \mathbf{k} can therefore only stem from a resonance of the $\mathbf{K} = 0$ term.

In the treatment of $\sum_{\mathbf{K}} \widetilde{\mathcal{G}^{(0)}}(\mathbf{k} - \mathbf{K}, \omega)$ for pure media, after having separated the divergent term $\mathcal{G}^{(0)}(0, \omega)$, we restricted ourselves to the high density limit, for which we only kept the $\mathbf{K} = 0$ contribution (see discussion in section 7.3). In the discussion of magneto-dielectric materials we also specialize to $\mathbf{K} = 0$. Hence the resonant term $[\omega^2/c^2 - |\mathbf{k}|^2]^{-1}$ is accounted for in the condition (9.13) for the derivation of the dispersion $\mathbf{k}(\omega)$.

Bibliography

- [1] J. B. Pendry, *Negative refraction makes a perfect lens*, Phys. Rev. Lett. **85**, 3966 (2000).
- [2] U. Leonhardt, *Optical conformal mapping*, Science **312**, 1777 (2006).
- [3] J. B. Pendry, D. Schurig, D. R. Smith, *Controlling electromagnetic fields*, Science **312**, 1780 (2006).
- [4] D. Schurig, J. J. Mock, B. J. Justice, S. A. Cummer, J. B. Pendry, A. F. Starr, D. R. Smith, *Metamaterial electromagnetic cloak at microwave frequencies*, Science **314**, 977 (2006).
- [5] D. R. Smith, W. J. Padilla, D. C. Vier, S. C. Nemat-Nasser, S. Schultz, *Composite medium with simultaneously negative permeability and permittivity*, Phys. Rev. Lett. **84**, 4184 (2000).
- [6] R. Shelby, D. R. Smith, S. Schultz, *Experimental verification of a negative index of refraction*, Science **292**, 77 (2001).
- [7] T. J. Yen, W. J. Padilla, N. Fang, D. C. Vier, D. R. Smith, J. B. Pendry, D. N. Basov, X. Zhang, *Terahertz Magnetic Response from Artificial Materials*, Science **303**, 1494 (2004).
- [8] S. Zhang, W. Fan, B. K. Minhas, A. Frauenglass, K. J. Malloy, S. R. J. Brueck, *Midinfrared resonant magnetic nanostructures exhibiting a negative permeability*, Phys. Rev. Lett. **94**, 037402 (2005).

- [9] C. Enkrich, M. Wegener, S. Linden, S. Burger, L. Zschiedrich, F. Schmidt, J. F. Zhou, T. Koschny, C. M. Soukoulis, *Magnetic Metamaterials at Telecommunication and Visible Frequencies*, Phys. Rev. Lett. **95**, 203901 (2005).
- [10] V. M. Shalaev, W. Cai, U. K. Chettiar, H.-K. Yuan, A. K. Sarychev, V. P. Drachev, A. V. Kildishev, *Negative index of refraction in optical metamaterials*, Opt. Lett. **30**, 3356 (2005).
- [11] G. Dolling, C. Enkrich, M. Wegener, C. M. Soukoulis, S. Linden, *Simultaneous negative phase and group velocity of light in a metamaterial*, Science **312**, 892 (2006).
- [12] E. Yablonovich, *Inhibited spontaneous emission in solid-state physics and electronics*, Phys. Rev. Lett. **58**, 2059 (1987).
- [13] S. John, *Strong localization of photons in certain disordered dielectric superlattices*, Phys. Rev. Lett. **58**, 2486 (1987).
- [14] M. Notomi, *Theory of light propagation in strongly modulated photonic crystals: refractionlike behavior in the vicinity of the photonic band gap*, Phys. Rev. B **62**, 10696 (2000).
- [15] P. V. Parimi, W. T. Lu, P. Vodo, J. Sokoloff, J. S. Derov, S. Sridhar, *Negative Refraction and Left-Handed Electromagnetism in Microwave Photonic Crystals*, Phys. Rev. Lett. **92**, 127401 (2004).
- [16] A. Berrier, M. Mulot, M. Swillo, M. Qiu, L. Thylén, A. Talneau, S. Anand, *Negative Refraction at Infrared Wavelengths in a Two-Dimensional Photonic Crystal*, Phys. Rev. Lett. **93**, 073902 (2004).
- [17] Z. Lu, J. A. Murakowski, C. A. Schuetz, S. Shi, G. J. Schneider, D. W. Prather, *Three-Dimensional Subwavelength Imaging by a Photonic-Crystal Flat Lens Using Negative Refraction at Microwave Frequencies*, Phys. Rev. Lett. **95**, 153901 (2005).
- [18] C. Luo, S. G. Johnson, J. D. Joannopoulos, J. B. Pendry, *All-angle negative refraction without negative effective index*, Phys. Rev. B **65**, 201104(R) (2002).

- [19] L. I. Mandel'shtam, *Group velocity in a crystal lattice*, Zh. Eksp. Teor. Fiz. **15**, 475 (1945).
- [20] D. V. Sivukhin, *The energy of electromagnetic waves in dispersive media*, Opt. Spektrosk. **3**, 308 (1957).
- [21] V. G. Veselago, *The electrodynamics of substances with simultaneously negative values of ϵ and μ* , Sov. Phys. Usp. **10**, 509 (1968).
- [22] X. S. Rao, C. K. Ong, *Amplification of evanescent waves in a lossy left-handed material slab*, Phys. Rev. B **68**, 113103 (2003).
- [23] M. L. Brongersma, P. G. Kik (eds.), *Surface Plasmon Nanophotonics*, Springer (2007).
- [24] J. B. Pendry, A. J. Holden, W. J. Stewart, I. Youngs, *Extremely low frequency plasmons in metallic mesostructures*, Phys. Rev. Lett. **76**, 4773 (1996).
- [25] J. B. Pendry, A. J. Holden, D. J. Robbins, W. J. Stewart, *Magnetism from conductors and enhanced nonlinear phenomena*, IEEE Trans. Micro. Theory Tech. **47**, 2075 (1999).
- [26] M. Bayindir, K. Aydin, E. Ozbay, P. Markoš, C. M. Soukoulis, *transmission properties of composite metamaterials in free space*, Appl. Phys. Lett. **81**, 120 (2002).
- [27] C. G. Parazzoli, R. B. Greegor, K. Li, B. E. C. Koltenbah, M. Tanielian, *Experimental verification and simulation of negative index of refraction using Snell's law*, Phys. Rev. Lett. **90**, 107401 (2003).
- [28] N.-C. Panoiu, R. M. Osgood, Jr., *Influence of the dispersive properties of metals on the transmission characteristics of left-handed materials*, Phys. Rev. E **68**, 016611 (2003).
- [29] R. B. Greegor, C. G. Parazzoli, K. Li, M. H. Tanielian, *Origin of dissipation losses in negative index of refraction materials*, Appl. Phys. Lett. **82**, 2356 (2003).

- [30] D. R. Smith, S. Schultz, P. Markoš, C. M. Soukoulis, *Determination of effective permittivity and permeability of metamaterials from reflection and transmission coefficients*, Phys. Rev. B **65**, 195104 (2002).
- [31] N. Katsarakis, G. Konstantinidis, A. Kostopoulos, R. S. Penciu, T. F. Gundogdu, M. Kafesaki, E. N. Economou, Th. Koschny, C. M. Soukoulis *Magnetic response of split-ring resonators in the far-infrared frequency regime*, Opt. Lett. **30**, 1348.
- [32] S. Linden, C. Enkrich, M. Wegener, J. F. Zhou, T. Koschny, C. M. Soukoulis, *Magnetic Response of Metamaterials at 100 Terahertz*, Science **306**, 1351 (2004).
- [33] S. Linden, C. Enkrich, G. Dolling, M. W. Klein, J. Zhou, T. Koschny, C. M. Soukoulis, S. Burger, F. Schmidt, M. Wegener, *Photonic metamaterials: magnetism at optical frequencies*, IEEE Journal of selected topics in quantum electronics **12**, 1097 (2006).
- [34] A. N. Grigorenko, A. K. Geim, H. f. Gleeson, Y. Zhang, A. A. Firsov, I. Y. Khrushchev, J. Petrovic, *Nanofabricated media with a negative permeability at visible frequencies*, Nature **438**, 335 (2005).
- [35] G. Dolling, C. Enkrich, M. Wegener, J. F. Zhou, C. M. Soukoulis, S. Linden *Cut-wire pairs and plate pairs as magnetic atoms for optical metamaterials*, Opt. Lett., **30**, 3198 (2005).
- [36] H.-K. Yuan, U. K. Chettiar, W. Cai, A. V. Kildishev, A. Boltasseva, V. P. Drachev, V. M. Shalaev, *A negative permeability material at red light*, Opt. Express **15**, 1076 (2007).
- [37] J. Zhou, L. Zhang, G. Tuttle, T. Koschny, C. M. Soukoulis, *Negative index materials using simple short wire pairs*, Phys. Rev. B **73**, 041101(R) (2006).
- [38] V. P. Drachev, W. Cai, U. K. Chettiar, H.-K. Yuan, A. K. Sarychev, A. V. Kildishev, G. Klimeck, V. M. Shalaev, *Experimental verification of an optical negative-index material*, Laser Phys. Lett. **3**, 49 (2006).

- [39] M. Born, *Optik*, Springer (1985).
- [40] J. D. Jackson, *Classical Electrodynamics*, Wiley (New York) (1999).
- [41] S. Zhang, W. Fan, K. J. Malloy, S. R. J. Brueck, *Near-infrared double negative metamaterials*, Optics Express **13**, 4922 (2005).
- [42] G. Dolling, C. Enkrich, M. Wegener, C. M. Soukoulis, S. Linden, *Low-loss negative-index metamaterial at telecommunication wavelengths*, Opt. Lett. **31**, 1800 (2006).
- [43] G. Dolling, M. Wegener, C. M. Soukoulis, S. Linden, *Negative-index metamaterial at 780 nm wavelength*, Opt. Lett. **32**, 53 (2007).
- [44] S. Zhang, W. Fan, N. C. Panoiu, K. J. Malloy, R. M. Osgood, S. R. J. Brueck, *Experimental demonstration of near-infrared negative-index metamaterials*, Phys. Rev. Lett. **95**, 137404 (2005).
- [45] C. M. Soukoulis, S. Linden, M. Wegener, *Negative refractive index at optical wavelengths*, Science **315**, 47 (2007).
- [46] V. M. Shalaev, *Optical negative-index metamaterials*, Nature photon. **1**, 41 (2007).
- [47] G. Dolling, M. Wegener, C. M. Soukoulis, S. Linden, *Design-related losses of double-fishnet negative-index photonic metamaterials*, Opt. Express **15**, 11536 (2007).
- [48] Z. Ku, S. R. J. Brueck, *Comparison of negative refractive index materials with circular, elliptical and rectangular holes*, Optics Express **15**, 4515 (2007).
- [49] K.-J. Boller, A. Imamoğlu, S. E. Harris, *Observation of electromagnetically induced transparency*, Phys. Rev. Lett. **66**, 2593 (1991).
- [50] J. E. Field, K. H. Hahn, S. E. Harris, *Observation of electromagnetically induced transparency in collisionally broadened lead vapor*, Phys. Rev. Lett. **67**, 3062 (1991).

- [51] F. Beil, J. Klein, G. Nikoghosyan, T. Halfmann, *Electromagnetically-Induced Transparency and Retrieval of Light Pulses in a $Pr^{3+} : Y_2SiO_5$ Crystal*, *J. Phys. B* **41**, 074001 (2008).
- [52] C. L. Garrido Alzar, M. A. G. Martinez, P. Nussenzveig, *Classical analog of electromagnetically induced transparency*, *Am. J. Phys.* **70**, 37 (2002).
- [53] W. W. Chow, H. C. Schneider, M. C. Phillips, *Theory of quantum-coherence phenomena in semiconductor quantum dots*, *Phys. Rev. A* **68**, 053802 (2003).
- [54] M. Jain, A. J. Merriam, A. Kasapi, G. Y. Yin, S. E. Harris, *Elimination of Optical Self-Focusing by Population Trapping*, *Phys. Rev. Lett.* **75**, 4385 (1995).
- [55] S. E. Harris, *Electromagnetically induced transparency*, *Physics Today* **50**, 36 (1997).
- [56] S. E. Harris, J. E. Field, A. Imamoğlu, *Nonlinear optical processes using electromagnetically induced transparency*, *Phys. Rev. Lett.* **64**, 1107 (1990).
- [57] M. Fleischhauer, A. Imamoğlu, J. P. Marangos, *Electromagnetically induced transparency: Optics in coherent media*, *Rev. Mod. Phys.* **77**, 633 (2005).
- [58] A. B. Matsko, O. Kocharovskaya, Y. Rostovtsev, G. R. Welch, A. S. Zibrov, M. O. Scully, *Slow, ultraslow, stored, and frozen light*, *Adv. At. Mol. Opt. Phys.* **46**, 191 (2001).
- [59] M. D. Lukin, *Colloquium: Trapping and manipulating photon states in atomic ensembles*, *Rev. Mod. Phys.* **75**, 457 (2003).
- [60] E. Arimondo, *Coherent population trapping in laser spectroscopy*, *Progress in Optics* **35**, 257, (1996).

- [61] T. Halfmann, J. P. Marangos, *Electromagnetically Induced Transparency*, in “Handbook of Optics”, **4**, edt. by F. Bass, McGraw-Hill Publ. Co. (New York) (2007).
- [62] N. V. Vitanov, M. Fleischhauer, B. W. Shore, K. Bergmann, *Coherent manipulation of atoms and molecules by sequential laser pulses*, Adv. At. Mol. Opt. Phys. **46**, 55 (2001).
- [63] K. Hakuta, L. Marmet, B. P. Stoicheff, *Electric-field-induced second-harmonic generation with reduced absorption in atomic hydrogen*, Phys. Rev. Lett. **66**, 596 (1991).
- [64] M. D. Lukin, P. R. Hemmer, M. O. Scully, *Resonant nonlinear optics in phase-coherent media*, Adv. At. Mol. Opt. Phys. **42**, 347 (2000).
- [65] W. H. Louisell, *Quantum statistical properties of radiation*, John Wiley & Sons (1990).
- [66] L. Knöll, S. Scheel, D.-G. Welsch, *QED in dispersing and absorbing media*, Coherence and Statistics of Photons and Atoms, ed. by J. Peřina, Wiley (New York), (2001).
- [67] R. D. Cowan. *The theory of atomic structure and spectra*, University of California Press (1981).
- [68] A. A. Kaminskii, *Laser crystals: their physics and properties*, Springer (Berlin), (1981).
- [69] J. Klein, F. Beil, T. Halfmann, *Rapid Adiabatic Passage in a $Pr^{3+} : Y_2SiO_5$ crystal*, J. Phys. B **40**, 345 (2007).
- [70] M. Born, *Über die natürliche optische Aktivität von Flüssigkeiten und Gasen*, Phys. Z. **16**, 251 (1915).
- [71] A. Lakhtakia, V. K. Varadan, V. V. Varadan, *Time-Harmonic Electromagnetic Fields in Chiral Media*, Springer-Verlag (1989).
- [72] F. I. Fedorov. *On the theory of optical activity in crystals. I. The law of conservation of energy and the optical activity tensors*, Opt. Spectrosc.

6, 49 (1959); F. I. Fedorov. *On the theory of optical activity in crystals. II. Crystals of cubic symmetry and plane classes of central symmetry*, Opt. Spectrosc. **6**, 237 (1959).

[73] B. D. H. Tellegen, *The gyrator: A new electric network element*, Phillips Res. Repts. **3**, 81 (1948).

[74] D. K. Cheng, J. A. Kong, *Covariant description of bianisotropic media*, Proc. IEEE **56**, 248 (1968).

[75] J. A. Kong, *Theorems of bianisotropic media*, Proc. IEEE **60**, 1036 (1972); J. A. Kong, *Optics of bianisotropic media*, J. Opt. Soc. Am. **64**, 1304 (1974).

[76] W. C. Röntgen, *Über die durch Bewegung eines im homogenen elektrischen Felde befindlichen Dielectricums hervorgerufene elektrodynamische Kraft*, Ann. Phys. **271**, 264 (1888).

[77] H. A. Wilson, *On the electric effect of rotating a dielectric in a magnetic field*, Phil. Trans. Roy. Soc. London A **204**, 121 (1905).

[78] D. N. Astrov, Soviet Phys. JETP **11**, 708 (1960).

[79] I. E. Dzyalochinskii, *On the magnetoelectrical effect in antiferromagnets*, Sov. Phys. – JETP **10**, 628 (1960).

[80] T. H. O'Dell, *The electrodynamics of magneto-electric media*, North-Holland Publishing Group (1970).

[81] J. B. Pendry, *A Chiral Route to Negative Refraction*, Science **306**, 1353 (2004).

[82] J. C. Monzon, *Radiation and scattering in homogeneous general bi-isotropic regions*, IEEE Transactions on Antennas and Propagation **38**, 227 (1990).

[83] R. R. Birss, R. G. Shrubshall, *The propagation of electromagnetic waves in magnetoelectric crystals*, Phil. Mag. **15**, 687 (1967).

- [84] R. Fuchs, *Wave propagation in a magnetoelectric medium*, Phil. Mag. **11**, 647 (1965).
- [85] J. A. Kong, *Optics of bianisotropic media*, J. Opt. Soc. Am. **64**, 1304 (1974).
- [86] C.-W. Qiu, H.-Y. Yao, L.-W. Li, S. Zouhdi, T.-S. Yeo, *Routes to left-handed materials by magnetoelectric couplings*, Phys. Rev. B **75**, 245214 (2007).
- [87] A. Lakhtakia, W. S. Weiglhofer, *Constraint on linear, homogeneous, constitutive relations*, Phys. Rev. E **50**, 5017 (1994).
- [88] M. Ö. Oktel, Ö. E. Müstecaplioglu, *Electromagnetically induced left-handedness in a dense gas of three-level atoms*, Phys. Rev. A **70**, 053806 (2004).
- [89] Q. Thommen, P. Mandel, *Electromagnetically Induced Left Handedness in Optically Excited Four-Level Atomic Media*, Phys. Rev. Lett. **96**, 053601 (2006).
- [90] M. O. Scully, M. S. Zubairy, *Quantum Optics*, Cambridge University Press (1997).
- [91] R. W. Boyd, *Nonlinear optics*, Academic Press (2003).
- [92] J. Klein, F. Beil, T. Halfmann, *Robust Population Transfer by Stimulated Raman Adiabatic Passage in a $Pr^{3+} : Y_2SiO_5$ crystal*, Phys. Rev. Lett. **99**, 113003 (2007).
- [93] D. M. Cook, *The Theory of the Electromagnetic Field*, Prentice-Hall (New Jersey) (1975).
- [94] S. A. Cummer, *Simulated causal subwavelength focusing by a negative refractive index slab*, Appl. Phys. Lett. **82**, 1503 (2003).
- [95] E. Cubukcu, K. Aydin, E. Ozbay, S. Foteinopolou, C. M. Soukoulis, *Subwavelength resolution in a two-dimensional photonic-crystal-based superlens*, Phys. Rev. Lett. **91**, 207401 (2003).

- [96] P. V. Parimi, W. T. Lu, P. Vodo, S. Sridhar, *Imaging by flat lens using negative refraction*, *Nature* **426**, 404 (2003).
- [97] A. Grbic, G. V. Eleftheriades, *Overcoming the Diffraction Limit with a Planar Left-Handed Transmission-Line Lens*, *Phys. Rev. Lett.* **92**, 117403 (2004).
- [98] D. R. Smith, J. B. Pendry, M. C. K. Wiltshire, *Metamaterials and negative refractive index*, *Science* **305**, 788 (2004).
- [99] R. Ruppin, *Surface polaritons of a left-handed material slab*, *J. Phys.: Condens. Matter* **13**, 1811 (2001).
- [100] D. R. Smith, D. Schurig, M. Rosenbluth, S. Schultz, S. A. Ramakrishna, J. B. Pendry, *Limitations on subdiffraction imaging with a negative refractive index slab*, *Appl. Phys. Lett.* **82** 1506 (2003).
- [101] R. Merlin, *Analytical solution of the almost-perfect-lens problem*, *Appl. Phys. Lett.* **84**, 1290 (2004).
- [102] N. Fang, H. Lee, C. Sun, X. Zhang, *Sub-diffraction-limited optical imaging with a silver superlens*, *Science* **308**, 534 (2005).
- [103] D. O. S. Melville, R. J. Blaikie, *Super-resolution imaging through a planar silver layer*, *Opt. Express* **13**, 2127 (2005).
- [104] M. Weissbluth, *Atoms and molecules*, Academic Press (New York) (1978).
- [105] H. Giessen, private communication
- [106] P. Tassin, Lei Zhang, Th. Koschny, E. N. Economou, C. M. Soukoulis, *Low loss metamaterials based on Electromagnetic Induced Transparency*, *Phys. Rev. Lett.* (submitted).
- [107] O. F. Mossotti, *Memorie di Matematica e di Fisica della Societa Italiana delle Scienze Residente in Modena* **24**, 49 (1850).
- [108] R. Clausius, *Die Mechanische Behandlung der Electrizität*, Vieweg (Braunschweig), (1879).

- [109] L. Lorenz, Wiedem. Ann. **11**, 70 (1880).
- [110] H. A. Lorentz, *The Theory of Electrons* Teubner (Leipzig), (1909), reprinted by Dover, New York, (1952).
- [111] C. J. F. Böttcher, *Theory of electric polarization*, Elsevier Scientific Publishing Company (1973).
- [112] S. E. Schnatterly, C. Tarrio, *Local fields in solids: microscopic aspects for dielectrics*, Rev. Mod. Phys. **64**, 619 (1992).
- [113] M. Fleischhauer, *Spontaneous emission and level shifts in absorbing disordered dielectrics and dense atomic gases: A Green's-functions approach*, Phys. Rev. A **60**, 2534 (1999).
- [114] E. M. Purcell, *Spontaneous emission probabilities at radio frequencies*, Proceedings of the American Physical Society, Phys. Rev. **46**, 681 (1946).
- [115] D. Kleppner, *Inhibited spontaneous emission*, Phys. Rev. Lett. **47**, 233 (1981).
- [116] P. Goy, J. M. Raimond, M. Gross, S. Haroche, *Observation of cavity-enhanced single-atom spontaneous emission* Phys. Rev. Lett. **50**, 1903 (1983).
- [117] R. G. Hulet, E. S. Hilfer, D. Kleppner, *Inhibited spontaneous emission by a Rydberg atom*, Phys. Rev. Lett. **55**, 2137 (1985).
- [118] D. J. Heinzen, J. J. Childs, J. E. Thomas, M. S. Feld, *Enhanced and inhibited visible spontaneous emission by atoms in a confocal resonator*, Phys. Rev. Lett. **58**, 1320 (1987).
- [119] D. J. Heinzen, M. S. Feld, *Vacuum radiative level shift and spontaneous-emission linewidth of an atom in an optical resonator*, Phys. Rev. Lett. **59**, 2623 (1987).
- [120] Y. Yamamoto, S. Machida, Y. Horikoshi, K. Igeta, *Enhanced and inhibited spontaneous emission of free excitons in GaAs quantum wells in a microcavity*, Opt. Comm. **80**, 337 (1991).

- [121] K. H. Drexhage, *Influence of a dielectric interface on fluorescence decay time*, J. Lumin. **1-2**, 693 (1970).
- [122] H. Morawitz, *Self-coupling of a two-level system by a mirror*, Phys. Rev. **187**, 1792 (1969).
- [123] E. Snoeks, A. Lagendijk, A. Polman, *Measuring and Modifying the Spontaneous Emission Rate of Erbium near an Interface*, Phys. Rev. Lett. **74**, 2459 (1995).
- [124] N. Danz, J. Heber, A. Bräuer, R. Kowarschik, *Fluorescence lifetimes of molecular dye ensembles near interfaces*, Phys. Rev. A **66**, 063809 (2002).
- [125] A. M. Amos, W. L. Barnes, *Modification of the spontaneous emission rate of Eu^{3+} ions close to a thin metal mirror*, Phys. Rev. B **55**, 7249 (1997).
- [126] G. Nienhuis, C. T. J. Alkemade, *Atomic radiative transition probabilities in a continuous medium*, Physica B+C **81**, 181 (1976).
- [127] R. J. Glauber, M. Lewenstein, *Quantum optics of dielectric media*, Phys. Rev. A **43**, 467 (1991).
- [128] J. J. Maki, M. S. Malcuit, J. E. Sipe, R. W. Boyd, *Linear and nonlinear optical measurements of the Lorentz local field*, Phys. Rev. Lett. **67**, 972 (1991).
- [129] H. van Kampen, V. A. Sautenkov, C. J. C. Smeets, E. R. Eliel, J. P. Woerdman, *Measurement of the excitation dependence of the Lorentz local-field shift*, Phys. Rev. A **59**, 271 (1999).
- [130] C.-K. Duan, M. F. Reid, *Local field effects on the radiative lifetimes of Ce^{3+} in different hosts*, Current Applied Physics **6**, 348 (2006).
- [131] G. L. J. A. Rikken, Y. A. R. R. Kessener, *Local field effects and electric and magnetic dipole transitions in dielectrics*, Phys. Rev. Lett. **74**, 880 (1995).

- [132] F. J. P. Schuurmans, D. T. N. de Lang, G. H. Wegdam, R. Sprik, A. Lagendijk, *Local-field effects on spontaneous emission in a dense supercritical gas*, Phys. Rev. Lett. **80**, 5077 (1998).
- [133] G. M. Kumar, D. N. Rao, *Measurement of local field effects of the host on the lifetimes of embedded emitters*, Phys. Rev. Lett. **91**, 203903 (2003).
- [134] P. de Vries, D. V. van Coevorden, A. Lagendijk, *Point scatterers for classical waves*, Rev. Mod. Phys. **70**, 447 (1998).
- [135] A. Lagendijk, B. Nienhuis, B. A. van Tiggelen, P. de Vries, *Microscopic approach to the Lorentz cavity in dielectrics*, Phys. Rev. Lett. **79**, 657 (1997).
- [136] P. de Vries, A. Lagendijk, *Resonant scattering and spontaneous emission in dielectrics: microscopic derivation of local-field effects*, Phys. Rev. Lett. **81**, 1381 (1998).
- [137] S. M. Barnett, B. Huttner, R. Loudon, R. Matloob, *Decay of excited atoms in absorbing dielectrics*, J. Phys. B: At. Mol. Opt. Phys. **29**, 3763 (1996).
- [138] R. Friedberg, S. R. Hartmann, J. T. Manassah, *Mirrorless optical bistability condition*, Phys. Rev. A **39**, 3444 (1989).
- [139] R. H. Dicke, *Coherence in Spontaneous Radiation Processes*, Phys. Rev. **93**, 99 (1954).
- [140] R. G. DeVoe, R. G. Brewer, *Observation of Superradiant and Subradiant Spontaneous Emission of Two Trapped Ions*, Phys. Rev. Lett. **76**, 2049 (1996).
- [141] K. B. Kahan, *Green functional-approach to resonant cavity analysis*, IEEE Journal of Quantum Electronics **28**, 1232 (1992)
- [142] J. M. Ziman, *The T matrix, the K matrix, d bands and l-dependent pseudo-potentials in the theory of metals*, Proc. Phys. Soc. London **86**, 337 (1965).

- [143] P.M. Morse, H. Feshbach, *Methods of Theoretical Physics, Part I*, McGraw-Hill (New York), (1953).
- [144] T. Gruner, D.-G. Welsch, *Green-function approach to the radiation-field quantization for homogeneous and inhomogeneous Kramers-Kronig dielectrics*, Phys. Rev. A **53**, 1818 (1996).
- [145] W. Vogel, D.-G. Welsch, *Quantum optics*, Wiley-VCH, (2006).
- [146] L. Tsang, J. A. Kong, R. T. Shin, *Theory of Microwave Remote Sensing*, John Wiley & Sons (New York), (1985).

List of Figures

1.1	The perfect flat lens.	5
1.2	The first realization of a negative refracting material.	6
1.3	Modern designs of metamaterials.	7
1.4	The evolution of metamaterial research.	8
1.5	The Λ -scheme of EIT.	10
1.6	Explanations for EIT.	11
1.7	Closed loop Λ -scheme	13
2.1	Refractive index of the 2-species model	22
2.2	Angle dependent Poynting vector mismatch	31
2.3	Misalignment between \mathbf{S} and \mathbf{k}	32
3.1	Simple 3-level scheme	36
3.2	Level scheme modification	39
3.3	5-level scheme	41
3.4	Spectra of the polarizabilities	47
3.5	Spectra of the polarizabilities including strong coupling	48
3.6	Limits of linear response theory	52
3.7	Spectra of the polarizabilities including additional broadenings	54
3.8	Spectra of the polarizabilities including strong coupling and additional broadenings	55
3.9	Local field effects for the permittivity	57
3.10	Spectra of the polarizabilities including strong coupling, additional broadenings and local field corrections	58
3.11	Refractive index for $\varrho = 5 \cdot 10^{14} \text{ cm}^{-3}$ and $\varrho = 5 \cdot 10^{16} \text{ cm}^{-3}$. .	59

3.12	Spectrum of the non-chiral refractive index	60
3.13	Phase dependence of the refractive index	61
3.14	Index of refraction for $\varrho = 5 \cdot 10^{17} \text{cm}^{-3}$ as well as <i>FoM</i>	62
3.15	Density dependence of the response	63
4.1	Spectrum of impedance.	67
4.2	Tunability of the index of refraction.	69
4.3	Explicit implementation for 1D	71
4.4	Explicit implementation for 3D	74
4.5	Dependence of n on the polar angle θ	77
5.1	Single SRR and corresponding resonance	79
5.2	EIT in metamaterials	80
5.3	Effective Λ -type 3-level scheme for EIT in metamaterials.	81
6.1	Virtual sphere separating the near zone from the far zone.	86
6.2	Local field effects for dielectric media	93
6.3	Local field effects for magneto-dielectric media.	94
7.1	Microscopic model of a pure dielectric material.	98
8.1	Microscopic model of a pure diamagnetic material.	118
9.1	Unit cell of a magneto-dielectric material.	126
9.2	Local field effects for magneto-dielectric media with density dependent absorption	131
10.1	Sketch of the quantization scheme	138
11.1	Atom in front of a perfect mirror	144
11.2	3-layer geometry	145
11.3	Spatial dependence of the linewidth	149
12.1	$\gamma_A^{\parallel}/\gamma_A^{(0)}$ as function of the imaginary part $\text{Im}[n]$	152
12.2	Finite extension of the geometry in transverse direction.	153
12.3	$\gamma_A^{\parallel}/\gamma_A^{(0)}$ as a function of the transverse radius a	154
12.4	$\gamma_A^{\parallel}/\gamma_A^{(0)}$ as a function of a with infinite mirror	155
12.5	Spectra of exact and approximative $\text{Im}[\mathcal{G}^{(00)}(\omega)]$	157

Publications

Publications in refereed journals and proceedings:

[Kästel2003] H. T. Dung, S. Y. Buhmann, L. Knöll, D.-G. Welsch, S. Scheel, J. Kästel, *Electromagnetic-field quantization and spontaneous decay in left-handed media*, Phys. Rev. A **68**, 043816 (2003).

[Kästel2005a] J. Kästel, M. Fleischhauer, *Quantum electrodynamics in media with negative refraction*, Laser Phys. **15**, 135 (2005).

[Kästel2005b] J. Kästel, M. Fleischhauer, *Suppression of spontaneous emission and superradiance over macroscopic distances in media with negative refraction*, Phys. Rev. A **71**, 011804(R) (2005).

[Kästel2007a] J. Kästel, M. Fleischhauer, *Comment on “Electromagnetically Induced Left Handedness in Optically Excited Four-Level Atomic Media”*, Phys. Rev. Lett. **98**, 069301 (2007).

[Kästel2007b] J. Kästel, M. Fleischhauer, S. F. Yelin, R. L. Walsworth, *Tunable negative refraction without absorption via electromagnetically induced chirality*, Phys. Rev. Lett. **99**, 073602 (2007).

[Kästel2007c] J. Kästel, M. Fleischhauer, G. Juzeliūnas, *Local-field effects in magnetodielectric media: Negative refraction and absorption reduction*, Phys. Rev. A **76**, 062509 (2007).

[Kästel2008] J. Kästel, M. Fleischhauer, S. F. Yelin, R. L. Walsworth, *Tunable negative refraction without absorption using Electromagnetically Induced Chirality*, Coherence and Quantum Optics IX, ed. N. P. Bigelow, J. H. Eberly, C. R. Stroud, Jr., 529 (2008).

Publications in non-refereed journals:

[Kästel2006] J. Kästel, M. Fleischhauer, *Ein Stern-Gerlach-Experiment für langsames Licht*, Physik Journal **5**, 19 (2006).

Duttweilerstraße 22
67435 Neustadt an der Weinstraße

Jürgen Kästel

Tel: 0631 - 205 23 17
Tel (privat): 06327 - 50 78 86
Mobil: 0170 - 767 97 87
E-Mail: jkaestel@physik.uni-kl.de



Name: Jürgen Kästel
Geburtsdatum: 24. Februar 1975
Geburtsort: Neustadt an der Weinstraße
Verheiratet, 1 Kind
Deutsch

CURRICULUM VITAE

Werdegang:

1981 - 1985	Besuch der Grundschule Geinsheim
1985 - 1994	Besuch des Leibniz-Gymnasiums Neustadt an der Weinstraße
Juni 1994	Abitur
1994 - 1997	Ausbildung zum Physiklaboranten bei BASF AG, Ludwigshafen
Juli 1997	IHK-Abschlussprüfung zum Physiklaboranten
1997 - 1998	Vollzeitbeschäftigung als Physiklaborant bei BASF AG, Ludwigshafen
Sept. 1997 -	Freistellung zur Ableistung des Grundwehrdienstes in der
Juni 1998	Unteroffizier-Krüger-Kaserne, Kusel
1998 - 2004	Studium der Physik an der Technischen Universität Kaiserslautern Abschluss als Diplom-Physiker, Note: Mit Auszeichnung
Januar 2004	Diplomarbeit in theoretischer Physik: "Strahlungswechselwirkung von Atomen in Medien mit negativem Brechungsindex"
seit 2004	Wissenschaftlicher Mitarbeiter im Fachbereich Physik, Technische Universität Kaiserslautern Stipendiat des Graduiertenkollegs 792 "Nichtlineare Optik und Ultrakurzzeitphysik"
Juni - Aug. 2005	Besuch Harvard University und Harvard-Smithsonian center for Astrophysics (ITAMP)
September 2008	Promotion in Physik, Dissertation in theoretischer Physik zum Thema "Quantum interference and absorption suppression in negative index materials", Note: Mit Auszeichnung

Qualifikationen:

Gremientätigkeit

Mitarbeit im Fachausschuss für Studium und Lehre, Diplomprüfungsausschuss, Arbeitsgemeinschaft Zukunft der Physikausbildung, Sprecher des Fachschaftsrats, studentischer Koordinator des Graduiertenkollegs 792 "Nichtlineare Optik und Ultrakurzzeitphysik"

Lehre

Betreuung der Übungen zu den Vorlesungen "mathematischer Einführungskurs", "Mathematik für Physiker 2", "Experimentalphysik 2" (2x), "Theoretische Mechanik", "Quantenmechanik 1" (3x), "Quantenmechanik 2" (2x)

EDV

Administration von Linux-Client-Server-Architekturen, Erfahrung im Umgang mit MATHEMATICA, MATLAB, L^AT_EX, gängigen Officepaketem (MS Office, OpenOffice), Grundkenntnisse in Fortran, Shell-Skripte

Sprachkenntnisse

Englisch fließend in Wort und Schrift, Schulkenntnisse Latein

Weitere Aktivitäten

Klettern, Bergsteigen, aktiver Musiker im Landesblasorchester Baden-Württemberg und im Musikverein Haßloch

Preise:

September 1997: Auszeichnung für hervorragende Leistungen bei der Abschlussprüfung zum Physiklaboranten.

November 2004: "Preis des Freundeskreises der Technischen Universität Kaiserslautern e.V." für die Diplomarbeit "Strahlungswechselwirkung von Atomen in Medien mit negativem Brechungsindex".